TECHNISCHE UNIVERSITÄT MÜNCHEN

Department of Chemistry and Catalysis Research Center
Chair of Technical Electrochemistry

Boosting High Current Density Performance of Durable, Low Pt-Loaded PEM Fuel Cells

Gregor Simon Harzer

Vollständiger Abdruck der von der Fakultät für Chemie der Technischen Universität München zur Erlangung des akademischen Grades eines

Doktors der Naturwissenschaften (Dr. rer. nat.)

genehmigten Dissertation.

Vorsitzender:	Prof. Dr. Tom Nilges
Prüfer der Dissertation:	1. Prof. Dr. Hubert A. Gasteiger
	2. Prof. Dr. Klaus Köhler

Diese Dissertation wurde am 26.07.2018 bei der Technischen Universität München eingereicht und durch die Fakultät für Chemie am 29.08.2018 angenommen.

"The stone age did not end because the world ran out of stones, and the oil age will not end because we run out of oil."

Don Huberts
Head of Shell Hydrogen – 1999

Abstract

For large scale implementation of fuel cell technology, significant advances in system performance and durability need to be achieved while simultaneously lowering cost. In this thesis, approaches to increase the high current density performance of proton exchange membrane fuel cells by tailoring catalyst and catalyst layer properties are presented as well as the influence of different accelerated stress tests on their durability. First, the beneficial effect of altering the carbon support surface with -NH_x groups to enhance ionomer homogeneity in the catalyst layer is presented. Then, the catalyst morphology, i.e., the distribution of platinum nanoparticles on the external surface or inside the carbon black support, is controlled by the synthesis method and shown to result in better fuel cell performance when Pt particles are deposited preferentially on the outer surface of the support. Lastly, the degradation of catalyst layers by accelerated stress test is investigated, with a special focus on mass transport related phenomena. It could be shown that carbon corrosion during voltage cycling up to 1.0 V is negligible and that the oxygen transport resistance scales inversely with the available Pt surface area. By restricting the upper potential, low loaded catalyst layers could sustain 30000 potential cycles without performance degradation, pointing out a promising way for increasing system lifetime.

Kurzfassung

Um eine flächendeckende Verbreitung der Brennstoffzellentechnologie zu ermöglichen, muss die Leistung und Haltbarkeit des Systems weiter verbessert und deren Kosten reduziert werden. Diese Doktorarbeit befasst sich sowohl mit der Steigerung der Leistung von Protonenaustauschmembran-Brennstoffzellen im Hochstrombereich durch gezielte Veränderungen des Katalysators und der Katalysatorschicht als auch mit der Bestimmung von Degradationsphänomenen. Zunächst wird der positive Einfluss einer -NH_x Modifzierung des Kohlenstoffträgers auf die Ionomerverteilung und die daraus resultierende, höhere Leistung der Brennstoffzelle gezeigt. Die Morphologie des Katalysators, also die Verteilung der Platin Nanopartikel auf der äußeren Oberfläche oder innerhalb des Kohlenstoffträgers und der positive Effekt auf die Leistung, der aus einer bevorzugten Ablagerung von Platin auf der äußeren Oberfläche folgt, wird im folgenden Teil beschrieben. Zuletzt wird die Untersuchung der Lebensdauer durch beschleunigte Alterungstest beschrieben, wobei besonders die Degradation in Bezug auf Massentransportverluste im Vordergrund steht. Hier zeigt sich, dass die Kohlenstoffkorrosion bei Zellspannungen bis 1 V einen vernachlässigbaren Anteil an Sauerstoff Massentransportverlusten hat und dass diese hauptsächlich invers proportional zur verfügbaren Platinoberfläche sind. Wird die Zellspannung auf niedrige Werte beschränkt, führen 30000 Spannungszyklen zu keinerlei Einbußen der Leistung, wodurch ein vielverprechender Weg zur Steigerung der Halbarkeit von Brennstoffzellensystemen aufgezeigt wird.

Acknowledgments

This work was prepared during the time from November 2014 until August 2018 at the Chair of Technical Electrochemistry of the Department of Chemistry at the Technical University of Munich (TUM).

First of all, I would like to express my sincerest gratitude to my supervisor

Prof. Dr. Hubert A. Gasteiger

for his guidance and support during the past years. Your curiosity and passion for electrochemistry has always been inspiring for me and was a motivation even when experiments did not turn out as expected. The way you promote the honest and critical analysis of results and share your exceptional knowledge and experience with all your students is outstanding. Thank you very much for the almost endless possibilities you provided me during my time as PhD student and the time and effort you spend to help me pursue my academic goals.

The board of examiners is greatly acknowledged for accepting the responsibility of evaluating this thesis.

Certainly, this work would not have been possible without the help, guidance and support of a lot of other people to whom I would like to say thank you. My first contact to electrochemistry and the group of Prof. Gasteiger was during the Bachelor's Thesis (working on lithium-air batteries), so I am very thankful to my former supervisor **Cüneyt Kavakli** to lay the foundation for my academic career path. To **Frédéric Hasché**, my supervisor of the Master's Thesis, I have to give special thanks as he gave me the possibility to advance from battery to fuel cell research. In addition, I would like to acknowledge his support as mentor of my PhD project. I have learned a lot from both of you, which was certainly a crucial basis for the success this work.

Moreover, I would like to thank everyone I had the pleasure to work with during projects or for joint publications. I'm thankful to **Sourov Ghosh**, my project co-worker, for the endless times of trouble-shooting fuel cell test stations together as well as **Daniel Herein** and **Annett Reichl** for the fruitful discussions during our project meetings. My colleagues **Alin Orfanidi**, **Hany El-Sayed** and **Pankaj Madkikar** are acknowledged

for the great working atmosphere and productiveness during our joint research projects. **Jan Schwämmlein** deserves a special thanks as colleague during quite stressful times of holding submission deadlines for joint publications and finishing paper or lab work at every day or nighttime. Also, I appreciate the enthusiasm and hard work of **Ana Marija Damjanović** during her involvement in our projects. Your happiness combined with the constant singing or whistling in the hallway (or in the lab) was contagious and often helped to overcome the dejection of experimental backlashes.

Additionally, the hard work of student researchers which I had the pleasure to supervise should be acknowledged here. Thank you **Simon Qian**, **Philipp Pfändner**, **Andrea Blankenship** and **Ana Marija Damjanović** for your contributions to this work.

My office colleagues **Benjamin Strehle**, **Alexandra Weiß**, **Dominik Haering**, **Davide Menga** and **Michael Striednig** are acknowledged for their help and their ready ear in every situation; from answering "simple" thermodynamic or engineering questions to filing administrative paperwork or finding the right wording for a publication. **Christoph Simon** also deserves my gratitude for assistance with any problems in the lab as well as being the best conference-buddy on our common business trips. Speaking of conference trips and administrative paper work, **Veronika Pichler** is acknowledged for her constant help and great support related to any non-scientific question.

Most importantly, my special thanks go to **Thomas Mittermeier**, who has always greatly supported me with his seemingly endless knowledge of electrochemistry and German bureaucracy. Your selfless assistance in the lab or solving difficult scientific questions has greatly contributed to the success of this work.

Many thanks go to the mechanical and electrical workshop for their support. Additionally, the efforts of **Katia Rodewald** and **Hany El-Sayed** for acquiring electron microscopy images are greatly acknowledged.

I also do not want to miss on acknowledging the great working atmosphere which was created by all members of the Chair of Technical Electrochemistry during working hours as well as during leisure activities. Special thanks go to **Max Bernt**, **Christoph Simon** and **Armin Siebel** for thrilling matches of darts and exciting biking trips.

A very big thank you goes to my family, with my sisters **Laura**, **Carla** and **Nora**, and my parents **Ingrid** and **Gerd** for their constant support and encouragement. Also, the motivation (knowingly or not) by my friends is highly acknowledged. If you have been wondering what I did the last years, you now have the chance to read it in the following.

Lastly, I would like to address my gratitude to my girlfriend **Anja**. Almost since the beginning of our studies you have motivated me in times of scientific backlashes and helped to redirected my focus when the workload was overwhelming. Thank you very much for your constant support and the valuable time we spend together.

Contents

List of Acronyms

Abbreviation	Description
AST	Accelerated stress test
BET	Brunauer-Emmett-Teller method
BOP	Balance of plant
CCM	Catalyst coated membrane
COR	Carbon oxidation reaction
CV	Cyclic voltammetry
ECSA	Electrochemically active surface area
EW	Equivalent weight
FTIR	Fourier-transform infrared spectroscopy
GEIS	Galvanostatic electrochemical impedance spectroscopy
GDE	Gas diffusion electrode
GDL	Gas diffusion layer
GDS	Gas diffusion substrate
HFPO	Hexafluoropropylen oxide
HOR	Hydrogen oxidation reaction
HUPD	Hydrogen under potential deposition
MEA	Membrane electrode assembly
MPL	Microporous layer
MW	Molecular weight
ORR	Oxygen reduction reaction
PEFC	Polymer electrolyte fuel cell
PEIS	Potentiostatic electrochemical impedance spectroscopy
PEMFC	Proton exchange membrane fuel cell
PFSA	Perfluorosulfonic acid
PMFC	Polymeric membrane fuel cell
PTFE	Poly tetra-fluoroethylene
rf	Roughness factor
RH	Relative humidity
RSU	Rearranged sultone
SEM	Scanning electron microscope

SUSD	Start-up/shut-down
TEM	Transmission electron microscope
TFE	Tetra-fluoroethylene
TGA	Thermogravimetric analysis
TS	Tafel slope

1 Introduction

Disastrous air quality in cities around the world and the understanding that changes in the personal transportation sector are necessary to address this problem, lead to increasing number of electric vehicle sales. In China, sales were reaching almost 800000 in 2017, making it the world leader. For a populous country like China, this number appears relatively low, equating to only 1.37% of newly registered cars being electrically powered, e.g., battery electric vehicles. However, the German share of electric cars for newly registered vehicles is even lower with only 0.73% in 2017.[1] The question now arises, why the share of electric vehicle registrations is still marginal, despite financial incentives such as the "Umweltbonus" of 4000 € or tax cuts for electric vehicles; even the charging infrastructure is developing rapidly, making it possible to charge your vehicle almost everywhere, e.g., while you are shopping or in the cinema.

From recent studies it becomes evident that one of the main reasons (apart from high costs) is the large discrepancy between current battery electric vehicles and customer expectations with respect to range and recharging time, with an expected driving range of 463 km and a tolerable recharging time of less than one hour.[2] Current high speed chargers like the Tesla Supercharger are able to provide about 270 km of range in about 30 min for their *Model S* and *X* when the battery is at a low state of charge.[2] If the customer expectations with regards to range and charging time are the most important requirements, why are fuel cell electric vehicles not becoming bestsellers, as they are meeting customer requirements of more than 500 km range and less than 5 min refueling time already today, with the first commercial fuel cell vehicles like the Hyundai *ix35 Fuel Cell* or the Toyota *Mirai* available in Germany since 2015?[3,4]

A major impediment is that the infrastructure of hydrogen refueling stations is still limited, with only 43 fueling stations currently operating (additionally 33 planned) in Germany,[5] while electric charging stations are becoming readily available (> 8800, April 2018).[1] However, due to the extended range of fuel cell vehicles, a lower amount of fueling stations would be tolerable for a sufficient coverage.

More importantly, the price for a fuel cell electric vehicle is still significantly higher compared to battery electric cars and especially internal combustion engine cars. This is mainly due to the cost of the catalyst which contains the expensive and scarce platinum metal, as well as other specialized components like the perfluorinated membrane or the hydrogen tank. As the price is expected to decrease by economy of scales for some com-

ponents, most direct price reduction can be achieved by reducing the amount of platinum needed from currently ~30 g per car to levels which are closer to the amount commonly used in today's exhaust catalytic converters, namely to about 5 g Pt.[6] This reduction is also required in order to avoid Pt supply constraints once several millions of fuel cell vehicles per year would be produced.

An additional approach is to increase the power density of the fuel cell stack (in terms of W/cm^2), as this will reduce the total cell area and thus the cost for bipolar plates, diffusion media and membranes. This endeavor has become a major research focus, bringing together experts from the fields of catalyst synthesis, polymer membrane fabrication, catalyst layer design, cell component design and system engineering in order to address this challenge.

In the following, possible ways to increase the fuel cell performance, especially in the high current density region (i.e., at high power density), while reducing the Pt loading will be depicted at the catalyst and catalyst layer level. In addition, the durability of fuel cells is investigated by an imposed accelerated stress test to evaluate long term stability, which will ultimately allow to propose operational parameters to extend the lifetime.

1.1 Proton exchange membrane fuel cells

Proton exchange membrane fuel cells (PEMFC) are energy conversion devices which produce electricity and heat from the spatially separated oxidation of hydrogen and reduction of oxygen as shown in equations 1.1 and 1.2, respectively. The concept of electricity generation from the two gases was discovered in the year 1839 by Sir William Robert Grove and Professor Christian Friedrich Schönbein, while it took until 1957 when Willard T. Grubb invented the fuel cell comprising a polymer based ion exchange membrane. In the literature, several abbreviations such as PMFC (polymeric membrane fuel cell) and PEFC (polymer electrolyte fuel cell) exist for this type of fuel cell.[7] As also anion exchange membrane fuel cells could be summarized under the term PEFC, nowadays PEMFC (proton exchange membrane fuel cell) is widely accepted to specify the cation conductivity of the membrane, as opposed to existence of the polymer electrolyte membrane.

$$\text{HOR}: \quad \mathrm{H_2} \longrightarrow 2\,\mathrm{H^+} + 2\,\mathrm{e^-} \tag{1.1}$$

$$\text{ORR}: \quad \tfrac{1}{2}\mathrm{O_2} + 2\,\mathrm{e^-} + 2\,\mathrm{H^+} \longrightarrow \mathrm{H_2O} \tag{1.2}$$

$$\textstyle\sum: \quad \mathrm{H_2} + \tfrac{1}{2}\mathrm{O_2} \longrightarrow \mathrm{H_2O} \tag{1.3}$$

In a PEMFC, hydrogen is oxidized at the anode into protons and electrons in the hydrogen oxidation reaction (HOR, equation 1.1). Protons travel through the membrane towards the cathode, while the electrons are routed through an external circuit where they perform the electrical work. At the cathode, oxygen from air, protons and electrons

recombine in the oxygen reduction reaction (ORR, equation 1.2) to form water. In the following section, the essential components of a fuel cell are described with a focus on components that were of special interest for this thesis.

1.1.1 Fuel cell components

The components of a fuel cell are summarized in terms of a flow diagram in figure 1.1 and an illustration of an experimental cell setup is shown in figure 1.2. A single cell fuel cell is made of four major component groups, namely the structural components, i.e., endplates and flow fields, sealing materials, the gas diffusion layer (GDL) and the catalyst coated membrane (CCM), which will be described in more detail in the following. As a single fuel cell is able to provide about 0.8 V, several (hundred) single cells are stacked to form a so called fuel cell stack to increase the available voltage, which is required for high power (>0.1 kW) applications.

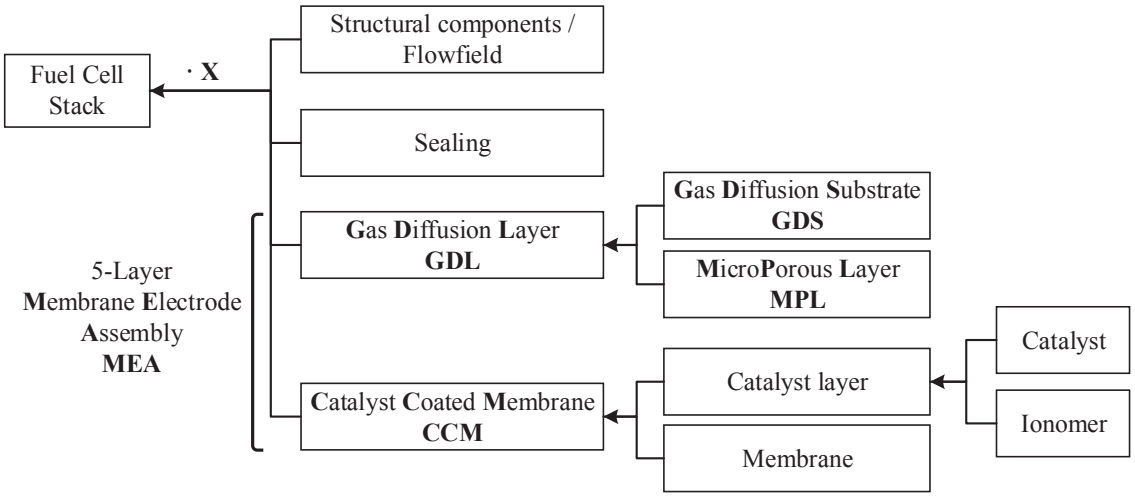

Figure 1.1: Flow diagram presenting the components of a fuel cell. Multiple fuel cells comprise a fuel cell stack.

Membrane electrode assembly

The membrane electrode assembly (MEA) is the heart of the fuel cell, as this is where the electrochemical conversion occurs. An MEA is built up symmetrically with a membrane in the center and the catalyst layers (anode and cathode) as well as the gas diffusion layers (GDL) on each side. As this assembly is made up of 5 different layers (one membrane, two catalyst layers and two gas diffusion layers), it is often referred to as a 5-layer MEA. Two different ways of fabricating an MEA are commonly employed, namely the deposition of a catalyst layer on the membrane (catalyst coated membrane – CCM) or the deposition of the catalyst/ionomer on the GDL (catalyst coated substrate – CCS or gas diffusion electrode – GDE).[8] As the MEAs for this thesis have been prepared from CCMs, the focus will be on

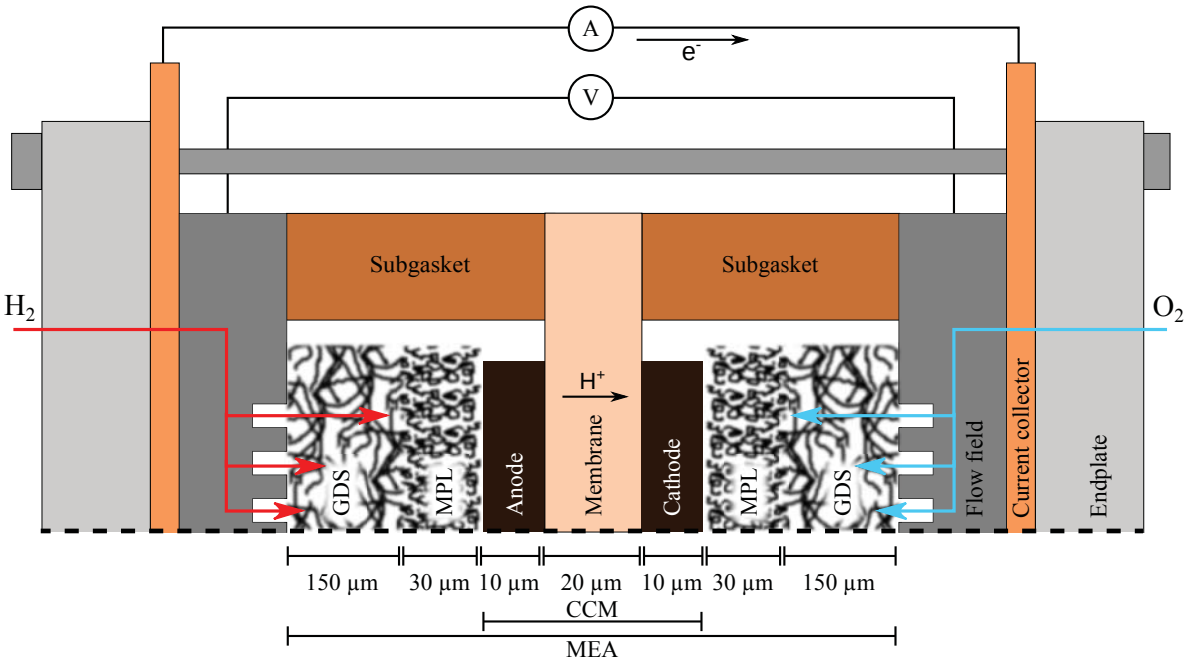

Figure 1.2: Schematic illustration of an experimental fuel cell setup (not drawn to scale) with indication of approximate dimensions of each component of the catalyst coated membrane (CCM) and membrane electrode assembly (MEA).

this preparation technique, while similarities between CCS and GDEs will be given when appropriate. As this section describes the general structure and components of an MEA, please refer to the experimental section (section 2) for more details on the manufacturing process.

CCM – Membrane and ionomer – In this section, the catalyst layer ionomer and the membrane are discussed simultaneously, as they are composed of the same class of material, namely a perfluorinated polymer containing ionic groups. Besides good ionic conductivity, the chemical stability of ionomers is of major importance, since the harsh operating conditions of a fuel cell are simultaneously reducing, oxidizing and thermally demanding. For this reason, perfluorinated ionomers are nowadays commonly used in PEMFCs, due to their excellent chemical stability and high ionic conductivity.[9] The ionic conductivity is obtained by the introduction of ionic side chains like perfluorocarboxylic acid, or more commonly, perfluorosulfonic acid (PFSA). Commercial ionomers are Nafion® (DuPont), Flemion® (Asahi Glass) or Aciplex® (Asahi Chemical), which mostly differ in the type of co-monomer, i.e., in the ionic sidechain of the final ionomer.[9,10] These polymers are produced industrially by the reaction of SO_3 with tetra-fluoroethylene (TFE), followed by a conversion to a rearranged sultone (RSU). This can then be reacted with two equivalents of hexafluoropropylen oxide (HFPO) to produce sulfonyl fluoride adducts, which, when heated with sodium carbonate, yield the vinyl ether PSEPVE. The synthesis process is shown in figure 1.3, including the co-polymerization with TFE to the final Nafion® ionomer by a free radical polymerization mechanism.[9]

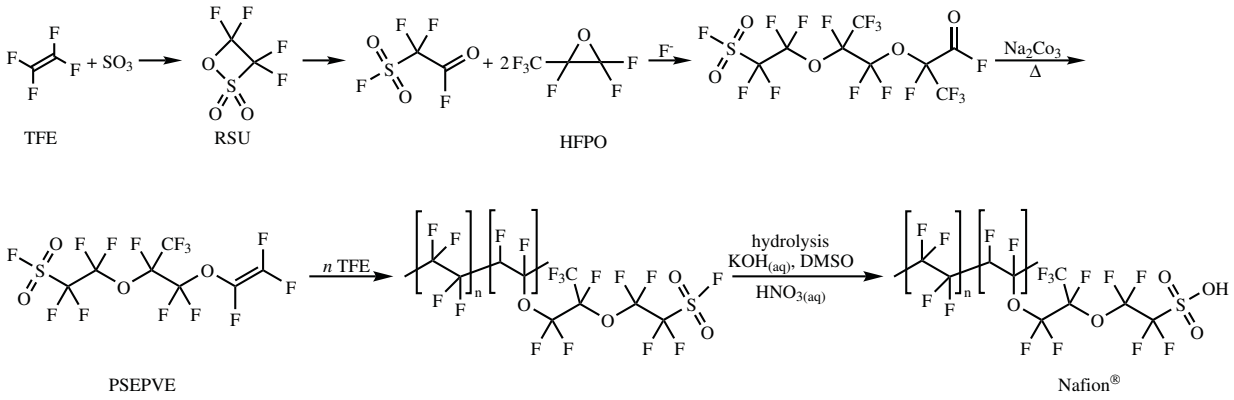

Figure 1.3: Synthesis process for the membrane co-monomer PSEPVE and polymerization with n TFE ($n \approx 3$ for 700 EW) to the final Nafion® ionomer.[9]

As this synthesis involves dangerous reactants, e.g., TFE under high pressure and at high temperature, only few chemical companies in the world prepare these polymers, which results in a relatively high cost of these types of materials ($2000-5000/kg).[11] Additionally, the low production volume of approximately 65 t/year (2003)[9,11] compared to high-volume polymers (Nylon: 5.4×10^6 t/year; 2016)[12] results in very high material cost. However, a price estimate by DuPont in the year 1998 for high volume manufactured membrane materials already stated a price of about $10/kW,[9] which in recent cost estimations from 2016 is even reduced to below $8/kW, equating to about $250/kg, even though these studies express a large uncertainty for ionomer cost prediction.[11,13,14]

The final ionomer is made of a hydrophobic backbone from the TFE co-polymerization and an ionic sidechain of the PSEPVE monomer terminated by the sulfonic acid group. Due to the large difference in polarity, the polymer arranges in spherical clusters with ionic domain sizes in the range of 3-4 nm being surrounded by a continuous fluorocarbon domain. This model has been proposed by Hsu and Gierke in 1983,[15] and is still used to describe and explain ionomer properties today, while more recent models include a third domain, namely an interfacial region which depends on the amount of ionic groups in the polymer.[9,10,16–18] Important characteristics of ionomeric polymers are the molecular weight (MW) and the equivalent weight (EW). With the MW of an ionomer being generally difficult to assess – lying in the range of $1\text{-}10\times10^5$ g/mol – the more important parameter is the EW, as it describes the amount of ionic groups referenced to the mass of the polymer (in units of $g_{polymer}/mol_{SO_3^-}$).[9,17] For most ionomers, the EW ranges from about 700 to 1500 $g_{polymer}/mol_{SO_3^-}$, where these boundaries are posed by excessive swelling or dissolution at low EW on the one hand and by an insufficient ionic conductivity at high EW on the other hand. The determination of the equivalent weight is usually accomplished by FTIR techniques, atomic sulfur determination or acid-base titration.[9,10,17] For fuel cell applications, the physical properties of the ionomer like the swelling behavior, the ionic conductivity or the gas permeability are of major interest and need to be optimized for

different fuel cell operating conditions. This can be achieved by selection of the MW, of the sidechain length and type, and most importantly by the EW. A thorough discussion of the relevant relationships is presented in Ref[19]. In general, a lower EW and higher relative humidity (*RH*) or temperature lead to a higher ionic conductivity (0.1 S/cm, 80°C, 80% *RH*) but also to increased ionomer swelling, particularly in the presence of liquid water. The gas permeability generally increases with temperature and relative humidity for the same type of ionomer, while it is generally higher for a low-EW ionomer. While high ionic conductivity in the membrane and catalyst layer is important for high current density operation, swelling of the ionomer in the catalyst layer reduces its porosity, hence the available pore volume for oxygen diffusion. Therefore, a proper selection of ionomer and membrane is crucial for optimum fuel cell performance and will be discussed in more detail in section 1.2 (page 19).

The fabrication of membranes from the ionomer can be either done by extrusion of the polymer in the SO_2F form and subsequent hydrolysis, solution casting of the ionic form,[9,20] impregnation of a reinforcement layer,[21] or direct printing from solution in the MEA fabrication process.[22] Nowadays, most membranes contain a reinforcement layer, e.g., expanded PTFE, and have a thickness on the order of 20 µm, whereas a further decrease of the thickness is desired in order to reduce the cell resistance (10 µm are considered to be the practical limit imposed by the H_2 and O_2 permeation).

During the harsh conditions of fuel cell operation, the ionomer material in the catalyst layer and membrane can degrade due to chemical attack and/or due to mechanical failure from repeated volume expansion/contraction induced by *RH* cycles. The chemical degradation occurs generally by an attack of non-fluorinated endgroups by a highly reactive $^{\cdot}OH$ radical according to figure 1.4.[20,23–25] At dry operating conditions, the $^{\cdot}OH$ radical can also easily attack the $R{-}CF_2{-}SO_3H$-group which will then decompose to $R{-}CF_2^{\cdot}$ from where the chain unzipping continues in a similar manner.[26] By post fluorinating the ionomer, introducing radical scavengers, reinforcement of the membrane and carefully controlling the fuel cell operating conditions, the durability of the membrane and ionomer has been extended beyond 10000 h, posing almost no lifetime limitations to fuel cell applications.[25,26]

CCM – Catalyst layer – Platinum metal is the state of the art catalyst for PEM fuel cells on both anode and cathode, due to its high activity for hydrogen oxidation and oxygen reduction as well as its excellent stability.[27,28] To increase the available surface area for electrochemical reactions, Pt is usually introduced as nanoparticles into the catalyst layer to increase its specific surface to volume ratio. The Pt nanoparticles are supported on carbon black, which enables high dispersions of the metal and avoids agglomeration as well as ascertains good electrical conductivity throughout the electrode. In addition, the carbon creates a porous structure in the catalyst layer to enable gas transport.[29,30] An exemplary electron microscope image of a catalyst particle is shown in figure 1.5.

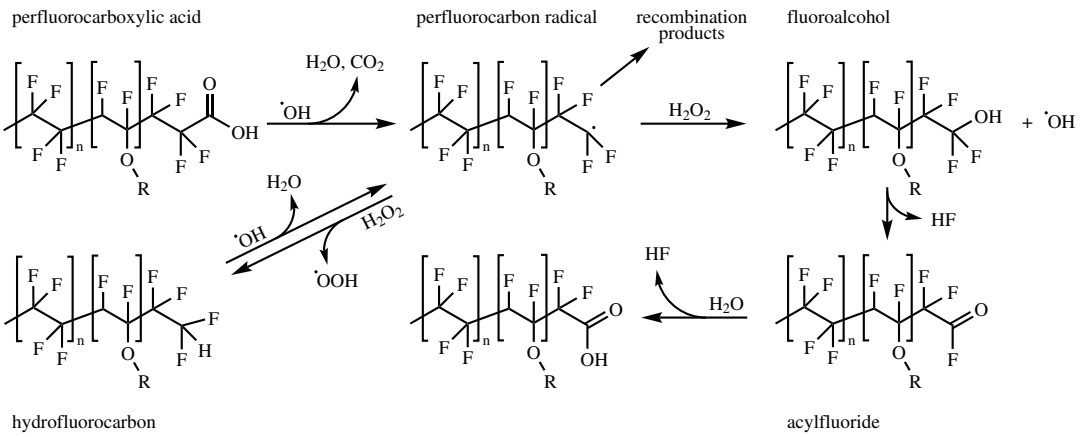

Figure 1.4: General degradation of PFSA ionomers by the main chain unzipping mechanism following the mechanism proposed in Ref[23].

Carbon blacks are available in a variety of different structures, with differences in surface area and pore size distribution as well as in the degree of graphitization. They are usually prepared by pyrolysis or incomplete combustion of carbon containing precursors and classified as furnace, channel, thermal or lamp black. Carbon blacks usually form primary, spherical particles of about 5-400 nm diameter from graphitic planes, which intergrow or overlap to form a branched network referred to as secondary structure (see figure 1.5).[30–33] This secondary structure is mechanically highly stable and in the process of catalyst layer fabrication, leads to the desired, high porosity of the final catalyst layer. The degree of graphitization, the size of the primary particle and the amount of secondary structuring ultimately affects the surface properties of the carbon black material. In general, the BET surface area ranges from about 60 m^2/g for a relatively dense "Acetylene Black" with large, 40 nm diameter primary particles, to 1500 m^2/g for "Black Pearls 2000" with about 10 nm primary particles and a large micropore volume.[30,34] For fuel cell applications, the most widely used carbon supports are "Vulcan XC-72" with a BET area of 250 m^2/g and "Ketjenblack" with a BET area of about 800 m^2/g due to its higher micropore volume.[30,35,36] Beside the morphology and structure of the carbon support, its surface properties, e.g., polarity or hydrophilicity, are of major importance. In section 3.1, the beneficial effect of a surface treatment of a commercial carbon support with -NH_x moeities on fuel cell performance is presented. The increased performance is attributed to a better ionomer distribution during catalyst layer fabrication due to increased interaction of the positively charged carbon surface with the negatively charged sulfonic acid groups of the ionomer.[36] In addition to common carbon materials, new types of supports with defined pore geometries, so-called ordered mesoporous carbons, were developed and tested for fuel cell applications.[37–39] Their beneficial effect on fuel cell performance will be described in more detail in section 1.2 (page 19).

Several different synthesis methods exist to deposit Pt nanoparticles on the carbon

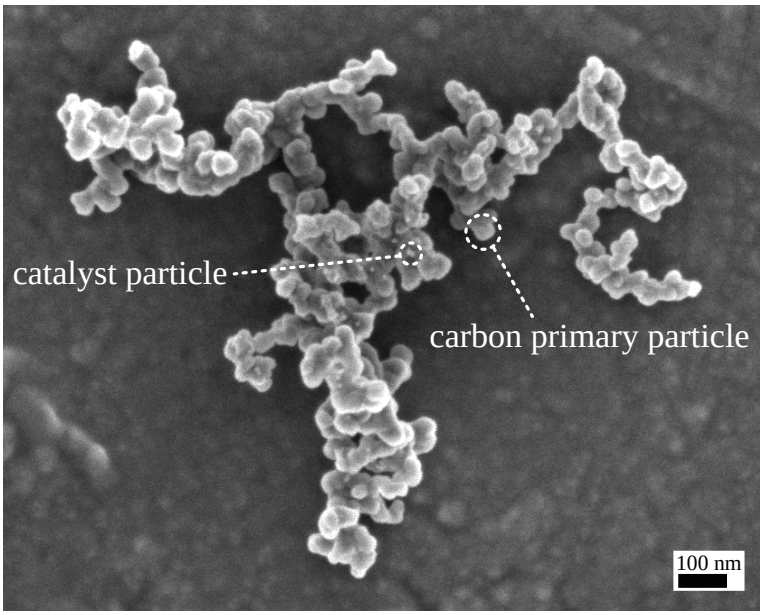

Figure 1.5: Scanning electron microscope image (50000× magnification) of a primary carbon black agglomerate used as a support for a Pt catalyst. The assembly of fused carbon primary particle agglomerates in an electrode creates a porous network (secondary agglomerate structure) providing sufficient void volume (average pore size of 50-200 nm) for gas transport in the catalyst layer. Image recorded by Katia Rodewald, Wacker Chair of Macromolecular Chemistry, TUM.

black that are based on electrochemical methods, wet chemical redox reactions or impregnation-reduction techniques.[40–42] Attributed to the well controllable synthesis and the good scale-up potential, the industrial production of catalysts mainly focuses on impregnation-reduction techniques or wet chemical redox reactions. Depending on the type of catalyst and the annual production, the estimated catalyst cost for automotive applications varies between about $\$30/g_{cat}$ for a Pt alloy cathode catalyst at low annual production to about $\$10/g_{cat}$ for a pure Pt/C catalyst at high annual production. For a car with a total amount of about 15 g platinum (anode and cathode), and a loading of $30\%_{wt}$ Pt on carbon for the cathode catalyst and $20\%_{wt}$ Pt on the anode catalyst, this would translate to roughly \$1500 of catalyst costs for an automotive fuel cell stack at low manufacturing numbers of 1000 units per year, however decreases to about \$700 at production volumes of 500000 units per year.[13]

Lowering the catalyst costs whilst maintaining the overall performance requires a reduction of the noble metal content, accompanied by an increased activity and surface area of the catalyst. The activity of platinum for the oxygen reduction is affected by the exposed facets of the Pt crystallites, which in turn is influenced by the Pt particle size as the ratio of each crystal plane changes with particle size and shape.[43,44] Furthermore, the adsorption strength of oxygen species onto the Pt surface changes with particle size, leading to different ORR activities for different particle sizes.[45,46] In general, the activity of Pt surfaces (in adsorbing electrolytes, e.g., $H_2SO_{4\ (aq)}$ or sulfonic acid ionomer) decreases in

the order of Pt(110)>Pt(100)>Pt(111) and with decreasing particle size, imposing a lower limit of feasible particle sizes (about 3–5 nm).[43–48]

In addition to particle size and crystal plane effects on the ORR activity of pure platinum, the ORR activity is strongly increased by the introduction of other metals to form Pt alloys. The field of catalyst optimization by alloy formation has developed strongly in the past decades, bringing together theoretical modeling for the identification of the most active and stable alloys,[49–52] high throughput synthesis and characterization to validate theoretical calculations as well as advanced characterization techniques to determine reaction mechanisms.[53,54] The currently most frequently applied Pt alloys as cathode catalyst for the ORR are PtNi and PtCo alloys due to their good stability and excellent activity of about 1000 A/g_{Pt} compared to 200 A/g_{Pt} for a pure Pt catalyst (referenced at 0.9 V, room temperature and O_2 saturated 0.1 M $HClO_4$).[28,55,56] It is for these reasons that first commercial fuel cell products (e.g., the Toyota *Mirai* fuel cell vehicle) and fuel cell cost predictions are based on this type of catalyst.[13] Besides binary alloy nanoparticles with varying composition, advances in ORR activity have been made by introducing ternary (or quaternary) platinum alloys or controlling the alloy particle shape to promote ORR activity.[57–61] As described above for pure platinum crystal planes, the ORR activity also depends on the surface planes for Pt alloys, hence the catalyst performance can be increased by selectively creating nanoparticles with the preferred crystal plane surfaces. For Pt_3Ni alloys, the most active plane is the (111) plane, outperforming a pure Pt catalyst surface by a factor of ten.[62] As this surface plane is exclusively terminating octahedrally shaped particles, the shape-controlled synthesis of Pt alloy particles has developed to a major research field for catalyst optimization.[58,63,64] Yet, the high mass activity of catalysts does not necessarily translate into superior fuel cell performance, as its implementation into an MEA imposes several other constrains as described in section 1.2.

For any fuel cell application, the catalyst not only needs to be highly active, but needs to have a sufficient durability under operating conditions. It is well known that Pt catalysts degrade during operation and that this degradation occurs on several levels, namely the degradation of the Pt active surface area – introducing a kinetic penalty – or degradation of the carbon support, leading to an increased mass transport resistance and hence lower performance at high current density. The degradation of the cathode catalyst is usually much more severe compared to the anode catalyst, which is attributed to the change of the cathode potential upon load cycles of the fuel cell, resulting in voltage cycles imposed onto the cathode catalyst. For this reason, voltage cycling is a frequently applied tool to study and estimate the durability of cathode catalysts and MEAs. In contrast, the anode potential usually stays close to the hydrogen potential.[65] Catalyst degradation can be studied by rotating disk electrode (RDE) experiments, however the results may not always be directly compared to the degradation occurring in an MEA due to the different amount of water and ionomer per catalyst surface in wet electrochemical tests (in an aqueous acid)

compared to tests in an actual fuel cell.[66] Hence, the best estimation of fuel cell durability can be obtained from accelerated stress tests (ASTs) of MEAs in single-cell fuel cells (5-50 cm^2 active area) or in actual fuel cell stacks (typically so-called "short-stacks", with 10-20 full active area MEAs). The most common ASTs cycle the potential in triangular waves (TW),[65–72] square waves (SW),[68,72–74] or a combination thereof (triangular wave with hold, TW-H).[75,76] The repeated potential change leads to oxidation/reduction cycles of the Pt surface, which ultimately results in a dissolution of ionic Pt species from the metal surface. The ions can diffuse through the ionomer phase and redeposit on existing Pt particles – a process referred to as Ostwald ripening – or they can diffuse towards the membrane, where they are reduced to metallic platinum by hydrogen which is crossing over from the anode compartment.[65] As smaller particles are more susceptible to dissolution, Ostwald ripening will lead to an increase of the average particle size, thus a decrease of the electrochemically available surface area.[72] A decrease of available Pt surface area is also observed when the Pt ions are reduced in the ionomer film/membrane phase, resulting in electrically insulated Pt particles. These Pt deposits can be easily visualized post-mortem by different imaging techniques like transmission or scanning electron microscopy.[65,71,76] Furthermore, the carbon support is thermodynamically unstable above 0.2 V_{RHE} (considering CO_2 as reaction product),[77] even though the sluggish kinetics of the carbon oxidation reaction (COR) enable its use as catalyst support in fuel cells under normal operating conditions ($<$1 V_{cell}).[78] Unfortunately however, certain operating conditions like the hydrogen/air front passing through the anode during start-up or shut-down (SUSD) can create high voltages on the cathode ($\simeq$1.5 V), leading to severe carbon corrosion accompanied by the so-called cathode catalyst layer thinning.[79] This reduces the void volume in the catalyst layer, hence increasing the resistance for oxygen transport, ultimately leading to a severe decrease of performance. In addition, carbon corrosion can lead to a detachment of Pt particles from the support, rendering them electrically disconnected, thus decreasing the active surface area for catalysis.

Gas Diffusion Layer – The outermost layer of an MEA is the gas diffusion layer, GDL, which is in contact with both the flow field and the catalyst layer of the CCM. Its purpose is manifold, namely to distribute the gas from the flow channel evenly towards the catalyst layer surface as well as to transport produced water from the electrode back towards the flow field. In addition, the GDL is important for heat removal from the electrode and is indisputably necessary to create electrical contact between the catalyst layer and the flow field/current collector. For these reasons, the GDL must have good thermal and electrical conductivity, as well as a high porosity for gas transport while having a low contact resistance towards the flow field and the catalyst layer.[80] In general, a GDL is composed of a gas diffusion substrate, GDS, which usually consists of a carbon fiber paper that may or may not be woven and a microporous layer which is made of carbon black or similar material. The optimization of the GDL is an important determining factor for high

current density performance of the fuel cell, for which good transport of gaseaous O_2/H_2O and liquid water is crutial. For better water management, i.e., to avoid flooding of the pores with liquid water, the GDS and/or MPL are hydrophobically treated with PTFE or similar fluorocarbon polymers.[80,81] As the GDL is required to provide a two-phase flow, i.e., gas transport towards the catalyst layer and liquid water transport away from it, large pore sizes in the MPL were found to be advantageous due to the lower capillary pressure and the more facile removal of water under wet conditions.[81] In addition to the properties of the GDL itself, the assembly of the MEA into the hardware influences the fuel cell performance as well. Higher compression of the GDL is advantageous due to a lower contact resistance, however the concomitant decrease in porosity leads to poorer mass transport properties, hence lower performance at higher current density. On the other hand, too low compression of the GDL results in water accumulation between the MPL and the catalyst layer, which also leads to a higher transport resistance.[82] The optimum performance was found to lie in the range of 20% compression of the GDL in the case of most carbon fiber papers (e.g., from Toray or Freudenberg). The compression for a laboratory scale cell is commonly adjusted by choosing the appropriate thickness of the subgasket material, as all components except the GDL are considered incompressible. For fuel cell stacks, the compression is achieved by applying a certain pressure on the endplates and maintaining the displacement by fixation straps.[13]

The prize for GDL materials is estimated at ≈\$2000 for a 80 kW stack (about 8 m^2 total active area) at 1000 units per year (≈\$120/m^2), and \$95/stack at 500000 units per year (approximately 8 mio m^2 total production per year). The relatively high price results from the substantial energy demand for heat treating the GDS fiber material and is not primarily due to high material costs.[13]

Structural components, sealing and flow fields

For laboratory scale experiments, the MEA is assembled into a single-cell comprised of flow fields, sealing and gaskets, as well as endplates (see figure 1.2) The flow field is usually made from graphite or a graphite composite with a flow pattern machined into its surface for gas distribution over the active area of the MEA. Since the flow channel pattern, e.g., serpentine or straight channels, and the channel dimensions determine the pressure drop across the cell hardware, the flow field is an important design parameter to influence the fuel cell performance.[83] When the pressure drop across the cell is not correctly adjusted to the desired operating range, e.g., cell pressure, flow or *RH*, water condensation within the flow channel may occur, leading to a partial blockage of the catalyst layer, hence a decrease in performance. On the other hand, a very high pressure drop induces a reactant pressure gradient along the active area, rendering the quantification of fundamental kinetic or transport parameters more complex and imprecise.[82] For automotive applications, the flow field in a stack is designed as a bipolar plate, with one side of the plate being the

anode of one MEA and the other side being the cathode of the adjacent MEA with cooling channels in their center. The bipolar plate is usually made of stainless steel, titanium or carbon/polymer composite materials due to their better large scale processability compared to graphite plates.[84] For metal plates, the flow channels can be embossed or stamped, followed by the addition of a corrosion protection layer, providing short cycle times for mass production.[13,85]

The MEA is sealed gas-tight against the flow field or bipolar plate by rubber seals for automotive applications and by a PTFE coated fiberglass gasket in most small-scale single-cell experimental setups. The incompressible gasket is also used to control the compression of the GDL by choosing the appropriate thickness for a desired displacement of the GDL. The structural integrity of the assembly is assured by endplates which serve to distribute the compression force evenly across the fuel cell stack or the single-cell. A copper current collector is added between the endplate and the flow field to channel the electron flow, while the cell voltage is usually measured directly at the flow field in the experimental setup.

Cost analysis of an automotive fuel cell system

The cost estimations for each component described in the previous sections are summarized in figure 1.6 as a pie chart at low (a) and high (b) manufacturing volumes of automotive fuel cell systems.

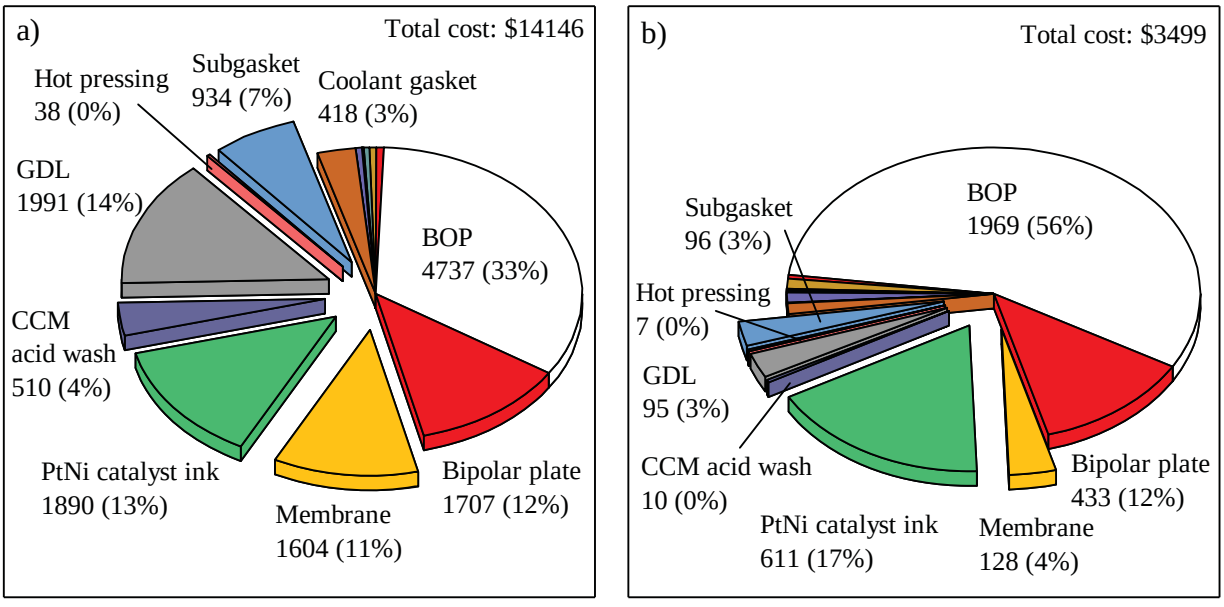

Figure 1.6: Cost estimation for a 80 kW_{net} (88 kW_{gross}) automotive fuel cell system (based on the year 2017) at 1000 units per year (a) and 500000 units per year (b), with the MEA components highlighted by separation from the pie chart. The number specifies the component cost (in $US) with the respective percentage of total cost given in parentheses. The graphs are made based on data by James et al.[13]

At low manufacturing numbers of 1000 units per year, the fabrication cost of an au-

tomotive fuel cell system is estimated to be around $14000 of which the MEA accounts to roughly half of the entire system, with the CCM contributing about 28% as the cost for the membrane and Pt based catalyst are relatively high. In addition, the GDL has a substantial contribution of 14% to the overall system cost. Small contributions to the overall cost such as the current collector, the stack housing and others are not independently labeled as their contribution is marginal. Beside the MEA fabrication, the bipolar plates contribute a significant fraction of total cost, due to their complex fabrication and the high number of required plates, i.e., one plate per MEA. The balance of plant (BOP) consisting of, e.g., humidifiers, air/fuel and cooling loops, system controller and auxiliary electric components contributes about 33% to the overall system cost.

At higher manufacturing volumes of 500000 units per year, the cost estimate for the entire system amounts to $3499, with the main contributor being the BOP with roughly 56%. The cost share of bipolar plates remains at 12% due to the large number of required plates, while the MEA fabrication cost is reduced to 27%. The largest share for a single component arises from the Pt catalyst ink due to the high cost of platinum; the cost of the catalyst does therefore not reduce significantly by an increased manufacturing volume and may even increase when production increases. This analysis reveals the necessity to further reduce the catalyst loading to decrease the overall system cost at high manufacturing volumes.

In comparison to an internal combustion engine (with the same 80 kW power as the FC system), where the estimated cost ranges between $28.5/kW ($2280 for 80 kW)[86] to $1691 for 80 kW ($531+$14.5/kW),[87] the price for the FC system is still significantly higher even at 500000 units per year. As a direct comparison of different energy storage and propulsion technologies, e.g., battery electric vehicle, FC electric vehicle, internal combustion engine (ICE) vehicle or hybrids thereof, is difficult due to different system architectures, the total cost of ownership (TOC) for the customer is usually estimated. Several studies with different focus and cost assumptions have estimated that by the year 2030, the TOC for fuel cell vehicles will be similar to internal combustion engines or battery electric vehicles and that the most economic selection of the powertrain depends on the anticipated use and driving range.[86,88] Hence, an implementation of FC vehicles appears reasonable from a technological and economical point of view, its commercial success however depends on customer preferences and the availability of a hydrogen refueling infrastructure.

1.1.2 Fuel cell chemistry

In the following section, relevant thermodynamic and kinetic aspects of fuel cell chemistry are briefly described. The cell voltage, E_{cell} [V], at operating conditions, i.e., at a given current density i [mA/cm^2], can be calculated by subtraction of all known voltage loss contributions according to equation 1.4 from the reversible cell voltage E_{rev}.[89]

$$E_{\text{cell}} = E_{\text{rev}} - i \cdot \underbrace{(R_{\text{membrane}} + R_{\text{contact}})}_{R_{\text{HFR}}} - \eta_{\text{HOR}} - |\eta_{\text{ORR}}| - i \cdot (R^{\text{eff}}_{\text{H}^+,\text{cath}} + R^{\text{eff}}_{\text{H}^+,\text{an}}) - \eta_{\text{tx}} \quad (1.4)$$

Here, R_{membrane} and R_{contact} refer to the ionic and electric resistance from the membrane and the contact resistances inside the cell, which are experimentally accessible by the high frequency resistance, R_{HFR}. The kinetic overpotentials for the hydrogen oxidation reaction (HOR) on the anode and oxygen reduction reaction (ORR) on the cathode are termed η_{HOR} and η_{ORR}, respectively. Due to the fast kinetics of the HOR on Pt catalysts, the overpotential on the anode is usually insignificant ($\eta_{\text{HOR}} \approx 0$) and the reaction occurs close to the membrane-electrode interface. Hence, the effective resistance for proton transport in the anode, $R^{\text{eff}}_{\text{H}^+,\text{an}}$, is small, resulting in a negligible potential drop ($i \cdot R^{\text{eff}}_{\text{H}^+,\text{an}} \approx 0$). As the overpotential for the ORR is substantial, the entire thickness of the catalyst layer is utilized for the reaction, requiring extended proton transport across the thickness of the electrode. The resistance for proton transport in the cathode catalyst layer is termed $R^{\text{eff}}_{\text{H}^+,\text{cath}}$ and contributes significantly to observed voltage losses. Note that E_{rev}, η_{HOR} and η_{ORR} are calculated for the local electrode conditions (temperature, reactant concentration), however, the evaluation is usually based on the conditions in the flow field. Consequently, a resistance for species transport from the flow channel to the reaction site, η_{tx}, needs to be incorporated. A graphical representation of the loss contributions is given in figure 1.7 for a fuel cell polarization curve. It is evident that the most substantial loss arises from the significant overpotential for the ORR (η_{ORR}). In the following, each loss contribution is described in detail.

The reversible cell voltage, E_{rev}, is the difference between the cathode and anode reversible potential that follow the Nernst equation (equation 1.5) depending on the reactant species, its activity, a_i, and stoichiometric coefficient, ν_i, exemplarily shown for the hydrogen oxidation reaction 1.1. Here, E_{H_2} denotes the reversible potential, while $E^0_{\text{H}_2}$ denotes the reversible potential at standard conditions (298 K, reactant activity is unity), both referenced to the standard hydrogen electrode (SHE). R denotes the universal gas constant (8.3145 J/molK), T [K] is the temperature, n is the number of transferred electrons in the reaction (n=2 for reaction 1.1) and F is the Faraday constant (96485 As/mol).

$$E_i = E^0_i + \frac{\text{R}T}{n\text{F}} \ln\left(\frac{\prod^i a^{|\nu_i|}_{i,\text{ oxidized}}}{\prod^i a^{|\nu_i|}_{i,\text{ reduced}}}\right) \qquad E_{\text{H}_2} = E^0_{\text{H}_2} + \frac{\text{R}T}{2\text{F}} \ln\left(\frac{a^2_{\text{H}^+}}{a_{\text{H}_2}}\right) \quad (1.5)$$

By convention, the cell potential is calculated by subtracting the potential of the anode in a galvanic cell from the cathode potential, which in the case of the fuel cell reaction 1.3 is $E_{\text{rev}} = E_{\text{O}_2} - E_{\text{H}_2}$. Writing the general Nerst equation (left equation in 1.5) for the HOR and the ORR reaction and simplifying mathematically results in equation 1.6, relating the

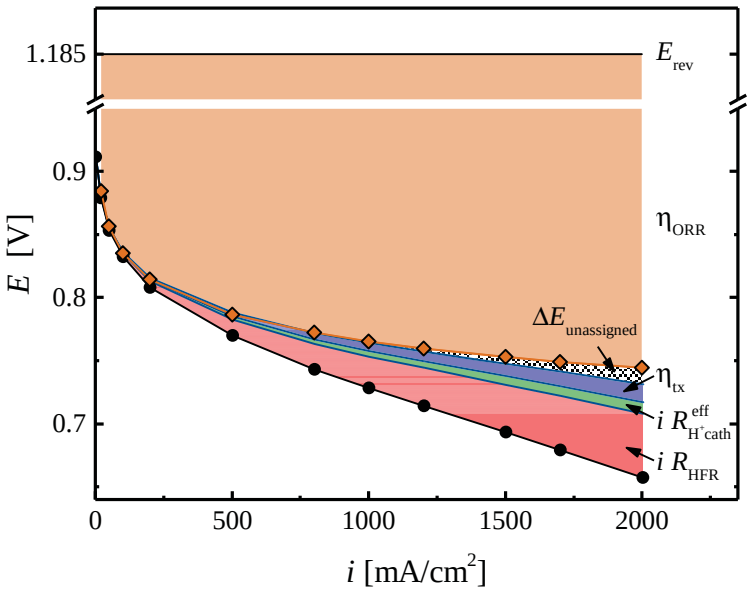

Figure 1.7: Fuel cell polarization curve recorded in a 5 cm^2 MEA at differential flow of H_2/air, 80°C, 170 kPa_{abs} and 100% *RH* (black circles). Each loss contribution, namely the ohmic resistances, R_{HFR}, the resistance for proton transport in the cathode catalyst layer, $R^{eff}_{H^+,cath}$ and the oxygen transport resistance, η_{tx}, are subtracted from the measured curve and compared to a purely kinetically limited polarization curve (orange diamonds). This curve was calculated from catalyst specific properties ($i^{mass}_{0.9\,V}$=101 A/g, *ECSA*=56 m^2_{Pt}/g_{Pt}) and a cathode loading of 0.4 mg_{Pt}/cm^2. The discrepancy between the fully corrected polarization curve and the kinetically predicted is termed $\Delta E_{unassigned}$.

reversible cell voltage, E_{rev}, to the activity of H_2, O_2 and H_2O.[90]

$$E_{rev} = E^0 + \frac{RT}{2F} \ln\left(\frac{a_{H_2} \cdot (a_{O_2})^{\frac{1}{2}}}{a_{H_2O}}\right) \tag{1.6}$$

E^0 represents the reversible H_2/O_2 cell voltage at standard conditions and can be calculated according to equation 1.7 from the Gibbs free energy change, $\Delta G^R = \Delta G^f_{H_2O} - \left(\Delta G^f_{H_2} + \frac{1}{2}\Delta G^f_{O_2}\right)$ for reaction 1.3, for which the free energies of formation, ΔG^f_i, can be conveniently obtained from thermodynamic tables.

$$E^0 = \frac{-\Delta G^R}{nF} \tag{1.7}$$

However, care must be taken as the free energy of formation not only depends on temperature but also on the physical state, i.e., liquid or gaseous state. When the product water is considered as a liquid, ΔG^R equals 237.13 kJ/mol which corresponds to a standard potential of 1.23 V.[91] In this case, the activity of water is defined according to equation 1.8 as the ratio of the partial pressure of water, p_{H_2O}, and the saturation vapor pressure, $p^{sat}_{H_2O}$, respectively. This relation is also referred to as relative humidity, *RH*.[89]

$$a_{H_2O} = \frac{p_{H_2O}}{p^{sat}_{H_2O}} \equiv RH \tag{1.8}$$

When water is considered in the gaseous state ($\Delta G^R = 228.57$ kJ/mol) the standard potential is 1.18 V while the water activity is defined acording to equation 1.9. Here, the activity, a_i, is defined as the reactant's partial pressure, p_i, divided by the reference pressure, $p^0 = 101.13$ kPa.[90,91]

$$a_i = \frac{p_i}{p^0} \tag{1.9}$$

The potential drop at a given current density, i, due to contact resistances, R_{contact}, and ionic/ohmic resistances in the membrane, R_{membrane}, can be determined from the high frequency resistance, *HFR*, obtained from AC impedance analysis, typically as the high frequency intersect of the impedance data with the real axis in a Nyquist plot.

As the reaction kinetics of the HOR are very fast on Pt surfaces in acidic medium, the overpotential η_{HOR} is usually negligible.[27,92] On the other hand, η_{ORR} is substantial and can be calculated by equation 1.10 with the hydrogen crossover current, i_{x,H_2} [A/cm^2], the cathode catalyst layer Pt loading, $L_{\text{Pt, cath}}$ [mg$_{\text{Pt}}$/cm^2], the electrochemically active surface area (*ECSA*), A_{Pt} [m$^2_{\text{Pt}}$/g$_{\text{Pt}}$], and the catalyst specific exchange current density at a given temperature and oxygen partial pressure, $i^0_{\text{ORR},(T,p_{O_2})}$ [A/cm$^2_{\text{Pt}}$].[89,93] The product of $L_{\text{Pt, cath}}$ and A_{Pt} is often referred to as the roughness factor, rf [cm$^2_{\text{Pt}}$/cm^2], for which the number 10 in equation 1.10 is a unit conversion factor.

$$\eta_{ORR} = \underbrace{\frac{2.303 \cdot \text{R}T}{\alpha_c \cdot \text{F}}}_{TS} \cdot \log \left[\frac{i + i_{x,\text{H}_2}}{\underbrace{10 \cdot L_{\text{Pt, cath}} \cdot A_{\text{Pt}}}_{rf} \cdot i^0_{\text{ORR},(T,p_{O_2})}} \right] \tag{1.10}$$

The first term in equation 1.10 corresponds to the Tafel Slope, TS, where α_c denotes the cathodic transfer coefficient (describing the symmetry of the energy barrier and the number of exchanged electrons in the rate determining step). The catalyst specific exchange current density can be calculated by equation 1.11 from the specific exchange current density normalized to reference conditions, $i^{0,\text{ref}}_{\text{ORR,}}$ (T_{ref}=80°C, $p^{\text{ref}}_{\text{O}_2}$=101.3 kPa) using the reaction order, γ_{O_2} (≈0.5) with respect to the O_2 partial pressure and the activation energy for the ORR at zero overpotential, $E^{\text{ref}}_{\text{act, ORR}}$ (≈67 kJ/mol).[93,94]

$$i^0_{\text{ORR},(T,p_{O_2})} = i^{0,\text{ref}}_{\text{ORR}} \cdot \left(\frac{p_{\text{O}_2}}{p^{\text{ref}}_{\text{O}_2}} \right)^{\gamma_{\text{O}_2}} \cdot \exp \left[\frac{-E^{\text{ref}}_{\text{act, ORR}}}{\text{R}T} \cdot \left(1 - \frac{T}{T_{\text{ref}}} \right) \right] \tag{1.11}$$

The determination of $i^0_{\text{ORR},(T,p_{O_2})}$ can become erroneous due to considerable extrapolation errors from the measurement range of 0.7-0.9 V to the reversible potential (≈1.2 V), since inaccuracies of Tafel Slope determination would lead to a significant deviation at zero overpotential. Hence, it has become widely accepted to determine the catalyst activity at 0.9 V$_{iR\text{-free}}$, where usually little or no extrapolation is needed.[94] In general, the specific activity at 0.9 V$_{iR\text{-free}}$, 80°C, and 100 kPa$_{\text{abs}}$ O_2, normalized to the available Pt surface is

termed $i^{\text{spec}}_{0.9\text{ V}}$ in this thesis. In addition, referencing the catalyst activity to these typical measurement conditions (temperature and gas partial pressure) avoids the inaccuracies when using thermodynamic and kinetic parameters to transpose activities to other conditions. Incorporating the above assumptions, a purely kinetically limited cell voltage of a fuel cell in the absence of ohmic and mass transport losses can be calculated by equation 1.12 with the apparent (sum of thermodynamic and kinetic) reaction order, m (0.75), the activation energy at 0.9 V, $E^{0.9\text{ V}}_{\text{act, ORR}}$ (≈10 kJ/mol), the partial pressures, p^*_i and temperature, T^*, at the measurement conditions of the specific activity and the partial pressures, p_i and temperature, T at the desired modeling conditions.[94]

$$E_{\text{ORR}} = 0.9 - \frac{2.303 \cdot \text{R}T}{\alpha_c \cdot \text{F}} \cdot \log\left[\frac{i + i_{x,\text{H}_2}}{10 \cdot L_{\text{Pt, cath}} \cdot A_{\text{Pt}} \cdot i^{\text{spec}}_{0.9\text{ V}} \cdot \left(\frac{p_{\text{O}_2}}{p^*_{\text{O}_2}}\right)^m \cdot \left(\frac{p_{\text{H}_2}}{p^*_{\text{H}_2}}\right)^{(\alpha_c/2)} \cdot \exp\left[\frac{-E^{0.9\text{ V}}_{\text{act, ORR}}}{RT} \cdot \left(1 - \frac{T}{T^*}\right)\right]}\right] \tag{1.12}$$

Any difference between a measured iR and H_2-crossover corrected polarization curve and one predicted by equation 1.12, must be due to transport resistances represented by the last two terms in equation 1.4, i.e., proton transport in the cathode catalyst layer and oxygen mass transport from the flow channel towards the reaction sites in the cathode electrode (see page 14).

The proton conduction resistance across the electrode can be estimated from impedance spectroscopy according to Liu et al.[95] by using a transmission line model to determine the catalyst layer proton sheet resistance, $R_{\text{H}^+,\text{cath}}$.[96] The effective proton transport resistance, $R^{\text{eff}}_{\text{H}^+,\text{cath}}$, needs to be calculated according to equation 1.13 as the utilization of the catalyst layer, hence the position of the reaction front to which protons need to travel, will depend on the proton resistance in the layer and the activity of the catalyst. The correction factor ζ correlates with the dimensionless factor of $iR_{\text{H}^+,\text{cath}}/TS$, which represents the ratio of proton transport resistance over kinetic resistance and is related to the electrolyte phase potential.[93]

$$R^{\text{eff}}_{\text{H}^+,\text{cath}} = \frac{R_{\text{H}^+,\text{cath}}}{3 + \zeta} \tag{1.13}$$

The overpotential arising from oxygen transport, η_{tx}, can be calculated from the total oxygen mass transport resistance, $R^{\text{total}}_{\text{O}_2}$, according to equation 1.14, derived by Zirhul et al.[74]

$$\eta_{tx} = \frac{\text{R}T}{\text{F}} \cdot \left(\frac{1}{4} + \frac{\gamma_{\text{O}_2}}{\alpha}\right) \cdot \left(\frac{p_{\text{O}_2} - \frac{RT}{4\text{F}} \cdot R^{\text{total}}_{\text{O}_2} \cdot i}{p_{\text{O}_2}}\right) \tag{1.14}$$

Here, γ_{O_2} represents the kinetic reaction order of the ORR with respect to the partial

pressure of oxygen (γ_{O_2}=0.54). The total oxygen transport resistance can be calculated from limiting current measurements according to a method developed by Baker et al. where the transport resistance is defined as the oxygen concentration difference, Δc, from the flow channel to the electrode surface, divided by the molar flux of oxygen, N_O.[97] The molar flux can also be expressed in terms of a current, i, according to equation 1.15.

$$R_{O_2}^{\text{total}} = \frac{\Delta c}{N_O} = 4\text{F}\frac{\Delta c}{i} \tag{1.15}$$

At limiting current conditions, i.e., at $i = i_{\text{lim}}$, the oxygen concentration at the electrode surface is zero, hence Δc becomes equal to the concentration of oxygen in the flow channel. This oxygen concentration can be rewritten with the dry mole fraction of oxygen, $\chi_{O_2}^{\text{dry}}$ and the total gas pressure, which corresponds to the total pressure, p_{total}, minus the partial pressure of water, p_{H_2O}, resulting in equation 1.16.

$$R_{O_2}^{\text{total}} = \frac{4\text{F} \cdot \chi_{O_2}^{\text{dry}} \cdot (p_{\text{total}} - p_{H_2O})}{i_{\text{lim}} \cdot \text{R}T} \tag{1.16}$$

Determining $R_{O_2}^{\text{total}}$ at different pressures enables the differentiation between pressure dependent transport resistances ($R_{O_2}^{\text{PD}}$) in the gas phase, i.e., intermolecular diffusion in large pores, from pressure independent transport resistances ($R_{O_2}^{\text{PI}}$) i.e., diffusion in small pores, in liquid water or in the ionomer phase.[97] The importance of differentiating the transport resistances is explained in more detail in section 1.2.

With the previous explanations, all voltage loss contributions to the cell voltage according to equation 1.4 of a fuel cell operating at certain conditions (e.g., H_2/air, 80°C, 100% *RH*, 170 kPa_{abs}) have been described, and a so-called voltage loss analysis can be performed. This was also used for the publications described in chapter 3. In these cases, the measured cell voltage, E_{cell}, at any current density, i (in H_2/air configuration) is corrected by the potential drop due to the ohmic resistance, iR_{HFR}, due to resistance of proton conduction in the catalyst layer, $iR_{H^+,\text{cath}}^{\text{eff}}$, and due to the transport overpotential, η_{tx}, which is summarized in equation 1.17.

$$E_{\text{corrected}} = E_{\text{cell}} + iR_{\text{HFR}} + iR_{H^+,\text{cath}}^{\text{eff}} + \eta_{\text{tx}} \tag{1.17}$$

The corrected voltage $E_{\text{corrected}}$ can then be compared to the purely kinetically limited voltage, E_{ORR}, calculated by equation 1.12 to determine the unassigned voltage losses $E_{\text{unassigned}} = E_{\text{ORR}} - E_{\text{corrected}}$. In the case of accurately calculated loss contributions, perfect overlap of both curves should occur in the entire current range. However, unassigned voltage losses may remain at high current density as can be seen in figure 1.7 (dashed surface), pointing to inaccuracies of the in situ determination of the here described loss contributions.

1.2 Striving for high current density operation

Increasing the high current density performance while lowering the Pt loading in a fuel cell is the best way to reduce the size and cost of the fuel cell stack. On the one hand, a lower platinum loading directly reduces material costs, while on the other hand, the reduced active area allows to reduce the required amounts of membrane, GDL material, and other structural components. As this target is a multidimensional optimization problem, researchers from the fields of catalyst and ionomer synthesis as well as system engineers need to closely collaborate for a successful implementation. In the following, several aspects of performance limitations on the level of catalyst and catalyst layers are discussed.

As described in section 1.1.1, the catalyst activity for the oxygen reduction reaction can be increased by alloying and controlling the shape of the Pt particles. In principle, a higher activity (increased $i^{\mathrm{spec}}_{0.9\,\mathrm{V}}$) by one order of magnitude should lead to a decrease in overpotential (η_{ORR}) by TS [V] according to equation 1.12 and thus to better polarization curves . However, a high mass activity determined in a rotating disk electrode (RDE) setup in liquid electrolyte, which is the primary screening tool for catalysts in the development phase, does often not translate into an improved MEA performance.[6,98,99]

One problem that has been identified is attributed to the low catalytic surface area of these alloys (≈25-50 $\mathrm{m^2_{Pt}/g_{Pt}}$),[58,59] hence to a low *rf* value of the catalyst layer. For pure platinum catalysts, it was shown that the pressure independent transport resistance, which is attributed to oxygen diffusion through water or ionomer, increases significantly with decreasing *rf*,[76,100–102] which was later proven for alloy based catalysts as well.[98] This observation appears to result from a higher local flux of oxygen to the Pt surface through the ionomer film covering the catalyst particle; this is summarized in figure 1.8. Thus, it is clear that a high surface area of catalyst needs to be available to minimize the losses, even though the reason for the substantial losses at low *rf* still remains unclear.

One hypothesis is related to a large oxygen transport resistance for diffusion through the ionomer phase. However, the average thickness calculated for a homogeneously distributed ionomer film in the catalyst layer of a few nanometers is unlikely to result in the observed losses based on the oxygen permeability of the bulk ionomer phase. Hence, it was hypothesized that a very thin ionomer film behaves significantly differently compared to the bulk material.[19,101] This hypothesis could not be validated for ionomer thicknesses down to 50 nm[103] and led to the assumption of an additional transport resistance arising from the contact of the ionomer with the Pt surface, termed a Pt interfacial resistance.[101,102] Molecular dynamics (MD) studies modeling the ionomer structure in the vicinity of platinum revealed significant variations in polymer density and oxygen permeability, pointing towards a non-linear behavior of oxygen permeability at the Pt-ionomer interface, supporting this hypothesis,[104,105] while some propose a potential dependence of the transport resistance due to anion adsorption.[106] In contrast, other modeling studies suggest that the

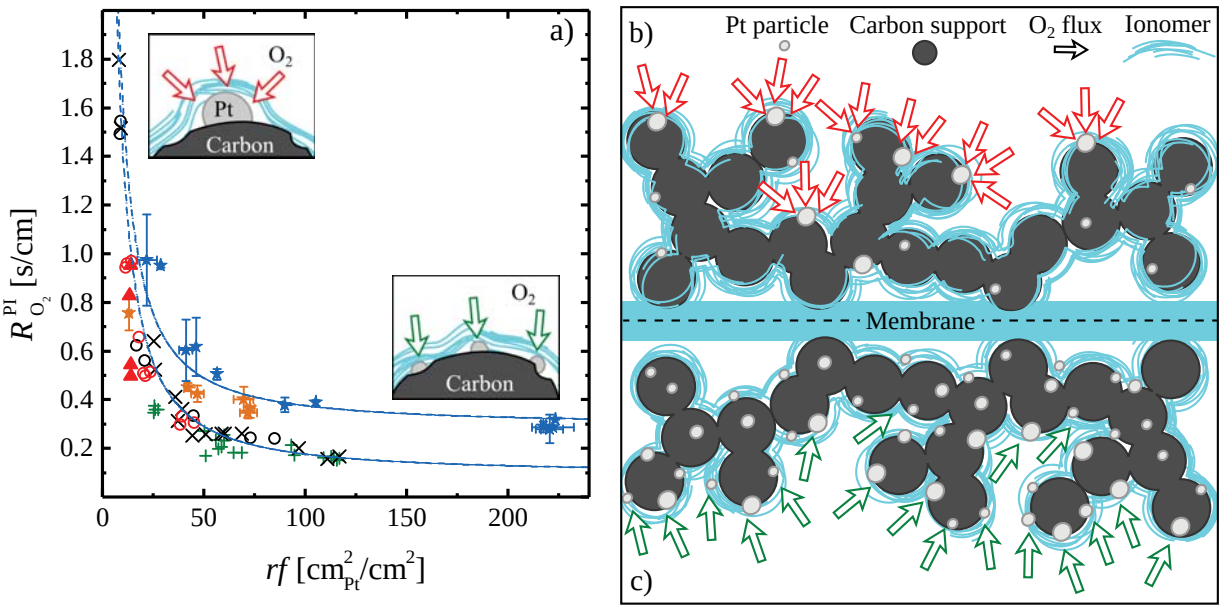

Figure 1.8: a) Pressure independent transport resistance, $R_{O_2}^{PI}$, for different catalyst materials as a function of the cathode electrode roughness factor, *rf*. Data for Pt/C catalysts from Harzer et al.[76] are shown as orange and blue stars and $R_{O_2}^{PI}$ values from Kongkanand et al.[6] are shown for Pt/C (×), PtCo/C (○), Pt-ML/Pd/C (+) and NSTF with 2–4 nm ionomer coatings (△). Inset sketches depict the local transport resistance towards the Pt surface. Hypothetical oxygen flux for low Pt loaded (b) and high Pt loaded (c) catalyst layers according to Owejan et al.[102]

higher resistance for low loaded catalyst layers arises from their lower vaporization capability, i.e., their inferior ability to reject produced reaction water through the gas phase, leading to an early onset of catalyst layer and GDL flooding, which results in a higher apparent diffusion coefficient of oxygen.[107]

Apart from theoretical approaches, several experimental studies focus on the influence of ionomer properties on fuel cell performance. Firstly, a lower equivalent weight of the ionomer has been reported to result in lower MEA performance at high current density at both high and low *RH*.[108] Although not fully explained by the authors, these observations could be due to stronger water absorption of the ionomer, resulting in higher O_2 transport resistance through the liquid film, or due to a stronger adsorption of sulfonic acid groups leading to a higher interfacial resistance. Although ionomers with low EW show increased proton conductivity, their oxygen transport properties seem to be of greater importance.[108] Another approach is to replace the sulfonic acid endgroup of the side chain (strongly adsorbing on Pt surface) by different ionic end groups. One new type of ionomer is terminated by sulfonimide acid end group, which show weaker adsorption on platinum, hence better ORR activity.[109] In addition, their bulk proton conductivity and oxygen permeability is higher compared to Nafion type ionomer.[110] A similar concept is the backbone modification of the ionomer by ”spacer”-moieties to increase the oxygen permeability while keeping the sulfonic acid end groups. The less dense packing of the ionomer on the catalyst results in an approximately two-fold increase in gas permeability

and enhanced fuel cell performance.[111]

It is clear that the scientific debate about the ionomer and its impact on the observed resistances is still ongoing, and that a better understanding of thin ionomer films and their interplay with the catalyst itself is needed to further increase the high current density performance of PEMFCs. Nevertheless, it is obvious that a high ORR mass activity alone is not sufficient to reach fuel cell performance targets but that a high catalyst surface area is just as much needed as a well-designed catalyst layer containing an ionomer best suited for the desired operating conditions.[6]

The first part of this thesis was devoted to a better understanding of catalyst and catalyst layer properties with respect to their influence on fuel cell performance. Most fuel cell models are based on the assumption of a thin and homogeneously distributed ionomer film over the entire surface area of the carbon support. However, for non-catalyzed carbon support, it could be shown by TEM images that the ionomer is not homogeneously distributed (at least in the carbon/ionomer composite electrode prepared in this study) but that parts of the carbon are left uncovered while ionomer is found to agglomerate in other parts, depending on the amount of ionomer used. In addition, the authors claim that no significant difference was observed when the carbon support contained Pt particles, even though high resolution TEM tomography was not possible any more in this case.[112] To begin with, our analysis focuses on the ionomer film distribution and the implementation of electrochemical techniques to assess ionomer film quality in situ. As an inhomogeneous distribution of ionomer would lead to ionically disconnected parts of the catalyst in certain areas while other parts would be covered with a thick ionomer layer resulting in high O_2 diffusion resistance, the quality of the ionomer distribution on the carbon support should at least be reflected by the outcome of an overall voltage loss analysis.[36] This follows the reasoning that the total voltage loss can only be quantitatively assessed when each contribution is accurately measured and valid under different operating conditions. For example, quantification of $R^{\mathrm{eff}}_{\mathrm{H^+,cath}}$ and $R^{\mathrm{total}}_{\mathrm{O_2}}$ is based on assuming a homogeneous ionomer distribution, so that incorrect values would be determined if this is not the case. An indication for an inhomogeneous ionomer distribution would be a significant *ECSA* variation with *RH*. This results from the fact that proton conductivity in the absence of ionomer can be ascertained though a liquid phase at high *RH* but not on a dry carbon surface. As the temperature of the catalyst layer increases with current density (higher current density, i.e., lower voltage, hence more heat production), the local *RH* decreases, making parts of the Pt surface area unavailable if not sufficiently covered with ionomer.

By increasing the interaction between the ionomer and the carbon surface through carbon surface modification, the ionomer distribution is expected to be improved, reducing the unassigned voltage losses compared to a unmodified catalyst by about 50% to only 40 mV (see section 3.1, page 37).[36] This also leads to an increased high current density performance, attributed to the optimum balance of proton conduction through a thin and

homogeneous ionomer film that does not pose a substantial O_2 transport resistance. From these results it becomes clear that the ionomer distribution in the catalyst layer is of significant importance for optimum fuel cell performance.

In addition to the influence of the catalytically active metal, i.e., pure Pt or Pt alloy, and the ionomer distribution in the catalyst layer, the morphology of the carbon support is known to strongly affect the performance of a fuel cell. In general, the mass/specific activity of a catalyst on high surface area carbon, e.g., Ketjenblack, is higher compared to the same catalyst on a low surface area support, e.g., Vulcan, when measured in an MEA.[39,113] This relates to the fact that on a high surface area carbon, a substantial amount of Pt particles (≈60%[113]) is located inside the carbon primary particles, where they are not in contact with ionomer.[39,113–117] It has been shown that the contact of ionomer with the Pt surface leads to a reduced activity due to anion adsorption.[118] Although the catalyst particles are not in direct contact with the ionomer, they are still able to contribute to the ORR through the ionic connection generated by a water film at sufficiently high humidity. However, proton and oxygen transport into a relatively deep pore filled with water is rather limited, hence the contribution from these particles is only visible at low current density, i.e., in the region where the kinetic activity is determined, but vanishes at higher current density.

On the other hand, a low surface area carbon supported catalyst shows superior high current density performance, although having lower catalytic activity resulting from ionomer poisoning. The simplest explanation is the reduced mass transport resistance as the oxygen does not need to diffuse into the pore of the carbon particle to reach the active site. As almost the entire platinum surface area is located on the outside of the carbon surface, all particles can contribute to the current density at high rate.[113,117] In addition, as the catalyst utilization in this case does not change significantly with *RH*,[115,116] the available surface area of platinum does not change at high current density, i.e., at higher temperature and lower local *RH* of the catalyst layer. For Pt inside the pores of high surface area carbon, the lack of ionomer contact probably impedes their ability to contribute to the ORR at dry operating conditions due to the absence of proton conducting pathways.

The above described differences in performance have always been ascribed to differences in the morphology of the carbon black support. However, the results have only pointed towards the influence of the Pt particle location, i.e., inside or outside the pores of the carbon black support, and not towards a direct involvement of the carbon black itself. For this reason, we investigated the influence of Pt particle location on the identical high surface area Ketjenblack, by preferentially depositing Pt on the inside or the outside of the support. This was achieved by implementing different synthesis methods (see section 3.2, page 57).[76] The same trends for catalytic activity and performance as described above were found, namely that a catalyst with Pt particles on the inside of the support shows good mass activity but poor high current density performance and vice versa for a catalyst

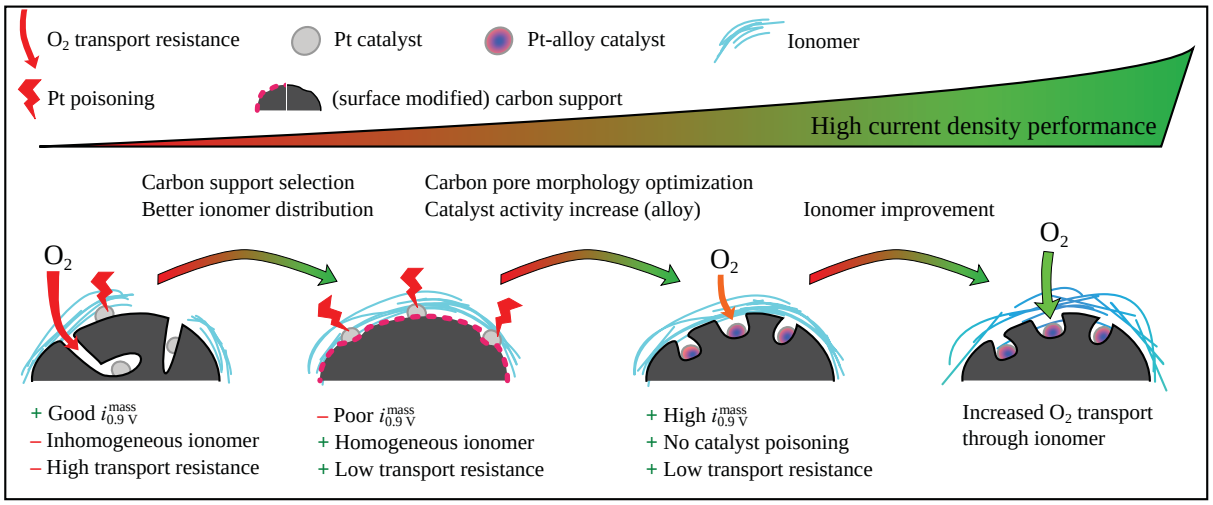

Figure 1.9: Schematic representation of the expected correlation between ionomer (blue), catalyst (silver or blue/red) and carbon support (black) and their influence on high current density performance of MEAs, outlining the conceptual pathway for a catalyst with both high ORR activity and good high current density performance.

with Pt particles located on the outside of the carbon particles. This study disproves the hypothesis that it is the carbon support which affects high current density fuel cell performance, but relates it unambiguously to the location of the Pt particle, either on the exterior surface or within the pore of the carbon support primary particle. Therefore it is clear, that the Pt particle location determined by the synthesis method of the catalyst is an additional parameter that needs to be optimized in order to achieve good high current density performance.

The currently expected relations between ionomer, catalyst and carbon support as well as their influence on high current density fuel cell performance are summarized in figure 1.9.

2 Experimental methods

The following experimental section will give additional, detailed information, especially focusing on describing proper handling of materials and minimizing problems when working with fuel cell test equipment. Details on experimental procedures specific to each topic can be found in the respective publications in chapter 3.

2.1 Preparation of materials

General material handling – To enable efficient lab work and avoid excessive material scrap by incorrectly cutting from the supply roll, all materials are pre-cut and stored in a folded paper in separate plastic bags. In general, all materials delivered as a roll are cut with a roller blade on either a PVC board (for thick material, e.g., Gylon® or Fiberflon®>80 µm) or a metal board (for thin foils, e.g., Kapton® or Fiberflon®<80 µm) using a blade guide to enable straight cuts over the entire roll width. For narrower roll widths, a guillotine trimmer is used. Not cutting the entire width from the roll should be avoided as it creates more edges which are prone to kinks, ultimately leading to higher amounts of scrap material. If the material is very sensitive to contamination (membrane without a second protective layer), it is placed into a PE bag to avoid contact to any surfaces during cutting. In addition to the time benefit of having material at the right size available, the supply roll does not need to be handled for each MEA preparation, hence the risk of contamination or accidents during material handling is reduced. Table 2.1 provides an overview of the materials needed and their size for the preparation of 5 and 50 cm^2 MEAs.

Catalyst powders are only handled wearing a lab coat, nitrile gloves and a respiratory mask (class FFP3). As catalyst powders can ignite upon contact with alcohol and other easily oxidized solvents, all catalyst powder residues are immediately wetted with water and

Table 2.1: Sizes of materials required for the preparation of 5 cm^2 and 50 cm^2 MEAs. The number in parentheses represents amount of cutting dies on one plate.

	Cut to size [cm]			Cut from roll [cm]		
Cell size [cm^2]	Membrane	Kapton®	Gylon®	Fiberflon®	Decal	GDL
50	10 × 10	11 × 11	10 × 10	11	8.5	8.5
5	7 × 5	8 × 6	7 × 5	8.5	11 (4×4)	9 (3×3)

later disposed off in a separate, self-extinguishing, metal waste container. The immediate wetting also reduces the risk of raising catalyst dust.

GDLs, decals and subgaskets are preferentially cut with the automated hydraulic press (Collin P200 PM, Collin GmbH), as the pressure distribution is more homogeneous compared to a manual press and as the applied force can be adjusted more precisely, avoiding cutting too deep into the backing plate. All materials should be cut in a way that the side which will later face the membrane (e.g., MPL side of GDL), is facing the blades during cutting. This creates a burr which is pointing away from the membrane, reducing the risk of membrane punctuation during CCM fabrication and MEA assembly.

Ink fabrication – The ink composition is based on mass fractions, nevertheless liquids are added by volume with an Eppendorf pipette for convenience. An overview of general catalyst compositions is given in table 2.2. For catalyst ink preparation, 16.5 g of 5 mm ZrO_2 beads (VHD ZrO, Glen Mills Inc.) as grinding medium are weighed in a 15 mL capped HDPE bottle. The catalyst powder is weighed on a weighing paper and transferred into the bottle. Then, water is added by pipetting the appropriate volume and controlling the added weight on the balance. The total weight of the bottle is determined so that the amount of added solvent can later be calculated. The required amount of solvent (1-propanol, 2-propanol, acetone, etc.) is weighed in a separate HDPE bottle. To avoid catalyst ignition upon mixing, both bottles are transferred into a nitrogen purged glovebox where the mixing is being performed. Trapped air in the catalyst powder is removed by repeatedly (3 times) tapping the closed bottle to the workbench, opening it and carefully shaking it to replace the gas phase inside. The solvent bottle is shaken and opened three times to remove trapped air. Subsequently, the solvent is poured quickly into the catalyst containing bottle. This fast addition of the relatively cold solvent dissipates any produced heat more quickly, reducing the risk of ignition. For easily ignitable catalyst powders, pre-cooling of the solvent may be appropriate. The catalyst bottle is removed from the glovebox, the added weight is determined and adjusted if necessary. As the catalyst cannot ignite when fully wetted, this solvent adjustment does not require inert atmosphere. For accurate weighing, it is advised to determine the weight of the closed bottle as the evaporation of solvent will not allow the precision balance to reach a steady reading. Lastly, the ionomer solution is added by pipetting the appropriate volume with an Eppendorf pipette, verifying the final weight on the balance. Then, the bottle is closed and the lid and body of the bottle is wrapped with Parafilm® to increase friction on the roller mill and avoid unscrewing of the cap. Care must be taken to avoid Parafilm® on the faces or edges of the bottle as this might result in them falling off the roller mixer. Mixing is usually done for 18 h at about 60 rpm and room temperature (25°C). The correct mixing speed is reached when a clicking noise is produced from the beads.

Decal fabrication – Decals are produced by coating the ink onto virgin PTFE foil

Table 2.2: General composition of catalyst inks for the manufacturing of decals by the Mayer rod technique. I/C refers to the ionomer to carbon mass ratio and was varied for different studies. The carbon content of the ink is adjusted in the given range to achieve optimal viscosity for the coating process.

Catalyst	I/C [g/g]	V_{ink} [mL]	carbon content of ink [mg_C/mL_{ink}]	water content of ink [%]
$20\%_{wt}$ Pt/Vulcan	0.25 – 1.00	5	30 – 32	≈16
$50\%_{wt}$ Pt/Vulcan	0.65 – 1.00	5	35 – 40	≤10%
$20\%_{wt}$ Pt/Ketjenblack	0.40 – 1.00	5	22 – 30	≤10%

(50 µm) using the Mayer rod technique. Therefore, a sheet of PTFE foil is cleaned from both sides and adhered to a glass plate by isopropanol. The top edge of the foil is additionally fixed by scotch tape over the entire length. Care must be taken to not trap air bubbles or dust underneath the foil and that no kinks or wrinkles are present on the surface as this would result in an inhomogeneous coating. To avoid that edges of the foil are caught by the rod during the coating process, it is cut to a slight V-shape, which becomes narrower in the coating direction. The catalyst layer loading is adjusted by the wet film thickness of the Mayer rod (K Bar, RK PrintCoat Instruments Ltd, usually rod 100-150). The appropriate Mayer rod is fixed into the coating machine without using the additional weights, making sure that it is in contact with the foil over the entire length. Then, the ink is added with a disposable plastic pipette in front of the Mayer rod (touching its surface), while the required amount depends on the wet film thickness and ink viscosity. Care should be taken that no bubbles are introduced into the ink, as they may be transferred onto the coating. For best coating results, the viscosity of the ink should be adjusted to a slightly flowing, honey-like texture, which is influenced by the carbon content of the ink. The coating speed setting on the machine (K Control Coater, RK PrintCoat Instruments Ltd) is set to two. A good criterion for optimum ink viscosity is when the stripes produced from the coating rod wires vanish a few seconds after the rod has spread the ink. If the stripes persist after drying, the ink viscosity was too high; if no stripes are visible during coating and the desired loading is not reached, the viscosity is too low. To get the most coating area from an ink, it is possible to pour the rest of the ink (which cannot be removed with the pipette) with the ZrO_2 beads onto the foil and perform the coating. This may however lead to poor quality coatings.

After the coating is removed from the coating machine, it is dried in air, followed by drying at 80°C in an oven. The quality of the coating is evaluated by shining light from the back to identify any inhomogeneity in the coating. A good coating is characterized by an even surface which entirely blocks the light passing through. Then, the desired decal size (5 or 50 cm^2) is cut in the automated press with a cutting die, whereby the coating side should face the blades. The decals are stored in a folded paper in a plastic bag for

later use.

CCM assembly and hot-pressing – The CCM assembly is done on a glass plate to ascertain a clean working area. Several of the decals required for CCM fabrication are put in a petri dish, covered by a GDL to avoid rolling up, and dried at 80°C for at least one hour. Then, two sheets of Kapton® (25 µm) are cleaned and adhered to the glass plate with isopropanol. The surfaces are dusted-off by pressurized air. The anode decal is weighed, dusted-off and put on the Kapton® foil with the electrode side facing up. Next, the membrane is put over the decal, ensuring that no membrane wrinkles are present on the active area. To avoid contamination of the membrane, the second Kapton® foil is added, covering the assembly. Then, the cathode decal is weighed, dusted-off and inserted between the Kapton® and the membrane with the electrode side facing the membrane and perfectly aligned with the edges of the anode decal. Labeling the Kapton® foil is necessary to identify the respective electrode after hot-pressing.

The electrode-membrane stack is put between two sheets of Gylon® (Type 3545, 2 mm thick, Garlock®, ENPRO Industies Inc.) as pressure leveling layer and hot-pressed at 155°C for three minutes and an applied pressure of 0.11 $kN/cm^2_{Gylon®}$. The temperature is chosen to be above the glass transition temperature of the polymer to allow it to flow and create a connection between the membrane and the ionomer contained in the catalyst layer. After hot-pressing, the Kapton® foil is partially removed to peel off the decal and label the cathode side on the edge of the membrane with a pen. By weighing the decal after the transfer, the mass of the catalyst layer is determined. From the ink composition and the catalyst layer weight, the platinum (mg_{Pt}/cm^2) and carbon (mg_C/cm^2) loading of the catalyst layer is calculated. Knowing the specific packing density of carbon in the catalyst layer, determined from SEM cross sections (22±4 µm/(mg_C/cm^2)),[76] the thickness of the catalyst layer is calculated. Covering the CCM, especially the catalyst layers with the Kapton® foil, helps to avoid contamination during handling.

MEA assembly – The CCM is assembled in the test hardware with PTFE coated fiberglass gaskets (Fiberflon®, Fiberflon GmbH) as sealing material and to adjust the compression of the GDL. The thickness of the gasket is determined to allow a 20±1% thickness reduction of the GDL while assuming that the electrodes are incompressible and using a compressibility of 7% for the gasket. First, the GDL needs to be inspected for substrate fibers that are sticking out, as they are easily able to puncture the membrane, rendering the CCM unusable. Then, the thickness of each GDL is measured with a touch sensitive digital micrometer (Mitutoyo series 543) at five different locations. From the average GDL and electrode thicknesses, the thickness of the gaskets is calculated which is measured at 9 positions around its perimeter close to the active area. The CCM is assembled in the test hardware with the MPL side of the GDL facing the electrodes. Lastly, the hardware is tightened with a torque of 12 Nm. The electric resistance between

the flow fields measured by a multimeter gives a first indication about MEA integrity if resistances above 2.5 $k\Omega cm^2$ are obtained. Lower resistances point towards a short circuit by, e.g., a GDL fiber.

Fuel cell measurements – Fuel cell test are performed on customized, automated test stations (G60, Greenlight Innovation) equipped with a 120 A load bank (N3301A, Agilent Technologies) and potentiostat (Reference3000, Gamry Instruments). All measurements are performed using the Emerald automation software.

The fuel cell is connected to the test station (gas lines, thermocouples, load bank/potentiostat connections, heater and cooling fan) and the cathode is purged at high flow rates (>5000 nccm, e.g., emergency purge) with nitrogen. After a few minutes, the anode flow is turned on to high flow rates. This procedure minimizes the possible cathode degradation due to H_2/air fronts in the anode. Then, the gas tightness of the cell is tested by applying 100 kPa_g pressure (N_2/N_2), turning off the flow and monitoring the pressure decay of the cell over 2 minutes. A pressure drop of less than 5 kPa is tolerable during this time.

2.2 Electrochemical techniques

MEA conditioning – To activate the MEA and remove possible contamination from the manufacturing process, all MEAs are conditioned prior to testing by a voltage-controlled ramp-in procedure. It consists of a repeated sequence of holding the potential for 45 min at 0.6 V, at OCV for 5 min, and for 10 min at 0.85 V, repeating this procedure for ten cycles in H_2/air (flows of 1390/3320 nccm) at 80°C, 100% *RH*, and 150 kPa_{abs}. After this procedure, reproducible and close to maximum performance is obtained. For performance testing, an MEA recovery step should be implemented before each polarization curve to recuperate from reversible voltage losses. Failing to do so will lead to lower catalytic activity and reduced MEA performance. The recovery procedure consists of a hold time in H_2/air (2000 nccm/5000 nccm) at 0.3 V for 2 h at 40°C, 270 kPa_{abs}, and 100% *RH*.

***ECSA* determination** – The *ECSA* of catalysts is either determined from the H-desorption and H-adsorption charge (H_{UPD}) or from CO stripping. Exemplary voltammograms are shown in figure 2.1. The measurements are performed at 40°C as higher temperatures lead to less defined features in the cyclic voltammogram (CV), while lower temperatures cannot be controlled satisfactorily by the test station. Prior to *ECSA* evaluation, CVs of the cathode electrode are recorded between 0.07 and 1.00 V_{RHE} at a scan rates of 50, 100 and 150 mV/s at ambient pressure, while the *ECSA* is determined from CVs with a upper potential of 0.6 V_{RHE} (avoiding contributions from Pt oxide reduction), averaging the H-desorption and H-adsorption charge (using the same scan rates as above). The integration limits are set to the onset of hydrogen evolution at the low potential limit and to the double layer capacity at the high potential limit (see figure 2.1). A specific

charge of 210 $\mu C/cm^2_{Pt}$ is used for the conversion. The anode (counter/reference electrode) is fed with 5% H_2 in N_2 at 200 nccm during the measurement. The working electrode (cathode) is first purged with dry N_2 (500 nccm; dry bypass, humidifier isolation valve closed), while the flow is interrupted for the measurement. This avoids any oxygen reduction currents arising from oxygen residues in the gas lines, which would compromise the later evaluation of the CV.

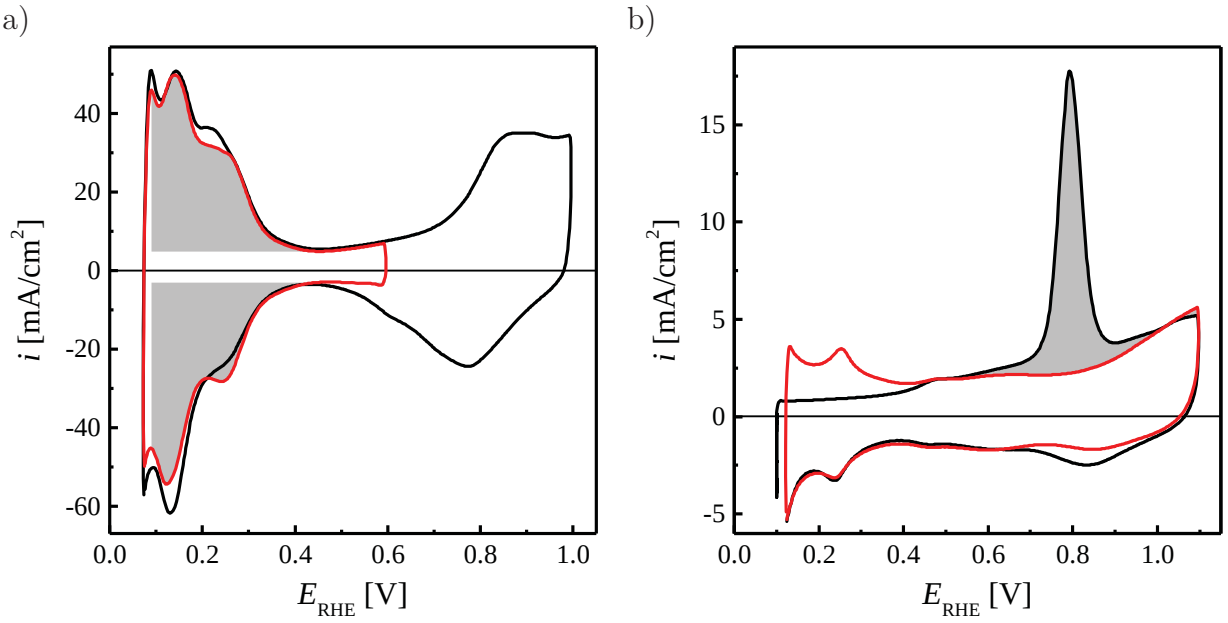

Figure 2.1: Cyclic voltammograms for the determination of the *ECSA* from both H_{UPD} and CO stripping for a 50%$_{wt}$ Pt/C catalyst (TEC10V50E, TKK; Vulcan carbon support) with the integrated areas shown in gray. a) CVs conducted at a scan rate of 150 mV/s from 0.07 to 1.00V_{RHE} (black line) and 0.07 to 0.60V_{RHE} to determine the *ECSA* (red line) at ambient pressure and 40°C, 200 nccm of 5% H_2 (in N_2) on the anode (counter and reference electrode) and no flow on the cathode (working electrode). b) CO stripping voltammogram (black line) with subsequent scan (red line) at a scan rate of 100 mV/s to 1.10 V_{RHE} at 150 kPa_{abs} and 40°C (constant flows of 200 nccm 5% H_2 (in N_2) on the anode and 5 nccm N_2 on the cathode).

Prior to any CO stripping experiment, the cathode humidifier needs to be free of oxygen, as traces of oxygen might lead to chemical CO oxidation during the purging procedure. For this reason, the humidifier is flushed with nitrogen at various flow rates and pressures for about 40 min. The CO stripping experiment is done by adsorbing CO (10% CO in N_2, 100 nccm) at 40°C and 150 kPa_{abs} for 10 min while maintaining the cathode potential at 0.1 V_{RHE}. The CO needs to be removed quantitatively from the cell and the gas lines, for which a purging procedure is implemented. During about 1.5 h, the CO line, adjacent lines for other gases (depending on the type of test station) and the entire cathode manifold is purged at various flow rates with nitrogen. The adsorbed CO is oxidized by a CV from the holding potential to 1.2 V_{RHE} at a scan rate of 100 mV/s with a flow of 5 nccm dry nitrogen on the cathode to maintain the pressure. To verify the full oxidation of CO and its removal from the system, two additional sweeps are recorded. By integration of the first

anodic scan with the subsequent scan being the baseline, the *ECSA* is calculated, using a specific charge of 420 $\mu C/cm^2_{Pt}$.

Fuel cell performance measurements – Performance measurements are conducted with differential flow conditions, i.e., at high reactant stoichiometries (>10). This minimizes gradients in gas concentration and *RH*, as the change in reactant concentration is negligible at such high flows and ascertains more defined measurement conditions compared to stoichiometric flow ($S < 2$) relevant for automotive applications. Polarization curves with 5 cm^2 MEAs are recorded in current-control mode at 80°C and at constant flows of 2000 nccm of H_2 on the anode and 5000 nccm of O_2, air, or 10% O_2 (in N_2) on the cathode. The gas feed of anode and cathode is operated in counter-flow configuration. The inlet to outlet pressure drop at these conditions in anode and cathode is about 2 and 22 kPa_{abs}, respectively, including the supply lines to the cell. Firstly, the cell potential is held at 0.75 V for 15 min to reduce Pt oxides prior to recording a polarization curve from low to high current density (20 mA/cm^2 to 2000 mA/cm^2). This pre-conditioning is required to obtain a metallic Pt surface with higher activity compared to a partially oxidized surface. The conditions at each current density measurement point (temperatures of cell and humidifiers, pressures and flows) are held constant for at least 10 min with a tolerance of ±1 K and ±3 kPa_{abs}. The resulting voltage and current density is then averaged over the final 30 s.

Determination of kinetic parameters – The ORR kinetics (mass activity, specific activity, and Tafel slopes) are determined from H_2/O_2 polarization curves after correcting the potential for the iR-drop, using the high frequency resistance (*HFR*), correcting the current for the ohmic short of the membrane and the H_2 crossover current (i_{x,H_2}) and normalizing to the surface area or mass of Pt. Galvanostatic electrochemical impedance spectroscopy (GEIS, normal sample mode) is recorded at each current density point in the frequency range from 100 kHz to 10 Hz, with an AC amplitude of 10% of the momentary current setpoint (limited to a minimum/maximum of 0.1/3 A). The H_2 crossover and ohmic short is determined at the identical conditions as the polarization curve for which the corrections will be applied, i.e., at the same temperature, pressure and *RH*, however in H_2/N_2 configuration. The anode flow is set to 600 nccm, while the cathode flow is set to 150 nccm of dry N_2. By using the dry bypass on the cathode, reductive currents due to oxygen residues from the humidifier are avoided, while the comparatively high flow on the anode provides sufficient humidification of the membrane and catalyst layers. A linear regression of the current recorded at constant potentials of 0.2, 0.3, 0.4, 0.5, 0.6 and 0.7 V for 2 min each (averaging the final 30 s) provides i_{x,H_2} as the y-axis intersect and the slope corresponds to $1/R_{short}$. Representative graphs of the determination of the *HFR* and i_{x,H_2} are shown in figure 2.2.

The proton conduction resistance of the cathode, $R_{H^+,cath}$ (in units of Ωcm^2), is de-

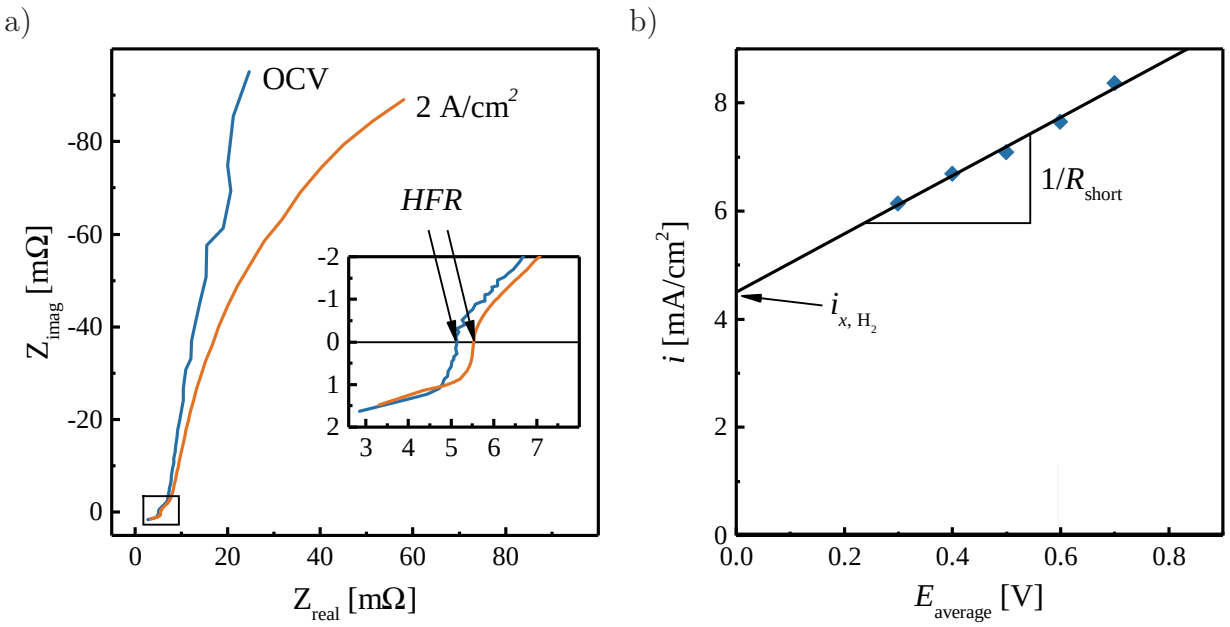

Figure 2.2: a) Galvanostatic electrochemical impedance spectroscopy (GEIS) of a 5 cm^2 MEA with a 15 µm thick, reinforced membrane (cathode: 0.4 mg_{Pt}/cm^2, TEC10V50E; anode: 0.1 mg_{Pt}/cm^2, TEC10V20E) recorded at 170 kPa_{abs}, 80°C, and 100% *RH* at OCV and 2 A/cm^2, with the high frequency resistance (*HFR*) determined from the x-axis intersect. b) H_2 crossover measurement of the same MEA recorded at 170 kPa_{abs}, 80°C, and 100% *RH* with the average current at each potential and the regression analysis to determine the H_2 crossover current, i_{x,H_2}, and the ohmic resistance of the cell (R_{short}).

termined from AC impedance spectra recorded in H_2/N_2 (anode/cathode) at 0.2 V with a peak-to-peak perturbation of 3.5 mV between 500 kHz and 0.2 Hz (20 points per decade). To ensure reproducibility, each measurement is repeated three times at each condition: 100, 70, 50, and 30% *RH*, while maintaining constant gas partial pressures (i.e., at cell pressures of 270, 255, 246, and 236 kPa_{abs}, respectively) under differential flow conditions (H_2/N_2 at 1000/1000 nccm) at 80°C. The resulting experimental data is fitted to an equivalent circuit comprised of a resistor (R1) corresponding to the *HFR*, a restricted linear diffusion element ($M_{a,\,2}$) corresponding to $R_{H^+,cath}$ and a modified inductor, $L_{a,\,3}$, for the cell inductance. The "Z-fit" impedance fitting tool from EC-Lab (V10.44, Bio-Logic Science Instruments) is used. Representative measurement data (solid lines) with the corresponding fits (dashed lines) are shown in figure 2.3. At low *RH* and for low I/C mass ratios, it may not be possible to obtain reasonable fits to the transmission line model, thus the proton conduction resistance is determined by a linear regression analysis as shown in figure 2.3.

Once all the correction terms are determined, the evaluation of the H_2/O_2 polarization curve (see figure 2.4 a) for the kinetic parameters can be performed. Firstly, the current is corrected for the hydrogen crossover and short current ($i_{corrected} = i_{measured} + i_{x,H_2} + \frac{E_{cell}}{R_{short}}$), normalized to the amount of Pt in the catalyst layer (L_{Pt}) and transferred into a logarithmic scale (figure 2.4 b). Then, the measured voltage is corrected by the *HFR* ($E_{HFR\text{-}free} = E_{cell} + i \cdot R_{HFR}$) and the effective proton transport resistance in the cathode ($E_{HFR,R^{eff}_{H^+,cath}\text{-}free} =$

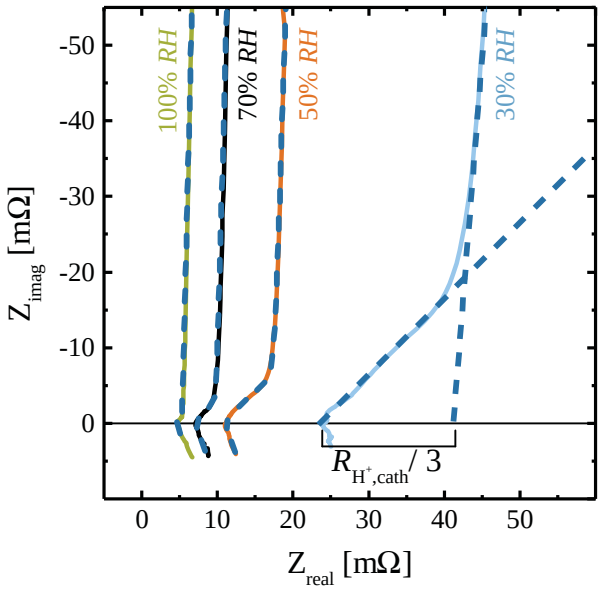

Figure 2.3: Potentiostatic electrochemical impedance spectroscopy (PEIS) recorded for different *RH* (solid lines) at 0.2 V, H_2/N_2 (1000/1000 nccm), 80°C and constant gas partial pressures (i.e., at cell pressures of 270, 255, 246, and 236 kPa_{abs}, respectively) for a 5 cm^2 MEA with 15 µm thick membrane (cathode: 0.06 mg_{Pt}/cm^2, 20%$_{wt}$ Pt/V-NH_x, I/C=0.25; anode: 0.1 mg_{Pt}/cm^2, TEC10V20E). Dashed lines show the corresponding fit to the transmission line model (50-100% *RH*) or the linear fit approach in the case of low *RH* (30%), when a fit to the transmission line model is not satisfactory. The data is obtained from Orfanidi et al.[36]

$E_{\text{HFR-free}} + i \cdot R^{\text{eff}}_{\text{H}^+,\text{cath}}$). From a linear regression analysis restricted to the current density points from 50 to 500 mA/cm^2, the mass activity, $i^{\text{mass}}_{0.9\text{ V}}$, is obtained by inter/-extrapolating to 0.9 V. This current density range is applied to minimize errors in the analysis, as the lower limit is chosen to be 10 times higher than the hydrogen crossover current, while the upper limit is generally not yet affected by the oxygen mass transport resistance.

The total mass transport resistance, $R^{\text{total}}_{O_2}$, is determined from limiting current measurements at 80°C and 100% *RH*. Measurements at lower *RH* (70%) were also used but showed no difference for $R^{\text{total}}_{O_2}$. Differential flow conditions (2000 nccm of H_2 and 5000 nccm of O_2/N_2 mixtures) are used. The dry mole fraction of oxygen in the cathode is altered from 4 to 24% O_2 in N_2, while the limiting current is determined at cell potentials of 0.30, 0.15, 0.10, and 0.05 V_{cell} for 2 min each. Lower dry mole fractions of oxygen would in principle be desirable, however, the accurate measurement by the test station is not guaranteed. To disentangle pressure-independent, $R^{\text{PI}}_{O_2}$, and pressure-dependent, $R^{\text{PD}}_{O_2}$, oxygen transport resistances, limiting current measurements are conducted at 170, 270, 350, and 500 kPa_{abs}. The analysis is performed according to Baker et al.[97]

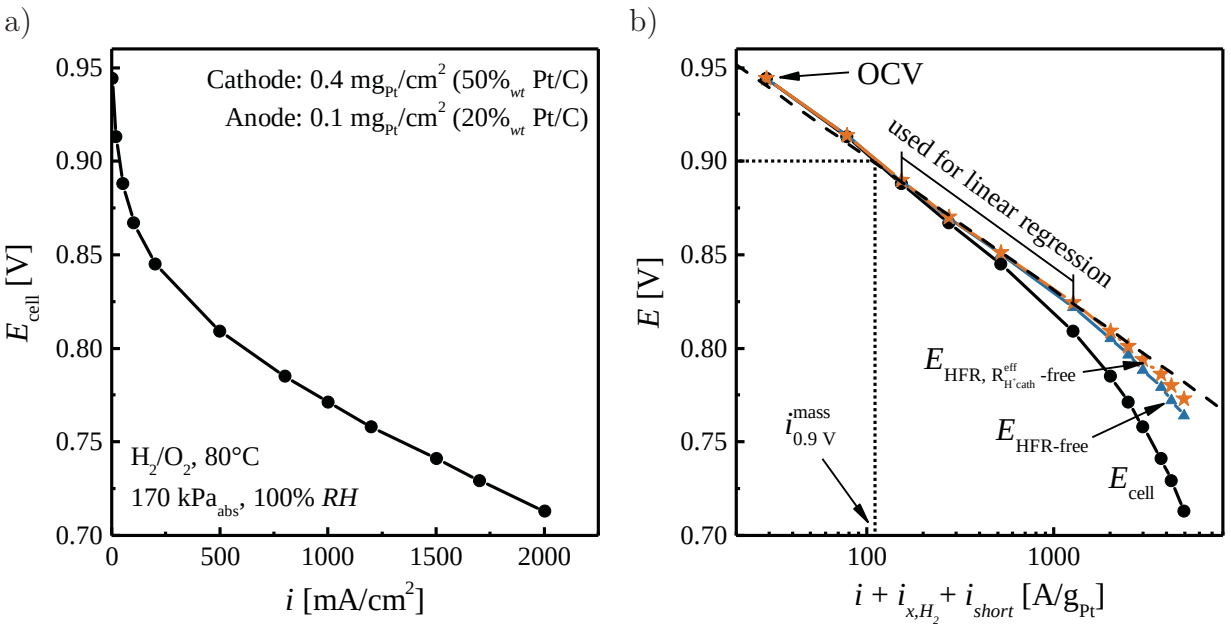

Figure 2.4: a) Polarization curve for 50%$_{wt}$ Pt/C catalyst (TEC10V50E) at a cathode loading of 0.4 mg$_{Pt}$/cm^2 under differential flow of H_2/O_2 (2000/5000 nccm), 80°C, 170 kPa$_{abs}$ and 100% *RH*. b) Tafel representation of the polarization curve with the applied corrections for the H_2 crossover and short current, the *HFR* (blue triangle) and proton resistance in cathode (orange star). The dashed black line corresponds to the linear regression performed through the indicated points and is used to determine the Tafel slope (here 71 mV/dec) while the dotted line shows the determination of $i^{mass}_{0.9\ V}$.

2.3 Further experimental methods

In addition to MEA characterization on fuel cell test stations, other characterization techniques have been applied which will be described briefly in the following.

TGA

Thermogravimetric analysis (TGA) of materials was performed with a TGA/DSC 1 instrument (Mettler Toledo). In short, the sample is weighed into an Al_2O_3-crucible (THEPRO GbR) and covered by a lid with hole. Generally, the sample weight is adjusted to around 10 mg. Samples are heated in argon or oxygen to quantify the amount of volatile surface groups or combustible carbon to determine the Pt loading.

Elemental analysis

Elemental analysis is done at the central analytic lab of the department. CHNS analyses are performed using a EURO EA analyzer (Hekatech) and determination of platinum is done photometrically using a UV 160 photometer (Shimadzu).

N_2-sorption

The surface area of materials is evaluated by N_2 physisorption at 77 K using an Autosorb-iQ instrument (Quantachrome). Prior to the measurement, all samples are degassed under vacuum (90°C for 15 h). Adsorption and desorption isotherms are recorded in the relative pressure range of $10^{-5} \leq (p/p_0) \leq 0.995$, with p being the gas pressure and p_0 the saturation pressure. For sufficient accuracy, a sample weight equivalent to a minimum absolute surface area of >10 m^2 is used. The specific surface area and pore volume distribution are calculated by the Brunauer-Emmett-Teller (BET) method and by the quenched solid density functional theory (QSDFT) method, respectively (using the ASiQwin program).

XRD

X-ray diffraction (XRD) is used to determine crystal compositions and estimate crystal sizes by the Scherrer equation. A Stadi P (Stoe & Cie) diffractometer with a Mythen 1K areal detector (Dectris Ltd.) and Cu $K_{\alpha 1}$-radiation ($\lambda(K_{\alpha 1})$=1.54059 Å, 50 kV, 30 mA, Germanium (111) monochromatized) is used. The sample preparation is either done as capillary (0.5-0.7 mm, Hilgenberg) or as flat bed using scotch tape.

MEA cross-section by SEM

The thicknesses of MEAs are determined from cross-section images, obtained by scanning electron microscopy (SEM). Generally, MEAs are cut in quarters, fixed in a Teflon holder and embedded in epoxy resin (EpoThin 2 resin and hardener, Buehler Ltd.). In a desiccator, gas bubbles are removed by lowering the pressure. After hardening overnight, the resin block is removed from the holder and ground on SiC grinding paper (CarbiMet S, P280, Buehler Ltd.) to a flat sample surface. This sample preparation method was developed by Philipp Rheinländer, a PhD student of the group. SEM (JCM-6000PLUS NeoScope, Jeol) images with a magnification of 2000× are taken in backscattering mode at 15 kV accelerating voltage. Ten arbitrarily chosen locations for each quarter of an MEA are chosen for the analysis. A more accurate thickness determination is obtained by integration of the electrode area with ImageJ (version 1.51j8) and dividing by the length of the image. This enables the analysis of the entire image as opposed to a single point measurement.

TEM

Transmission electron microscopy (TEM) is used to determine the Pt particle size distribution and location on the carbon support. Electron microscopy samples are prepared by dispersing the catalyst in water and depositing a few drops of the suspension onto carbon-coated Cu400 TEM grids (Science Services). A Philips CM100 EM operated at 100 kV at a resolution of 0.5 nm is used for imaging. Evaluation of Pt particle size distribution is done by measuring >400 individual particles using the software ImageJ (v. 1.51j8).

3 Published Work

In this section, the journal articles comprising this PhD thesis are presented thematically, rather than in chronological order of publication. Firstly, a strategy for increasing the high current density performance of PEM fuel cells is presented in section 3.1 which was addressed by increasing the homogeneity of the ionomer in the catalyst layer by a surface modification of the carbon black support. Following the surface modification approach, the publication presented in section 3.2 extends the previous research by investigating the influence of the location of Pt particles on the surface of the support. Lastly, the durability of catalyst layers in accelerated stress tests with different voltage profiles is presented in section 3.3 while special focus is put on the evaluation of their oxygen mass transport resistance. Additionally, the impact of the catalyst layer loading and carbon support corrosion is investigated.

3.1 The Key to High Performance Low Pt Loaded Electrodes

In this section, the article "The Key to High Performance Low Pt Loaded Electrodes"[36] is presented, which was submitted in November 2016 and accepted for publication in *The Journal of The Electrochemical Society* in March 2017 as an open access article, distributed under the terms of the Creative Commons Attribution 4.0 License (CC BY). The permanent web link to the article is http://jes.ecsdl.org/content/164/4/F418. This paper was presented e.g., at the 6$^{\text{th}}$ European PEFC and Electrolyser Forum in Lucerne, Switzerland in July 2017 (abstract number: B0405).

In this manuscript we show the impact of ionomer distribution in the catalyst layer on the fuel cell performance and how a homogeneous ionomer distribution can be obtained by a surface modification of the carbon support. Firstly, the synthesis approach for the surface modification of Vulcan carbon by -NH_x groups is described. The hypothesis on which this approach is based stems from the fact that the negatively charged sulfonic acid groups of the ionomer would exhibit a better interaction with a positively charged carbon surface in the fuel cell environment. By anchoring -NH_x groups to the carbon surface which can be protonated to cationic species in the acidic environment of the MEA, the strong ionomer-support interactions would be expected to lead to a more homogeneous ionomer

distribution over the catalyst surface. As a direct imaging of ionomer in the catalyst layer by ex-situ techniques, e.g., TEM, is very difficult and may not represent the entity of the catalyst layer, our characterization focuses on electrochemical testing. By ionomer free RDE experiments in 0.1 M $HClO_4$, we first confirm that the surface modification does not lead to differences in catalyst activity for the ORR. Then, extended testing in 5 cm^2 MEAs reveals the superior performance of the surface modified catalyst. The proton conductivity of the catalyst layer comprised of this catalyst is higher compared to a standard commercial catalyst, while the oxygen mass transport resistance, $R_{O_2}^{total}$, is significantly lower. This is explained by a thinner, more homogeneous ionomer film covering the entire catalyst surface, which is further validated by MEA test with different I/C ratios. For a non-functionalized catalyst, a stronger interaction of the ionomer with the hydrophilic Pt surface is expected, which should lead to a higher transport resistance through the thick ionomer film.

The conclusion of this article is nicely summarized in Figure 7 (page F425), depicting the influence of ionomer thickness and homogeneity on transport phenomena. Taking into account the voltage losses that are accessible by in situ techniques, e.g., the high frequency resistance, the proton resistance in the catalyst layer and the oxygen mass transport resistance, a voltage loss analysis between the kinetically predicted performance and the fully transport corrected measured polarization curve can be conducted, showing that minimal unaccounted losses are obtained in the case of the surface modified catalyst, while a significantly larger discrepancy is observed for the standard catalyst.

Author contributions

A.O. and P.M. carried out catalyst synthesis and characterization. A.O., P.M., H.S. and G.H. performed electrochemical testing and evaluated experimental results. T.K. performed XPS measurements and analysis. A.O., P.M., H.S. and G.H. drafted the manuscript. All authors discussed the experimental results and revised the manuscript.

The Key to High Performance Low Pt Loaded Electrodes

A. Orfanidi,[a,=,*,z] P. Madkikar,[a,=,*] H. A. El-Sayed,[a] G. S. Harzer,[a,*] T. Kratky,[b] and H. A. Gasteiger[a,]**

[a]*Chair of Technical Electrochemistry, Department of Chemistry and Catalysis Research Center, Technische Universität München, D-85748 Garching, Germany*
[b]*Chair of Physical Chemisty with Focus on Catalysis, Department of Chemistry and Catalysis Research Center, Technische Universität München, D-85748 Garching, Germany*

The effect of ionomer distribution on the oxygen mass transport resistance, the proton resistivity of the cathode catalyst layer, and the H_2/air fuel cell performance was investigated for catalysts with surface modified carbon supports. By introducing nitrogen containing surface groups, it was shown that the ionomer distribution in the cathodic electrode can be optimized to decrease mass transport related voltage losses at high current density. The in house prepared catalysts were fully characterized by TEM, TGA, elemental analysis, and XPS. Thin-film rotating disk electrode measurements showed that the carbon support modification did not affect the oxygen reduction activity of the catalysts, but exclusively affects the ionomer distribution in the electrode during electrode preparation. Limiting current measurements were used to determine the pressure independent oxygen transport resistance – primarily attributed to oxygen transport in the ionomer film – which decreases for catalysts with surface modified carbon support. Systematically lowering the ionomer to carbon ratio (I/C) from 0.65 to 0.25 revealed a maximum performance at I/C = 0.4, where an optimum between ionomer thickness and proton conductivity within the catalyst layer is obtained. From this work, it can be concluded that not only ionomer film thickness, but more importantly ionomer distribution is the key to high performance low Pt loaded electrodes.

Manuscript submitted November 28, 2016; revised manuscript received February 17, 2017. Published March 2, 2017.

Since 2015, proton exchange membrane fuel cell (PEMFC) electric vehicles (FCEVs) are emerging in the market. Despite the major breakthroughs in achieving the durability and performance targets for automotive applications, the cost of fuel cell stacks is still higher compared to the competing internal combustion engines, which is partly related to the cost and supply constraints of the platinum based catalysts, especially for the air cathode (the fast kinetics of the hydrogen oxidation reaction allow for low anode Pt loadings without compromising performance[1]). For large-scale commercial viability, it has been estimated that the Pt loading, especially at the cathode needs to be reduced below 0.1 mg_{Pt}/cm^2_{geo}.[2,3]

Over the past decade there have been numerous studies focusing on the optimization of the catalyst layer and seeking to gain fundamental insights into the various kinetic and transport resistances, which limit the performance of air cathodes, particularly at low Pt loadings.[4–8] While several methods were developed to quantify the voltage losses, there still remain unexplained voltage losses at high current density, particularly in the case of low Pt loading cathodes.[9–14] These have been rationalized by suggesting more complex oxygen reduction reaction (ORR) kinetics with variable Tafel slope,[4] by an interfacial resistance at the ionomer/platinum interface,[9,15] and/or by unusually high oxygen transport resistances through an assumed homogeneous thin ionomer film covering the Pt particles.[16,17] However, recent high-resolution transmission electron microscopy studies suggested that the ionomer coverage in the electrode may be rather inhomogeneous[18] and that the solvents used for preparing catalyst inks for electrode preparation influence the ionomer distribution in the final electrode, which in turn affects MEA (membrane electrode assembly) performance.[19] Therefore, one of the challenges in preparing MEAs is to achieve catalyst layers with a homogeneous ionomer distribution. This is not only expected to lead to maximum MEA performance, but also to allow for a more quantitative assignment of the transport related voltage losses, as all transport resistance measurements and voltage loss corrections are based on assuming uniform ionomer distribution in the electrode.

In the following, we will show that a modification of the carbon support of the platinum catalyst and an optimization of the ionomer content of the cathode catalyst layer result in a significant improvement of the MEA performance with ultra-low Pt loadings (ca. 0.07 mg_{Pt}/cm^2). We hypothesize that this is due to achieving a more homogeneous ionomer coverage on the carbon support (Vulcan XC72) which we functionalized with amide/imide/lactam groups ($–NH_x$), which are known to ionically interact with the ionomer's sulfonic acid groups ($–SO_3H$).[20,21] This hypothesis is consistent with a very recent conference report[22] and with our finding that the unassigned MEA voltage losses, i.e., after correction for the measured proton and oxygen transport resistances, are reduced to unprecedentedly low values in MEAs based on NH_x-functionalized carbon supports.

Experimental

Carbon functionalization with NH_x surface groups.—2 g of commercially available Vulcan XC72 (Tanaka Kikinzoku Kogyo K.K.) was mixed with 100 ml of 70% HNO_3 (Sigma Aldrich, ACS reagent) and then immersed into a pre–heated oil bath (70°C, reflux conditions) for 30 min. The carbon (further on referred to as "V-Ox") was filtrated and washed with hot water until neutral filtrate pH; then it was dried in a vacuum oven for 12 h at 80°C. Thereafter, 1 g of the sample was placed in a tube furnace (Carbolite Gero GmbH & Co KG, Germany) for 4 h at 200°C under pure NH_3 gas with a flow rate of 1 l/min to prepare aminated Vulcan carbon (further on referred to as "V-NH_x"). This procedure closely follows that described by Jansen et al.[23]

Synthesis of ca. 20 wt% Pt/V-NH_x.—300 mg of the aminated Vulcan support, 200 ml of ethylene glycol, 100 ml of deionized water, and 1.54 ml of H_2PtCl_6 (8 wt% H_2PtCl_6 in H_2O (≡ 0.25 mol/l) from Alfa Aesar) were placed in a round-bottom flask and stirred for 18 h at 25°C. Thereafter, the flask was immersed in a pre-heated oil bath at 120°C and stirred for 2 h. The catalyst was separated by filtration and washed with hot water until the filtrate was pH neutral and chloride free; subsequently, the catalyst was dried in a vacuum oven at 70°C for 12 h.[24] The final platinum loading was quantified by both TGA and elemental analysis.

Microstructure of carbon.—The surface areas of the commercial and aminated Vulcan carbon were evaluated by N_2 physisorption at 77 K using a Autosorb-iQ instrument (Quantachrome, UK). All samples were degassed under vacuum at 90°C for 15 h prior to physisorption measurements. Adsorption and desorption isotherms of all sam-

=These authors contributed equally to this work.
*Electrochemical Society Student Member.
**Electrochemical Society Fellow.
zE-mail: alin.orfanidi@tum.de

ples were recorded in the relative pressure range of $10^{-5} \leq (p/p_o) \leq 0.995$, where p represents the gas pressure and p_o the saturation pressure. This specific relative pressure range was chosen in order to ensure high resolution in the micro and mesopore region; to ensure high accuracy, the sample weight was adjusted to have a minimum absolute surface area of >10 m^2. The specific surface area and pore volume distribution were calculated by the Brunauer-Emmett-Teller (BET) method and by the quenched solid density functional theory (QSDFT) method, respectively (using the ASiQwin program). The adsorption branch was used for the BET surface area (best fit within $0.01 \leq (p/p_o) \leq 0.25$) using a multipoint fit. In addition, a slit/cylindrical pore and adsorption QSDFT kernel was used for the characterization of the nanopore size distribution (small mesopores and micropores with <30 nm) of the carbons. It should be noted that QSDFT is more accurate than other theories or non-local density functional theory (NLDFT), as it takes into consideration the heterogeneity of the carbon surface and thus gives a more realistic estimate of the micro and mesopores contribution.[25,26]

Transmission electron microscopy.—Transmission electron microscopy (TEM) was used to evaluate the Pt distribution on the carbon support. Samples for TEM analysis were prepared by dispersing a very small amount of the catalyst in deionized water and then depositing a few drops of the suspension onto carbon-coated Cu400 TEM grids (Science Services, Germany). Imaging was performed using a CM100 EM (Philips, Netherlands) operated at 100 kV and a resolution of 0.5 nm. For the evaluation of the average Pt particle size distribution, 230 individual particles were measured manually using ImageJ.

Thermogravimetric analysis.—Thermogravimetric analysis (TGA) of the carbons (V, V-Ox, and V-NH_x; all without platinum) was performed with a TGA/DSC 1 (Mettler Toledo, Switzerland) in pure argon at 5 K/min in order to quantify the amount of functional groups on the pristine, oxidized, and aminated carbons. The Pt content was also evaluated by TGA from the residual sample weight after burning the carbon by heating the sample to 1000°C under 83% O_2 in Ar atmosphere.

While the nominal Pt loadings for the here prepared catalyst (supported on V-NH_x) and the commercial catalyst (supported on V) is 20.0 wt%, it is critical for this study to precisely quantify the Pt loadings, which we have done by TGA. The thus determined Pt content of the here prepared Pt/V-NH_x catalyst was 20.3 wt% and that of the commercial Pt/V catalyst was 19.4 wt% (which was in perfect agreement with the value provided by the manufacturing company, 19.6 wt%). For this study we used for the commercial Pt/V the Pt loading provided by the manufacturing company.

Elemental analysis.—CHNS analyses were done using a EURO EA analyzer (Hekatech, Germany), which is based on the dynamic flash combustion technique. The Pt content was analyzed photometrically using a UV 160 photometer (Shimadzu, Japan).

X-ray photoelectron spectroscopy.—Surface chemical analysis was accomplished by X-ray photoelectron spectroscopy (Leybold−Heraeus LHS 10 XPS with a non-monochromatized Mg Kα source). The powder samples were pressed and fixed onto a vacuum compatible copper foil adhesive tape. The spectra were recorded at a constant pass energy of 100 eV, corresponding to an energy resolution of ∼1.1 eV. The measured C 1s peak at a binding energy of 284.5 eV indicates the absence of sample charging. All spectra were recorded at a pressure below $5 \cdot 10^{-8}$ mbar. The core level spectra were fitted by Voigt functions after subtraction of a linear background.

Rotating disk electrode.—Electrochemical characterization of the catalysts was done by the thin–film rotating disk electrode (RDE) technique, comparing the intrinsic activities of commercial Vulcan XC72 supported platinum catalyst (19.6 wt% Pt/V from TKK) with that of the here synthesized Pt/V-NH_x catalyst (20.3 wt% Pt). The catalyst inks were prepared by mixing 7.8 mg of Pt/V in 5.57 ml of DMF and 7.0 mg of Pt/V-NH_x in 5.0 ml of DMF (both equating to 1.4 $mg_{catalyst}$/ml). Ink suspensions were bath-sonicated for 15 min. No Nafion was added to the inks in order to ascertain the true mass and specific activities of catalysts without any poisoning caused by Nafion.[27] 5 µl of the ink was drop-cast onto a polished (0.05 µm alumina, Bühler, Germany) and pre-cleaned stationary 5 mm diameter GC electrode (Pine, USA), resulting in a catalyst loading of 36 $\mu g/cm^2$. The electrode was covered with a beaker and the catalyst film was dried overnight at room temperature in order to yield a homogeneous film. All electrochemical measurements were conducted in a home-made three-electrode jacketed glass cell. The electrode was attached to a rotator (Pine, USA), which was connected to a potentiostat (Autolab, Germany). A reversible hydrogen electrode (RHE) was used as a reference electrode, which was calibrated at the beginning of each experiment. All measurements were done at 25°C in 0.1 M $HClO_4$ which was prepared from 18 MΩ · cm Milli-Q water (Merck Millipore, Germany) and $HClO_4$ (60%, analytical grade, Kanto Chemical, Japan). All gases (Ar, O_2, and H_2) were of 6.0 grade (Westfalen, Germany). The reported potentials are referenced to the RHE scale and are iR-free. ORR activities were extracted at 1600 rpm from 20 mV/s anodic scans. Mass and specific activities are extracted after applying the mass transport correction for RDE.[28]

Membrane electrode assembly preparation.—All 5 cm^2_{geo} membrane electrode assemblies (MEAs) were fabricated using the decal transfer method. Catalyst inks were prepared by mixing the catalyst with a low-EW ionomer containing water-solvent dispersion (Asahi Kasei, Japan, 700 EW (EW ≡ $g_{polymer}/mol_{H+}$)). The ink components were added into a 8 ml HDPE capped bottle containing 16.5 g of 5 mm ZrO_2 beads in the following sequence: catalyst, water, 1-propanol, and finally the ionomer dispersion. The water concentration in the inks was 10 wt%, while the solid content was 0.03 g/ml_{ink} in order to obtain a suitable viscosity for the coating process. Three ionomer to carbon weight ratios (I/C) were used: 0.65, 0.40, and 0.25. The inks were mixed by placing the bottles onto a roller-mill (60 rpm) for 18 h at room temperature. Thereafter, the inks were coated onto virgin PTFE using a mayer rod coater.

The noble metal loading of the cathode electrodes was ca. 0.07 mg_{Pt}/cm^2_{geo} (see details in Table III) for all cases. The loading of the electrodes was determined by weighting the decals before and after the catalyst layer transfer. The same anodes were used for all measurements: 0.1 mg_{Pt}/cm^2_{geo} consisting of 19.6 wt% Pt/V (TKK) with an I/C ratio of 0.65. The MEAs were assembled by hot pressing a 15 µm membrane (Asahi Kasei) placed between the anode and cathode decals at 155°C for 3 min with an applied force of 0.11 kN/cm^2. All inks and decals were manufactured twice to verify reproducibility. For each MEA type, two independent fuel cell measurements were conducted; the average value of the measurements with error bars corresponding to the standard deviation are depicted in all figures.

Fuel cell operation.—The electrochemical measurements were performed using a single-cell hardware purchased from Fuel Cell Technologies Inc., fitted with 5 cm^2_{geo} active area graphite flowfields[29] (0.5 mm lands/channels; made by Poco Graphite). The assembling torque applied was 12 Nm and the compression of the gas diffusion media (Freudenberg H14C7) was set to 20% by using incompressible fiber-glass PTFE sub-gaskets.

Fuel cell tests were performed on an automated Greenlight Innovation fuel cell test station (type G60). All MEAs were conditioned before each test using the same voltage-controlled ramp-in procedure (H_2/air flows of 1390/3320 nccm at 80°C, 100% relative humidity, and 150 $kPa_{abs,inlet}$): 0.6 V for 45 min, 5 min at OCV, and 10 min at 0.85 V. This sequence was repeated 10 times, after which constant performance was reached. Differential-flow polarization curves were recorded in current-control mode at 80°C, 170 kPa_{abs} inlet controlled pressure, 100% relative humidity (RH) for both reactants, and constant flows of 2000 nccm of H_2 and 5000 nccm of air or O_2 (at these conditions, the inlet to outlet pressure drop in anode and cathode are 2 and 22 kPa, respectively). Prior to recording a polarization curve from

low to high current densities, MEAs were conditioned at 0.75 V for 15 min; each current density point was held for 10 min. and the resulting voltage was averaged over the final 30 s. AC impedance spectra were collected at each current density to determine the respective high frequency resistance (Gamry Ref3000 potentiostat).

Fuel cell diagnostic measurements.—The electrochemically active surface area (ECSA) of the cathode electrode was evaluated via cyclic voltammetry, averaging the H-desorption and H-adsorption charge and using a reference value of 210 $\mu C/cm_{Pt}^2$. The counter/reference electrode was fed with 200 nccm of fully humidified 5% H_2 in nitrogen, while the working electrode was first flushed with dry N_2, the flow of which was stopped during recording the CVs. The potential was cycled at 150 mV/s between 0.03 and 1.0 V (vs. RHE) at 40°C and ambient pressure. The shorting resistance and the H_2 cross-over currents were measured with H_2/N_2 at 170 $kPa_{abs,inlet}$, 80°C, and 100% RH.

The proton conduction resistance in the cathode electrode was determined by AC impedance (Gamry Ref3000 potentiostat) under H_2/N_2 (anode/cathode) at 0.2 V, following previous work[43] (peak-to-peak perturbation of 3.5 mV between 500 kHz and 0.2 Hz, with 20 points per decade). Three spectra were collected at each condition to verify reproducibility. Proton conduction resistances ($R_{H+,cath}$) were determined at 100, 70, 50, and 30% RH at 80°C under differential flow conditions (H_2/N_2 at 1000/1000 nccm), maintaining constant gas partial pressures (i.e., at cell pressures of 270, 255, 246, and 236 $kPa_{abs,inlet}$ respectively). Under these operating conditions the pressure drop over the flow field was negligible (<2 kPa_{abs}), which resulted in no change in the RH between the inlet and outlet of the cell.

The effective proton resistance $R^{eff}_{H+,cath}$ (in units of $\Omega \cdot cm^2$) was calculated by using Equation 10 from Liu et al.[42] and was used to correct for the proton conduction resistance induced voltage loss. The proton resistivity $\rho_{H+,cath}$ (in units of $\Omega \cdot cm$) was calculated by dividing the proton resistance ($R_{H+,cath}$) by the cathode electrode thickness (calculated from the well-known packing density of Vulcan carbon based electrodes of 28 $\mu m/(mg_C/cm^2)$[30]).

The total mass transport resistance was derived from limiting current measurements[5,11] at 80°C cell temperature and at 70% RH under differential conditions (2000 nccm of H_2 and 5000 nccm of O_2/N_2 mixtures). The dry mole fraction of oxygen was altered from 0.5 to 24% O_2 in N_2, while the cell potential was set to 0.3, 0.15, 0.1, and 0.05 V for 2 min each. To quantify pressure-independent and pressure-dependent oxygen transport resistances, limiting current measurements were conducted at 170, 270, 350, and 500 $kPa_{abs,inlet}$. Under these experimental conditions there was no significant change of the RH over the whole active area of the MEA. To be more precise, the RH in the inlet of the cell was set at 70% for all cases, while the resulting RH at the outlet was 68%, 70%, 71%, and 73% for the 170, 270, 350, and 500 $kPa_{abs,inlet}$, respectively, based on the measured pressure drop at a given flow rate and pressure as well as a water production corresponding to 4 A/cm^2_{geo}.

Results

Carbon and catalyst characterization.—CHNS elemental analysis (see Table I) was conducted in order to determine the functionalization degree of the pristine Vulcan XC72 carbon (V), after its oxidation (V-Ox), and after its subsequent amination (V-NH_x). It is well known that oxidation of carbon in concentrated HNO_3 leads to a surface functionalization with carboxylic, hydroxyl, and NO_x groups.[31,32] Accordingly, the N-content of the oxidized Vulcan support is significantly higher than that of the pristine carbon (see Table I). It further increases after the heat-treatment in NH_3 to 0.9% (see V-NH_x in Table I), owing to the formation of amides/imides/lactams upon reaction with NH_3.[23] With the increase in N-content, a simultaneous increase in the C-content is also seen (from 95.1 to 96.8 wt%), which is due to the loss of less stable O-containing functional groups during heat-treatment. The carbon content determined by CHNS analysis (see Table I) is in excellent agreement with that determined by TGA analysis (see Figure S1).

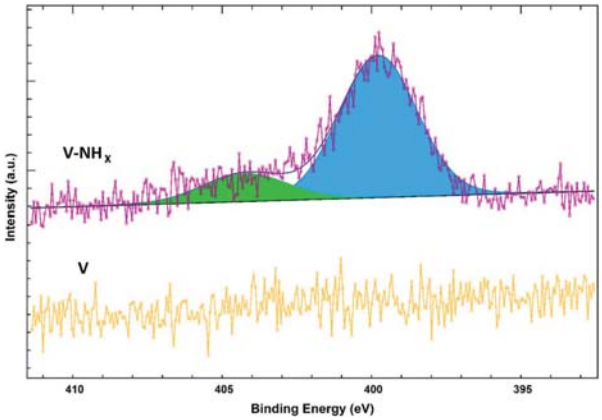

Figure 1. XP spectra of V and V-NH_x carbons in the N 1s region.

The presence and nature of the N-containing functional groups on the V-NH_x support was examined by X-ray Photoelectron Spectroscopy (XPS). The broad peak at 399.8 eV (see Figure 1) is consistent with the presence of imides/lactams/amides;[33] while it is not possible by XPS to distinguish between the different groups.[34] The pristine Vulcan XC72 carbon was also subjected to the same analysis and, as expected, no N-containing surface groups could be detected (Figure 1).

The microstructure of the pristine (V) and functionalized carbon (V-NH_x) was investigated via N_2 adsorption isotherm, seeking to determine any potential changes in the microstructure of the support by the amination treatment, as this could affect the performance of the catalyst in low Pt loaded electrodes.[35] Table II depicts the results from the BET and the QSDFT analysis. The total surface area estimated by BET (first row in Table II) and QSDFT (i.e., the sum of micro and mesopore areas from QSDFT analysis) are in perfect agreement. QSDFT determines the contribution of the micropores and mesopores to the total area (see experimental for more details). Using the IUPAC classification,[36] the contribution of the micropores (<2 nm) and the mesopores (>2 nm) to the total surface area was quantified (see Table II and Figure S2). The area of the micropores is commonly referred to as internal surface area, while the one of the mesopores is referred to as external area of a carbon support. Functionalization of the Vulcan carbon with NH_x groups clearly results in a decrease of the internal porosity of the carbon support (from 127 to 74 m^2/g),

Table I. Elemental analysis (CHNS) of the different carbon supports.

Sample	C [%]	H [%]	N [%]	S [%]
V	98.8 ± 0.3	0.0	0.2 ± 0.3	0.5 ± 0.3
V-Ox	95.1 ± 0.3	0.1 ± 0.3	0.4 ± 0.3	0.5 ± 0.3
V-NH_x	96.8 ± 0.3	0.2 ± 0.0	0.9 ± 0.0	0.5 ± 0.0

Table II. Surface area analysis of pristine Vulcan carbon (V) and aminated carbon (V-NH_x). 1st row: total surface area determined by BET; 2nd and 3rd row: meso and micropore areas determined by QSDFT.

Carbon	Units	V	V-NH_x
Surface area	m^2/g_C	231	175
Mesopores	m^2/g_c	102	101
Micropores	m^2/g_C	127	74

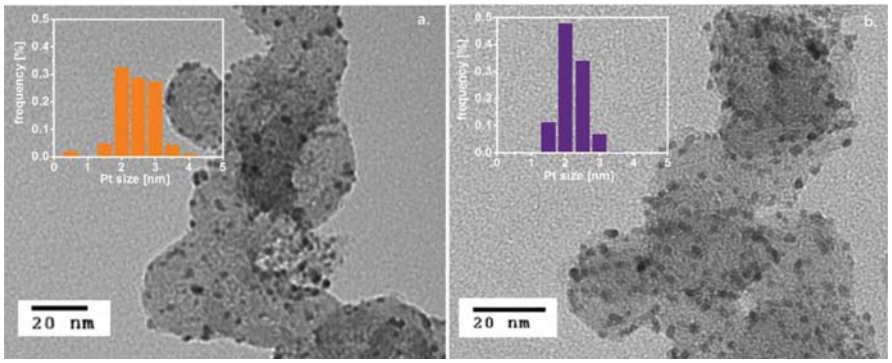

Figure 2. TEM micrographs and their corresponding Pt size distribution for: a. 19.6 wt% Pt/V and b. 20.3 wt% Pt/V-NH_x.

without, however, affecting the external surface area of the carbon and the mesopore size distribution (see Figure S2). The observed decrease in micropore area was previously suggested to be due to the blocking of micropores by functional groups.[37]

TEM micrographs of the commercial Pt/V and the here prepared Pt/V-NH_x catalyst were obtained to determine their Pt particle size distribution. Representative micrographs and the corresponding particle size distribution histograms are shown in Figure 2. It is clear that both catalysts exhibit a similar and reasonably narrow Pt distribution over the carbon support (see also Figure S3), as well as similar average Pt particle diameters of 2.4 ± 0.6 nm for the 19.6 wt% Pt/V catalyst and of 2.2 ± 0.4 nm for the 20.33 wt% Pt/V-NH_x, catalyst (see Table S4).

No changes of the surface functionalization are expected to occur during the Pt deposition procedure used in the present work, as was demonstrated by XPS measurements in an earlier work.[24]

Evaluation of the ORR activity by RDE.—Thin-film RDE ORR activity measurements were performed on the catalysts with functionalized and non-functionalized carbon support. These were done on a Nafion-free thin-film in order to avoid any poisoning of Pt due to Nafion and to exclude any interaction of Nafion with the functionalized catalyst. The obtained mass and specific activities are in good agreement with the literature for Nafion-free films.[27] Table III shows that the ORR mass activity of the catalyst with the functionalized support (Pt/V-NH_x) is the same as that of the non-functionalized support (Pt/V), both also displaying the same Tafel slope (see Table III and Figure S5). The specific activity of the Pt/V-NH_x catalyst is slightly higher than that of the Pt/V catalyst due to the difference in the ECSA (see Table III). This clearly confirms that both catalysts have essentially identical ORR activity and that the functionalization does not significantly influence the ORR activity. Thus, any of the below shown differences in the MEA performance of Pt/V vs. Pt/V-NH_x can be unambiguously attributed to the interaction between the ionomer and the support.

Fuel cell characterization.—All cathode electrodes had similar Pt loading (68–78 $\mu g_{Pt}/cm^2_{geo}$) and their detailed specifications, including their electrochemically active surface area (ECSA) are summarized in Table IV. The ionomer to carbon weight ratio (I/C) was altered in order to highlight the role of the ionomer film thickness on the mass transport resistance, as will be discussed further on. The uncorrected H_2/O_2 differential flow performance curves at 80°C, 100% RH, and 170 kPa_{abs} inlet pressure as well as the corresponding HFR values are depicted in Figure 3a. Figure 3b shows the H_2/O_2 performance vs cathode Pt-mass normalized current density (in units of A/g_{Pt}), corrected for the HFR, the effective cathode proton transport resistance ($R^{eff}_{H+,cath}$; calculated from $\rho_{H+,cath}$ in Figure 6a), and the H_2 crossover (4 ± 0.5 mA/cm^2_{geo}), i.e, an analogous correction which had been applied previously.[11] For each catalyst, two MEAs were prepared and tested to check for reproducibility, with the error bars corresponding to the standard deviation between those two measurements.

The ORR mass activity values (i_m) for the 19.6 wt% Pt/V and 20.3 wt% Pt/V-NH_x based cathodes were extracted from Figure 3b and are summarized in Table IV. As can be seen, the mass activities of the Pt/V and the Pt/V-NH_x catalysts are essentially identical, consistent with the identical mass activities determined by RDE (see Table III). In addition, to facilitate a better comparison with the literature, the here obtained ORR mass activities at a total pressure of 170 $kPa_{abs,inlet}$ (i.e., O_2 and H_2 partial pressures of 123 $kPa_{abs,inlet}$) were also converted to those ORR mass activities (i_m^*) which are obtained at a cell pressure of 150 $kPa_{abs,inlet}$ (i.e., O_2 and H_2 partial pressures of 103 $kPa_{abs,inlet}$) using Equation 12 from Ref. 38. The ORR mass activity of all MEAs are in good accordance with literature values reported for 20 wt% Pt/V[39] and other carbon supported catalysts.[40] Tafel slopes were determined from Figure 3b between 50 and 800 mA/cm^2 (~850 and ~12500 A/g_{Pt} in Figure 3b), following the approach by Neyerlin et al.,[38] to only use current densities greater than 10 times the H_2 crossover current density and up to below 1 A/cm^2. The Tafel slopes of all electrodes range between 72 and 76 mV/dec. (see Table IV),

Table III. Electrochemically active surface area (ECSA), ORR mass (i_m), and specific (i_s) activity at 0.9 V, and Tafel slope (TS) determined by RDE measurements (from the anodic going scan at 20 mV/s and 1600 rpm in O_2 saturated 0.1 M $HClO_4$ at 25°C). All data are corrected for iR and oxygen mass transport; the errors represent the standard deviations from 3 independent experiments.

Catalyst	ECSA [m^2/g_{Pt}]	i_m [mA/mg_{Pt}]	i_s [$\mu A/cm^2_{Pt}$]	TS [mV/dec.]
Pt/V	74 ± 2.4	548 ± 37	828 ± 26	56 ± 3.0
Pt/V-NH_x	60 ± 0.5	614 ± 36	1036 ± 65	56 ± 2.0

Table IV. Cathode electrode Pt loadings (L_{Pt}) and I/C mass ratios, their electrochemically active surface area (ECSA) determined by cyclic voltammetry, and their ORR mass activity at 0.9 V, 80°C, and 100% RH at the experimentally used H_2 and O_2 partial pressures of 123 $kPa_{abs,inlet}$ (i_m) as well as extrapolated to H_2 and O_2 partial pressures of 103 $kPa_{abs,inlet}$ (i_m*). The last column shows the Tafel slopes. Mass activities and Tafel slopes were obtained from Figure 3b, i.e., after correction for the HFR, the effective proton conduction resistance in the electrodes, and H_2 crossover correction. The indicated variation represents the standard deviation from two independent measurements.

Catalyst	I/C	L_{Pt} [$\mu g_{Pt}/cm^2_{geo}$]	ECSA [m^2/g_{Pt}]	i_m [A/g_{Pt}]	i_m* [A/g_{Pt}]	TS [mV/dec.]
Pt/V	0.65	68 ± 1	52 ± 2	119 ± 2	93 ± 2	76 ± 1
Pt/V-NH_x	0.65	78 ± 2	55 ± 1	110 ± 6	86 ± 6	76 ± 0
Pt/V-NH_x	0.40	74 ± 2	56 ± 3	127 ± 2	100 ± 2	72 ± 1
Pt/V-NH_x	0.25	68 ± 4	59 ± 4	146 ± 8	105 ± 8	74 ± 1

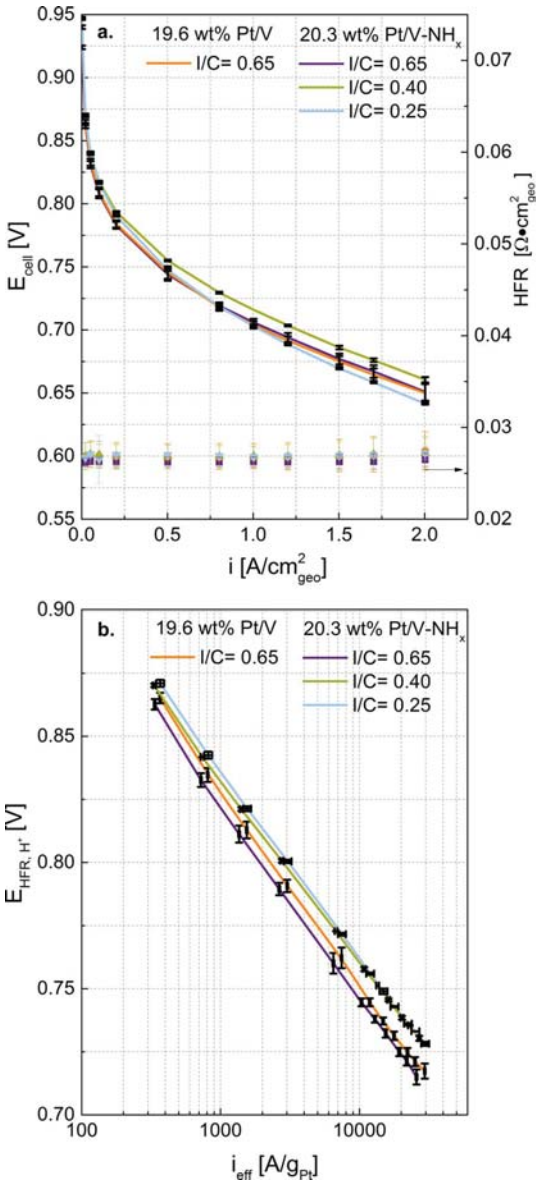

Figure 3. H_2/O_2 (2000/5000 nccm) differential flow performance of MEAs with ultra-low Pt cathode loadings (68–78 $\mu g_{Pt}/cm^2_{geo}$; see Table IV) at 80°C, 100% RH, and P_{cell} = 170 $kPa_{abs,inlet}$ for the 19.6 wt% Pt/V cathode catalyst at an I/C mass ratio of 0.65 (orange curves) and for the 20.3 wt% Pt/V-NH_x cathode catalyst at I/C mass ratios of 0.65 (purple), 0.40 (green), and 0.25 (light blue): a. uncorrected performance curves (left y-axis) with their corresponding HFR (right y-axis); b. performance curves referenced to the Pt-mass normalized current density corrected for HFR, H^+ conduction resistance in the cathode ($R^{eff}_{H+,cath}$), and the H_2 crossover current. Anode Pt loading were 0.1 mg_{Pt}/cm^2_{geo} and the error bars correspond to the standard deviation between two independent measurements on two different MEAs.

and are thus quite close to their theoretical value of 70 mV/dec. (i.e., based on a transfer coefficient of $\alpha = 1$), as reported by Neyerlin et al.[38] Larger Tafel slopes of ~80 mV/dec. for 0.05 mg_{Pt}/cm^2 cathodes were observed by Owejan et al.[11] (evaluated from their transport-corrected H_2/O_2 polarization curves between 40 and 800 mA/cm^2_{geo}). Considering that residual and/or not accurately corrected for transport resistances always lead to higher apparent Tafel slopes, we ascribe the slightly higher Tafel slopes in their study to unaccounted transport losses, possibly due to not fully optimized electrodes (e.g., inhomogeneous ionomer distribution), which were shown to yield higher Tafel slopes.[39]

To estimate H_2/air performance of MEAs by differential flow experiments, the stack inlet conditions and the stack outlet conditions are commonly simulated by using 21% and 10% O_2, respectively[41] (the latter corresponds to an air stoichiometry of ~1.9). Thus, polarization curves were measured under differential flows of 21% and 10% O_2 in N_2 at 80°C, 100% RH, and 170 $kPa_{abs,inlet}$. Figure 4 shows the effect of the carbon support functionalization on the MEA performance for 21% O_2 (dashed lines) and 10% O_2 (solid lines). The performance at 0.6 V for the 19.6 wt% Pt/V catalyst (orange lines) is in excellent agreement with recently published data under essentially identical conditions (differential flow, 80°C, 100% RH, and 150 $kPa_{abs,outlet}$) for a graphitized carbon supported Pt catalyst at the same loading[41]: 1.4 A/cm^2_{geo} (our data) vs 1.3 A/cm^2_{geo} at 21% O_2 and 0.78 A/cm^2_{geo} (our data) vs. 0.83 A/cm^2_{geo} at 10% O_2. Significantly better performance, however, is observed with our NH_x-functionalized catalyst (1.65 A/cm^2_{geo} at 21% O_2 and 0.91 A/cm^2_{geo} at 10% O_2). Kongkanand et al.[41] showed that the carbon support surface area (particularly the fraction of surface in micropores) and the location of the Pt particles on the primary carbon particles can significantly influence the local O_2 mass transport resistance and in turn the performance of the MEA. Pt particles that are located in the interior of the catalyst (Pt supported on a high-surface area carbon, Pt/MSC-a), versus Pt particles located exclusively on the exterior of the carbon (Pt supported on a graphitized carbon support, Pt/GrC-a) can significantly influence the performance under low O_2 partial pressure and low Pt loadings.

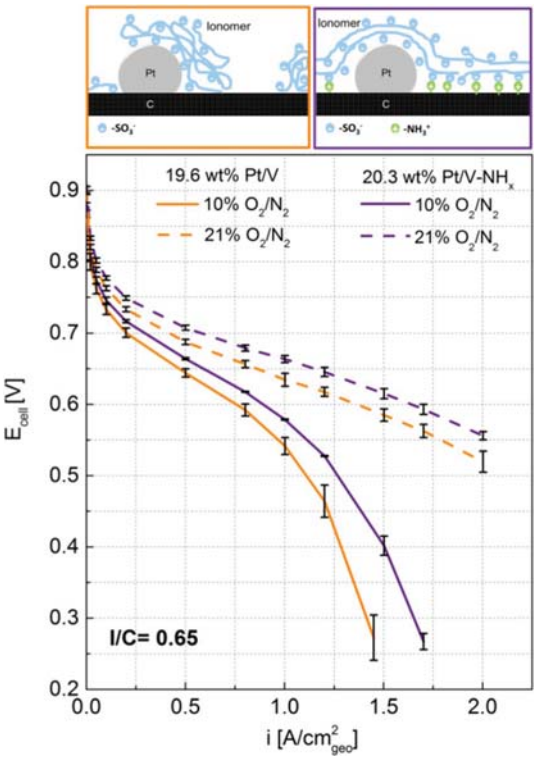

Figure 4. Differential flow polarization curves at 80°C and 100% RH of 19.6 wt% Pt/V (orange) and 20.3 wt% Pt/V-NH_x (purple) cathodes with I/C of 0.65 with 21% O_2 (dashed lines) and 10% O_2 (solid lines) in the cathode gas feed at a cell pressure of 170 $kPa_{abs,inlet}$. Cathode Pt loadings were 68 ± 1 and 78 ± 2 $\mu g_{Pt}/cm^2_{geo}$ for the Pt/V and the Pt/V-NH_x electrodes, respectively. The error bars correspond to the standard deviation for repeat measurements with two different MEAs. Schemes: sketch of the hypothesized ionomer distribution on the different carbon supports.

In our study, the V-NH_x has a surface area of 175 m^2/g_C, out of which 75m^2/g_C are micropores, so roughly 40% less micropores are accessible on the V-NH_x compared to the V support. Part of the performance improvement which is observed for the Pt/V-NH_x vs the Pt/V could be attributed to the reduced micropores of the carbon support. Nevertheless, by comparing the performance of the GrC-a (100 m^2/g_C) used in the study by Kongkanand et al. which has no micropores, with the V-NH_x supported catalyst, the latter exhibits better performance under the same operating conditions. This indicates that the performance improvement between Pt/V-NH_x and Pt/V cannot be solely attributed to the difference of microporosity of the carbon supports.

We hypothesize that this is due to a more homogeneous ionomer distribution on the NH_x-functionalized carbon support (illustrated by the sketches in Figure 4), which would result in a homogeneous ionomer film thickness over the whole electrode. This hypothesis is based on the known coulombic interaction between the NH_x groups on the carbon support with the SO_3^- groups of the ionomer[20,21] (Figure 4, purple-framed sketch).

In the case of Pt/V, the ionomer distribution is expected to be more inhomogeneous with a more random ionomer film thickness, which would lead to a high O_2 transport resistance in the regions where the ionomer film is thicker and to high proton conduction resistance in the regions where the ionomer film is thinner (Figure 4, orange-framed sketch). The latter would not only be expected to result in a performance decrease at high current densities and low oxygen concentrations, but also to larger discrepancies between transport resistance corrected performance curves and the kinetically predicted performance curve.

The above hypothesis, namely that the performance difference between the Pt/V and the Pt/V-NH_x is related to a difference in ionomer homogeneity and thus improved oxygen mass transport is further supported by the dependence of the performance to the I/C ratio, evaluated in Figure 5 for the 20.3 wt% Pt/V-NH_x catalyst: as the I/C is decreased

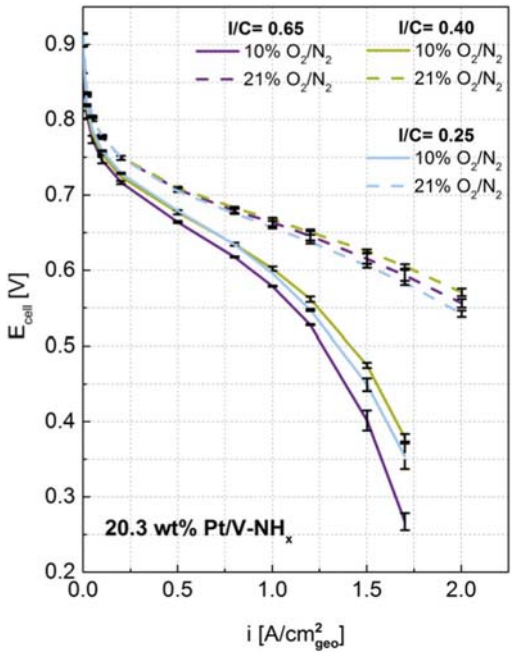

Figure 5. Differential flow polarization curves at 80°C and 100% RH of 20.3 wt% Pt/V-NH_x cathodes with I/C mass ratios of 0.65 (purple), 0.4 (green) and 0.25 (blue) with 21% (dashed lines) and 10% O_2 (solid lines) in the cathode gas feed at a cell pressure of 170 $kPa_{abs,inlet}$. Cathode Pt loadings were 78 ± 2, 74 ± 2, and 68 ± 4 $\mu g_{Pt}/cm^2_{geo}$ for the MEAs with ionomer mass ratios of 0.65, 0.40, and 0.25, respectively. The error bars correspond to the standard deviation for repeat measurements with two different MEAs.

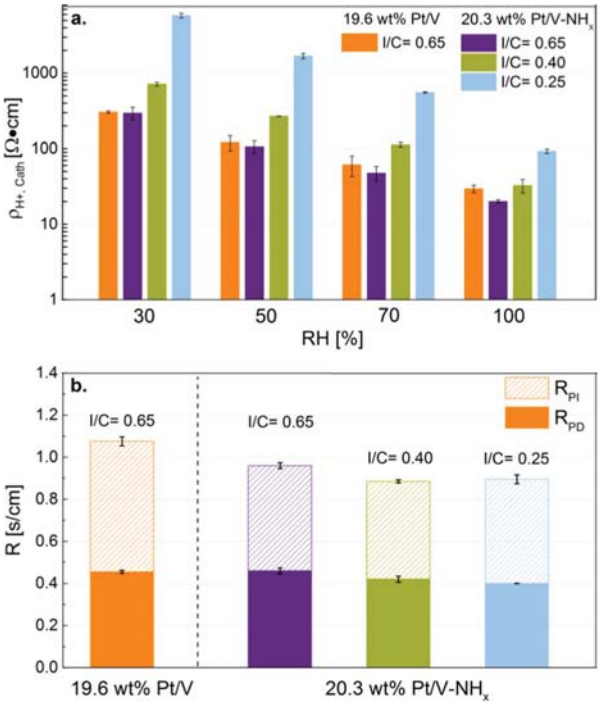

Figure 6. The effect of the cathode catalyst layer composition on: a. the cathode proton resistivity ($\rho_{H+,eff.}$) at different relative humidities (RH) and different I/C ratios; b. the total oxygen mass transport resistance ($R_{total} \equiv$ sum of the solid and hatched bars), which can be separated into a pressure dependent term (R_{PD}) and a pressure independent term (R_{PI}). The error bars correspond to the standard deviation between independent measurements with two different MEAs.

to 0.40 (green lines), the performance at 0.6 V further increases to 1.75 A/cm^2_{geo} at 21% O_2 and 1.0 A/cm^2_{geo} at 10% O_2, which can only be attributed to the O_2 permeability through the ionomer film.[9] As the I/C ratio is further decreased to 0.25, the performance decreases due to poor proton conductivity in the catalyst layer, as will be quantified in the following.

The proton resistivity of the different cathodes was measured according to the method developed by Liu et al.[43] As shown in Figure 6a, the cathode proton resistivity strongly depends on RH and the cathode I/C ratio, as what would be expected.[43] Comparing the Pt/V and the Pt/V-NH_x based MEAs with an I/C ratio of 0.65, the difference between their proton resistivities at the various RH values is identical within the error of the measurement. It is known that the intrusion of the ionomer into the micropores of the primary carbon particles reduces the ionomer film thickness on the external surface of the carbon support.[42] Thus, to estimate the average ionomer film thickness at the external carbon surface, it is necessary to determine the effective I/C ratio ($I/C_{eff.}$) from the overall I/C ratio, as was done by Liu et al.[42] Using this approach, we estimated the effective ionomer thickness ($t_{ionomer,eff.}$) by considering the cumulative pore volume in pores smaller than 3 nm, which was obtained from Figure S2 (highlighted). As shown in Table V, the effective ionomer film thickness at the I/C ratio of 0.65 is similar for the catalyst with the aminated (Pt/V-NH_x) and the untreated carbon (Pt/V). In summary, even though one might have expected that a less homogeneous ionomer film at equal average film thickness (i.e., at equal $t_{ionomer,eff.}$) would lead to a higher proton resistivity, this is not the case. However, differences in proton resistivity would also be expected to be negligible for inhomogeneous ionomer films, as long as there exists a continuous ionomer pathway throughout the electrode. Therefore, the homogeneity of the ionomer on the catalyst surface cannot necessarily be deduced from proton

Table V. Effective I/C ratio ($I/C_{eff.}$) and effective ionomer thickness ($t_{ionomer,eff.}$) for cathodes with different catalysts and overall I/C ratios, calculated by considering ionomer absorption into micropores of ≤3 nm.

Catalyst	I/C	$I/C_{eff.}$	$t_{ionomer,eff.}$ [nm]
Pt/V (TKK)	0.65	0.53	2.6
Pt/V-NH_x	0.65	0.58	2.8
Pt/V-NH_x	0.40	0.33	1.6
Pt/V-NH_x	0.25	0.18	0.9

resistivity measurements. Decreasing the I/C ratio of the Pt/V-NH_x cathodes, the proton resistivity increases substantially, as expected for a decrease in the effective ionomer thickness.[43,44]

To quantify the oxygen mass transport resistance (R_{total}), O_2 limiting current measurements were performed.[5] Since the same gas diffusion layer (GDL) was used for all measurements, one would expect that any differences observed originate from the changes in the catalyst layers and that the contributions from the diffusion medium and the microporous layer remain unchanged. To examine this aspect, the total oxygen mass transport resistance can be separated into a pressure dependent resistance (R_{PD}) and a pressure independent resistance (R_{PI}), which can be quantified by conducting limiting current measurements at various O_2 concentrations and at different cell pressures. Here, the R_{PD} term describes Fickian intermolecular gas diffusion through larger pores (>100 nm diameter), while the R_{PI} term comprises Knudsen diffusion in small pores of the microporous layer and the catalyst layers (<100 nm diameter) as well as diffusion through the ionomer film covering the Pt particles.[11]

Figure 6b shows the effect of the catalyst layer composition on the total transport resistance R_{total}, which is the sum of R_{PD} (solid bars) and R_{PI} (hatched bars). For all MEAs, R_{PD} was relatively constant between 0.41–0.45 s/cm, i.e., essentially identical within the error of the measurement, and thus consistent with the fact that the same diffusion media were used for all experiments. This suggests that the clearly lower total transport resistance for the 20.3 wt% Pt/V-NH_x cathode with an I/C mass ratio of 0.65 (purple bars) compared to the 19.6 wt% Pt/V catalyst with the same I/C (orange bars) must be due to a lower pressure independent oxygen transport resistance (R_{PI}) of the former, which we ascribe to a more homogeneous ionomer distribution on the NH_x-functionalized carbon support. As the I/C mass ratio of 20.3 wt% Pt/V-NH_x cathodes is reduced from 0.65 to 0.40, corresponding to reduction of the estimated ionomer film thickness from ~2.8 to ~1.6 nm (see Table V), R_{total} and R_{PI} decrease slightly, qualitatively consistent with a very recent report by Putz et al.,[45] who showed a decrease of R_{PI} when the effective ionomer thickness is decreased from ~3.5 to ~2 nm. In their study, a further decrease of the effective ionomer thickness down to ~0.5 nm did not lead to any further decrease in R_{PI}, identical to what we observe when decreasing the I/C ratio from 0.40 to 0.25 (blue bars), i.e., from an effective ionomer film thickness of ~1.6 nm to ~0.9 nm. While this independence of R_{PI} from the ionomer film thickness at very low I/C ratios is not yet understood, the data in Figure 6b clearly demonstrate that cathodes prepared with NH_x-functionalized carbon supports exhibit lower values of R_{PI} (and R_{total}), which is consistent with our hypothesis that a more homogeneous ionomer distribution can be achieved by NH_x-functionalized carbon supports.

Discussion

The above presented MEA performance data clearly demonstrate superior H_2/air performance at high current densities of the cathodes based on NH_x-functionalized carbon supports (see dashed lines in Figures 4 and 5), which is consistent with their lower oxygen mass transport resistance (Figure 6b). Based on the above data, we hypothesize that this is due to a more homogeneous distribution of the ionomer in the MEA. In this case, however, one would expect a more quantitative agreement between the ORR kinetics limited performance and the transport-corrected H_2/air performance curves, as all transport resistance measurements and voltage loss corrections are based on assuming a uniform ionomer distribution in the electrode. In order to examine this assumption, we will first correct the H_2/air polarization curves shown in Figures 4 and 5 (dashed lines) by the ohmic losses due to membrane and electronic resistances (i.e., by the HFR), by the total oxygen transport resistance (i.e., by R_{total} shown in Figure 6b), and by the effective proton conduction resistance in the cathode ($R^{eff}_{H+,cath}$); this will then be compared to the performance predicted by the ORR kinetics (see Table IV).

The transport-corrected H_2/air cell voltage, $E_{cell,tx\text{-}corr}$, is described by:

$$E_{cell,tx\text{-}corr} = E_{cell} + i_{geo} \cdot HFR + \Delta E_{O2-tx} + i_{geo} \cdot R^{eff}_{H+,cath} \quad [1]$$

where U_{cell} is the measured H_2/air cell voltage, $\Delta U_{O2\text{-}tx}$ is the total oxygen transport induced voltage loss, and $R^{eff}_{H+,cath}$ is the effective proton transport resistance in the cathode electrode. As shown by Neyerlin et al.,[46] the latter is related to the measured proton conduction resistance in the cathode, $R_{H+,cath}$, by:

$$R^{eff}_{H+,cath} = R_{H+,cath}/(3 + \xi) \quad [2]$$

where ζ is a scaling parameter which depends on ($i_{geo} \cdot R_{H+,cath}$) divided by the ORR Tafel slope.[46] The voltage loss due to the total oxygen mass transport resistance (R_{total}) is calculated using Equation 3, derived by Zihrul et al.:[47]

$$\Delta E_{O2-tx} = \frac{RT}{F} \cdot \left(\frac{1}{4} + \frac{\gamma}{\alpha}\right) \cdot \ln\left(\frac{p_{O2,channel} - \frac{RT}{4F} \cdot R_{total} \cdot i_{geo}}{p_{O2,channel}}\right) \quad [3]$$

where, γ is the ORR reaction order with respect to oxygen partial pressure ($\gamma = 0.54$),[38] α is the transfer coefficient ($\alpha = 1$),[38] R is ideal gas constant, T is the cell temperature, and $p_{O2,channel}$ is the partial pressure of O_2 in the channel of the flow field. The transport corrected H_2/air performance curves calculated from the H_2/air performance and HFR data as well as from the measured R_{total} and $R_{H+,cath}$ values (for the reader's convenience, all tabulated in the SI) using Equations 1–3 are shown in Figure 7a for the four different cathodes.

These can now be compared to the purely kinetically limited ORR performance, U_{ORR}, obtained from the reversible cell voltage, E_{rev}, and the ORR overpotential, η_{ORR}:

$$E_{ORR} = E_{rev} - \eta_{ORR} \quad [4]$$

whereby the reversible cell voltage at the H_2/air operating conditions is $E_{rev} = 1.17$ V (based on Equation 2 in Ref. 38. Under the assumption that the ORR kinetics follow the simple Tafel kinetics with a constant Tafel slope of $2.303 \cdot R \cdot T/(\alpha \cdot F)$, U_{ORR} can be related to the ORR mass activity at the reference conditions of 0.9 V, $T^* = 80°C$, and $p^*_{H2} = p^*_{O2} = 103\ kPa_{abs}$ (corresponding to i^*_m in units of A/g_{Pt}; see Table IV) by Equation 11 in Neyerlin et al.[38]:

$$E_{ORR} = 0.900\,V - \frac{2.303 \cdot R \cdot T}{\alpha \cdot F} \cdot \log\left(\frac{i_{eff}}{i^*_m \cdot L_{Pt} \cdot 10^{-3} \cdot \left(\frac{P_{O2}}{p^*_{O2}}\right)^m \cdot \left(\frac{P_{H2}}{p^*_{H2}}\right)^{\alpha/2} \cdot \exp\left[\frac{E^{(0.9V)}_{act}}{R \cdot T} \cdot \left(1 - \frac{T}{T^*}\right)\right]}\right) \quad [5]$$

where $\alpha = 1$ (≡ 70 mV/dec. at 80°C), L_{Pt} is the cathode platinum loading (in mg_{Pt}/cm^2_{geo}), p_{O2} and p_{H2} are the actual O_2 and H_2 partial pressures, respectively, m is the reaction order with respect to O_2 (m = 0.79)[38] and $E^{(0.9V)}_{act}$ is the activation energy at 0.9 V (note that this last term in Equation 5 vanishes for $T = T^*$). The average of the ORR kinetics limited performance curves derived from Equation 5 using the ORR mass activities and Pt loadings of the different MEAs (i^*_m and L_{Pt}, see Table IV) is plotted as black line in Figure 7a, whereby the error bars represent the standard deviation between the calculated ORR curves for each MEA.

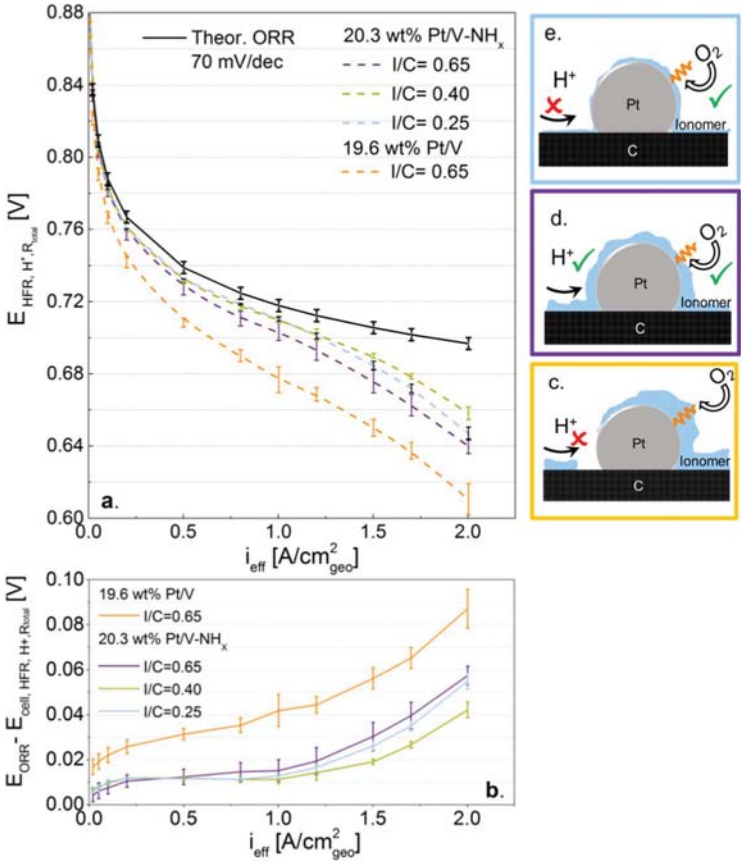

Figure 7. a. Transport-corrected H_2/air performance curves derived from Equation 1 for the various MEA types (dashed lines) and average value of the purely ORR kinetics limited performance curve derived from Equation 5; b. unaccounted voltage losses for each MEA type; c.-e. schematic illustration of the effect of the ionomer distribution and thickness on proton conductivity and mass transport. The error bars correspond to the standard deviation for repeat measurements with two different MEAs. Measurement conditions: H_2/air at differential flow conditions, 80°C, 100% RH, 170 $kPa_{abs,inlet}$.

We will first discuss the outcome of this analysis by comparing the two different catalysts in cathodes with the same I/C ratio of 0.65 (orange and purple lines in Figure 7a). Quite clearly, the Pt/V-NH_x based MEAs exhibit lower unaccounted voltage losses, i.e., their transport-corrected performance curve is closer to the purely kinetically limited ORR performance curve (black line). To more clearly illustrate the extent of unaccounted voltage losses, Figure 7b depicts the unaccounted loss of each MEA, obtained by subtracting the transport-corrected performance curves from the ORR kinetics limited performance of the same MEA. Figure 7b illustrates that the unaccounted voltage losses of the Pt/V-NH_x based MEAs (purple line) are substantially smaller than those of the MEAs based on Pt/V (orange line), which we attribute to a more homogeneous ionomer distribution and thus more homogeneous local ionomer film thickness on the former, illustrated schematically in Figures 7d (Pt/V-NH_x) and 7c (Pt/V). While for the case of the V-NH_x supported catalyst the unaccounted voltage losses decrease as the I/C ratio decreases.

Under the assumption of a homogeneous ionomer distribution, decreasing the I/C ratio would result in thinner ionomer film over the Pt particles, thereby facilitating higher O_2 permeability to the Pt/ionomer interface. This is consistent with the lower oxygen mass transport resistance observed for the Pt/V-NH_x based cathodes with an I/C ratio of 0.4 (see Figure 6b) and with their much reduced unaccounted voltage losses (see green line in Figure 7b). Therefore, from this analysis we can conclude that the ionomer distribution and thickness is a key factor in controlling oxygen mass transport resistances. On the other hand, for the Pt/V-NH_x based cathodes with an I/C of 0.25, which corresponds to an effective ionomer film thickness of ~0.9 nm (see Table V), the proton resistivity increases dramatically (see Figure 6a), which is reasonable considering that this film thickness corresponds to only ~2 monolayers of ionomer (based on a PFSA side chain thickness of ~0.5 nm[48]). Thus, as the ionomer film thickness becomes very small, the contribution from oxygen mass transport to the voltage loss becomes very small in contrast to the voltage losses due to poor proton conduction in the cathode (Figure 7e). Thus, a delicate balance between good oxygen mass transport and proton conduction has to be achieved in order to obtain the highest possible performance.

In summary, the here prepared MEAs based on cathodes with NH_x-functionalized carbon support show the highest cell voltage performance at ultra-low Pt loadings reported in the literature. However, even with the evidence for a more homogeneous ionomer distribution achievable with an NH_x-functionalized carbon support, there still remain ~40 mV of unaccounted voltage loss at 2 A/cm^2_{geo} (see Figure 7b). In principle, the origin of the unaccounted voltage loss could be due to: i) a not yet optimized MEA design; ii) a deviation from simple Tafel kinetics at low cathode voltages as suggested by Subramanian et al.;[8] and/or, iii) an oxygen mass transport resistance higher than that obtained in the currently used limiting current measurements. While we cannot exclude any of these possibilities, we consider the latter to be most probable, due to the fact that the ratio of heat flux to water generation is higher during limiting current measurements at 0.2 V than that during polarization curve measurements in H_2/air at 0.5 V, which affects the oxygen mass transport.

Conclusions

We presented a novel concept for tailoring the ionomer distribution in the catalyst layer. We provide evidence that by functionalizing the surface of a commercially available carbon with –NH_x groups, the ionomer is homogeneously distributed throughout the catalyst layer, caused by the coulombic attraction between the sulfonate anions of the ionomer and the NH_x surface groups on the carbon support. This, to our best knowledge, results in the highest H_2/air performance for

MEAs with ultra-low cathode loadings presented in the literature so far, shown to be due to reduced oxygen mass transport losses through a more homogeneous ionomer film. The presented voltage loss analysis based on proton resistivity and oxygen transport resistance measurements provided detailed insights into the major contributions to the voltage losses in MEAs with low Pt loaded cathodes. Lowering the ionomer/carbon mass ratio from 0.65 to 0.4, i.e., reducing the effective ionomer film thickness, resulted in reduced oxygen transport resistances and improved fuel cell performance. At I/C ratios of 0.25, however the performance was limited by poor proton conductivity. Therefore, the key to high performance low Pt loaded cathodes relies on the exquisite balance between good ionomer distribution and low ionomer/carbon ratio with adequate proton conductivity.

Acknowledgments

This work has been supported by Greenerity GmbH and the German Federal Ministry of Economy (BMWi project support number 03ET2058C) within the HyMotion5 research collaboration. The authors thank Prof. Dr. Sebastian Günther for his help in XPS measurements and Christoph Simon for consulting in mass transport resistance measurements.

References

1. J. Durst, A. Siebel, C. Simon, F. Hasche, J. Herranz, and H. A. Gasteiger, *Energy Environ. Sci.*, **7**, 2255 (2014).
2. O. Groeger, H. A. Gasteiger, and J. P. Suchsland., *J. Electrochem. Soc.*, **162**, A2605 (2015).
3. A. Kongkanand and M. F. Mathias, *J. Phys. Chem. Lett.*, **7**, 1127 (2016).
4. U. Beuscher, *J. Electrochem. Soc.*, **153**, A1788 (2006).
5. D. R. Baker, D. A. Caulk, K. C. Neyerlin, and M. W. Murphy, *J. Electrochem. Soc.*, **156**, B991 (2009).
6. Y. Wang and C.-Y. Wang, *J. Electrochim. Acta*, **50**, 1307 (2005).
7. Y. Liu, M. W. Murphy, D. R. Baker, W. Gu, C. Ji, J. Jorne, and H. A. Gasteiger, *ECS Trans.*, **11**, 473 (2007).
8. N. P. Subramanian, T. A. Greszler, J. Zhang, W. Gu, and R. Makharia, *J. Electrochem. Soc*, **159**, B531 (2012).
9. A. Z. Weber and A. Kusoglu, *J. Mater. Chem. A*, **2**, 17207 (2014).
10. A. Ohma, T. Mashio, K. Sato, H. Iden, Y. Ono, K. Sakai, K. Akizuki, S. Takaichi, and K. Shinohara, *Electrochim. Acta*, **56**, 10832 (2011).
11. J. P. Owejan, J. E. Owejan, and W. Gu, *J. Electrochem. Soc.*, **160**, F824 (2013).
12. Y. Ono, T. Mashio, S. Takaichi, A. Ohma, H. Kanesaka, and K. Shinohara, *ECS Trans.*, **28**, 69 (2010).
13. T. A. Greszler, D. Caulk, and P. Sinha, *J. Electrochem. Soc.*, **159**, F831 (2012).
14. R. Makharia, N. Subramanian, S. Kumaraguru, T. Greszler, B. Litteer, and Z. Liu, *Fuel Cell Seminar and Exposition, Phoenix, AZ, Presentation # GHT 33-2*, 2008.
15. S. Jomori, K. Komatsubara, N. Nonoyama, M. Kato, and T. Yoshida, *J. Electrochem. Soc.*, **160**, F1067 (2013).
16. K. Kudo, T. Suzuki, and Y. Morimoto, *ECS Trans.*, **33**, 1495 (2010).
17. N. Nonoyama, S. Okazaki, A. Z. Weber, Y. Ikogi, and T. Yoshida, *J. Electrochem. Soc.*, **158**, B416 (2011).
18. M. Lopez-Haro, L. Guétaz, T. Printemps, A. Morin, S. Escribano, P. H. Jouneau, P. Bayle-Guillemaud, F. Chandezon, and G. Gebel, *Nat. Commun.*, **5**, 5229 (2014).
19. T. Ngo, T. L. Yu, and H. L. Lin, *J. Power Sources*, **225**, 293 (2013).
20. K. Miyazaki, N. Sugimura, K. Kawakita, T. Abe, K. Nishio, H. Nakanishi, M. Matsuoka, and Z. Ogumia , *J. Electrochemical Soc.*, **157**, A1153 (2010).
21. L. Sun and T. Okada, *J. Membr. Sci.*, **183**, 213 (2001).
22. L. Xin, Y. Kang, F. Yang, A. Uzunoglu, T. Rockward, P. J. Ferreira, R. L. Borup, J. Ilavsky, L. Stanciu, and J. Xie, *ECS Conference*, Hawai 2016, Abstract 2584.
23. R. J. J. Jansen and H. van Bekkum, *Carbon*, **32**, 1507 (1994).
24. A. Orfanidi, M. K. Daletou, and S. G. Neophytides, *J. Appl. Cat. B: Envir.*, **106**, 379 (2011).
25. A. V. Neimark, Y. Lin, P. I. Ravikovitch, and M. Thommes, *Carbon*, **47**, 1617 (2009).
26. G. Y. Gor, M. Thommes, K. A. Cychosz, and A. V. Neimark, *Carbon*, **50**, 1583 (2012).
27. K. Shinozaki, Y. Morimoto, B. S. Pivovar, and S. S. Kocha, *J. Power Sources*, **325**, 745 (2016).
28. K. J. J. Mayrhofer, D. Strmcnik, B. B. Blizanac, V. Stamenkovic, M. Arenz, and N. M. Markovic, *Electrochim. Acta*, **53**, 3181 (2008).
29. C. Simon, F. Hasché, D. Müller, and Hubert A. Gasteiger, *ECS Trans.*, **69**, 1293 (2015).
30. W. Gu, D. R. Baker, Y. Liu, and H. A. Gasteiger, in *Handbook of Fuel Cells: Advances in Electrocatalysis, Materials, Diagnostics and Durability* (editors: W. Vielstich, H. A. Gasteiger, and H. Yokokawa), John Wiley & Sons, UK Chichester, 631 (2009).
31. S. Kundu, Y. Wang, W. Xia, and M. Muhler, *J. Phys. Chem. C*, **112**, 16869 (2008).
32. G. Zhang, S. Sun, D. Yang, J. Dodelet, and E. Sacher, *Carbon*, **46**, 196 (2008).
33. R. J. J. Jansen and H. van Bekkum, *Carbon*, **33**, 1021 (1995).
34. S. Kundu, W. Xia, W. Busser, M. Becker, D. A. Schmidt, M. Havenith, and M. Muhler, *Phys. Chem. Chem. Phys.*, **12**, 4351 (2010).
35. Y. Park, H. Tokiwa, and K. Kakinuma , M. Watanabe and M. Uchida, *J. Power Sources*, **315**, 179 (2016).
36. J. Rouquerol, D. Avnir, C. W. Fairbridge, D. H. Everett, J. M. Haynes, N. Pernicone, J. D. F. Ramsay, K. S. W. Sing, and K. K. Unger. "Recommendations for the characterization of porous solids (Technical Report)." *Pure and Appl. Chem.*, **8**, 66 (1994).
37. M. Toupin and D. Be´langer, *Langmuir*, **24**, 1910 (2008).
38. K. C. Neyerlin, W. Gu, J. Jorne, and H. A. Gasteiger, *J. Electrochem. Soc.*, **153**, A1955 (2006).
39. H. A. Gasteiger, S. S. Kocha, B. Sompalli, and F. T. Wagner, *J. Appl. Catal. B*, **56**, 9 (2005)
40. F. T. Wagner, S. G. Yan, and P. T. Yu, *Handbook of Fuel Cells - Fundamentals, Technology and Applications* (eds.: H. Yokokawa, H. A. Gasteiger, and W. Vielstich), John Wiley & Sons Chichester, **5**, 250 (2009).
41. A. Kongkanand, V. Yarlagadda, T. Garrick, T. E. Moylan, and W. Gu, *ECS Trans.*, **75**, 25 (2016).
42. Y. Liu, C. Ji, W. Gu, J. Jorne, and H. A. Gasteiger, *J. Electrochem. Soc.*, **158**, B614 (2011).
43. Y. Liu, M. W. Murphy, D. R. Baker, W. Gu, C. Ji, J. Jorne, and H. A. Gasteiger, *J. Electrochem. Soc.*, **156**, B970 (2009).
44. Y. Liu, C. Ji, W. Gu, D. R. Baker, J. Jorne, and H. A. Gasteiger, *J. Electrochem. Soc.*, **157**, B1154 (2010).
45. A. Putz, D. Susac, V. Berejnov, J. Wu, A. P. H. Hitchcock, and J. Stumper, *ECS Trans.*, **75**, 3 (2016).
46. K. C. Neyerlin, W. Gu, J. Jorne, Jr. A. Clark, and H. A. Gasteiger, *J. Electrochem. Soc.*, **154**, B279 (2007).
47. P. Zihrul, I. Hartung, S. Kirsch, G. Huebner, F. Hasche, and H. A. Gasteiger, *J. Electrochem. Soc.*, **163**, F492 (2016).
48. M. Yamaguchi, T. Matsunaga, K. Amemiya, A. Ohira, N. Hasegawa, K. Shinohara, M. Ando, and T. Yoshida, *J. Phys. Chem. B*, **118**, 14922 (2014).

Supporting information

The key to high performance low Pt loaded electrodes

A. Orfanidi[a,c,+,*] , P. Madkikar[a,c,*], H. A. El-Sayed[a], G. S. Harzer[a,*], T. Kratky[b] and H. A. Gasteiger[a,**]

[a] *Chair of Technical Electrochemistry, Department of Chemistry and Catalysis Research Center, Technische Universität München, D-85748 Garching, Germany*

[b] *Chair of Physical Chemisty with Focus on Catalysis, Department of Chemistry and Catalysis Research Center, Technische Universität München, D-85748 Garching, Germany*

[c] *Equal contribution authors*

[*] *Electrochemical Society Student Member*

[**] *Electrochemical Society Fellow*

[+] *Corresponding author: alin.orfanidi@tum.de*

TGA analysis of the various carbon supports: The weight loss observed in TGA experiments under argon of pristine Vulcan XC72 carbon (V), oxidized carbon (V-Ox), and aminated carbon (V-NH_x) was used to examine the desorption of surface groups upon heating. The lowest onset temperature for a significant weight loss is found for V-Ox (~120 °C), much earlier than in the case of V-NH_x (~190 °C) (Figure S1). The higher desorption temperature for the latter is attributed either to the generation of more stable surface functional groups upon reaction with NH_3 during the heat-treatment and/or to the temperature of the heat-treatment itself, which might lead to the loss of less stable surface groups. The final weight of the sample after analysis (only carbon) and the elemental analysis results for carbon are in close agreement with each other (s. Table 1).

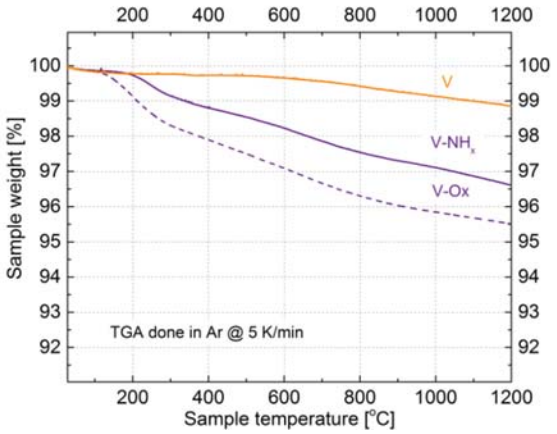

S1| TGA of V, V-Ox, and V-NH_x conducted in pure Ar at 5 K/min.

Nitrogen adsorption analysis: Analysis of the nitrogen adsorption isotherms by the QSDFT method was used to determine the pore size distribution both in terms of pore area (left panel of Figure S2) and pore volume (right panel of Figure S2).

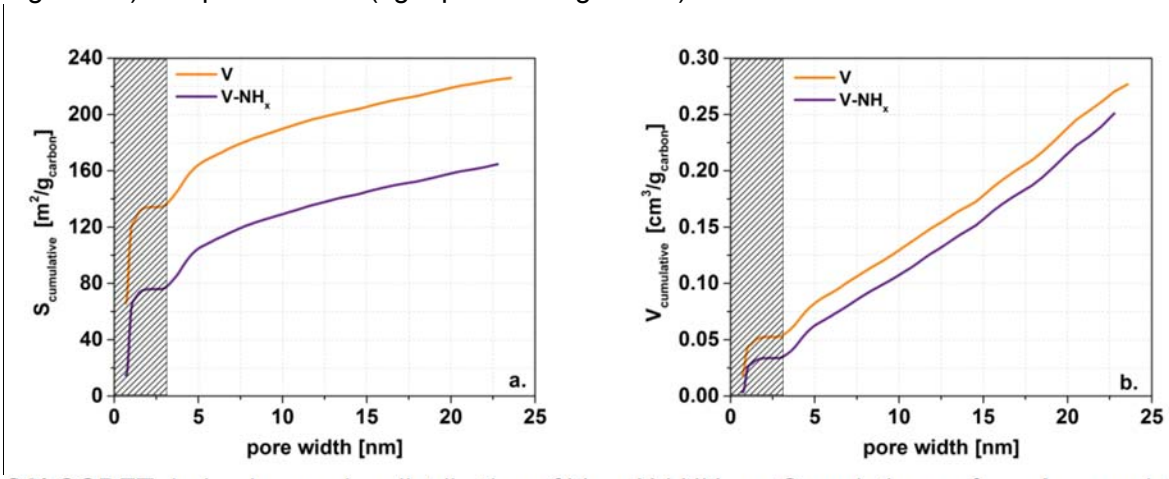

S2| QSDFT derived pore size distribution of V and V-NH_x: **a.** Cumulative surface; **b.** cumulative volume.

TEM analysis: TEM analysis was conducted to determine the Pt particle size distribution and to examine the homogeneity of platinum deposition on the support. As shown in Figure S3 (the scale bar is 20 nm), the platinum deposition on both the Pt/V (s. Figure S3a) and the Pt/V-NH_x (s. Figure S3b) is very homogeneous.

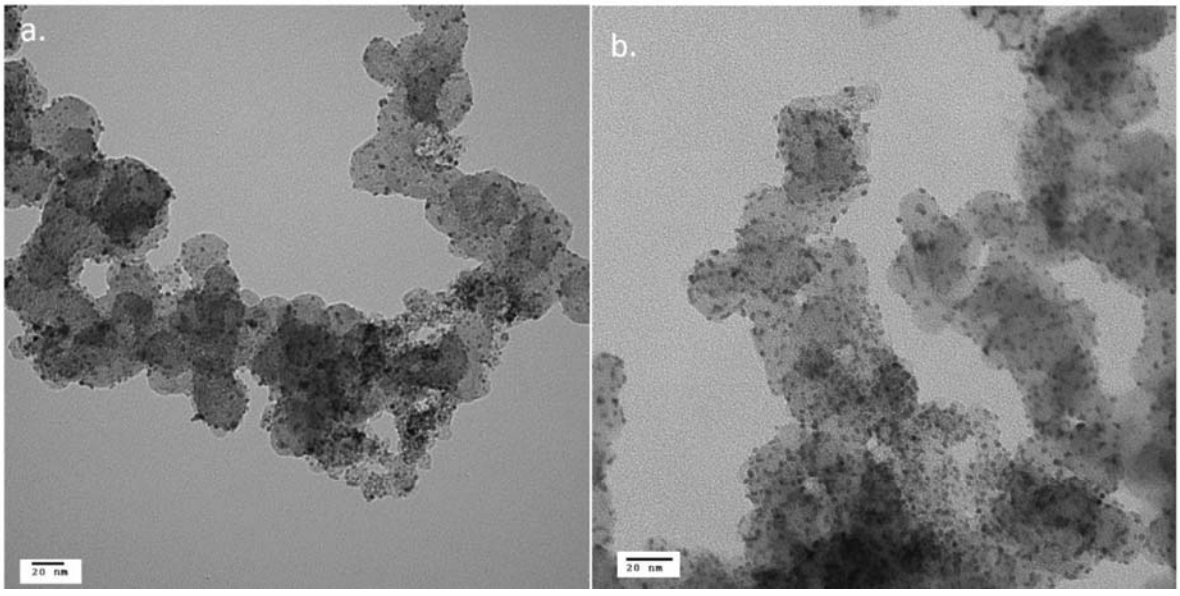

S3| TEM micrographs of: **a.** 19.6 wt% Pt/V and **b.** 20.3 wt% Pt/V-NH_x.

Exemplary higher magnification images are shown in Figure 2 in the main text and a detailed analysis is shown in Table S4.

S4| Results of the particle size analysis of the 19.6 wt% Pt/V and the 20.3 wt% Pt/V-NH_x catalysts based on analyzing approximately 230 particles from several high magnification TEM images: i) d corresponds to the number averaged particle diameter and its standard deviation (SD); ii) d_s is the surface-averaged diameter, defined as $d_s = \Sigma d_i^3/\Sigma d_i^2$ and its standard deviation which is derived in Equations S1 and S2; iii) $ECSA_{TEM}$ is the TEM derived electrochemically active surface area, defined as $ECSA_{TEM} = 6/(d_s \cdot \rho)$ with ρ being the density of platinum.

Sample	$d \pm SD$ [nm]	$d_S \pm SD_S$ [nm]	$ECSA_{TEM}$ [m^2/g]
Pt/V	2.4 ± 0.6	2.7 ± 1.7	104
Pt/V-NH_x	2.2 ± 0.4	2.4 ± 1.0	117

The standard deviation (SD_s) of the surface-averaged diameter can be calculated from Equation S1:

$$SD_S = \left(\frac{\partial D_S}{\partial d}\right) \cdot SD \qquad \text{Eq. S1}$$

This can be transformed into Equation S2:

$$SD_S = \left[3 - \frac{(2\sum d_i^3)(d)}{(\sum d_i^2)^2}\right] \cdot SD \qquad \text{Eq. S2}$$

RDE: The following figure shows exemplary of the ORR activity data obtained from the thin-film RDE experiments in form of a Tafel plot, displaying a Tafel slope of 56 mV/dec.

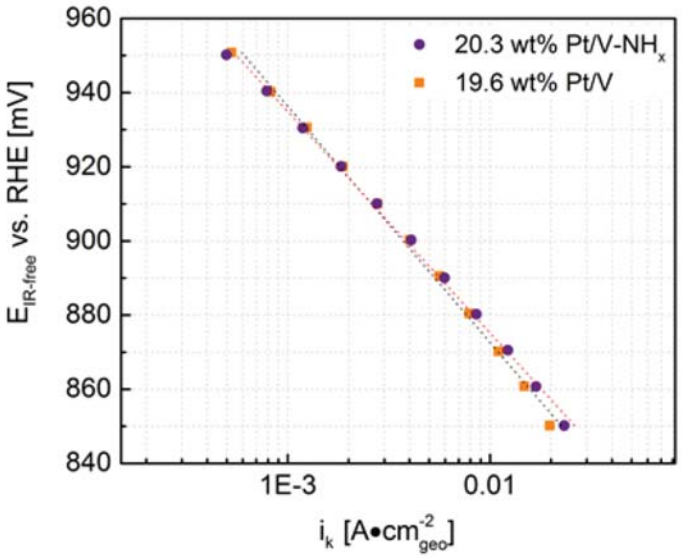

S5| Representative Tafel plots for the oxygen reduction reaction in oxygen saturated 0.1 M $HClO_4$ at 20 mV/s (positive-going scans) for the 19.6 wt% Pt/V and the 20.3 wt% Pt/V-NH_x catalysts. The kinetic current (i_{kin}) obtained after mass transport correction is normalized to geometric area of the disk and the potential is referenced to the reversible hydrogen electrode (RHE) scale and iR-corrected.

Proton conductivity measurements: Two different methods were used to determine the cathode electrode proton conductivity from impedance spectroscopy measurements. At high I/C ratios (0.65 and 0.4) or high relative humidity (>50%), the experimental data were fitted to the transmission line model equivalent circuit shown in Figure S6, using the "Z-fit" impedance fitting tool from EC-Lab (V10.44, Bio-Logic Science Instruments):

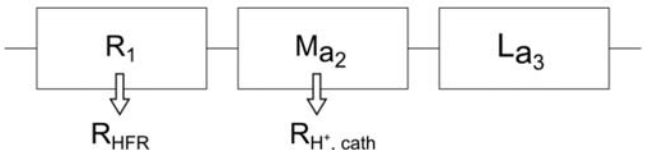

S6| Transmission line equivalent circuit and the derived resistances, based on the following elements: i) R_1 is the sum of the membrane proton conduction resistance and the electronic

resistances, corresponding to the HFR; M_{a2} represents a modified restricted linear diffusion element to determine $R_{H+,cath}$ iii) L_{a3} is a modified inductor to account for cell inductance.

The high frequency resistance, R_{HFR} [mΩ·cm^2], is determined from R1. The proton conduction resistance in the cathode, $R_{H+,cath}$ [mΩ·cm^2], is obtained from the resistance value of the M_{a2}-element. The proton resistivity of the catalyst layer is obtained by dividing $R_{H+,cath}$ by the electrode thickness. Representative impedance spectra are shown in Figure S7.

At low 30% RH and for the low I/C mass ratio of 0.25, it was not possible to obtain reasonable fits to the transmission line model. In these cases, the HFR was determined by the x-axis intercept of a linear approximation of the 45° section in the Nyquist plot, as illustrated by the dash-dotted line in Figure S7. By linear approximation of the low-frequency segment of the Nyquist plot, the proton resistance of the cathode catalyst layer, $R_{H+,cath}$, was obtained from the resistance difference between its intercept with the real axis and the HFR value (s. Figure S7). This linear approximation method yields larger errors at high RH values where the linear 45° segment is less pronounced (s., e.g., 100% RH data in Figure S7) and is more accurate at low RH values where an extended 45° segment is observed (e.g., 30% RH data in Figure S7). Proton conductivity values determined at intermediate I/C ratios and/or RH yielded comparable results (<10% deviation) for both the transmission line model and linear approximation.

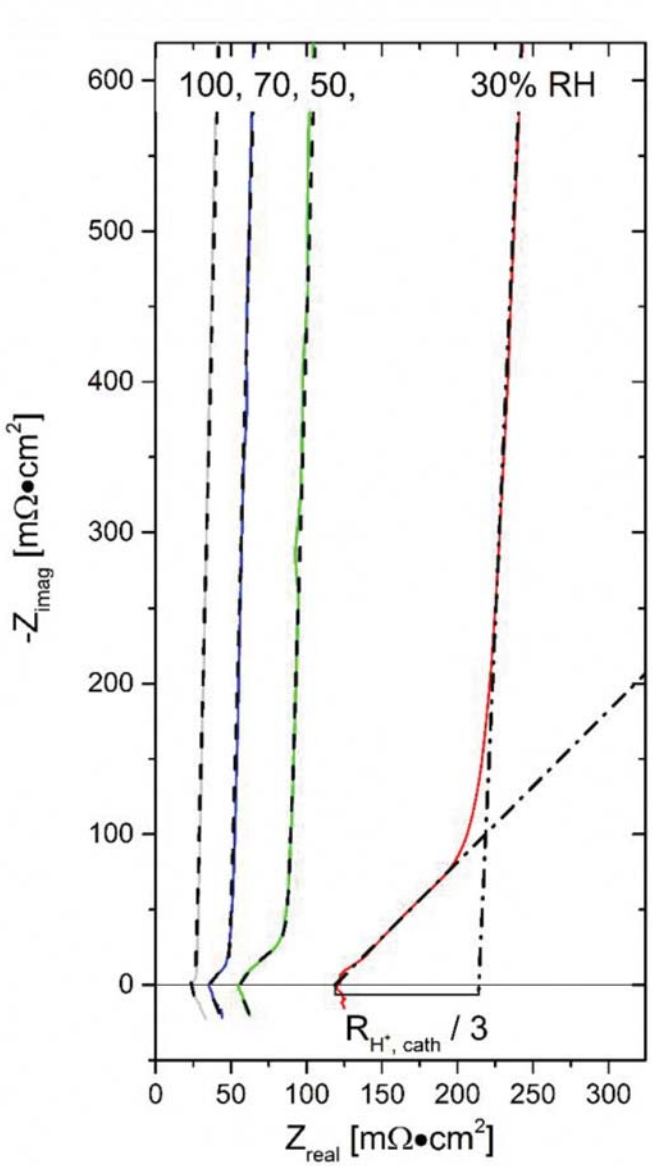

S7| Representative impedance data (solid lines) of a Pt/V-NH_x based cathode at 100% RH (gray), 70% RH (blue), 50% RH (green), and 30% RH (red). The dashed black lines represent numerical fits to the transmission line model shown in Figure S6. The dash-doted lines illustrate the linear approximation method to determine $R_{H+,cath}$ at low RH and low I/C values.

MEA raw data: For the reader's convenience, the H_2/air differential flow performance data and HFR values are shown below for all the MEAs used in this study (at 80 °C, 100% RH, 170 $kPa_{abs,inlet}$). The HFR was estimated by fitting the impedance spectra obtained during the polarization curve measurements with a standard fuel cell equivalent circuit provided by Gamry

(Gamry Echem Analyst, v. 6.25). In addition, R_{total} and $R_{H+,\ cath}$ measured under these conditions are also listed for each MEA.

20.3 wt% Pt/V-NH_x , I/C=0.65

MEA 1 :	$R_{H+,cath}$=16.5 [mΩ • cm^2]	R_{total}=0.95 [s/cm]	MEA 2 :	$R_{H+,cath}$=17.8 [mΩ • cm^2]	R_{total}=0.97 [s/cm]
i [A/cm^2_{geo}]	E_{cell} [V]	HFR [Ω]	i [A/cm^2_{geo}]	E_{cell} [V]	HFR [Ω]
2E-4	0.906	--	2E-4	0.909	--
0.0204	0.831	0.00531	0.0204	0.835	0.00517
0.0504	0.799	0.00533	0.0504	0.804	0.00521
0.1004	0.775	0.00533	0.1004	0.779	0.0052
0.2006	0.747	0.00533	0.2006	0.751	0.00518
0.501	0.705	0.00533	0.501	0.71	0.00517
0.8022	0.676	0.00531	0.8014	0.682	0.00517
1.0024	0.66	0.00532	1.0016	0.667	0.00518
1.2024	0.641	0.00534	1.2018	0.65	0.00516
1.5028	0.61	0.00538	1.5024	0.62	0.00514
1.7028	0.588	0.00543	1.7026	0.598	0.00514
2.003	0.552	0.00551	2.003	0.56	0.00519

19.6 wt% Pt/V , I/C=0.65

MEA 3 :	$R_{H+,cath}$=21.4 [mΩ • cm^2]	R_{total}=1.09 [s/cm]	MEA 4 :	$R_{H+,cath}$=18.4 [mΩ • cm^2]	R_{total}=1.06 [s/cm]
i [A/cm^2_{geo}]	E_{cell} [V]	HFR [Ω]	i [A/cm^2_{geo}]	E_{cell} [V]	HFR [Ω]
4E-4	0.896	--	4E-4	0.904	--
0.0204	0.818	0.00558	0.0206	0.823	0.00517
0.0506	0.786	0.0056	0.0506	0.791	0.00521
0.1006	0.76	0.00556	0.1006	0.765	0.0052
0.2008	0.731	0.00555	0.2008	0.736	0.00518
0.501	0.685	0.00554	0.501	0.69	0.00517
0.8014	0.653	0.00553	0.8014	0.66	0.00517
1.0018	0.628	0.00552	1.0018	0.641	0.00518
1.202	0.613	0.00555	1.202	0.622	0.00516
1.5024	0.579	0.00561	1.5024	0.591	0.00514
1.7026	0.556	0.00566	1.7026	0.569	0.00514
2.003	0.509	0.00578	2.003	0.53	0.00519

20.3 wt% Pt/V-NH_x , I/C=0.40

MEA 5 :	$R_{H+,cath}$=23.6 [mΩ • cm^2]	R_{total}=0.89 [s/cm]	MEA 6 :	$R_{H+,cath}$=30.7 [mΩ • cm^2]	R_{total}=0.88 [s/cm]
i [A/cm^2_{geo}]	E_{cell} [V]	HFR [Ω]	i [A/cm^2_{geo}]	E_{cell} [V]	HFR [Ω]
4E-4	0.911	--	4E-4	0.91	--
0.0204	0.834	0.00558	0.0204	0.833	0.00517
0.0506	0.803	0.00562	0.0504	0.802	0.00521
0.1006	0.778	0.00561	0.1006	0.777	0.0052
0.2008	0.75	0.00559	0.2006	0.75	0.00518
0.5012	0.709	0.00556	0.501	0.71	0.00517
0.8014	0.682	0.00557	0.8014	0.684	0.00517
1.0016	0.666	0.00557	1.0016	0.669	0.00518
1.2018	0.648	0.00558	1.202	0.653	0.00516
1.5024	0.624	0.00564	1.5024	0.627	0.00514
1.7026	0.603	0.00569	1.7026	0.607	0.00514
2.003	0.567	0.00569	2.003	0.574	0.00519

20.3 wt% Pt/V-NH_x , I/C=0.25

MEA 7 :	$R_{H+,cath}$=70.8 [mΩ • cm^2]	R_{total}=0.88 [s/cm]	MEA 8 :	$R_{H+,cath}$=70.6 [mΩ • cm^2]	R_{total}=0.91 [s/cm]
i [A/cm^2_{geo}]	Ecell [V]	HFR [Ω]	i [A/cm^2_{geo}]	Ecell [V]	HFR [Ω]
4E-4	0.914	--	4E-4	0.915	--
0.0204	0.834	0.00535	0.0204	0.836	0.00524
0.0506	0.803	0.00545	0.0506	0.805	0.00534
0.1006	0.777	0.00463	0.1006	0.778	0.00535
0.2008	0.749	0.00544	0.2008	0.749	0.00537
0.501	0.705	0.00544	0.501	0.705	0.00533
0.8014	0.675	0.00542	0.8014	0.676	0.00528
1.0016	0.656	0.0054	1.0016	0.658	0.00528
1.2018	0.636	0.00542	1.202	0.639	0.00527
1.5024	0.604	0.00544	1.5024	0.608	0.00528
1.7026	0.581	0.00545	1.7026	0.585	0.0053
2.003	0.539	0.00554	2.003	0.545	0.00536

3.2 Tailoring Catalyst Morphology towards High Performance for Low Pt Loaded PEMFC Cathodes

Here, the article "Tailoring Catalyst Morphology towards High Performance for Low Pt Loaded PEMFC Cathodes"[119] is presented, which was submitted to *The Journal of The Electrochemical Society* in April 2018 and accepted for publication on July 10th 2018 as an open access article, distributed under the terms of the Creative Commons Attribution 4.0 License (CC BY). The permanent web link to the article is http://jes.ecsdl.org/content/165/10/F770. The results in this paper were presented e.g., at the 232nd ECS Meeting in National Harbor, MA, USA in October 2017 (abstract number: I01D-1572).

In this article, the influence of the catalyst morphology, i.e., the distribution of platinum particles on the carbon support, is investigated. Many studies have shown significant impact of the carbon support properties, especially its surface area, on MEA performance. Yet, in this study, the same type of high surface area Ketjenblack carbon is used as support and the distribution of Pt nanoparticles on its surface is controlled by different deposition methods. Applying an incipient wetness synthesis, a highly concentrated solution of Pt precursor is absorbed into the pores of the carbon, resulting in Pt particles deposited primarily inside the carbon. From a polyol based synthesis, a catalyst with more Pt particles located on the outer surface of the Ketjenblack is obtained as indicated by TEM analysis. In addition, the polyol synthesis is applied to a Ketjenblack carbon which was previously modified by -NH_x groups to enhance ionomer distribution according to our previous publication (see section 3.1, page 37).[36]

Electrochemical characterization is carried out by thin-film RDE experiments and kinetic parameters as well as H_2/air performance and oxygen mass transport resistance are determined by single-cell fuel cell experiments with 5 cm^2 MEAs. When Pt is preferentially deposited on the inside of the carbon support, a high mass activity is obtained, as the platinum is shielded from ionomer poisoning inside the pores. The performance at high current density is however poor, due to a large mass transport resistance towards the Pt nanoparticles located inside the pores of the primary particles of the carbon support. When Pt is deposited preferentially on the exterior carbon particle surface, the mass activity is similar to results obtained for a more solid Vulcan type carbon and the high current density is superior, resulting from the lower oxygen mass transport limitations. Additionally, the effect of the Pt distribution on the validity of a voltage loss analysis is presented. When Pt particles are located preferentially on the outside of the support, a virtually quantitative agreement between the kinetically predicted performance and the polarization curve corrected for all known voltage loss contributions is observed. For catalysts with platinum predominantly located inside the pores, large unaccounted voltage losses are obtained at high current density, pointing towards the difficulty to accurately determine the oxygen

mass transport resistance for this type of morphology. This, we believe, originates from the fact that pore diffusion resistances are not considered in the analysis of voltage loss contributions.

In summary, this publication shows that not primarily the type of carbon support influences the fuel cell performance, but that it is the distribution of Pt particles on/within the primary particle of the carbon support, e.g., inside or outside the pores, which can be influenced by the synthesis procedure.

Author contributions

G.H., A.O. and P.M. prepared and characterized catalysts, G.H. and A.O. fabricated MEAs, performed electrochemical test and evaluated measurement data. H.S. conducted and evaluated RDE experiments. G.H. wrote the manuscript. All authors discussed the experimental results and revised the manuscript.

Tailoring Catalyst Morphology towards High Performance for Low Pt Loaded PEMFC Cathodes

Gregor S. Harzer,*,z Alin Orfanidi, Hany El-Sayed, Pankaj Madkikar,* and Hubert A. Gasteiger**

Chair of Technical Electrochemistry, Department of Chemistry and Catalysis Research Center, Technical University of Munich, D-85748 Garching, Germany

The effect of the catalyst synthesis method on the location of platinum nanoparticles on a high surface area Ketjenblack is investigated with respect to the high current density performance in low loaded proton exchange membrane fuel cells (PEMFC). Catalysts were prepared using various synthetic methods to deposit platinum nanoparticles at different locations on the carbon surface, e.g. inside or outside the pores of the primary particle. Transmission electron microscopy (TEM) suggested, that the Pt-particle deposition can be controlled to be preferentially on the outer carbon surface or within the pores. Electrochemical characterization was performed in thin-film rotating disk electrode (RDE) setup as well as in 5 cm^2 single cell MEA tests. Although the carbon support was identical for all catalysts, the one with more Pt particles deposited on the outer carbon surface performed superior at high current which was attributed to a lower oxygen mass transport resistance. From the presented data, it can be concluded that not only the type or the surface area of the carbon black support affects the fuel cell performance, but that the synthesis approach is an additional parameter to tune the fuel cell performance at high current density.

 [DOI: 10.1149/2.0311810jes]

Manuscript submitted April 4, 2018; revised manuscript received June 27, 2018. Published July 10, 2018. This was Paper 1572 presented at the National Harbor, Maryland Meeting of the Society, October 1–5, 2017.

One of the challenges for fuel cell electric vehicles (FCEVs) to become cost-competitive with internal combustion engines is the reduction of the platinum catalyst loading. As kinetics of the hydrogen oxidation in acidic media are fast,[1] only little Pt is needed on the anode (< 0.1 mg_{Pt}/cm^2_{MEA}), while loadings of about 0.2–0.4 mg_{Pt}/cm^2_{MEA} are typically used on the cathode due to the sluggish ORR kinetics. A significant reduction of the cathode Pt loading to below 0.1 mg_{Pt}/cm^2_{MEA} is estimated to be necessary for a large scale commercialization of FCEVs with a total platinum loading of about <10 g Pt per car in the future.[2,3]

One possibility to reach this target is to increase the mass activity of Pt for the oxygen reduction reaction (ORR) by using Pt-alloy catalysts while simultaneously decreasing the overall Pt loading at the cathode of the membrane electrode assembly (MEA). Additionally, the FC-stack should be operated at high current density, i.e., at high power density, in order to keep the overall stack size and cost small. So far, conventional Pt-alloy nanoparticle supported on high-surface area carbons show ≈3–4 times higher ORR activities when tested in RDE compared to actual proton exchange membrane (PEM) fuel cell test.[4,2] Unfortunately, for more advanced ORR catalyst concepts like shape-controlled Pt-alloys[5,6] and confined alloy nanoparticles[7] which show substantially higher ORR activities in rotating disk electrode (RDE) experiments, it has not yet been possible to prepare MEAs with good high current density performance.[4,8] Reasons for this may include the difficulty of preparing electrodes with suitable structure and homogeneous ionomer distribution.

In addition, the morphology of the carbon black catalyst support was shown to have a major influence on the high current density performance. Usually, better high current density performance is observed for low-surface area supports like Vulcan carbon compared to high-surface area supports like Ketjenblack, even though the latter show a higher ORR mass activity.[9–12] A detailed study of the influence of the carbon black support was conducted by Park et al.,[13] who investigated four different carbon black supports with different porosity and surface area. They concluded that a carbon black with high surface area and porosity shows poor high current density performance because a lot of Pt nanoparticles are located inside the pores and therefore are poorly accessible to oxygen at high current densities, i.e., at high local oxygen fluxes. The best high current density performance was observed for a carbon black support with very low surface area and minimal porosity, for which the majority of Pt particles were located on the outer surface of the support. Their observations with regards to the location of Pt particles as a function of the carbon support morphology are consistent with previous findings.[14]

In the present work, we show that neither the surface area nor the porosity of the carbon black support influences the high current density performance, but that the location of the Pt particles on the support, i.e., on the outer surface or inside the pores is the governing factor. Two different types of catalysts were prepared on the same high surface area Ketjenblack (KB) carbon support by an incipient wetness and a polyol reduction process to control the location of Pt particle deposition. Additionally, the polyol reduction was used to prepare a catalyst on a surface-modified KB support (functionalized by NH_x groups)[15] to investigate the effect of ionomer distribution in the catalyst layer. ORR mass activities obtained by RDE and fuel cell measurements as well as high current density performance under differential-flow conditions of the here synthesized catalysts were compared to a commercial catalyst on high surface area Ketjenblack (TEC10E20E, TKK).

Experimental

Carbon functionalization with NH_x surface groups - KB(NH_x).—The preparation of surface modified carbon and the deposition of Pt nanoparticles were performed as previously described in detail.[15] In short, commercially available Ketjenblack (E-type, Tanaka Kikinzoku Kogyo K.K., Japan) with a surface area of 930 m^2/g (determined by QSDFT from N_2 sorption) was dispersed in 100 ml of 70% HNO_3 (Sigma Aldrich, ACS reagent) and stirred under reflux conditions (70°C oil bath) for 30 min. After filtration, the carbon (further on referred to as "KB-Ox") was washed with hot water (from Milli-Q Integral System; >15 MΩ · cm) and dried in vacuo. Aminated Ketjenblack ("KB(NH_x)") was prepared by placing 1 g of KB-Ox in a tube furnace (HST12/400, Carbolite GmbH, Germany) for 4 h at 200°C under pure NH_3 gas with a flow rate of 1 l/min. The carbon was washed with hot water and dried in a vacuum oven at 70°C.

Synthesis of 20%$_{wt}$ Pt/KB$_{PO}$ and Pt/KB(NH_x)$_{PO}$.—300 mg of carbon black, 200 ml of ethylene glycol (Sigma Aldrich, ACS reagent), 100 ml of H_2O (>15 MΩ · cm), and 1.54 ml of H_2PtCl_6 (8 wt% H_2PtCl_6 in H_2O; 0.25 mol_{Pt}/l) from Alfa Aesar; corresponding to 1.3 $mmol_{Pt}/l$) were stirred for 18 h at room temperature. The flask was transferred to a pre-heated oil bath at 120°C and stirred for 2 h. The

*Electrochemical Society Student Member.
**Electrochemical Society Fellow.
zE-mail: gregor.harzer@tum.de

catalyst was separated by filtration, washed with hot water until the filtrate was pH neutral and chloride free and dried in a vacuum oven at 70°C for 12 h. The final platinum loading was quantified by TGA.

Synthesis of 20%$_{wt}$ Pt/KB$_{IW}$.—$H_2PtCl_6 \cdot x\ H_2O$ (x ≈ 5–6; Sigma Aldrich, >99.9% tmb, 0.2655 g) was dissolved in 2.2 ml acetone (Sigma Aldrich, Chromasolv; corresponding to ≈230 $mmol_{Pt}$/l) and added to 400 mg Ketjenblack (dried in vacuum at 110°C) to wet the entire carbon powder. The acetone was evaporated at 40°C under air in an oven. Then, the powder was finely ground and heated in 5% H_2/Ar (500 ml/min) to 250°C for 30 min (10 K/min heating rate) in a tube furnace (Carbolite). After cooling to room temperature under Ar flow, the gas was humidified by bubbling it through water at room temperature while air is slowly mixed into the Ar stream. This procedure was required to avoid catalysts ignition on removal from the tube furnace. The catalyst was then washed with hot water (>15 MΩ · cm) until the filtrate was pH neutral and chloride free and dried in vacuum at 70°C. The final platinum loading was quantified by TGA.

Transmission electron microscopy.—Transmission electron microscopy (TEM) was used to determine the Pt particle size distribution and location on the carbon support. Electron microscopy samples were prepared by dispersing the catalyst in deionized water and then depositing a few drops of the suspension onto carbon-coated Cu400 TEM grids (Science Services, Germany). Imaging was performed using a Philips CM100 EM operated at 100 kV at a resolution of 0.5 nm. For the evaluation of the average Pt particle size distribution, >400 individual particles were measured using the software ImageJ (v. 1.51j8).

Thermogravimetric analysis.—Thermogravimetric analysis (TGA) of the pure carbons (without platinum) was performed with a TGA/DSC 1 (Mettler Toledo, Switzerland) at a heating rate of 5 K/min in argon to quantify the amount of functional groups on the pristine, oxidized, and aminated carbons. The Pt loading on carbon was evaluated by the weight loss upon burning the carbon in 67% O_2 in Ar at a heating rate of 25 K/min to 1000°C. The residual after the TGA ramp was verified to be pure Pt by XRD.

Elemental analysis.—CHNS analyses were performed using a EURO EA analyzer (Hekatech, Germany). Determination of the Pt content was done photometrically using a UV 160 photometer (Shimadzu, Japan).

X-ray photoelectron spectroscopy.—Surface chemical analysis was accomplished by X-ray photoelectron spectroscopy (Axis Supra, Kratos, UK). The powder samples were dispersed in water and drop-cast onto a pre-cleaned copper foil, which was fixed to the sample holder. Subsequently, the sample was dried in ambient air followed by drying at 80°C in an oven. The spectra were recorded at a constant pass energy of 160 eV and at a pressure below $5 \cdot 10^{-8}$ mbar.

Electrochemical characterization.—Experimental details on rotating disk electrode (RDE) measurements and fuel cell testing are given in our previous publications.[15,16] In short, RDE inks were prepared by suspending the catalyst powder in DMF and drop-casting onto a polished 5 mm diameter GC electrode (Pine, USA) without the use of Nafion. All measurements were done at 25°C in 0.1 M $HClO_4$ with gases being of 6.0 grade. Measured potentials are referenced to the reversible hydrogen electrode (RHE) scale and corrected for the iR drop.

Membrane electrode assemblies (MEA) with an active area of 5 cm^2 were prepared by the decal transfer method. Catalyst inks were prepared by mixing the catalyst, water, 1-propanol and the ionomer dispersion (Asahi Kasei, Japan, 700 EW) in an 8 ml HDPE bottle containing 5 mm ZrO_2 grinding media. The carbon content of the dispersion was adjusted from 20–30 mg_C/ml_{ink} depending on the viscosity while the water content was fixed at 10%$_{wt}$. The ionomer to carbon ratio (I/C) was 0.65 g/g for all electrodes. Anodes were prepared by the same procedure using a commercial Pt/V (TEC10V20E, TKK) catalyst. The MEAs were prepared by hot-pressing 5 cm^2 anode and cathode decals at 155°C for 3 min to a 15 μm thick membrane (Asahi Kasei). For each catalyst, two independent fuel cell measurements were conducted under differential-flow conditions using a 5 cm^2 flow-field (see References 17 and 18), and the mean absolute deviation between both is shown as error bars in all figures (for more details on the fuel cell testing conditions see our previous publications).[15,16]

Table I. Elemental analysis (CHNS) of the carbon, hydrogen, oxygen, and sulfur content of the as-received Ketjenblack (KB), the oxidized Ketjenblack (KB-ox), and the Ketjenblack after the NH_x functionalization (KB(NH_x)).

Sample	C [%$_{wt}$]	H [%$_{wt}$]	N [%$_{wt}$]	S [%$_{wt}$]
KB	95.9 ± 0.0	0.2 ± 0.0	0.1 ± 0.0	0.0
KB-ox	90.8 ± 0.3	0.3 ± 0.1	0.5 ± 0.0	0.0
KB(NH_x)	94.9 ± 1.1	0.2 ± 0.0	1.1 ± 0.1	0.0

Results and Discussion

Characterization of carbon supports and catalysts.—Elemental analysis and X-ray photoelectron spectroscopy (XPS) was utilized to determine the bulk and surface composition of the Ketjenblack support before and after the functionalization procedure. Table I summarizes the carbon, hydrogen, nitrogen, and sulfur content of the as-received Ketjenblack (KB), after the oxidation with HNO_3 (KB-ox), and after the NH_x functionalization with ammonia (KB(NH_x)). In contrast to an untreated, low-surface area Vulcan carbon support, which has a carbon content of ≈99%$_{wt}$, the carbon content of as-received Ketjenblack was only ≈96%$_{wt}$ (see Table I) due the presence of oxygen-containing surface groups on this high-surface area support (it is also noteworthy that in contrast to Vulcan carbon, no sulfur could be detected in KB carbon).[15] Upon oxidation, the N content increased while the C content decreased (from 95.9 to 90.8%$_{wt}$), which was caused by the formation of chemisorbed nitrogen oxides (≈0.5%$_{wt}$, see Table I) and the increase of oxygen functionalities on the surface. Chemisorbed nitrogen oxides were identified by XPS (see black line in Figure 1) at binding energies above 405 eV.[19] After the ammonia treatment at

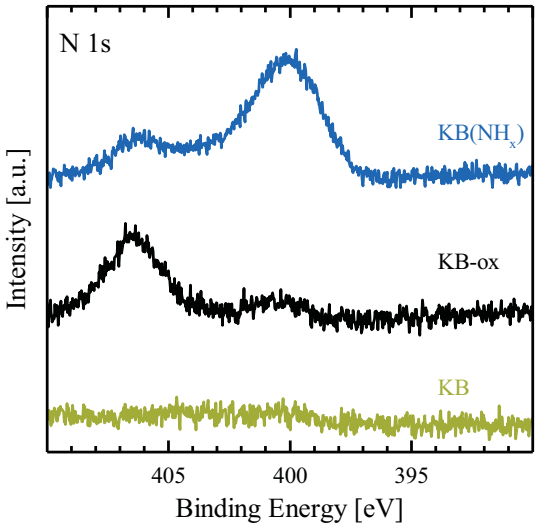

Figure 1. XP spectra in the N 1s region of the as-received Ketjenblack (KB), the oxidized Ketjenblack (KB-ox), and the Ketjenblack after the NH_x functionalization (KB(NH_x)).

Table II. Summary of results from rotating disk electrode experiments for the investigated catalysts in 0.1 M $HClO_4$ at 25°C. The *ECSA* was determined form the H_{UPD} region in cyclic voltammetry (20 mV/s) or from the TEM based particle size distribution (using Equation 1), while the mass- and specific activity was determined from O_2 saturated electrolyte at 1600 rpm (anodic going scan, 20 mV/s). The errors correspond to the standard deviation of 3 independent measurements.

Catalyst	Pt/C loading [$\%_{wt}$]	$ECSA_{HUPD}$ [m^2/g_{Pt}]	$ECSA_{TEM}$ [m^2/g_{Pt}]	$i_{0.9\,V}^{mass}$ [A/g]	$i_{0.9\,V}^{spec}$ [$\mu A/cm^2_{Pt}$]	TS [mV/dec.]
Pt/KB_{PO}	20.2	75 ± 6	85	814 ± 40	1076 ± 38	57 ± 2
$Pt/KB(NH_x)_{PO}$	20.3	79 ± 7	87	696 ± 18	878 ± 24	60 ± 1
Pt/KB_{IW}	19.6	70 ± 2	90	336 ± 7	486 ± 14	64 ± 2
Pt/KB_{TKK}	19.3	75 ± 2	99	982 ± 13	1305 ± 27	58 ± 1

200°C, the carbon content increased again, which can be explained by the loss of thermally instable oxygen functional groups like carboxylic acid groups.[20] Additionally, the nitrogen content increased further to about 1$\%_{wt}$, and the XPS data (see blue line in Figure 1) indicates the formation of pyridinic, pyrrolic, and pyridine-*N*-oxide groups which were observed at binding energies of 397–404 eV.[19] Further differentiation and quantification of each type of nitrogen functionality was not performed as it is beyond the scope of this work. However, from the N-content determined by elemental analysis (1.1 ± 0.1%, see Table I) and the external surface area of the modified Ketjenblack (total: 930 m^2/g; external: ≈400 m^2/g), an estimate of the ratio of surface nitrogen atoms to surface carbon atoms can be obtained, assuming a surface concentration of about 65 $\mu mol_C/m_C^2$ (for graphite structures).[21] For this estimation, the external surface area of Ketjenblack was used, as the pore-size analysis from N_2 sorption and evaluation by the QS-DFT method showed a blockage of small pores (< 4 nm) by the surface modification, indicating that only the external surface was NH_x modified. Based on the above assumptions, the ratio of suface nitrogen atoms to surface carbon atoms (N_{surf}/C_{surf}) was in the range of 0.03 (or 3% of a monolayer coverage). Compared to the modification of vulcan carbon, where a coverage of about 7% was estimated,[15] the lower coverage in the case of Ketjenblack might be due to a more limited accessibility of the entire carbon surface during the modification procedure or due to a lower reactivity of its surface. The platinum loading of each catalyst was determined by thermogravimetric analysis and is summarized in Table II. Generally, the Pt weight loading of all catalysts was within 20 ± 1$\%_{wt}$.

Transmission electron microscopy was used to evaluate the Pt particle size distribution and to gain insights into the location of the Pt particle location for the catalysts. Representative micrographs of the in-house made catalysts as well as the commercial catalyst are shown in Figure 2 with their corresponding Pt particle size distribution (insets in Figure 2). Here, N_{total} denotes the total number of counted particles, d_N denotes the number averaged diameter, while d_S is the surface normalized diameter calculated by Equation 1, where l_i represents the particle number and d its diameter.

$$d_S = \frac{\sum_{i=1}^{n} l_i d^3}{\sum_{i=1}^{n} l_i d^2} \quad [1]$$

For the catalysts prepared by the polyol reduction (Pt/KB_{PO} and $Pt/KB(NH_x)_{PO}$), a reasonably narrow distribution of Pt particles over the carbon surface was observed without major particle agglomeration (Figures 2a and 2b), and with similar number averaged particle sizes for the $Pt/KB(NH_x)_{PO}$ catalyst ($d_N = 3.0 \pm 0.5$ nm) and the Pt/KB_{PO} catalyst ($d_N = 2.9 \pm 0.7$ nm). For the catalyst prepared by incipient wetness (Pt/KB_{IW}) and for the commercial catalyst (Pt/KB_{TKK}), the particle size distributions were slightly wider, while both have smaller number-averaged particle sizes of $d_N = 2.2 \pm 0.9$ nm and $d_N = 2.4 \pm 0.7$ nm, respectively. Similarly, the surface averaged Pt particle sizes (d_S) which should be inversely proportional to the electrochemically active surface area (*ECSA*) of the catalysts were also substantially smaller for the catalyst prepared by incipient wetness and for the commercial catalysts (see inset in Figure 2).

When comparing the TEM images obtained for the catalysts made by the polyol method to those obtained for the catalyst made by either the incipient wetness method or the commercial catalyst, differences in the Pt particle location can be discerned. In case of the polyol reduction (Figures 2a and 2b), many Pt particles were found on the edge of the carbon primary particle and not "inside" its projection (circles show examples in Figures 2a and 2b). Although TEM is a 2D technique, one can rationalize that when a Pt particle is observed outside of the carbon primary particle projection, then it must be located on the outside of the carbon particle. When it is within the projection of the carbon primary particle, then it can be either on top or inside the carbon primary particle in the respective image. Clearly, it is not possible to determine the amount of Pt particles inside the carbon primary particle, but rather get an estimate of particles located on or close to the outer surface. A more in depth study of Pt particle distribution by STEM (as used by Park et al.[13]) could unfortunately not be performed for this study, as we did not have access to this technique. Therefore, we could not quantify the Pt particle distribution on/inside the carbon support, but we believe that the here presented TEM images show at least qualitatively that the polyol synthesis results in catalysts with Pt particles deposited preferentially on the exterior surface of the carbon support.

Pt particles at the edge of the carbon support were hardly observed for the commercial catalyst and the one synthesized by the incipient wetness method. A detailed study on the platinum distribution on the primary carbon black particle via STEM analysis by Park et al.[13] showed that about 62% of Pt particles are located within the carbon black for a commercial 30$\%_{wt}$ Pt/KB catalyst (TEC10E30E, TKK), which is very similar to the commercial 20$\%_{wt}$ Pt/KB catalyst used in this study (TEC10E20E, TKK). Based on the above study and the fact that almost no Pt particles were observed on the edge of the carbon black primary particles for both the commercial catalyst (Pt/KB_{TKK}) and the in-house made, incipient wetness based catalyst (Pt/KB_{IW}), it is reasonable to assume that the majority of the Pt particles for these two catalysts are also located inside the carbon particle. In contrast, the catalysts prepared by the polyol reduction method showed a significant amount of platinum particles on the edges of the carbon (examples marked by red circles in Figures 2a and 2b), which suggests a considerable amount of Pt particles to be located on the outside of the carbon black. Based on these observations, a simplified sketch of the platinum particle distribution on the primary carbon black is proposed in Figures 2e and 2f. Although it is impossible to determine the precise three-dimensional distribution of platinum particles on the carbon black from 2D TEM images, a clear difference in catalyst morphology was evident when comparing the TEM images of the commercial catalyst and the catalyst prepared by incipient wetness (Figures 2c and 2d) to the catalysts prepared by the polyol reduction (Figures 2a and 2b). However, no relevant difference in morphology was observed in the TEM images for the Pt particles deposited on either as-received or NH_x modified Ketjenblack by the polyol synthesis route. As will be shown later, the electrochemical activity and performance characteristics of the different catalysts are quite consistent with the differences in Pt location proposed in Figures 2e and 2f.

The observed differences in Pt location of the in-house made catalysts all prepared on the same support must be due to the different synthetic procedures which are sketched in Figure 3. In the case of the polyol reduction, the platinum salt was dissolved at a rather low concentration (1.3 $mmol_{Pt}/l$) in ethylene glycol which served as the solvent and reducing agent. When the temperature was reached at which the reduction starts rapidly, nucleation of Pt particles will

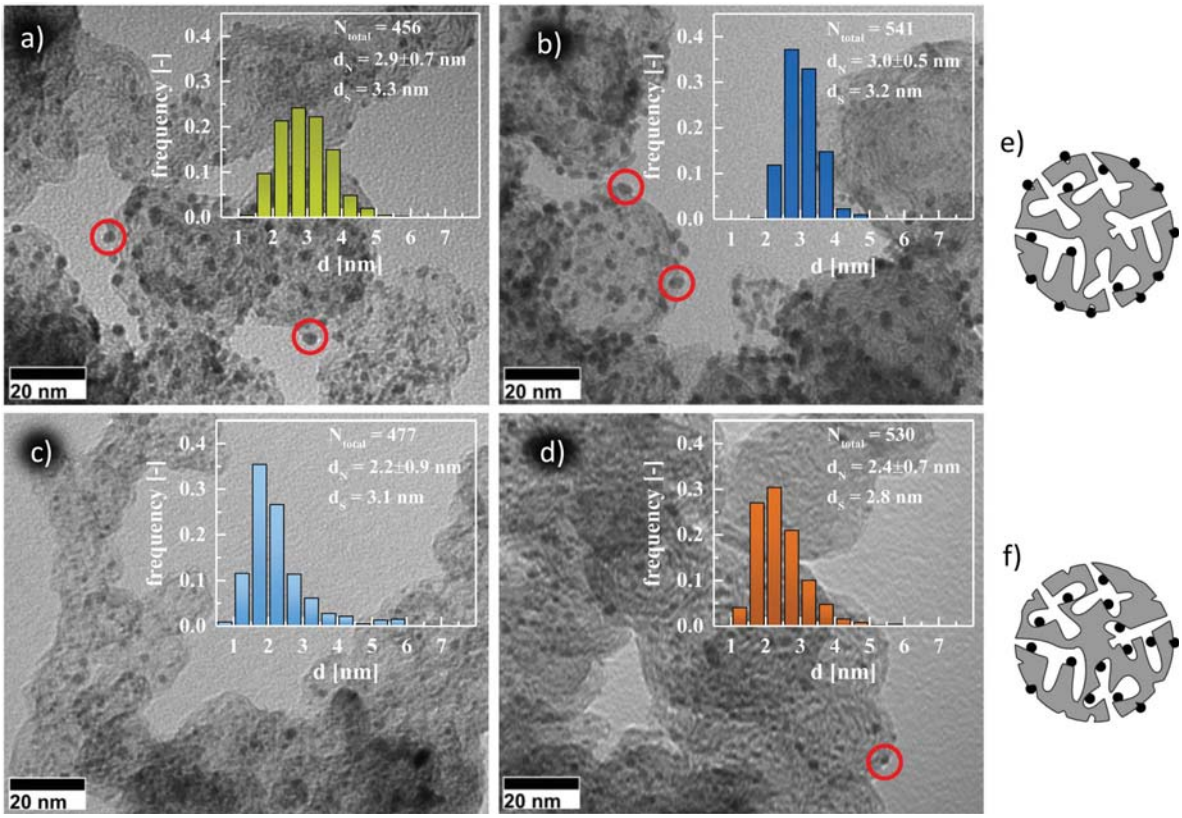

Figure 2. TEM micrographs and the corresponding particle size distribution for the various catalysts: (a) Pt/KB_{PO}; (b) $Pt/KB(NH_x)_{PO}$; (c) Pt/KB_{IW}; and, (d) Pt/KB_{TKK}. d_N denotes the number averaged diameter and their corresponding standard deviation, whereas d_S denotes the surface normalized diameter calculated by Equation 1. Simplified schematic representation of primary carbon particle (gray) with Pt nanoparticles (black) deposited preferentially on (e) the outside of the carbon support (hypothesized to be the case for Pt/KB_{PO} and $Pt/KB(NH_x)_{PO}$) and (f) on the inside of the carbon support (hypothesized to be the case for Pt/KB_{IW} and Pt/KB_{TKK}).

occur throughout the solution, but since the concentration of platinum ions inside the pores of the carbon black was very small and since the platinum salt diffusion into the pores was restricted, growth of Pt particles proceeded preferentially on the outer surface of the carbon black and in the free bulk solution. Particles formed in solution will ultimately deposit on the outer surface as they cannot anymore penetrate into the pores of the carbon black (this is sketched in Figure 3A). On the other hand, in case of the incipient wetness synthesis, a highly concentrated solution of platinum ions (≈230 $mmol_{Pt}/l$) was absorbed into the void volume of the carbon black pores during impregnation. Upon reduction, platinum particles nucleated evenly on the entire carbon surface which was covered with the Pt salt (Figure 3B). As a substantial volume fraction of Ketjenblack consists of small pores (a lot of it being of course internal surface),[10,22] which can be filled with the concentrated solution of platinum salt during impregnation, a considerable amount of Pt particles formed inside these pores similarly to what was observed for ordered mesoporous carbon supports with similar pore sizes.[23,24]

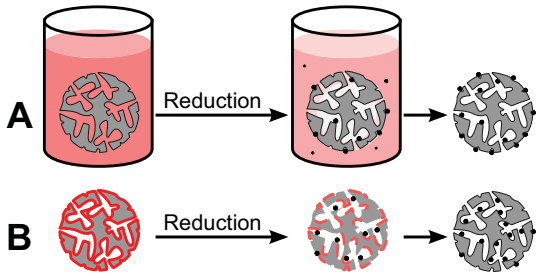

Figure 3. Simplified schematic representation of the synthetic methods and the time dependent formation of Pt particles; red color intensity depicts Pt precursor concentration. A) Reduction of a highly diluted Pt precursor in ethylene glycol in the polyol method, with a formation of Pt nanoparticles preferentially on the outside of the carbon surface and in the solution. B) Incipient wetness method, in which the carbon support is impregnated with a highly concentrated Pt precursor solution, so that a high concentration of Pt precursor is present inside the pores, leading to more particles deposited inside the carbon.

ECSA, ORR activity, and H_2/O_2 MEA performance.—Thin-film rotating disk electrode measurements were conducted on all catalysts to determine the electrochemically active surface area (*ECSA*) and the activity for oxygen reduction. Catalyst thin-films were prepared without the use of any binder (like Nafion) to avoid catalyst poisoning and thus reveal the true ORR activities in the absence of poisoning by ionomer.[25] Table II summarizes the results from RDE experiments for the investigated catalysts. The *ECSA* values obtained by cyclic voltammetry were rather similar for all catalyst, ranging between ≈70–79 m^2/g_{Pt}. The fact that these values are roughly 10–25% lower than the values one would estimate from the TEM measurements ($ECSA_{TEM}$) using Equation 1, is consistent with other literature reports.[26] The obtained mass and specific activities were also in good agreement with the literature for Nafion-free films.[25] Kinetic parameters of all catalysts are very comparable, except for Pt/KB_{IW} that

Table III. Cathode Pt loadings (L_{Pt}) of the ≈20 $\%_{wt}$ Pt/KB catalysts (s. Table II), electrochemically active surface areas (*ECSA*) determined from the H_{UPD} region in cyclic voltammetry, and ORR mass activity ($i^{mass}_{0.9\,V}$) determined at 0.9 V at the experimentally used conditions (80°C, 100% *RH*, H_2/O_2 (2000/5000 nccm), 170 kPa_{abs}), calculated as well for 101 kPa_{abs} O_2 ($i^{mass\,*}_{0.9\,V}$). The mass activity and Tafel slope (TS) were determined from the polarization curves after correction for the *HFR*, the proton conduction resistance in the catalyst layer, the H_2 crossover, and the shorting current (these corrected data are shown in Figure 4b). The specific activity ($i^{spec}_{0.9\,V}$) was calculated from the mass activity and the corresponding *ECSA* for each electrode. The variation represents the mean absolute deviation between two independent measurements.

Catalyst	L_{Pt} [$\mu g/cm^2_{geo}$]	*ECSA* [m^2/g_{Pt}]	$i^{mass}_{0.9\,V}$ [A/g]	$i^{mass\,*}_{0.9\,V}$ [A/g]	$i^{spec}_{0.9\,V}$ [$\mu A/cm^2_{Pt}$]	TS [mV/dec]
Pt/KB_{PO}	62 ± 1	69 ± 6	220 ± 11	175 ± 9	318 ± 11	76 ± 1
$Pt/KB(NH_x)_{PO}$	63 ± 2	66 ± 2	161 ± 2	128 ± 1	245 ± 10	76 ± 1
Pt/KB_{IW}	64 ± 1	79 ± 1	249 ± 1	198 ± 1	314 ± 4	85 ± 1
Pt/KB_{TKK}	62 ± 2	83 ± 1	372 ± 29	296 ± 23	450 ± 37	88 ± 2

has a slightly higher Tafel slope in addition to a lower ORR activity. Although the synthesis method used to prepare Pt/KB_{IW} was found to produce a catalyst with similar morphology as Pt/KB_{TKK} (determined by TEM), the catalytic properties of the former were significantly different from those of Pt/KB_{TKK}. These differences in RDE results may arise from different catalyst layer quality on the glassy carbon, as high-quality film preparation was challenging for the Pt/KB_{IW} catalyst. This difficulty may be explained by a less polar catalyst surface, resulting from the heat-treatment in reductive atmosphere during the preparation of Pt/KB_{IW}. Additional support to the hypothesis of low film quality is given by the fact that the *ECSA* is very similar for all catalyst, while only the ORR kinetic parameters are significantly worse. This observation has been directly attributed to a less homogeneous catalyst film by other researchers.[27]

5 cm^2 MEAs were fabricated to determine the influence of the catalyst preparation method on its specific properties like the *ECSA*, the ORR activity, and the performance at high current density in single-cell PEM fuel cell measurements. The cathode catalyst layers of all MEAs had very similar loadings of 62–64 $\mu g/cm^2_{MEA}$ to ensure comparability between measurements (for details see Table III), while the anode Pt loading was fixed at about 100 $\mu g_{Pt}/cm^2_{MEA}$. The electrochemically active surface area determined from H_{UPD} for the Pt/KB_{IW} and Pt/KB_{TKK} was found to be ≈79–83 m^2/g_{Pt} (see Table III). These values are consistent with previously reported values for high surface area carbon black supports.[13,28,29] Significantly lower *ECSA* values of ≈66–69 m^2/g_{Pt} were found for the catalysts prepared by the polyol method. This is another indication that this synthesis method results in a larger fraction of Pt particles on the exterior surface of the carbon support particles, where they are in intimate contact with the ionomer resulting in lower *ECSA* values due to ionomer poisoning.[25] The ORR mass activity trend with respect to the different catalyst preparation procedures which affect the location of the Pt particles on the primary carbon particle was also consistent with the observed *ECSA* trends: catalysts synthesized by the polyol method showed a lower ORR mass activity, consistent with the poisoning of the ORR when Pt nanoparticles are in more intimate contact with ionomer.[25] Furthermore, the

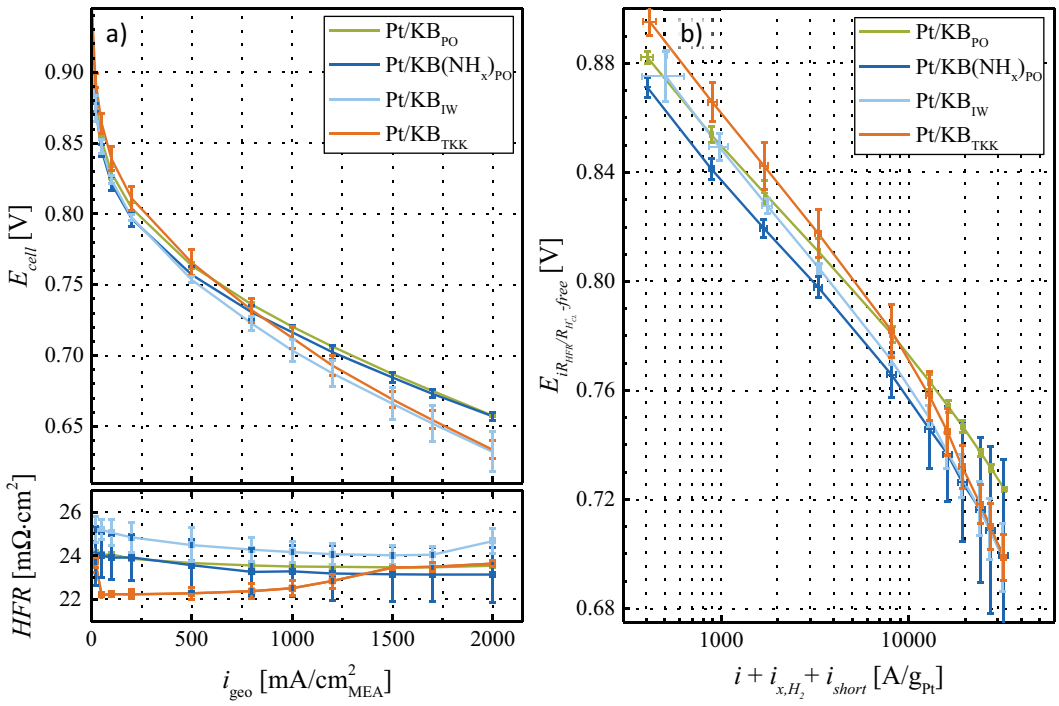

Figure 4. a) Uncorrected H_2/O_2 polarization curves (80°C, 100% *RH*, H_2/O_2 (2000/5000 nccm), 170 kPa_{abs}) for the different catalysts with ultra-low cathode Pt loading (62–64 $\mu g_{Pt}/cm^2_{MEA}$, see Table III) and the corresponding high frequency resistance (R_{HFR}). b) Performance curves normalized to the Pt loading and corrected for the *HFR* (R_{HFR}), the effective proton conduction resistance of the cathode catalyst layer ($R^{eff}_{H^+,cath}$) as well as H_2 crossover (i_{x,H_2}) and shorting currents. The anode platinum loading was ≈100 $\mu g_{Pt}/cm^2_{MEA}$ for all MEAs. The error bars correspond to the mean absolute deviation between two independent measurements.

low specific activity of the Pt/KB$(NH_x)_{PO}$ catalyst (245 $\mu A/cm^2_{Pt}$; see Table III) was nearly as low as that of an identically prepared $\approx 20\%_{wt}$ Pt catalyst on a Vulcan support (see Pt/V-NH_x with 200 $\mu A/cm^2_{Pt}$ in Ref. 15) tested under the same conditions and at the same I/C ratio, which provides further evidence for our claim that most of the Pt particles are deposited on the external KB carbon surface in the polyol synthesis process.

Figure 4 shows the uncorrected polarization curves in H_2/O_2 configuration at 170 kPa_{abs} for all catalysts (Figure 4a) as well as their corresponding Tafel plots after correction for the *HFR*, the effective proton conduction resistance of the cathode catalyst layer ($R^{eff}_{H^+,cath}$) the H_2-crossover (≈ 4 mA/cm^2_{MEA}) and the shorting current (Figure 4b), analogous to the procedure outlined in Ref. 15. As platinum inside the pores of a carbon black primary particle has no or only poor contact with ionomer,[30–32] it exhibits a higher mass activity due to the absence of poisoning effects.[25] For this reason, Pt/KB_{IW} and Pt/KB_{TKK} showed a mass activity of 249 ± 1 and 372 ± 29 A/g, while the Pt/KB_{PO} and Pt/KB$(NH_x)_{PO}$ catalysts synthesized by the polyol method had lower mass activities of 220 ± 11 and 161 ± 2 A/g, respectively. The lower mass activity of the latter most likely arises from a better ionomer distribution of the KB(NH_x) support as shown in a previous publication,[15] where we argued that an increased interaction of the ionomer with the modified carbon black surface[33] would lead to a more homogeneous ionomer distribution, reaching more platinum particles and thus lowering their ORR mass activity. In addition, part of this effect may also derive from a somewhat larger fraction of Pt being deposited on the outer surface of the NH_x-modified Ketjenblack due to a stronger Pt/support interaction during the deposition of Pt onto the surface-functionalized Ketjenblack.[34] The difference in mass activity between Pt/KB_{IW} and Pt/KB_{TKK} could be rationalized by a non-optimized synthetic method for the incipient wetness based catalyst, which had the broadest particle size distribution and largest particles.

From the H_2/O_2 polarization curves, it is also evident that the different catalyst preparation methods lead to different performance characteristics in the low and high current density region (see Figure 4a): while the catalysts prepared by the polyol method showed a lower cell voltage in the low current density region (consistent with their lower mass activity), they significantly outperformed the Pt/KB_{IW} and Pt/KB_{TKK} catalysts at high current density. For the latter two, the polarization curves appeared to be affected by stronger mass transport resistances at high current density, even in pure oxygen. This limitation is also reflected in Figure 4b, where a substantial deviation from a straight Tafel line is observed for these catalysts at high current density, while the catalysts prepared by the polyol method did not deviate much from a straight line over the entire current density range. Additionally, their Tafel slope of 76 mV/dec. (determined in the current density range of 50–500 mA/cm^2_{MEA}; see Table III) was much closer to the expected value of 70 mV/dec. (at 80°C),[35] indicating an optimized electrode where all non-kinetic limitations can be accounted for quantitatively.[15] On the other hand, the higher Tafel slope of around 85 mV/dec. for the Pt/KB_{IW} and Pt/KB_{TKK} catalysts points toward a non-optimized electrode or additional transport losses.[29] As will be explained in detail in the following, the electrode structure and ionomer distribution was homogeneous for all electrodes, so that we attribute the observed Tafel slope and performance limit at high current density to the catalyst morphology, namely the predominant location of Pt at the external surface of the carbon support or within the carbon nanopores.

The observed differences in mass activity and high current density performance have been commonly reported for Ketjenblack supported catalysts compared to Vulcan supported catalysts, and have been mainly attributed to differences in the support structure, especially support surface area and nanopore size distribution.[13,12] As we used the same carbon support for all catalysts, it is clear that an additional factor which must be considered, is the synthesis method of the catalyst, as it is able to control the fraction of Pt particles which are deposited at the external support surface compared to those deposited within the carbon nanopores. Thus, even on a conventional

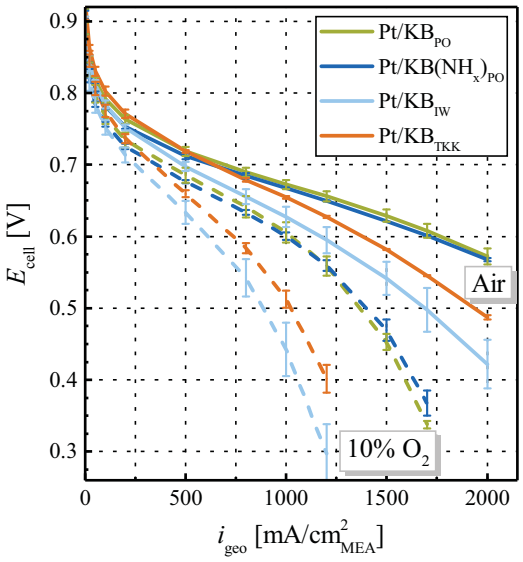

Figure 5. Polarization curves in air (solid lines) and 10% O_2 in N_2 (dashed lines) at 80°C, 100% *RH*, 2000/5000 nccm (A/C) at 170 kPa_{abs} for the different catalysts with a cathode loading of 62–64 $\mu g_{Pt}/cm^2_{MEA}$ (see Table III) and anode loadings of ≈ 100 $\mu g_{Pt}/cm^2_{MEA}$. Error bars represent the mean absolute deviation from two independent measurements.

Ketjenblack support with a large nanopore volume, the polyol synthesis method can lead to a predominant deposition of Pt particles on the external carbon support surface, so that the resulting Pt/KB catalyst shows a similar current-voltage profile as a catalyst supported on a more solid, Vulcan-type carbon. This finding is in excellent agreement with the studies from Kongkanand et al.[11] They showed that the carbon support surface area (particularly the fraction of surface in micropores) and the location of the Pt particles on the primary carbon particles can significantly influence the local O_2 mass transport resistance and in turn the performance of the MEA. Catalysts with Pt particles preferentially located on the outside of the carbon black support (Pt supported on a low surface area, solid carbon black, referred to as GrC) showed significantly better performance at high current density compared to catalysts with Pt particles located inside the carbon black support (Pt supported on a high surface area carbon black, referred to as HSC). In a recent study they showed that by maximizing the nanopore volume of the support in the 4–7 nm range, the high current density performance can be further improved, rationalized by striking the best balance between reduced ionomer poisoning of Pt particles within these pores while minimizing the transport path length for protons and oxygen to these near surface pore domains.[12]

MEA performance with H_2/air and in H_2/10% O_2.—To further visualize the high current density performance difference between catalysts prepared by the incipient wetness method and the polyol reduction method, polarization curves in air and 10% O_2 (in N_2; to simulate conditions at the cathode outlet of a PEMFC stack operated at an air stoichiometry of ≈ 1.75) are shown in Figure 5. Again, it was evident that the Pt/KB_{TKK} catalyst showed the highest cell voltage at low current density – consistent with its highest mass activity – while the high current density performance in air (solid lines in Figure 5) was significantly inferior to the catalysts prepared by the polyol method. This difference was even more pronounced for polarization curves in 10% O_2 (dashed lines in Figure 5), pointing toward a severe mass transport limitation for Pt/KB_{IW} and Pt/KB_{TKK} catalysts. As suggested by the TEM micrographs, a substantial fraction of Pt particles is located outside of the carbon black primary particle for the catalysts made by the polyol synthesis method (supported by the lower ORR

activity of these catalysts). Assuming that the pores would be ionically connected with the ionomer by absorbed water, platinum particles which are not poisoned by ionomer can contribute to the ORR reaction at low current density, i.e., in the region where the mass activity is determined. At high current densities, however, the transport of reactants (O_2 and H^+) and the removal of produced water becomes increasingly important, resulting in increased transport resistances to platinum particles located inside the pores and, thus, to the poor high current density performance.

On the contrary, much superior high current density performance was observed for the catalysts synthesized by the polyol method: independent of the surface modification of the carbon black support, Pt/KB_{PO} and $Pt/KB(NH_x)_{PO}$ showed almost identical current-voltage profiles. While the former had a ≈1.4 times higher ORR mass activity (see Table III), its ≈10 mV lower ORR overpotential (assuming an intrinsic Tafel slope of 70 mV/dec.) did not play a major role at high current densities, where performance is controlled by transport resistances rather than by kinetics. It is also noteworthy that the H_2/air and H_2/10% O_2 high current density performance of the polyol synthesized Ketjenblack supported catalysts was even slightly better than that of the polyol synthesized catalyst supported on NH_x functionalized Vulcan carbon.[15] Based on the evidence presented so far, we conclude that the superior high current density performance of the Pt/KB_{PO} and $Pt/KB(NH_x)_{PO}$ catalysts in both air and 10% O_2 is caused by a predominant deposition of platinum particles on the external surface of the carbon support in the polyol synthesis method. In summary, the inferior low current density and superior high current density performance of the polyol synthesized catalysts (Pt/KB_{PO} and $Pt/KB(NH_x)_{PO}$) reflects that of Pt catalysts supported on Vulcan supports, while that of the commercial and the incipient wetness synthesized catalysts (Pt/KB_{TKK} and Pt/KB_{IW}) reflects that of typical catalysts supported on Ketjenblack supports (see Figure S1 in Ref. 12), again emphasizing that the synthesis method can affect the location of the deposited Pt particles and that this is not solely a function of the carbon support.

A general idea about the ionomer distribution in the electrodes can be deduced from proton resistivity measurements via impedance spectroscopy according to Liu et al.[9] Figure 6 depicts the catalyst layer proton resistivity for all catalysts at different relative humidities. At high relative humidity (100% *RH*), the difference in proton resistivity between all catalysts was insignificant, whereby it must be noted that the error of measurement was relatively large (reflected by the error bars), due to the difficulty of fitting a transmission line model to the impedance data when the proton conduction resistance is very low. At lower relative humidities where the measurement error is reduced due to the larger proton conduction resistance, the catalysts prepared by the polyol reduction method showed a ≈1.5–2 times lower proton resistivity compared to Pt/KB_{IW} and Pt/KB_{TKK}. This difference may point toward a better ionomer distribution for the catalysts prepared by the polyol synthesis method. Additionally, a beneficial effect on the proton resistivity was observed for the surface modification by NH_x groups, which is consistent with our previous study on the modification of a Vulcan carbon support.[15]

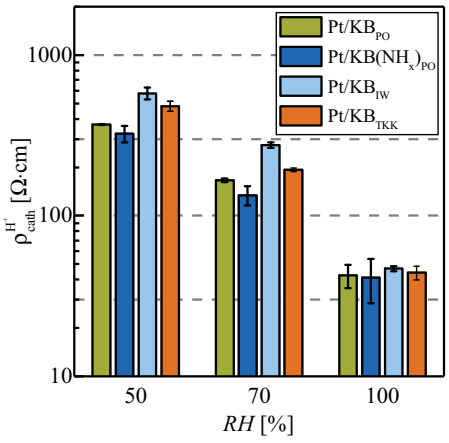

Figure 6. Cathode catalyst layer proton resistivity, $\rho^{H^+}_{cath}$, determined from impedance spectroscopy at 50, 70 and 100% *RH*. Error bars represent the mean absolute deviation from two independent measurements.

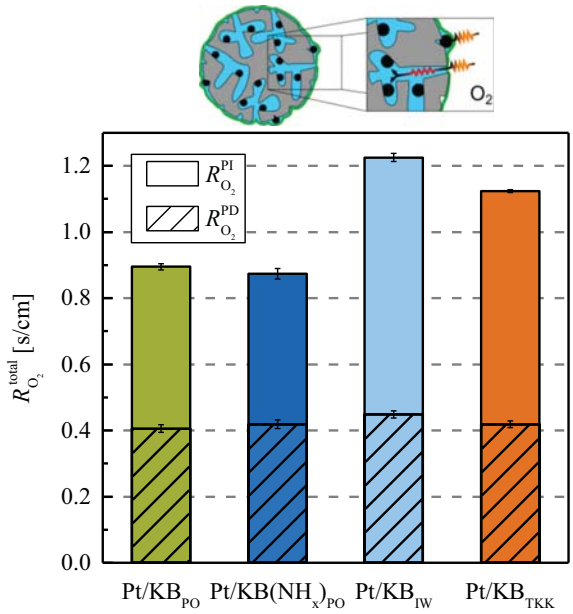

Figure 7. Total oxygen mass transport resistance divided into pressure dependent transport resistance ($R^{PD}_{O_2}$, hatched bar) and pressure independent transport resistance ($R^{PD}_{O_2}$, open bar) determined from limiting current measurements at 80°C, 70% *RH*, differential-flow (2000/5000 nccm) and 170, 270, 350, 500 kPa_{abs} at various O_2 concentrations. Simplified sketch depicting the different transport limitations depending on the location of the Pt particles on the carbon black support with additional resistance for the Pt particles inside the pore.

Oxygen mass transport resistance.—To evaluate whether the observed performance drop at high current density can be attributed to oxygen mass transport, the total oxygen mass transport resistance is shown in Figure 7, divided into a pressure dependent, $R^{PD}_{O_2}$ (hatched bar), and pressure independent, $R^{PI}_{O_2}$, resistance determined from limiting current measurements.[36] According to the limiting current method developed by Baker et al., we used a low relative humidity of 70% *RH* to avoid measurement artefacts due to condensation of water in the diffusion medium at high current density,[36] similar to what was done by Owejan et al.[37] In addition, we conducted the same limiting current experiments at 100% *RH* to exclude artefacts of insufficient proton conductivity at dry conditions. For all tested catalysts, no significant differences in total oxygen mass transport resistance were found at the two relative humidities (< 5% deviation), indicating that neither proton conductivity nor water condensation in the GDL/MPL or the electrode were leading to measurement artefacts in the tested *RH* range. Similar results were also obtained by Oh et al., who investigated the oxygen transport resistance from 30–90% *RH*.[38] Analogous with the works of Baker et al.[36] and Owejan et al.,[37] we report the oxygen mass transport resistance determined at 70% *RH* and use it later for the corrections of oxygen transport related voltage losses.

As one would expect, the pressure dependent transport resistance, which is attributed to intermolecular gas diffusion, was essentially identical for all measurements, as the same testing hardware and GDL materials were used throughout the experiments. The pressure independent resistance however, which describes either Knudsen diffusion contributions in the microporous layer, diffusion through liquid water or through the Pt/ionomer interface,[36,37] varied significantly for cathodes based on different types of catalysts. For the catalysts prepared by the polyol method, the total transport resistance was identical within the error of measurement (0.88 ± 0.02 s/cm), while Pt/KB$_{IW}$ and Pt/KB$_{TKK}$ showed considerably higher $R_{O_2}^{total}$ values (1.22 ± 0.01 and 1.12 ± 0.01 s/cm, respectively). In contrast to our previous study on the surface functionalization of a Vulcan carbon support with NH$_x$,[15] we found no significant influence of the NH$_x$ carbon surface modification on the mass transport resistance in the case of the here used Ketjenblack support at the same I/C mass ratio of 0.65/1. The rationalization for this is that the ionomer film at this I/C ratio is already very thin on the high surface area Ketjenblack support, as a significant fraction of the ionomer is being absorbed into the carbon nanopores (≈60% for an I/C mass ratio of 0.6/1[9]). The resulting ≈1.7 times thinner ionomer coverage on the outer surface of the Ketjenblack compared to the Vulcan carbon support may thus be so thin, that even a slightly inhomogeneous ionomer distribution on the carbon surface and/or in the electrode does not any more result in significant differences in the local oxygen transport resistance to the Pt surface.

In the case of Pt/KB$_{IW}$ and Pt/KB$_{TKK}$, the pressure independent oxygen mass transport resistance was substantially higher compared to the in-house made catalysts by the polyol reduction. Considering their morphological differences suggested by TEM and ORR mass activity measurements, these results clearly support our hypothesis for their inferior high current density performance, namely that it is due to the predominant location of Pt particles within the carbon black nanopores, leading to a higher oxygen transport resistance.[11–13] The latter is ascribed to the long, local diffusion pathways for oxygen through the nanopores – particularly aggravated when nanopores are (partially) filled with liquid water (see sketch on top of Figure 7) – and manifests itself in additional voltage losses at high current density. On the other hand, when the platinum particles are preferentially located on the external surface of the support, either controlled by the synthetic method as shown here or by the type of carbon black support,[11–13] the oxygen transport resistance is lower and, consequently, the performance at high current density is superior.

Voltage loss analysis.—To quantify the agreement between a kinetically predicted polarization curve and the measured H$_2$/air polarization curves (from Figure 5, solid lines) after correction for all known transport losses, a voltage loss analysis was performed as described in Ref. 15. Figure 8 shows the theoretical ORR curves (dashed lines; based on the mass activities given in Table III and assuming an intrinsic Tafel slope of 70 mV/dec.) for all catalysts compared to H$_2$/air polarization curves after correction for all measurable losses (solid lines), namely for the ohmic losses (i.e., the *HFR*), the effective proton transport resistance within the electrode ($R_{H^+,cath}^{eff}$), and the total oxygen mass transport resistance ($R_{O_2}^{total}$); for details see Ref. 15. The lower graph in Figure 8 depicts the difference between the kinetically predicted ORR performance (dashed lines) and the measured H$_2$/air polarization curves after the above described corrections (solid lines), which is equal to the unaccounted voltage losses in the electrode. A striking difference between the two types of catalysts becomes evident. While the unaccounted voltage losses for the catalysts prepared by the polyol synthesis method (Pt/KB$_{PO}$ and Pt/KB(NH$_x$)$_{PO}$) were identical and amount to ≈50 mV at 2 A/cm$^2_{MEA}$ (essentially identical to what we had found for a Pt/V-NH$_x$ catalyst[15]), the Pt/KB$_{IW}$ and Pt/KB$_{TKK}$ catalyst showed unexplained voltage losses of about 200 mV and 150 mV at 2 A/cm$^2_{MEA}$, respectively.

Thus, it is quite clear that catalysts with a large faction of Pt particles located on the external surface of the carbon black support (Pt/KB$_{PO}$ and Pt/KB(NH$_x$)$_{PO}$) show low unaccounted voltage losses

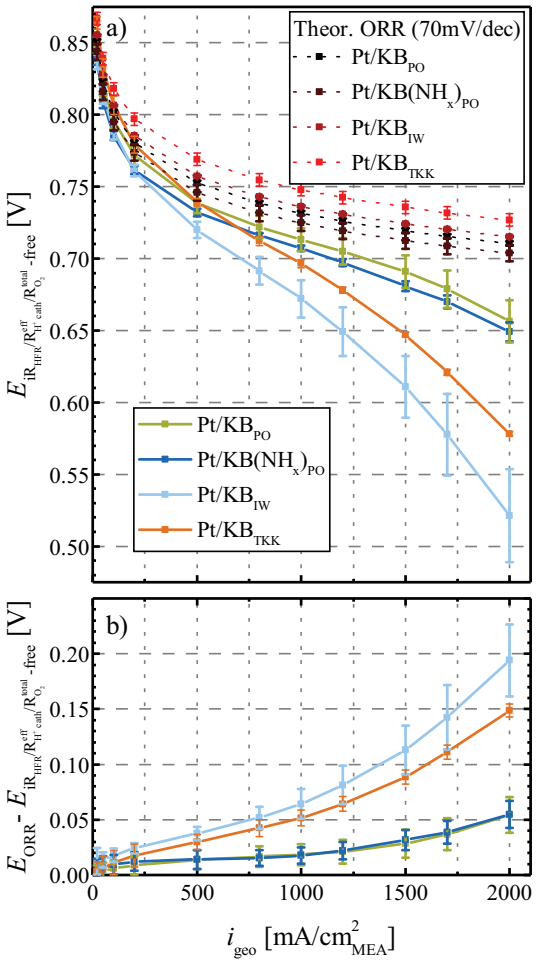

Figure 8. a) solid lines: polarization curves (H$_2$/air – differential-flow, 80°C, 100% *RH*, 170 kPa$_{abs}$) corrected by the *HFR* (R_{HFR}), the effective proton conduction resistance of the catalyst layer ($R_{H^+,cath}^{eff}$), and the total oxygen mass transport resistance ($R_{O_2}^{total}$); dotted lines: purely ORR kinetics limited polarization curves (black/red lines) determined from Equation 5 in Ref. 15 for the effective O$_2$ partial pressure of 25.8 kPa under these conditions. b) Unaccounted voltage losses obtained from the difference between the purely ORR kinetics limited performance (dotted lines in a) and the fully corrected H$_2$/air polarization curves (solid lines in a) for Pt/KB$_{PO}$, Pt/KB(NH$_x$)$_{PO}$, Pt/KB$_{IW}$, and Pt/KB$_{TKK}$.

in addition to their superior high current density H$_2$/air performance. This demonstrates that the morphology of the carbon black is not the only factor which controls high current density performance (as in previous studies),[11–13] as long as the catalyst synthesis method leads to a preferential deposition of Pt particles on the external surface of the carbon black. Unfortunately, this analysis also makes it evident that the extent of unaccounted voltage losses (Figure 8b) in a cathode catalyst layer critically depends on the type of catalyst and is never zero. The origin of this discrepancy is not clear, but it seems reasonable to assume that it is at least in part related to an inherent problem of the determination of the oxygen mass transport resistance by limiting current measurements for high surface area carbons, where platinum is found inside the pores. While it cannot be excluded that the unaccounted voltage losses originate from a not fully optimized electrode or from more complex ORR kinetics,[39] the inaccurate determination of the oxygen mass transport resistance appears to be the most likely explanation.

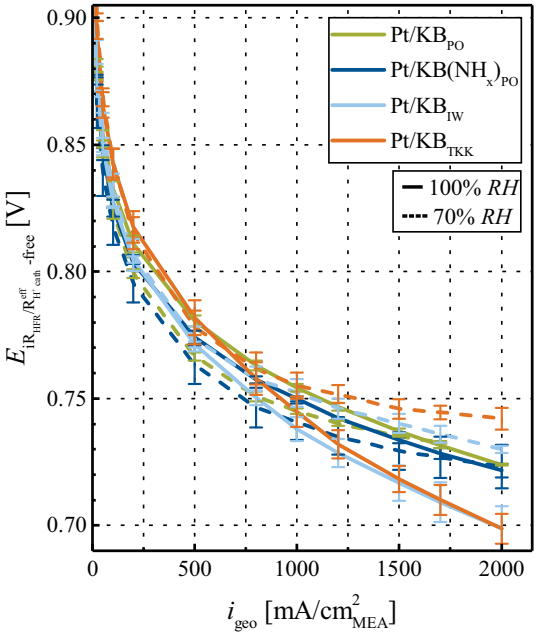

Figure 9. Differential-flow polarization curves in H_2/O_2 at 170 kPa_{abs}, 80°C, 100% *RH* (solid lines) and 70% *RH* (dashed lines) after correction of the measured cell voltage by the *HFR* (R_{HFR}) and catalyst layer effective proton conduction resistance ($R^{eff}_{H^+,cath}$). Error bars correspond to the mean absolute deviation from two independent measurements.

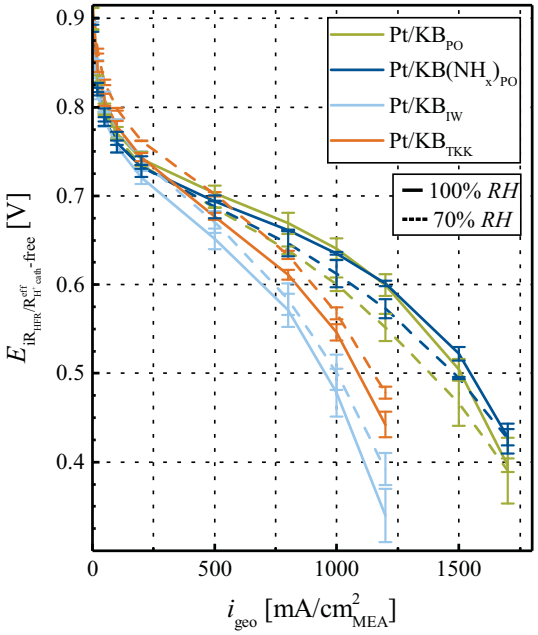

Figure 10. Differential-flow polarization curves in H_2/10% O_2 (balance N_2) at 80°C, 170 kPa_{abs}, 100% *RH* (solid lines) and 70% *RH* (dashed lines) for all catalysts after correction of the cell voltage by the *HFR* (R_{HFR}) and catalyst layer effective proton conduction resistance ($R^{eff}_{H^+,cath}$). Error bars correspond to the mean absolute deviation of two independent measurements.

Identification of performance limitations.—To gain further insights into the mass transport properties of the different types of catalysts, we investigated the effect of the relative humidity on performance, first with pure O_2 and then with 10% O_2 in N_2. First of all, when reducing the relative humidity from 100% to 70%, the *HFR* increases by ≈10 mΩ · cm^2 (from about 23–25 mΩ · cm^2 at 100% *RH* (see lower panel of Figure 4a) to 32–35 mΩ · cm^2 at 70% *RH*), which equates to approximately a doubling of the membrane resistance for the typical contact resistance of 15 mΩ · cm^2 in our setup. This ≈2-fold increase in membrane resistance is in good agreement with the reported changes of the bulk conductivity of a Nafion type membrane upon decreasing the relative humidity from 100% to 70% *RH*.[40] At the same time, the proton sheet resistivity in the cathode catalyst layer increased by ≈3-fold for the polyol synthesized catalysts and ≈5–7 fold for the other two catalysts (see Figure 6), reasonably consistent with the reported ionomer tortuosity of ≈2–3 in an electrode composed of a Ketjenblack supported catalyst and with an ionomer volume fraction of $\varepsilon_{ionomer} \approx 0.16$ (based on Equation 5 and Figure 9a in Ref. 41).

Figure 9 shows the *HFR* and $R^{eff}_{H^+,cath}$ corrected differential-flow oxygen polarization curves recorded at 100% (solid lines) and 70% *RH* (dashed lines) for all catalysts. H_2/O_2 polarization curves corrected this way would be expected to yield superimposing lines for both 70 and 100% *RH*, as the oxygen transport resistance in the absence of strong film diffusion resistances through a water or ionomer layer should be negligible in pure O_2. Within an error of ≈10 mV, this was indeed the case for the polyol synthesized catalysts (compare solid/dashed dark blue or green lines in Figure 9), where Pt particles are believed to be mostly located on the external carbon surface. However, for the Pt/KB_{IW} and Pt/KB_{TKK} catalysts (orange and light blue lines in Figure 9) with Pt particles mostly located in carbon nanopores, the corrected cell voltage increased with decreasing *RH* by ≈35 and ≈45 mV, respectively. This can be rationalized by a significant oxygen transport resistance from the exterior carbon surface to the Pt particles located in carbon nanopores, assuming that at 100% *RH* these pores are flooded with liquid water, but at 70% *RH* have a lower water content and a concomitantly lower local oxygen transport resistance. This indeed is consistent with the observed inferior high current density performance of the Pt/KB_{IW} and Pt/KB_{TKK} catalysts in pure O_2 compared to that of the Pt/KB_{PO} and Pt/KB(NH$_x$)$_{PO}$ catalysts (see Figure 4a).

To identify the interplay of O_2 mass transport resistance phenomena and relative humidity, differential-flow polarization curves in H_2/10% O_2 (balance N_2) were recorded at 70% and 100% *RH* and are shown in Figure 10 after the correction of cell voltage by the *HFR* (R_{HFR}) and the effective proton conduction resistance in the catalyst layer ($R^{eff}_{H^+,cath}$). In contrast to the data shown in Figure 9, the O_2 transport resistance is very important at 10% O_2 (see Figure 5) and thus enables further insight into transport-related phenomena of the different catalysts.

Analogous to the phenomenon observed in pure O_2, both the Pt/KB_{IW} and the Pt/KB_{TKK} catalysts showed a similar increase in the *HFR* and $R^{eff}_{H^+,cath}$ corrected performance as the relative humidity is reduced from 100 to 70% (see Figure 10). This again was consistent with the above proposed decrease of the local oxygen transport resistance to Pt located in nanopores as the relative humidity is decreased.

On the other hand, the corrected cell voltage in 10% O_2 of the Pt/KB_{PO} and Pt/KB(NH$_x$)$_{PO}$ catalyst based MEAs clearly decreased with decreasing *RH* (see Figure 10), which is contrary to what was observed with pure O_2 (see Figure 9). These results are unexpected, as differences in ionic conductivity should be accounted for by the *HFR* and $R^{eff}_{H^+,cath}$ correction. Unfortunately, at this point we can only conclude that not all resistances are captured quantitatively by the here used O_2 and H^+ transport resistance measurements and that further work is needed to understand the *RH* dependence of these catalysts where Pt is located predominantly on the external carbon support surface.

Conclusions

The effect of the synthesis method for the deposition of Pt nanoparticles on a high surface area Ketjenblack carbon support with respect to the *ECSA*, the ORR mass activity, and the fuel cell performance of the resulting catalysts was investigated. For catalysts prepared by a polyol synthesis method, strong evidence is supported that Pt particles were predominantly deposited on the external Ketjenblack support surface, as indicated by TEM images and by an analysis of the ORR activity. On the other hand, the same analysis suggested that catalysts prepared by an incipient wetness synthesis method as well as a commercial Pt/KB catalyst are characterized by a predominant location of Pt particles within the carbon nanopores.

The catalysts prepared by the polyol reduction showed superior high current density performance, but their ORR mass activity was comparatively low. In contrast, the catalysts with Pt particles located predominantly in carbon nanopores showed a higher ORR mass activity but poor high current density performance due to mass transport limitations. This trend has commonly been observed when comparing Vulcan supported catalysts (behaving like our polyol synthesized catalysts) with Ketjenblack supported catalysts and was attributed to differences in Pt particle location. Here we have shown that the Pt particle location on a given carbon support can also be controlled by the synthesis method. Thus, by tailoring the synthetic method so that Pt particles were deposited predominantly on the external carbon surface, a catalyst with low oxygen mass transport resistance and good high current density performance can be obtained; for these polyol synthesis based catalysts supported on Ketjenblack (often referred to as porous carbon), the unaccounted losses in a voltage loss analysis were minimized and are similarly low as for catalysts based on a Vulcan carbon support (often referred to as solid carbon). When Pt is predominantly located inside the carbon pores, a lower O_2 transport resistance, hence better performance at high current density is observed at 70% compared to 100% *RH* (after correction of increased ionic resistances), which points toward an additional O_2 transport resistance from (partially) water filled carbon pores at fully humidified conditions.

In summary, a catalyst should exhibit most Pt particles on the outer surface of the carbon black support to enable high current density operation with low mass transport related losses in addition to a small fraction of platinum particles shielded inside the pores from ionomer poisoning for high mass activity.

Acknowledgments

This work has been supported by Greenerity GmbH and the German Federal Ministry of Economy (BMWi project support number 03ET2058C) within the HyMotion5 research collaboration. We thank Matthias Binder, Christian Eickes, Peter Suchsland, and Jozsef Speder from Greenerity GmbH for their valuable and critical discussion of the here presented results.

ORCID

Gregor S. Harzer https://orcid.org/0000-0002-1830-1931

References

1. J. Durst, A. Siebel, C. Simon, F. Hasche, J. Herranz, and H. A. Gasteiger, *Energy Environ. Sci.*, **7**, 2255 (2014).
2. O. Gröger, H. A. Gasteiger, and J.-P. Suchsland, *J. Electrochem. Soc.*, **162**, A2605 (2015).
3. A. Kongkanand and M. Mathias, *J. Phys. Chem. Lett.*, **7**, 1127 (2016).
4. B. Han, C. E. Carlton, A. Kongkanand, R. S. Kukreja, B. R. Theobald, L. Gan, R. O'Malley, P. Strasser, F. T. Wagner, and Y. Shao-Horn, *Energy Environ. Sci.*, **8**, 258 (2015).
5. C. Cui, L. Gan, H.-H. Li, S.-H. Yu, M. Heggen, and P. Strasser, *Nano Lett.*, **12**, 5885 (2012).
6. C. Chen, Y. Kang, Z. Huo, Z. Zhu, W. Huang, H. L. Xin, J. D. Snyder, D. Li, J. A. Herron, M. Mavrikakis, M. Chi, K. More, N. Markovic, G. Somorjai, P. Yang, and V. Stamenkovic, *Science*, **343**, 1339 (2014).
7. C. Baldizzone, S. Mezzavilla, H. W. Carvalho, J. C. Meier, A. K. Schuppert, M. Heggen, C. Galeano, J.-D. Grunwaldt, F. Schüth, and K. J. Mayrhofer, *Angew. Chem. Int. Ed.*, **53**, 14250 (2014).
8. F. Van Schalkwyk, G. Pattrick, J. Olivier, O. Conrad, and S. Blair, *Fuel Cells*, **16**, 414 (2016).
9. Y. Liu, C. Ji, W. Gu, J. Jorne, and H. A. Gasteiger, *J. Electrochem. Soc.*, **158**, B614 (2011).
10. M. Uchida, Y. Fukuoka, Y. Sugawara, N. Eda, and A. Ohta, *J. Electrochem. Soc.*, **143**, 2245 (1996).
11. A. Kongkanand, V. Yarlagadda, T. R. Garrick, T. E. Moylan, and W. Gu, *ECS Trans.*, **75**, 25 (2016).
12. V. Yarlagadda, M. K. Carpenter, T. E. Moylan, R. S. Kukreja, R. Koestner, W. Gu, L. Thompson, and A. Kongkanand, *ACS Energy Letters*, **3**, 618 (2018).
13. Y.-C. Park, H. Tokiwa, K. Kakinuma, M. Watanabe, and M. Uchida, *J. Power Sources*, **315**, 179 (2016).
14. H. Jinnai, R. Spontak, and T. Nishi, *Macromolecules*, **43**, 1675 (2010).
15. A. Orfanidi, P. Madkikar, H. El-Sayed, G. S. Harzer, T. Kratky, and H. A. Gasteiger, *J. Electrochem. Soc.*, **164**, F418 (2017).
16. G. S. Harzer, J. N. Schwämmlein, A. M. Damjanović, S. Ghosh, and H. A. Gasteiger, *J. Electrochem. Soc.*, **165**, F3118 (2018).
17. C. Simon, F. Hasché, and H. A. Gasteiger, *J. Electrochem. Soc.*, **164**, F591 (2017).
18. C. Simon, F. Hasché, D. Müller, and H. A. Gasteiger, *ECS Trans.*, **69**, 1293 (2015).
19. S. Biniak, G. Szymański, J. Siedlewski, and A. Świątkowski, *Carbon*, **35**, 1799 (1997).
20. J. Jaramillo, P. Álvarez, and V. Gómez-Serrano, *Appl. Surf. Sci.*, **256**, 5232 (2010).
21. B. Strehle, S. Solchenbach, M. Metzger, K. U. Schwenke, and H. A. Gasteiger, *J. Electrochem. Soc.*, **164**, A2513 (2017).
22. J. Speder, A. Zana, and M. Arenz, *Catalysis today*, **262**, 82 (2016).
23. E. P. Ambrosio, C. Francia, C. Gerbaldi, N. Penazzi, P. Spinelli, M. Manzoli, and G. Ghiotti, *J. Appl. Electrochem.*, **38**, 1019 (2008).
24. C.-Y. Ahn, J.-Y. Cheon, S.-H. Joo, and J. Kim, *J. Power Sources*, **222**, 477 (2013).
25. K. Shinozaki, Y. Morimoto, B. S. Pivovar, and S. S. Kocha, *J. Power Sources*, **325**, 745 (2016).
26. P. Ferreira, G. J. la O', Y. Shao-Horn, D. Morgan, R. Makharia, S. Kocha, and H. A. Gasteiger, *J. Electrochem. Soc.*, **152**, A2256 (2005).
27. Y. Garsany, I. L. Singer, and K. E. Swider-Lyons, *J. Electroanal. Chem.*, **662**, 396 (2011).
28. M. Uchida, Y.-C. Park, K. Kakinuma, H. Yano, D. A. Tryk, T. Kamino, H. Uchida, and M. Watanabe, *Phys. Chem. Chem. Phys.*, **15**, 11236 (2013).
29. H. A. Gasteiger, S. S. Kocha, B. Sompalli, and F. T. Wagner, *Appl. Catal., B*, **56**, 9 (2005).
30. H. Iden and A. Ohma, *J. Electroanal. Chem.*, **693**, 34 (2013).
31. A. Ohma, T. Mashio, K. Sato, H. Iden, Y. Ono, K. Sakai, K. Akizuki, S. Takaichi, and K. Shinohara, *Electrochim. Acta*, **56**, 10832 (2011).
32. T. R. Garrick, T. E. Moylan, V. Yarlagadda, and A. Kongkanand, *J. Electrochem. Soc.*, **164**, F60 (2017).
33. F. Yang, L. Xin, A. Uzunoglu, Y. Qiu, L. Stanciu, J. Ilavsky, W. Li, and J. Xie, *ACS Appl. Mater. Interfaces*, **9**, 6530 (2017).
34. L. Xin, F. Yang, S. Rasouli, Y. Qiu, Z.-F. Li, A. Uzunoglu, C.-J. Sun, Y. Liu, P. Ferreira, W. Li, Y. Ren, L. Stanciu, and J. Xie, *ACS Catalysis*, **6**, 2642 (2016).
35. K. Neyerlin, W. Gu, J. Jorne, and H. A. Gasteiger, *J. Electrochem. Soc.*, **153**, A1955 (2006).
36. D. R. Baker, D. A. Caulk, K. C. Neyerlin, and M. W. Murphy, *J. Electrochem. Soc.*, **156**, B991 (2009).
37. J. P. Owejan, J. E. Owejan, and W. Gu, *J. Electrochem. Soc.*, **160**, F824 (2013).
38. H. Oh, Y. il Lee, G. Lee, K. Min, and S. Y. Jung, *J. Power Sources*, **345**, 67 (2017).
39. N. Subramanian, T. Greszler, J. Zhang, W. Gu, and R. Makharia, *J. Electrochem. Soc.*, **159**, B531 (2012).
40. C. Mittelsteadt and H. Liu, *in Handbook of Fuel Cells*, 1st ed., W. Vielstich, A. Lamm, and H. A. Gasteiger, vol **5**, p. 348, John Wiley & Sons Ltd, Chichester (2009).
41. Y. Liu, M. W. Murphy, D. R. Baker, W. Gu, C. Ji, J. Jorne, and H. A. Gasteiger, *J. Electrochem. Soc.*, **156**, B970 (2009).

3.3 Cathode Loading Impact on Voltage Cycling Induced PEMFC Degradation: A Voltage Loss Analysis

The article "Cathode Loading Impact on Voltage Cycling Induced PEMFC Degradation: A Voltage Loss Analysis",[76] was submitted in December 2017 and published as an open access article in the *JES Focus Issue on Proton Exchange Membrane Fuel Cell (PEMFC) Durability* of the peer-reviewed *Journal of The Electrochemical Society* in March 2018, distributed under the terms of the Creative Commons Attribution 4.0 License (CC BY). The permanent web link to the article is http://jes.ecsdl.org/content/165/6/F3118.

In this publication, the degradation of MEAs by different voltage cycling protocols and its dependence on the catalyst layer loading is investigated, while special focus lies on the determination and deconvolution of mass transport related resistances. For this, extended voltage cycling up to 30000 cycles with varying potential limits and voltage transients (shown in Figure 2, page F3120) is performed. Firstly, it is shown that the decrease of the *ECSA* is strongly dependent on the type of voltage transient, e.g., that a potential jump with a hold time at the vertex potential is more detrimental to the *ECSA* than a continuous, triangular potential scan. This has also been observed among other research groups.[72,75] While this may be due to the fast voltage transient in a square wave potential profile, we identify the main degradation mechanism as the hold time at the upper vertex potential, employing a protocol with a potential sweep and a hold time at the upper and lower vertex. The degradation induced by this protocol is almost identical to the one by the potential jump experiment, eliminating the sweep or step time as main influencing factor. In addition, no influence of the catalyst layer loading on the *ECSA* degradation could be identified, other than the observed differences in *ECSA* loss due to the different types of catalysts ($20\%_{\mathrm{wt}}$ Pt/C for low loaded and $50\%_{\mathrm{wt}}$ Pt/C for high loaded catalyst layers), which had to be used to maintain the same catalyst layer thickness to enable comparability of mass transport phenomena. The decrease of mass activity, $i_{0.9\,\mathrm{V}}^{\mathrm{mass}}$, was found to scale proportionally with the available *ECSA*, however, the specific activity, $i_{0.9\,\mathrm{V}}^{\mathrm{spec}}$, increased over the course of potential cycling due to the Pt particle size increase. The oxygen mass transport resistance, $R_{\mathrm{O_2}}^{\mathrm{total}}$, determined from limiting current experiments, showed a significant increase over the course of 30000 potential cycles, while we could prove that carbon corrosion and the concomitant collapse of the catalyst layer is absent in all of these voltage cycling experiments. The increase of the transport resistance is rather due to the decrease of the available Pt surface area, i.e., the *rf*, and hence the increase of the pressure independent transport resistance, $R_{\mathrm{O_2}}^{\mathrm{PI}}$. This phenomenon was also shown by Geszler et al.,[101] who prepared electrodes with different *rf*-values by dilution with carbon, while we achieved a similar decrease of the *rf*-values by potential cycling. Using two initial catalyst layer loadings of 0.4 $\mathrm{mg_{Pt}/cm^2}$ and 0.1 $\mathrm{mg_{Pt}/cm^2}$, a wide range of

roughness factors is spanned, verifying the previously observed correlation (see Figure 12, page F3128). Finally, we show that lowering the upper potential limit during voltage cycling by 150 mV to 850 mV (termed TW-LUPL), even low loaded catalyst layers can sustain 30000 potential cycles without degradation of the H_2/air performance and with only little *ECSA* loss. These results provide valuable guidelines for increasing the durability of PEM fuel cell systems by carefully controlling the operating potential.

Author contributions

G.H. and J.S. contributed equally to this publication by designing and performing experiments and drafting the manuscript. A.M.D. performed the experimental work. H.G. designed experiments and reviewed the manuscript. All authors discussed the experimental data, commented on the results and reviewed the manuscript.

JES Focus Issue on Proton Exchange Membrane Fuel Cell (PEMFC) Durability

Cathode Loading Impact on Voltage Cycling Induced PEMFC Degradation: A Voltage Loss Analysis

Gregor S. Harzer,[1,=,*,z] Jan N. Schwämmlein,[1,=,*] Ana Marija Damjanović,[2] Sourov Ghosh,[1] and Hubert A. Gasteiger[1,]**

[1] *Chair of Technical Electrochemistry, Department of Chemistry and Catalysis Research Center, Technical University of Munich, D-85748 Garching, Germany*
[2] *Faculty of Chemical Engineering and Technology, University of Zagreb, 10000 Zagreb, Croatia*

This study focuses on voltage cycling induced degradation of cathodes with different loading (0.4 and 0.1 mg_{Pt}/cm^2) when applying square wave or triangular wave based accelerated stress tests (ASTs) between 0.6 and 1.0 V_{RHE}. The degradation of the H_2/O_2 and H_2/air performance upon extended voltage cycling (up to 30000 cycles) was analyzed in terms of the voltage loss contributions from ORR kinetics, O_2 mass transport resistances and proton conduction resistances in the cathode. The extent of cathode thinning due to carbon support corrosion was determined by post mortem electrode thickness measurements. Square waves were found to cause a more rapid loss of *ECSA* and mass activity compared to triangular waves, which was shown to be due to the longer hold periods at high potentials rather than to the rate of the potential transient. The observed increase of the O_2 mass transport resistance with voltage cycling was found to mainly depend on the available Pt surface area, while mass transport resistances due to carbon corrosion were found to be insignificant. Finally, it was shown that by lowering the upper potential limit to 0.85 V_{RHE}, low-loaded catalyst layers can sustain 30000 potential cycles without degradation of the H_2/air performance.
 [DOI: 10.1149/2.0161806jes]

Manuscript submitted December 27, 2017; revised manuscript received February 28, 2018. Published March 14, 2018. *This paper is part of the JES Focus Issue on Proton Exchange Membrane Fuel Cell (PEMFC) Durability.*

Currently, proton exchange membrane fuel cells (PEMFCs) are on the verge of widespread commercialization as an alternative power source for the automotive market, impressively demonstrated by the launch of PEMFC based vehicles by Toyota,[1] Hyundai,[2] and Honda[3] in recent years. The major hurdle for a significant market penetration of PEMFC vehicles in the near future is the reduction of system cost and the amount of platinum, while meeting long-term durability targets.[4,5] Despite remarkable achievements in lowering the Pt loading of the cathode catalyst layer in state-of-the-art membrane electrode assemblies (MEAs) down to ≈0.1 mg_{Pt}/cm^2,[6–8] recent studies have shown that additional overpotentials occur at low loadings and high current density.[8–11] Even though the exact origin of these losses is subject to ongoing discussions in the literature, its occurrence was directly correlated to the available Pt surface area in the cathode, i.e., to the cathode roughness factor (*rf*, defined as Pt surface area per geometric surface area in units of cm^2_{Pt}/cm^2), so that it is often referred to as Pt specific O_2 mass transport resistance ($R^{Pt}_{O_2}$).[8–10] Additionally, it is well-known that MEAs degrade under the dynamic load-cycles relevant for automotive applications due to the associated voltage cycles. This made extended voltage cycling tests a frequently applied accelerated stress test (AST) to probe the durability of the cathode catalyst layer. Despite various reports in the literature employing different aging protocols, such as applying square wave (SW) potential perturbations or constant high potential phases, the most commonly applied aging protocol is based on triangular wave (TW) potential perturbations between cell voltages of 0.6 and 1.0 V at a scan rate of typically 50 mV/s.[12–21]

Thermodynamically, the carbon black support for the noble metal catalyst in the MEA is not stable under fuel cell operating conditions, since the equilibrium potential of the carbon oxidation reaction (COR) is only 0.2 V_{RHE} (considering CO_2 as reaction product).[22] Fortuitously, the sluggish kinetics of the COR prevent the oxidation of carbon at potentials < 0.9 V_{RHE}, i.e., within the typical fuel cell operating range,[17,23,24] and therefore enable its use in the cathode catalyst layer. On the other hand, high voltage periods, occurring for example during system start-up or shut-down, can oxidize the carbon structure in the catalyst layer, eventually leading to a loss of void volume and a thinning of the electrode (often referred to as "cathode thinning").[25–27] Since a sufficiently large void volume is crucial for the transport of O_2 through the cathode catalyst layer, significant corrosion of the carbon support causes an increase of the O_2 mass transport resistance and a decrease of PEMFC performance. In addition, carbon corrosion was found to cause a detachment of Pt from the carbon support, leaving the Pt nanoparticles electrically disconnected from the electrode, which decreases the available electrochemical surface area (*ECSA*) of Pt. Another source of *ECSA* loss during ASTs are repetitive changes of the cathode potential, leading to oxidation and reduction of the Pt surface.[13,14,20] Upon its reduction/oxidation, Pt surface atoms can dissolve from the nanoparticle into the electrolyte as ionic species, eventually redepositing on existing Pt nanoparticles via a process referred to as Ostwald ripening, resulting in an increase of the average Pt particle size and an associated *ECSA* loss.[28,29] Furthermore, as long as the electrode is held at high potentials, Pt ions can diffuse in the electrolyte phase towards the membrane where they can react with cross-over hydrogen to form electrically insulated Pt deposits within the membrane phase.[30] Since these Pt deposits can no longer contribute to the electrochemical processes in the cathode catalyst layer, a significant decrease of the *ECSA* is observed.

To gain a better understanding of the aging processes occurring during voltage cycling ASTs, high-loaded (0.4 mg_{Pt}/cm^2) and low-loaded (0.1 mg_{Pt}/cm^2) MEAs were exposed to different potential cycling profiles: square waves, triangular waves, and triangular waves with an upper and lower potential hold (TW–H). The associated losses of *ECSA* and ORR mass activity were quantified by cyclic voltammetry and by differential flow H_2/O_2 performance measurements, respectively. Furthermore, the performance degradation of differential flow H_2/air polarization curves was analyzed by quantifying the proton conduction resistance via electrochemical impedance spectroscopy (EIS) and by determining the oxygen transport resistance via limiting current diagnostics. The comparison of MEA performance vs *ECSA* over the course of extended voltage cycling provides insights into the voltage cycling induced increase of the O_2 transport resistance. In addition, by deliberately corroding the carbon support through a high-potential hold of the cathode, where substantial carbon corrosion occurs (1.2 V_{cell} for 8 h), resulting in pronounced cathode thinning at a

=These authors contributed equally to this work.
*Electrochemical Society Student Member.
**Electrochemical Society Fellow.
zE-mail: gregor.harzer@tum.de

reasonable *ECSA* retention, we were able to distinguish between the impact of carbon corrosion and *ECSA* loss on the limiting current measurements. Comparing the various voltage cycling protocols, it could be shown that the higher degradation observed for square wave compared to triangular wave modulation were due to the extended time at high potentials in the former rather than to the voltage ramp rate between upper and lower potential. Our analysis also showed that the oxygen transport resistances developing over the course of voltage cycling ASTs predominantly depends on the specific current density (in units of A/cm^2_{Pt}), independent of the initial Pt loading of the MEAs.

Experimental

Comprehensive experimental details on MEA preparation and fuel cell testing are given in our previous publication,[11] but the most pertinent information is given below. All potentials referred to in cyclic voltammograms and in voltage cycling experiments are referenced to the reversible hydrogen electrode (RHE) potential at a nominal H_2 pressure of 100 kPa_{abs} (V_{RHE}). This was obtained by correcting for the Nernstian shift of the hydrogen anode if the H_2 partial pressure was different from 100 kPa_{abs}. For the voltage cycling tests conducted under H_2/N_2 (anode/cathode) at 100 kPa_{abs}, 80°C, 100% *RH*, the different applied potential limits of 0.60, 0.85, and 1.00 V_{RHE} correspond to cell voltage limits of 0.59, 0.84, and 0.99 V_{cell}. If not stated otherwise, area-normalized currents (e.g., cm^2) refer to the geometric area of the electrode. Furthermore, note that all pressures were measured and controlled at the inlet of the fuel cell and are stated as absolute pressures.

Membrane electrode assembly preparation.—All fuel cell tests were conducted with 5 cm^2 MEAs, fabricated by the decal transfer method. Catalyst inks were prepared by mixing the catalyst with a low equivalent weight ionomer in a water-solvent dispersion (Asahi Kasei, 700 EW). To realize the same electrode thickness (identical carbon loading of 0.4 mg_C/cm^2), two catalysts with different Pt/C ratio were used. For low-loaded catalyst layers, a 20%$_{wt}$ Pt/Vulcan catalyst (TEC10V20E, Tanaka Kikinzoku Kogyo K.K., TKK) and for high-loaded catalyst layers, a 50%$_{wt}$ Pt/Vulcan (TEC10V50E, TKK) was used. The ink components were added into a 15 mL capped bottle (HDPE), already containing 16.5 g of 5 mm ZrO_2 beads as grinding medium in the following sequence: catalyst, water, 1–propanol, and finally the ionomer dispersion. The water concentration of the ink was 10%$_{wt}$, while the solid content was 0.03 g/mL_{ink} to obtain a suitable viscosity for the coating process. The ionomer to carbon weight ratio (I/C) was 0.65. The inks were mixed by placing the bottles onto a roller-mill (60 rpm) for 18 h at room temperature. Thereafter, the inks were coated on virgin PTFE using the mayer rod technique with the appropriate bar on a coating machine. The same type of anode was used for all experiments, namely 0.1 mg_{Pt}/cm^2 consisting of 20%$_{wt}$ Pt/C (TEC10V20E, TKK) with an I/C ratio of 0.65. The MEAs were assembled by hot pressing a 15 μm membrane (Asahi Kasei) placed between the anode and cathode decals at 155°C for 3 min with an applied force of 0.11 kN/cm^2. The cathode loadings were 0.1 mg_{Pt}/cm^2 and 0.4 mg_{Pt}/cm^2, with a maximum deviation of ±5%, as determined by weighing the decals before and after the catalyst layer transfer. For each aging procedure, two independent fuel cell measurements were conducted and subsequently averaged with error bars corresponding to the mean absolute deviation.

Fuel cell testing equipment.—Electrochemical measurements were performed on an in-house manufactured, single-cell hardware, using commercial graphite flow fields (0.5 mm lands/ channels; manufactured by Poco Graphite according to our design).[31] Gas diffusion layers (GDLs) were supplied by Freudenberg (H14C7) and the GDL compression was adjusted to 20 ± 1% by PTFE coated, incompressible fiberglass gaskets, assembled at a torque of 12 Nm (for details see Simon et al.).[32] Fuel cell tests were performed on automated test stations (G60, Greenlight Innovation) equipped with a potentiostat (Reference3000, Gamry) to conduct electrochemical impedance spectroscopy (EIS).

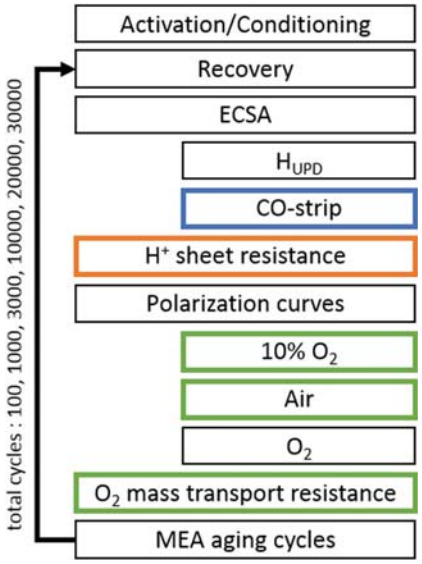

Figure 1. Overview of the experimental procedure for MEA aging. Complete MEA characterization (differential flow H_2/O_2 and H_2/air curves, cyclic voltammetry, CO stripping, limiting current measurements, and EIS) was performed at beginning-of-test (BOT) and end-of-test (EOT). The color of the boxes indicates the type of MEA characterization after specific MEA aging cycles: after every aging cycle (black); only at BOT and EOT (orange); after 10000 and 20000 cycles (blue), after 10000 cycles (green).

Voltage cycling procedure and diagnostic measurements.—The experimental testing procedure is depicted in Figure 1. All MEAs were conditioned prior to testing, using a voltage-controlled ramp-in procedure (H_2/air flows of 1390/3320 nccm at 80°C, 100% relative humidity (*RH*), and 150 kPa_{abs}): 0.6 V for 45 min, 5 min at OCV, and 10 min at 0.85 V. This sequence was repeated 10 times, after which constant performance was reached. Before each set of differential flow polarization curves and diagnostic measurements, an MEA recovery step was implemented, which consisted of a hold time in H_2/air (2000 nccm/5000 nccm) at 0.3 V for 2 h at 40°C, 270 kPa_{abs}, and 100% *RH*. The purpose of this procedure is to recover reversible losses prior to catalyst layer characterization.

Cyclic voltammograms (CVs) of the cathode electrode were recorded between 0.07 and 1.00 V_{RHE} at a scan rate of 150 mV/s, at 40°C and ambient pressure, while the *ECSA* was evaluated from CVs with a limited upper potential of 0.6 V_{RHE} by averaging the H-desorption and H-adsorption charge (using a specific charge of 210 $\mu C/cm^2_{Pt}$). The counter/reference electrode was fed with 200 nccm of fully humidified 5% H_2 in N_2, and the working electrode was initially purged with dry N_2 at 50 nccm, while interrupting the gas flow to record the CVs.

CO stripping was done by adsorbing CO (10% CO in N_2, 100 nccm) for 10 min at 40°C and 150 kPa_{abs} while maintaining the cathode potential at 0.1 V_{RHE}. Subsequently, residual CO was removed from the cell and the gas lines by purging with nitrogen for ≈1.5 h. A CV from the holding potential to 1.2 V_{RHE} at a scan rate of 100 mV/s was performed to oxidize the adsorbed CO. Two additional sweeps were recorded to verify the full oxidation and removal of CO from the electrode and the gas feed system. The *ECSA* was determined by integrating the area of the first anodic scan with the subsequent sweep as baseline, using a specific charge of 420 $\mu C/cm^2_{Pt}$.

The proton conduction resistance of the cathode, $R^{cath}_{H^+}$ (in units of $\Omega \cdot cm^2$), was determined from AC impedance spectra recorded in H_2/N_2 (anode/cathode) at 0.2 V_{cell} with a peak-to-peak perturbation of

3.5 mV between 500 kHz and 0.2 Hz (20 points per decade), according to a procedure reported in the literature,[33,34] based on a transmission line model.[35] In order to ensure reproducibility, the measurement was repeated three times at each condition: 100, 70, 50, and 30% *RH*, while maintaining constant gas partial pressures (i.e., at cell pressures of 270, 255, 246, and 236 kPa_{abs}, respectively) under differential flow conditions (H_2/N_2 at 1000/1000 nccm) at 80°C. The proton resistivity, $\rho_{H^+}^{cath}$ (in units of $\Omega \cdot cm$), was calculated by dividing $R_{H^+}^{cath}$ by the cathode thickness.

Differential flow polarization curves were recorded in current-control mode at 80°C, 170 kPa_{abs} inlet-controlled pressure, 100% *RH* for both reactants, and constant flows of 2000 nccm of H_2 on the anode and 5000 nccm of O_2, air, or 10% O_2 (balanced with N_2) on the cathode. Anode and cathode were operated in counter flow mode. At these conditions, the inlet to outlet pressure drop in anode and cathode was about 2 and 22 kPa_{abs}, respectively. Prior to recording a polarization curve from low to high current densities, the cathode potential was held at 0.75 V for 15 min to reduce Pt-oxides; each current density point was held constant for at least 10 min and the resulting voltage was averaged over the final 30 s. The ORR kinetics (mass activity, specific activity, and Tafel slopes) were determined from H_2/O_2 polarization curves after application of two corrections: i) the potential was corrected for the *iR*-drop, using the high frequency resistance (*HFR*) obtained from the x-axis intersect in the Nyquist plot measured by galvano electrochemical impedance spectroscopy (GEIS) in the frequency range from 100 kHz to 10 Hz at each current density (applying a 10% AC amplitude with respect to the current, limited to a minimum/ maximum of 0.1/3.0 A); ii) the current was corrected for the ohmic short of the membrane, as well as for the H_2 crossover, both determined in H_2/N_2 (150/600 nccm) at 170 kPa_{abs}, 80°C, and 100% *RH* by applying a constant potential of 0.2, 0.3, 0.4, 0.5, 0.6 and 0.7 V for 2 min each.

The total mass transport resistance ($R_{O_2}^{total}$) was extracted from limiting current measurements at 80°C and 100% *RH* under differential flow conditions (2000 nccm of H_2 and 5000 nccm of O_2/N_2 mixtures).[15,36,37] The dry mole fraction of oxygen was altered from 4 to 24% O_2 in N_2, while the cell potential was set to 0.30, 0.15, 0.10, and 0.05 V for 2 min each. To quantify pressure-independent and pressure-dependent oxygen transport resistances, limiting current measurements were also conducted at 170, 270, 350, and 500 kPa_{abs}.

Aging of the cathode electrodes was performed at 100 kPa_{abs}, 80°C, 100% RH and H_2/N_2 flows of 200 nccm/75 nccm on anode/cathode, respectively. In voltage cycling ASTs, various potential profiles were examined that are depicted in Figure 2: triangular wave modulation between a lower potential of 0.6 V_{RHE} and an upper potential of either 1.0 V_{RHE} (referred to as "TW", a) or a lower upper potential limit of 0.85 V_{RHE} (referred to as "TW–LUPL", d) at 50 mV/s; square wave (SW, b) modulation between 0.6 and 1.0 V_{RHE}; and triangular wave modulation with a potential hold at the lower (0.6 V_{RHE}) and upper (1.0 V_{RHE}) potential (referred to as "TW–H", c). Voltage cycling ASTs were controlled by a potentiostat (Reference3000, Gamry). To avoid reductive currents during potential cycling, all residual O_2 was removed from the humidifier and gas line system by a N_2 purging procedure, lasting about 45 min. The scan rate for all TW procedures was 50 mV/s, while the potential step in the SW procedure was completed in less than 0.1 seconds (corresponding to an average rate of >4 V/s). The hold times of 8 s at the vertex potentials in the SW procedure was chosen such that it is identical to the overall time required for one TW cycle (compare Figures 2a and 2b).

Electrode thickness determination by SEM.—The thicknesses of pristine (BOT), as well as aged MEAs (EOT) were determined from cross-section images, obtained by scanning electron microscopy (SEM). To get a more accurate comparison between BOT/EOT and to exclude any effects of cell assembly on the catalyst layer thickness, the pristine MEAs were assembled in a cell and operated at 80°C, 100% RH and 500 nccm N_2/N_2 flows at ambient pressure for 24 h before determining their initial thickness. The MEAs were cut in quarters, using one quarter close to the gas inlet and one close to outlet of the cell. The samples were fixed in a Teflon holder and embedded in epoxy resin (EpoThin 2 resin and hardener, Buehler Ltd.) at reduced pressure to remove gas bubbles. After hardening overnight at 40°C, the resin block was removed from the holder, ground on SiC (CarbiMet S, P280, Buehler Ltd.) under constant water flow and thoroughly cleaned by ultrasonification in water. SEM (JCM-6000PLUS NeoScope, Jeol) images were taken in backscattering mode at 15 kV accelerating voltage and a magnification of 2000x at ten arbitrarily chosen locations for each quarter of an MEA, generating 20 images per MEA. The thickness of the electrode was determined by integration of the electrode area with ImageJ (version 1.51j8) and dividing by the length of the image as shown in Figure 3. This way, the entire image is evaluated, which provides a more accurate measure of the catalyst layer thickness compared to a single point measurement.

The thickness of pristine electrodes was used to calculate the packing density of the Vulcan carbon based electrodes. The obtained packing density of 22 ± 4 $\mu m/(mg_C/cm^2)$ is in reasonable agreement with values in the literature.[38] The BOT thickness for all tested MEAs was

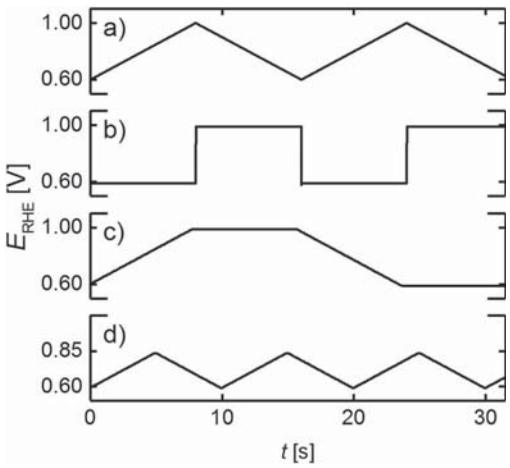

Figure 2. Voltage profiles used in voltage cycling ASTs performed at 100 kPa_{abs}, 80°C, 100% *RH* and H_2/N_2 flows of 200 nccm/75 nccm on anode/cathode, respectively. a) triangular wave modulation ("TW") between 0.6 and 1.0 V_{RHE} (corresponding to 0.59 and 0.99 V_{cell}) at a scan rate of 50 mV/s; b) square wave modulation ("SW"), applying a hold time of 8 s at the lower (0.6 V_{RHE}) and upper (1.0 V_{RHE}) potential; c) triangular wave modulation at a scan rate of 50 mV/s with 8 s potential hold at the lower (0.6 V_{RHE}) and upper (1.0 V_{RHE}) limits ("TW–H"); d) triangular wave modulation at 50 mV/s between 0.6 V_{RHE} and a lowered upper potential limit ("TW–LUPL") of 0.85 V_{RHE} (≡0.84 V_{cell}). The combination of an anodic and a cathodic scan is referred to as one cycle in this study.

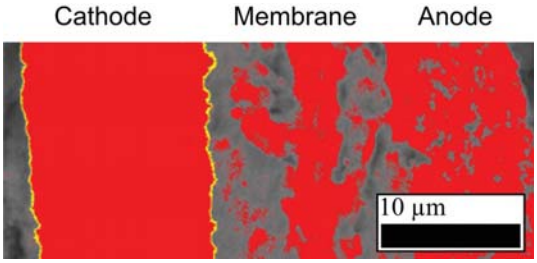

Figure 3. Cross-sectional SEM image of an MEA embedded in epoxy resin and taken at an acceleration voltage of 15 kV and a magnification of 2000x. The cathode edges are marked in yellow and the integrated area in between is shown in red, based on the grayscale of the image. Red areas outside the cathode are not included in the evaluation.

calculated from the transferred weight of carbon in the hot pressing process and the packing density.

Results and Discussion

In this study, we present the aging behavior of MEAs exposed to different voltage cycling protocols, with the respective voltage transients shown in Figure 2. The most commonly used AST is a potential scan between 0.6 and 1.0 V_{RHE} at a scan rate of 50 mV/s and 80°C in inert gas atmosphere, termed TW in this manuscript (Figure 2a). In addition, many researchers reported the aging behavior of MEAs exposed to square wave (SW) voltammetry (Figure 2b), since the combination of fast potential transients and hold periods has proven to accelerate catalyst layer degradation.[39,40] However, it is not well-understood yet, whether the holding time at the respective potential or the fast transient from one to the other potential is the dominating factor for the observed electrode degradation. To deconvolute between TW and SW modulations, triangular scans were combined with a potential hold period (TW–H) in order to eliminate the fast potential step while maintaining the effect of the hold time (Figure 2c). Furthermore, electrode aging by a TW modulation between 0.6 and 1.0 V_{RHE} will be compared to a TW modulation with the same lower voltage limit but with a lowered upper potential limit of 0.85 V_{RHE} (TW-LUPL), where carbon support corrosion can safely be assumed to be negligible and where Pt dissolution rates are expected to be reduced (Figure 2d). Finally, our study is complemented by a potential hold experiment at 1.2 V_{cell} for 8 h (under N_2 at 95°C, 100% *RH*, and 100 kPa_{abs}) to degrade the carbon support structure via COR, while maintaining a reasonably high electrode roughness factor. All of the aging procedures were conducted on high-loaded (0.4 mg_{Pt}/cm^2) and low-loaded cathodes (0.1 mg_{Pt}/cm^2) to identify similarities and/or differences in the aging behavior with respect to the *ECSA* and mass activity originating from different catalyst layer loadings. Moreover, changes of the cathode O_2 mass transport resistance upon aging, especially with respect to the local O_2 mass transport resistance which is commonly observed to be a function of the electrode *rf* was of major interest in this study.[9,10,41] The utilization of high- and low-loaded catalyst layers enables a comparison over a wide range of *rf*, i.e., to compare low Pt specific current densities (A/cm^2_{Pt}) for high-loaded MEAs (high *rf*) to high specific current densities after aging of low-loaded cathodes (low *rf*). However, to establish a valid comparison of the total mass transport resistance, the same catalyst layer thickness was maintained (≈10 μm) for all MEAs at BOT by utilizing a 50%$_{wt}$ Pt/C catalyst for high-loaded and a 20%$_{wt}$ Pt/C catalyst for low-loaded electrodes.

ECSA evaluation: H_{UPD} vs CO stripping.—To evaluate the degradation of the Pt surface area over the course of MEA aging, CVs were recorded after each aging stage, exemplarily shown in Figure 4a for a single low-loaded MEA (0.1 mg_{Pt}/cm^2) exposed to SW aging between 0.6 and 1.0 V_{RHE} (see Figure 2b). To determine the *ECSA* by integration of the H_{UPD} charge, additional CVs with a limited upper potential (0.6 V_{RHE}) were recorded (not shown) to avoid a contribution of charge originating from the reduction of the Pt surface.[42] Due to the above outlined Pt dissolution/redistribution mechanisms, the H_{UPD} features of the CV degrade significantly, i.e., a decrease of the cathode *rf* is observed over the course of extended voltage cycling. In general, the evaluation of the *ECSA* via integration of the pseudo-capacitive H_{UPD} current is influenced by a superimposed faradaic current at low potentials, originating from the hydrogen evolution reaction (HER). This superposition is especially dominant at low *rf*, as the rate of the HER above 0 V_{RHE} in cyclic voltammetry is mostly thermodynamically controlled (i.e., it does not depend significantly on the active Pt surface area), whereas the pseudo-capacitive H_{UPD} charge scales directly with the available Pt surface area. Hence, the strong decrease of the *rf* in the course of the voltage cycling AST renders the determination of the *ECSA* via the H_{UPD} method increasingly erroneous, requiring the implementation of CO stripping to reliably determine the remaining Pt surface area for very low *rf* values,[43] i.e., towards the end of the aging protocol.

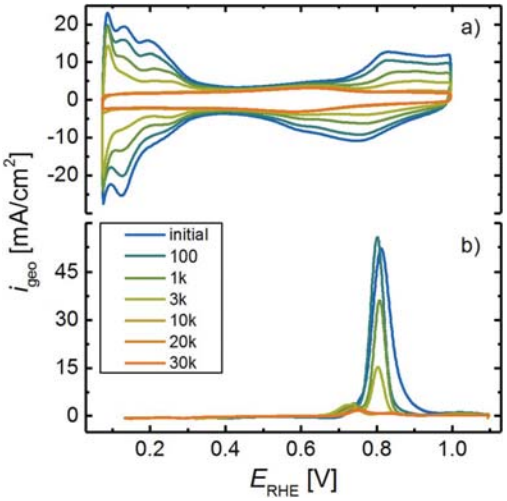

Figure 4. a) CVs of the cathode after different aging stages during a SW-based AST between 0.6 and 1.0 V_{RHE} (see Figure 2b). CVs were conducted at a scan rate of 150 mV/s from 0.07 to 1.00 V_{RHE} at ambient pressure and 40°C (the anode was supplied with 200 nccm of 5% H_2 (in N_2) and the cathode N_2 flow was 50 nccm (set to zero flow when recording the CVs)). b) CO stripping voltammograms after subtraction of the subsequent anodic sweep, recorded at a scan rate of 100 mV/s to 1.1 V_{RHE} at 150 kPa_{abs} and 40°C (constant flows of 200 nccm 5% H_2 on the anode and 5 nccm N_2 on the cathode). CO was adsorbed for 10 min at a flow rate of 100 nccm prior to the CV, maintaining the potential at 0.1 V_{RHE}. To remove residual CO gas from the cell and the test station, a purging procedure with N_2, lasting approximately 1.5 h was executed.

Representative CO stripping measurements are shown in Figure 4b after subtraction of the second anodic scan. The peak for CO oxidation occurs at ≈0.81 V_{RHE}, which is consistent with reports by other researchers for CO oxidation on Pt nanoparticles,[44] mainly dominated by CO oxidation on Pt(111) facets.[45,46] Furthermore, a second peak at ≈0.74 V_{RHE} is observed, representing Pt(110)-like planes.[47] Since those facets are less prone to dissolution upon surface oxidation/reduction, this peak becomes more dominant upon potential cycling. Consistent with the decrease in H_{UPD} features, the charge associated with the oxidation of CO_{ads} decreases significantly during cathode aging. Since *ECSA* determination via H_{UPD} is reasonably accurate for high *rf* values, the charge ratio between H_{UPD} and CO stripping remains constant ($\frac{ECSA_{H_{UPD}}}{ECSA_{CO}} \approx 0.8$) throughout the first phase of aging (up to ≈3000 cycles). As the H_{ad} formation is not quantitative in the applied potential range (≥ 0.07 V_{RHE}), the *ECSA* determined by the H_{UPD} method is slightly underestimated compared to the *ECSA* determined from CO stripping, hence their ratio is below unity.[48] In the course of potential cycling, the ratio decreases significantly ($\frac{ECSA_{H_{UPD}}}{ECSA_{CO}} < 0.1$ after 10000 cycles), as the electrode *rf* approaches very low values where the H_{UPD} currents are small compared to the capacitive current contributions from the carbon support. As CO stripping was only implemented for electrodes with a considerably low *rf,* and H_{UPD} was the preferred method for *ECSA* determination (due to its experimental simplicity), comparability of these two techniques was assured by introducing a scaling factor. The scaling factor was calculated as the ratio of *ECSA* determined by H_{UPD} and CO stripping at BOT and was used to correct the values determined by CO stripping to an "H_{UPD}-derived" *ECSA* at low *rf* (denoted by open symbols in figures showing *ECSA* data in this manuscript).

ECSA evolution during voltage cycling ASTs.—A decrease of the *ECSA* with increasing number of voltage cycles for each cathode loading and aging protocol is given in Figure 5, eventually reaching similarly low *ECSA* values on the order of 5–10 m^2_{Pt}/g after

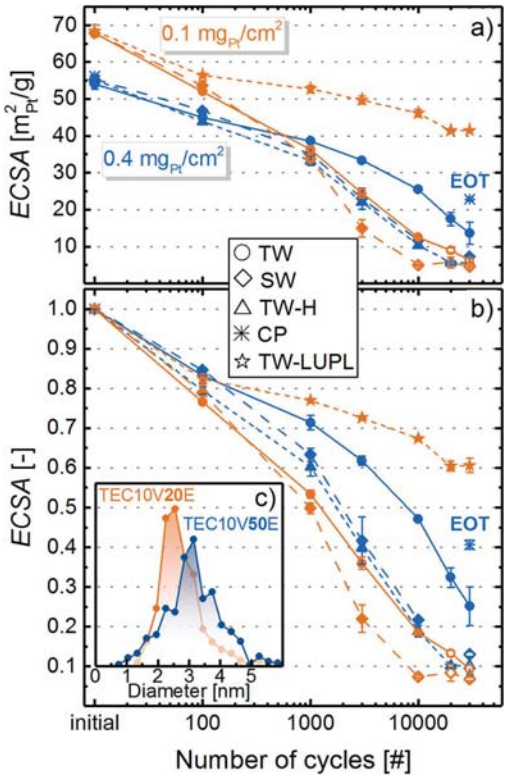

Figure 5. a) Cathode *ECSA* of all tested MEAs with cathode loadings of 0.4 mg_{Pt}/cm^2 (blue symbols) and 0.1 mg_{Pt}/cm^2 (orange symbols), recorded for TW cycling between 0.6 and 1.0 V_{RHE} (s. Figure 2a; solid lines, circles) as well as SW cycling between 0.6 and 1.0 V_{RHE} (s. Figure 2b; long-dashed lines, diamonds). For 0.4 mg_{Pt}/cm^2 loadings, also a TW-H profile (s. Figure 2c; short-dashed lines, triangles) was examined, while for 0.1 mg_{Pt}/cm^2 loadings a triangular cycle with a lowered upper potential limit of 0.85 V_{RHE} (s. Figure 2d; short-dashed lines, stars) was tested. The single point labeled CP (blue star symbol placed at 30000 cycles) depicts the *ECSA* after an 8 hour hold at 1.2 V_{cell}, (under N_2 at 95°C, 100% *RH*, and 100 kPa_{abs}), where substantial carbon support oxidation occurs. For high *rf* values, the *ECSA* was evaluated from the integration of the H_{upd} area, shown by a full symbol in the graph; for low *rf* values, the *ECSA* was determined by CO stripping and corrected by the scaling factor to allow comparability with the *ECSA* determined from H_{UPD} (denoted by open symbols). b) *ECSA* evolution over voltage cycling normalized to its initial value. The error bars represent the mean absolute deviation between two independently conducted experiments for each AST. c) Particle size distribution for the 20%$_{wt}$ Pt/C catalyst (orange) and the 50%$_{wt}$ Pt/C catalyst (blue).

30000 cycles (apart from the TW-LUPL and CP protocols). Since the change of potential in the applied ASTs results in a repetitive reduction/oxidation of the Pt surface, Ostwald ripening and a loss of Pt into the ionomer phase are expected to be the major contributors to the overall loss of active surface area. The gradual stabilization of the *ECSA* after extended voltage cycling, also observed in previous studies,[49] is likely due to the higher thermodynamic stability of larger Pt particles against dissolution. In contrast to the similar trend of decaying *ECSA* for all tested samples, its evolution with respect to the aging protocol and the cathode loading differs widely. First of all, it is noteworthy that the *ECSA* at BOT is higher for low-loaded cathodes (68 ± 1 m^2_{Pt}/g) compared to those with a higher loading (55 ± 1 m^2_{Pt}/g). As mentioned earlier, the electrode thickness was maintained constant for all tested MEAs (≈10 μm), which required a catalyst with 20%$_{wt}$ Pt content to prepare low-loaded catalyst layers, whereas 50%$_{wt}$ Pt/C was used for high-loaded electrodes. Even though both catalysts were obtained from the same supplier, Pt nanoparticles are commonly more homogeneously dispersed on the carbon support at low Pt to carbon ratio. This leads to a lower degree of Pt agglomeration, hence a lower average particle size and higher *ECSA*.[50] In fact, an evaluation of the particle size distribution (Figure 5c) by counting ≈400 individual particles (in TEM images) revealed a number averaged diameter of 2.8 ± 0.8 nm and 3.2 ± 1.0 nm for 20%$_{wt}$ and 50%$_{wt}$ Pt/C, respectively. As reported frequently by other researchers, Ostwald ripening is more pronounced for small particles compared to larger ones due to their intrinsically lower stability versus dissolution upon oxidation/reduction.[19] In accordance with this, for any given aging protocol, a faster decay of the *ECSA* is observed for low-loaded (orange colored in Figure 5) compared to high-loaded cathodes (blue colored in Figure 5). In summary, the observed relatively stronger *ECSA* fade for lower catalyst layer loadings in this study is not primarily caused by the cathode loading itself, but is most likely due to the different aging behavior of Pt nanoparticles with different size and different degrees of agglomeration.

Comparing different aging protocols, the *ECSA* loss is more pronounced for MEAs subjected to SW aging (long-dashed lines) compared to TW aging (solid lines), resulting in a dramatically low *ECSA* already after 10000 square wave cycles between 0.6 and 1.0 V_{RHE} (11 m^2_{Pt}/g for high-loaded and 5 m^2_{Pt}/g for low-loaded cathodes). The accelerated degradation caused by square wave compared to triangular wave aging has frequently been observed for PEMFCs,[40] as well as in liquid electrolyte.[39] There are four possible hypotheses to rationalize the faster degradation during SW cycling: i) a more significant carbon corrosion due to an extended hold period at high potential, eventually resulting in Pt particle detachment, accompanied by a thinning of the cathode catalyst layer; ii) the fast potential transient of the square wave modulation (>4 V/s) could induce more severe Pt dissolution forced by a fast reconstruction of the Pt surface from an oxidized to a reduced state; iii) the holding time at high potential induces a growth of the oxide, resulting in a stronger dissolution in the subsequent cathodic scan;[51] or, iv) the hold time at high anodic potentials provides more time for Pt dissolution and diffusion through the ionomer phase. As was shown by Cherevko et al., polycrystalline Pt in 0.1 M H_2SO_4 dissolves at constant anodic potential during about 600 s which is in the same order of magnitude as the dissolution during a potential transient.[52] The constantly released Pt ions can diffuse towards the membrane, where they are reduced by H_2 permeating through the membrane from the anode, causing a redeposition of electrically disconnected Pt particles within the ionomer phase.[20] The following analysis will shed some light onto the origin of the different aging of MEAs exposed to SW or TW potential profiles as well as at the degradation caused by holding at high potential to deliberately corrode the carbon support.

To investigate whether significant carbon support corrosion takes place over the course of the various voltage cycling protocols, which should lead to cathode thinning, MEA cross sections were prepared at EOT and imaged by SEM. Since the initial thickness of the electrodes at BOT could not be determined by SEM without damaging the MEA, the packing density of high-loaded and low-loaded catalyst layers was evaluated by measuring the thickness and catalyst loading of pristine MEAs (amounting to 22 ± 4 μm/(mg_C/cm^2), see experimental section), from which the initial thickness of each MEA could be calculated by its measured catalyst weight. The catalyst layers exposed to TW or SW aging between 0.6 and 1.0 V_{RHE} (Figures 6a/6b/6d/6e) show no catalyst layer collapse compared to a pristine MEA (Figure 6c), eliminating carbon corrosion as a likely contributor to the overall degradation. Interestingly, the catalyst layers depicted in Figures 6a/6b and 6d/6e show a bright area at the cathode/membrane interface, representing an accumulation of Pt in the membrane phase, caused by precipitation of dissolved Pt in the ionomer phase.[20,30] However, due to the rather qualitative nature of such SEM images, no conclusion on the quantitative differences between the amount of deposited Pt during TW and SW cycling can be drawn, even though the larger *ECSA* loss in the SW protocol points towards a higher amount of disconnected Pt. The absence of cathode thinning was also confirmed for all other

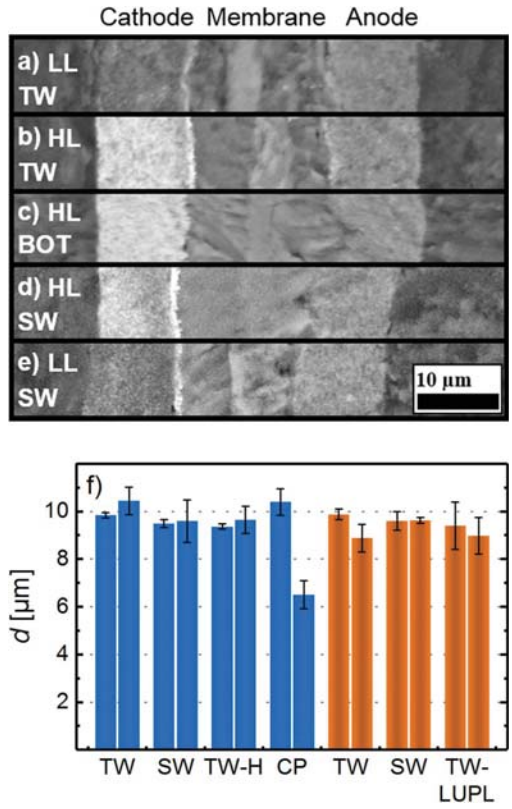

Figure 6. SEM cross-section images of MEAs at BOT and after 30000 potential cycles: low-loaded MEAs (0.1 mg_{Pt}/cm^2) after TW (a) and SW (e) aging between 0.6 and 1.0 V_{RHE}. High-loaded catalyst layers (0.4 mg_{Pt}/cm^2) of a pristine MEA (c), an MEA after 30000 TW cycles and c) an MEA after SW cycles between 0.6 and 1.0 V_{RHE}. Images were taken by SEM at a magnification of 2000x in electron back-scattering mode. f) Average cathode thickness of MEAs subjected to different aging protocols both at BOT (left-hand bars in each group) and at EOT (right-hand bars in each group), with high-/ and low-loaded cathodes shown in blue/orange color, respectively. The error bars represent the standard deviation between two independently conducted experiments for each aging protocol; voltage cycling aging protocols are described in Figure 2 and CP refers to cathodes subjected to an 8 hour potential hold at 1.2 V_{cell} (under N_2 at 95°C, 100% *RH*, and 100 kPa_{abs}).

cathode electrodes which had been subjected to voltage cycling tests, whose thicknesses was found not to change between EOT and BOT, as is shown in Figure 6f. Quite clearly, carbon support corrosion must be rather minor over 30000 voltage cycles between 0.6 and 1.0 V_{RHE} since any significant carbon corrosion is accompanied by cathode thinning (noticeable once ca. 5–7% carbon are corroded).[53] However, we cannot fully exclude the possibility that a small extent of carbon corrosion might occur (small enough to not lead to cathode thinning), which then could contribute to the observed *ECSA* degradation by a particle detachment mechanism. To determine the effect of substantial carbon support corrosion on the *ECSA*, cathodes were held for 8 hours at 1.2 V_{cell} (under N_2 at 95°C, 100% *RH*, and 100 kPa_{abs}), which resulted in a decrease of the catalyst layer thickness by ≈40%; despite the large extent of carbon corrosion, the *ECSA* remained at a reasonably large value of ≈22 m^2_{Pt}/g (blue asterisks in Figure 5).

To obtain further insights into the origin of the faster degradation upon SW aging, seeking to differentiate between *ECSA* loss caused by the holding time at high potential which might enhance Pt loss into the membrane phase and that originating from the fast Pt oxidation/reduction transient in SW cycling, the potential step in the SW protocol was replaced by a potential sweep with the same scan-rate as in the TW protocol (Figure 2c). This voltage cycling AST is referred to as TW–H. As shown in Figure 5, the decrease of the cathode *ECSA* over the course of SW (blue long-dashed line, diamonds) and TW-H (blue short-dashed line, triangles) is identical, indicating that the rapid potential transient has no influence on the *ECSA* degradation and that it is rather the holding time at each potential that is the controlling factor. This can either be explained by the higher oxide coverage of Pt formed at longer holds at high potential, which Gilbert et al. hypothesized to lead to a larger extent of Pt dissolution during a subsequent step to lower potentials at which the oxide is reduced, leading to faster *ECSA* losses for SW profiles.[51,39] An alternative explanation is that the holding time at high potentials allows for a longer time of Pt dissolution and subsequent diffusion in the ionomer phase towards the cathode/membrane interface, where it can deposit as electrically insulated particles by reduction with cross-over hydrogen. The latter mechanism would explain the apparently higher accumulation of Pt at the cathode/membrane interface for the SW compared to the TW modulation suggested qualitatively by the above SEM analysis (compare Figures 6a/6b and 6d/6e). Therefore, our experiments suggest that the faster degradation by SW cycling is caused by a more severe Pt dissolution and simultaneously allowing sufficient time for Pt diffusion towards the cathode/membrane interface and its deposition as electrically insulated particles, rather than by carbon support corrosion or the fast voltage transient. It shall be mentioned that the aging per time interval was in fact smaller for TW-H compared to SW, since both methods showed a similar degradation per cycle while one scan in the TW-H procedure required double the time (32 sec) compared to SW (16 sec). However, the cathode potential remains below 0.9 V_{RHE} for a substantial fraction of the time, while we believe that higher potentials are most detrimental for the *ECSA*.

To probe the degradation at lower potentials, a triangular scan procedure with a lower upper potential limit (TW-LUPL) of 0.85 V_{RHE} (orange star symbols and short-dotted lines in Figure 5) was tested. In this case, carbon corrosion most certainly will not play a role, so that aging from Pt detachment from the carbon support can surely be excluded (the above analysis suggests, carbon corrosion is not a major contributor to *ECSA* loss even for upper potentials as high as 1.0 V_{RHE}). In addition, Pt dissolution/redeposition effects should also decrease substantially, since the degree of Pt surface oxidation is limited, leading to less Pt dissolution, hence to a smaller overall *ECSA* loss (40% after 30000 aging cycles).[20] Since the *ECSA* loss during TW-LUPL is comparatively low, we conclude that most of the additional time during TW-H compared to SW is non-damaging, e.g. below 0.85 V_{RHE}. We therefore believe that the lower amount of *ECSA* loss per time (not per cycle) in the TW-H procedure can be mainly attributed to the additional time at these low, non-damaging potentials. In the light of the rather small *ECSA* loss when limiting the upper potential to 0.85 V_{RHE} (TW-LUPL) compared to the TW aging protocols with an upper potential limit of 1.0 V_{RHE} for which *ECSA* losses of ≈90% over 30000 cycles are observed, avoiding high voltages (e.g., OCV) appears highly advisable to maximize PEMFC durability.

AST induced ORR activity changes.—Assuming simple Tafel kinetics for the ORR according to Equation 1, lowering the cathode *rf* over the course of ASTs should directly cause an increase of the ORR overpotential according to:[6,54]

$$\eta = TS \cdot \left[\lg \left(\frac{i}{i_0} \cdot \frac{1}{rf} \right) \right] \quad [1]$$

where η denotes the ORR overpotential in mV, *TS* is the Tafel slope in mV/dec, *i* denotes the current density in A/cm^2, i_0 is the exchange current density in A/cm^2_{Pt}, and *rf* denotes the roughness factor in cm^2_{Pt}/cm^2.

In Figure 7a, differential flow H_2/O_2 polarization curves at 80°C and 100% *RH* are shown for all AST protocols at BOT and after 30000 aging cycles. First of all, a voltage offset is observed in the initial polarization curves of low-loaded (solid orange lines) compared to high-loaded (solid blue lines) cathodes at BOT. Based on simple Tafel

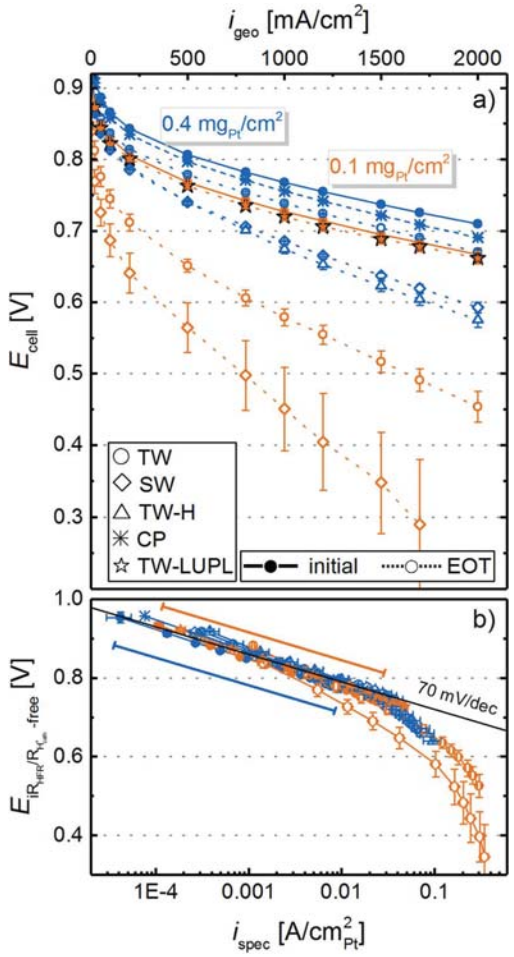

Figure 7. Differential flow H_2/O_2 (2000/5000 nccm) performance for MEAs with 0.4 mg$_{Pt}$/cm^2 (blue lines/symbols) and 0.1 mg$_{Pt}$/cm^2 (orange lines/symbols) cathodes at BOT (solid lines and filled symbols) and at EOT, i.e., after 30000 voltage cycles or an 8 hour hold at 1.2 V_{cell} (dotted lines or hollow symbols). a) Measured cell voltage curves at a pressure of 170 kPa$_{abs}$, a temperature of 80°C, and an *RH* of 100%. b) Tafel plot representation normalized to the *ECSA*, corrected by the *HFR*, the effective proton conduction resistance, as well as by the H_2 crossover and electrical short current. BOT polarization curves of all tested MEAs were averaged and error bars represent the standard deviation of all tested MEAs. Error bars for EOT curves represent the mean absolute deviation between two measurements. The two slanted lines in b) indicate the specific current density region for high-loaded (blue) and low-loaded (orange) MEAs at BOT.

kinetics (Equation 1) and an ORR Tafel slope of 70 mV/dec, four times lower Pt cathode loadings should result in an approximately four times lower roughness factor (as the catalyst *ECSA* is very similar) and thus to an additional overpotential of ≈42 mV at the same current density, which is in excellent agreement with the observed offset between high- and low-loaded MEAs (e.g., 737 ± 3 mV vs 695 ± 8 mV at 1.5 A/cm^2 (42 ± 11 mV) for high- and low-loaded electrodes, respectively).

Over the course of 30000 voltage cycles (≡ EOT condition), the polarization curves of all tested MEAs degrade significantly, with a more severe performance decay for low-loaded MEAs (e.g., 214 mV loss at 2 A/cm^2 for the TW protocol) compared to high-loaded MEAs (39 mV loss at 2 A/cm^2). When comparing polarization curves from different aging protocols, the previously identified higher *ECSA* loss for SW compared to TW cycling correlates well with the observed performance difference in the O_2 polarization curve at EOT for both loadings. Furthermore, a similar performance decay is observed for the TW-H and SW protocol, e.g., a voltage of 593 ± 8 mV for SW and 575 ± 1 mV for TW-H at 2 A/cm^2 and EOT, which is in accordance with the comparable loss of *ECSA*. In contrast to the other AST protocols, EOT polarization curves for the TW-LUPL protocol do not show any degradation compared to BOT, reflecting the comparably low degradation of the *ECSA*.

To determine the specific ORR activity for each MEA, the polarization curves were corrected by the *HFR* (R_{HFR}), the H_2 crossover current ($i_{H_2-cross}$, on the order of ≈4 mA/cm^2), the shorting current (i_{short}), the effective proton conduction resistance in the cathode catalyst layer ($R_{H^+}^{cath,eff}$), and were normalized to the Pt surface area (Figure 7b). As expected for H_2/O_2 polarization curves dominated by kinetic overpotentials, all data points fall on a straight line, with a BOT Tafel slope of 70 ± 3 mV/dec for high-loaded and 73 ± 3 mV/dec for the low-loaded MEAs. After 30000 voltage cycles, the apparent Tafel slope of high-loaded MEAs, determined in the low current density region (50–500 mA/cm^2), increases to 79 ± 1 mV/dec for TW aged MEAs and more significantly (≈90 mV/dec) for the SW and TW–H aging protocols. Tafel slopes of around 120–160 mV/dec were observed for low-loaded MEAs subjected to 30000 TW and SW cycle protocols, while the Tafel slope remained unchanged over the course of the TW-LUPL voltage cycling AST. An increasing Tafel slope upon aging was also observed by other researchers,[21] and is attributed to additional, non-kinetic overpotentials, such as O_2 mass transport or proton transport losses which apparently increase with extended voltage cycling. Since the electrode thickness remained unchanged (Figure 6f), even for the most damaging aging protocols (SW and TW-H), a hindrance of the gas phase mass transport caused by a deterioration of the overall catalyst layer structure can be excluded. Although, slight corrosion of the catalyst support and a concomitant slight decrease of the available pore volume cannot be fully excluded, cathode thinning was clearly not observed by SEM in any of our experiments. Additionally, changes of the Tafel slope due to loss or restructuration of the ionomer can be excluded as the proton transport resistance did not change significantly upon voltage cycling (not shown) and major chemical degradation of the ionomer can be excluded due to the absence of oxygen in the largest fraction of the experimental time.[56]

We would like to emphasize that these measurements were performed with pure O_2, where gas phase O_2 transport resistances can be excluded as possible cause for the increasing apparent Tafel slopes. It is also worth noting that these severe and unassigned mass transport overpotentials occur at similar values of the Pt specific current density (near ≈0.05 A/cm$^2_{Pt}$) in all H_2/O_2 polarization curves. At high Pt specific current densities, caused by ultra-low *rf* values, additional voltage losses have also been observed by other researchers.[9,10,55] Since this overpotential occurs at high geometric current densities and low cathode *rf* values, i.e., at high local oxygen flux to the Pt surface, we hypothesize that it is related to oxygen transport limitations at the catalyst/ionomer interface. Suggestions for the observed voltage losses at high Pt-specific currents by other research groups include a limited dissolution of oxygen into the ionomer phase,[57] an intrinsically high transport resistance of the thin ionomer phase,[58] a limited effective ionomer surface,[10,37] or a decrease of the ORR kinetics at low potential.[59] Although we cannot exclude any one of these effects, a Pt/ionomer specific resistance appears most reasonable to explain the observed voltage losses at high Pt-specific currents, as the voltage profile shows a shape resembling a mass transport limitation, rather than a kinetic phenomenon.

A linear regression of the measured data in the current density range from 50 to 500 mA/cm^2 and extrapolation to 0.9 V_{RHE} yields the kinetic ORR activity at 0.9 V_{RHE} (at 120 kPa$_{abs}$ O_2 partial pressure), commonly used to compare the catalytic activity of platinum. It can either be normalized to the measured *ECSA* to yield the specific current density for the ORR at 0.9 V_{RHE} ($i_{0.9\,V}^{spec}$, Figure 8b) or to the mass of Pt in the cathode catalyst layer to yield the mass activity for the ORR at 0.9 V_{RHE} ($i_{0.9\,V}^{mass}$, Figure 8a) to enable comparability between all experiments. In general, the here determined ORR

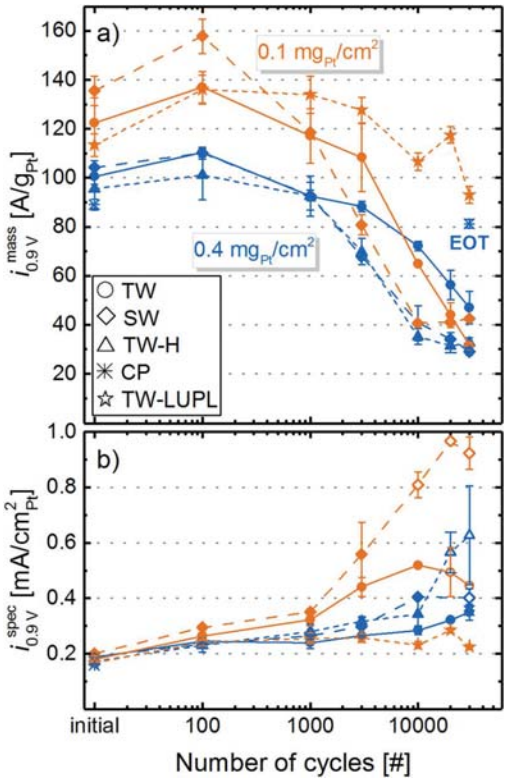

Figure 8. a) ORR mass activity at 0.9 V ($i^{mass}_{0.9\,V}$) and b) ORR specific activity at 0.9 V ($i^{spec}_{0.9\,V}$) extracted from Figure 7 for MEAs with 0.4 mg$_{Pt}$/cm^2 (blue lines/symbols) and 0.1 mg$_{Pt}$/cm^2 (orange lines/symbols) cathodes over the course of various ASTs. The exchange current density at 0.9 V was obtained by a linear regression of fully corrected polarization curves in O_2 between 50 and 500 mA/cm^2.

mass activities at BOT (≈110–140 A/g$_{Pt}$ for the 20%$_{wt}$ Pt/V catalyst and ≈85–105 A/g$_{Pt}$ for the 50%$_{wt}$ Pt/V catalyst) compare well with those reported by other researchers for Pt supported on Vulcan type carbon.[7,60,61] In accordance with the severe *ECSA* loss in most of the here examined aging protocols, the overall surface available for the ORR decreases significantly from BOT to EOT (low-loaded TW, SW and TW-H: ≈90% *ECSA* loss), there is also a significant loss of $i^{mass}_{0.9\,V}$ over the course of aging for all loadings and aging procedures (see Figure 8a). Comparing TW (solid lines, circles) and SW (long-dashed lines, diamonds), the decrease of $i^{mass}_{0.9\,V}$ as a function of cycle number is more pronounced for SW profiles, which is directly correlated to the stronger *ECSA* loss (see Figure 5). To clarify, the accelerated decrease of $i^{mass}_{0.9\,V}$ by SW compared to TW modulations most likely represents a true change in the ORR kinetics, as interference from O_2 mass transport resistances in pure O_2 in the low current density region (data evaluation was restricted to a maximum current density of 500 mA/cm^2) should be negligible. This assumption is reasonably justified since only a slight increase in the *apparent* Tafel slope was observed upon aging (e.g., 70 ± 3 mV/dec at BOT increases to 86 ± 2 mV/dec at EOT for high-loaded SW cycled cathodes) and since we eliminated regions at high specific current density (where local transport resistances could be important) from the analysis. As expected from our preceding analysis of the *ECSA* development (see Figure 5), the mass activity of electrodes aged by TW-H cycles is essentially identical to those aged by SW cycles (compare blue triangle and diamond symbols in Figure 8a), underlining our previous hypothesis that the potential hold phase is the dominating factor for MEA degradation during square wave aging. Finally, the ORR mass activity loss over the TW–LUPL procedure (orange stars) is significantly lower compared to the other protocols, which again is in accordance with the lower *ECSA* loss.

It is interesting to note that in contrast to the overall trend of decreasing ORR mass activity, $i^{mass}_{0.9\,V}$ reaches a maximum after 100 cycles, particularly noticeable for low-loaded MEAs. This could be ascribed to an activation of the catalyst particles due to cleaning of the Pt surface, which might overcompensate the *ECSA* loss of ≈20% in the initial 100 cycles. If true, this would mean that the initial activation procedure (see experimental section) was not sufficient to fully activate the cathode catalyst layer. Alternatively, there is the possibility that the measurement sequence (described in Figure 1) might influence the observed small variation of the measured ORR activity. While the O_2 polarization curves at BOT as well as at 10000, and at 30000 cycles were recorded after polarization curves in 10% O_2 and in air (each approximately 3.5 h), all other O_2 polarization curves were recorded directly after a recovery step. Thus, it is possible that after these two polarization curves without an intermediate recovery step, a certain extent of reversible degradation (i.e., Pt poisoning) might have occurred,[62] resulting in a lower ORR mass activity. Evidence for this behavior can be seen for the low-loaded MEAs tested with the TW-LUPL procedure (orange stars in Figure 8a), where ORR mass activities were always higher when measured directly after a recovery step (i.e., at 100, 1000, 3000 and 20000 cycles), while reproducibly lower values were obtained in the absence of a directly preceding recovery step (at BOT as well as at 10000 and 30000 cycles). Since the overall degradation rate induced by the TW-LUPL procedure is rather small (≈40% loss in *ECSA* and $i^{mass}_{0.9\,V}$ after 30000 cycles), this presumably testing procedure related inaccuracy of ≈10% in the quantification of $i^{mass}_{0.9\,V}$ might have become apparent. Nevertheless, this minor uncertainty in ORR mass activity values is of no consequence to the conclusions drawn from these data.

Further insights into the aging process can be obtained by examining the specific ORR activity at 0.9 V_{RHE}, $i^{spec}_{0.9\,V}$, as shown in Figure 8b. It is well-known that small Pt nanoparticles have a lower specific ORR activity due to their relatively larger amount of edge and corner sites compared to larger nanoparticles.[63] Amongst others, Mayrhofer et al. found an increase of the specific activity of Pt particles by a factor ≈2 when going from 1 nm sized particles to 5 nm.[64] In our case, the determined specific ORR activities of low-loaded (182 ± 18 μA/cm$^2_{Pt}$) and high-loaded MEAs (177 ± 16 μAcm$^2_{Pt}$) at BOT are essentially identical, consistent with the very similar average particle size of the two catalysts (2.8 ± 0.8 nm for 20%$_{wt}$ Pt/C and 3.2 ± 1.0 nm for 50%$_{wt}$ Pt/C). In the course of aging, the specific activity increases for all tested MEAs due to the constantly growing fraction of larger particles. The highest observed ORR activity (≈1 mA/cm$^2_{Pt}$) was found for low-loaded catalyst layers with the most significant *ECSA* loss (Figure 5) due to the harsh SW aging protocol. However, it shall be noted that the determination of the catalyst activity is slightly impaired by an increased Tafel slope for MEAs with a very small *rf* value, hence the calculation of $i^{spec}_{0.9\,V}$ becomes increasingly erroneous for strongly aged catalyst layers due to difficulties in determining kinetic parameters accurately.

AST induced H$_2$/air and H$_2$/10%O$_2$ performance losses.—To obtain further information about mass transport related overpotentials induced by the different aging protocols, polarization curves in air and 10% O_2 (to simulate conditions at the cathode outlet of a PEMFC stack operated at an air stoichiometry of ≈1.75) were measured at several aging stages (Figure 9). The solid lines are the average BOT performance of MEAs with 0.4 mg$_{Pt}$/cm^2 (blue) and 0.1 mg$_{Pt}$/cm^2 (orange) cathode loadings at the here investigated operating conditions of 170 kPa$_{abs}$, 80°C, and 100% *RH* (error bars represent the standard deviation across all measured MEAs, indicating the excellent reproducibility of the performance at BOT). Similarly to polarization curves in O_2 (Figure 7a), a clear offset between high-loaded and low-loaded cathodes, resulting from a different cathode *rf*, is observed for BOT polarization curves in air (e.g., 689 ± 3 mV vs 634 ± 10 mV at 1.5 A/cm^2 for high- and low-loaded electrodes, respectively) and 10% O_2 (e.g., 620 ± 10 mV vs 496 ± 9 mV at 1.5 A/cm^2 for high- and

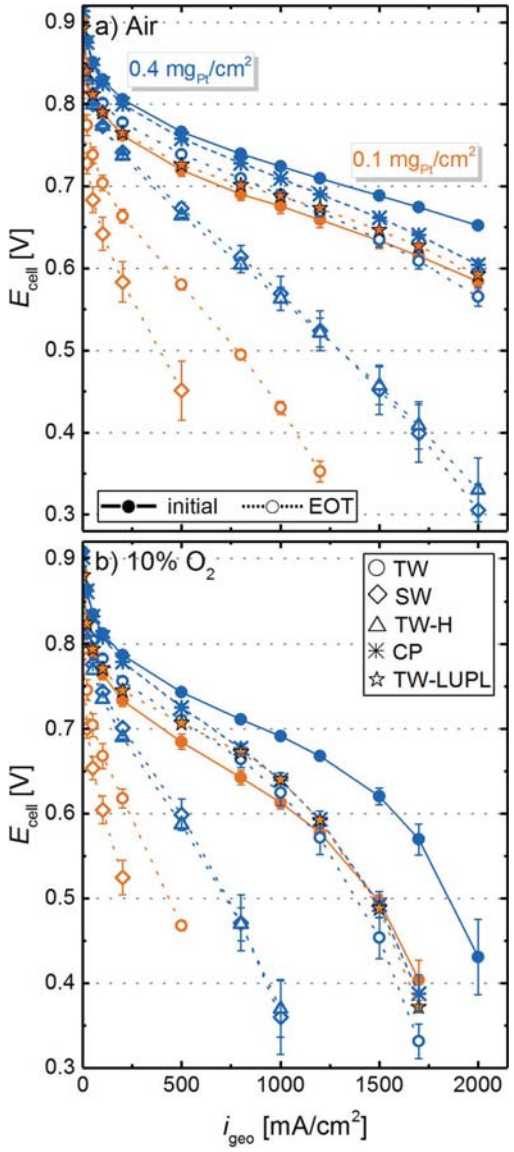

Figure 9. Differential flow a) H_2/air and b) H_2/10% O_2 (2000/5000 nccm) performance (170 kPa_{abs}, 80°C, and 100% *RH*) for MEAs with 0.4 mg_{Pt}/cm^2 (blue lines/symbols) and 0.1 mg_{Pt}/cm^2 (orange lines/symbols) cathodes at BOT (solid lines and filled symbols) and at EOT, i.e., after 30000 voltage cycles or an 8 hour hold at 1.2 V_{cell} (dotted lines or hollow symbols). BOT polarization curves of all tested MEAs were averaged and error bars represent the standard deviation of all measurement points. At EOT, error bars represent the mean absolute deviation of two measurements.

low-loaded electrodes, respectively). In contrast to pure O_2, where the offset perfectly matched the increase of η_{ORR} predicted by Equation 1, the voltage loss for low-loaded MEAs in air (e.g., 55 ± 13 mV at 1.5 A/cm^2) and 10% O_2 (e.g., 124 ± 19 mV at 1.5 A/cm^2) was much higher than the kinetically expected penalty. The additional voltage loss for low-loaded cathodes in air, being even more pronounced in 10% O_2, is an initial hint on a mass transport overpotential related to the *rf* value of the cathode. Several other researchers reported the occurrence of such a Pt surface area specific O_2 mass transport resistance (termed $R_{O_2}^{Pt}$ in this manuscript) for pristine cathodes with different loadings and showed its substantial increase with decreasing cathode *rf* values by limiting current measurements.[8–10,41]

High-loaded MEAs aged by the SW and TW-H protocol (open blue diamonds and triangles in Figure 9) show a similar performance at EOT, which was significantly lower compared to MEAs aged by the TW protocol (open blue circles). This is in accordance with the above discussed O_2 polarization curves (Figure 7a) and *ECSA* losses (Figure 5a). Even though the overall performance losses are rather dramatic for the low-loaded MEAs, they also show the same increased aging when subjected to SW rather than TW voltage cycling (open orange diamonds and circles). However, as one might have hoped based on the *ECSA* (Figure 5) and ORR mass activity (Figure 8a) data, even with low-loaded cathodes no voltage cycling induced performance losses occur over 30000 cycles when using the TW-LUPL protocol with a lowered upper voltage limit of 0.85 V_{RHE}, neither in H_2/air nor in H_2/10% O_2 (orange stars in Figure 9).

An interesting insight into the *rf* dependent $R_{O_2}^{Pt}$ induced losses can be gained by comparing the H_2/air EOT performance of the high-loaded cathode subjected to TW cycling (open blue circles) and the low-loaded cathode subjected to TW-LUPL cycling (orange stars). At EOT, the high-loaded cathode has a slightly higher roughness factor (56 ± 12 cm^2_{Pt}/cm^2) compared to the low-loaded cathode (42 ± 2 cm^2_{Pt}/cm^2), so that one would expect a similar or an even lower $R_{O_2}^{Pt}$ value for the former. At the same time, the specific ORR activity at 0.9 V_{RHE} for the high-loaded cathode (350 ± 29 $\mu A/cm^2_{Pt}$) is substantially larger than that for the low-loaded cathode (224 ± 7 $\mu A/cm^2_{Pt}$). Since the product of ($i_{0.9\,V}^{spec} \cdot rf$), equating to 19.6 mA/cm^2_{Pt} for the high-loaded and 9.2 mA/cm^2_{Pt} for the low-loaded cathode, is proportional to ($i_0 \cdot rf$) under the same operating conditions, the η_{ORR} difference predicted by Equation 1 is ≈23 mV, suggesting that the kinetically predicted EOT performance of the high-loaded cathode subjected to TW cycles should be ≈23 mV higher than that of the low-loaded cathode subjected to TW-LUPL cycles. This is consistent with the higher H_2/O_2 performance of the former (see Figure 7a) and also its superior low current density performance in H_2/air or H_2/10%O_2 (see Figure 9). However, despite its higher EOT roughness factor, the TW-aged high-loaded cathode exhibits a larger (unassigned) mass transport loss, evident by its lower H_2/air or H_2/10%O_2 performance at current densities above ≈1 A/cm^2 (see Figure 9). Since no significant differences in the effective proton conduction resistance (measured by EIS) were observed between these two electrodes, an apparently larger oxygen transport resistance, which is not simply related to the cathode *rf* value and produced by voltage cycling, must exist. Its origin is unclear at the moment, but it may be related to the morphological changes and redistribution of Pt within the cathode electrode caused by voltage cycling.

O_2 transport resistance evaluation.—In order to disentangle mass transport resistances originating from gas transport in the flow fields and the GDL from those in the catalyst layer, and to identify resistances dependent on the cathode *rf* value, limiting current measurements were executed according to the method developed by Baker et al.[36] In this approach, the concentration of O_2 (dry gas fraction in N_2) in the feed gas is varied from 4% to 24%, while a low potential between 0.05 and 0.30 V is applied to obtain the limiting current, where the O_2 concentration at the Pt surface decreases to zero and the current-voltage profiles at different O_2 concentrations resemble a vertical line (see Figure 10a). For each concentration, the O_2 mass transport resistance is calculated and plotted versus the respective limiting current density, as illustrated in Figure 10b for the low-loaded cathode MEAs at BOT and after 30000 SW cycles (for details on the analysis see Simon et al.).[32]

For all cathodes at BOT, the total oxygen mass transport resistance, $R_{O_2}^{total}$, is essentially independent of the limiting current density at all pressures (see triangles in Figure 10b and its inset), as is expected under these conditions for the Freudenberg GDL.[65] Furthermore, the determination of the limiting current density at various pressures enables the separation of $R_{O_2}^{total}$ into a pressure dependent ($R_{O_2}^{PD}$) and a pressure independent ($R_{O_2}^{PI}$) oxygen mass transport resistance via a linear regression of $R_{O_2}^{total}$ versus the absolute pressure (Figure 10c).

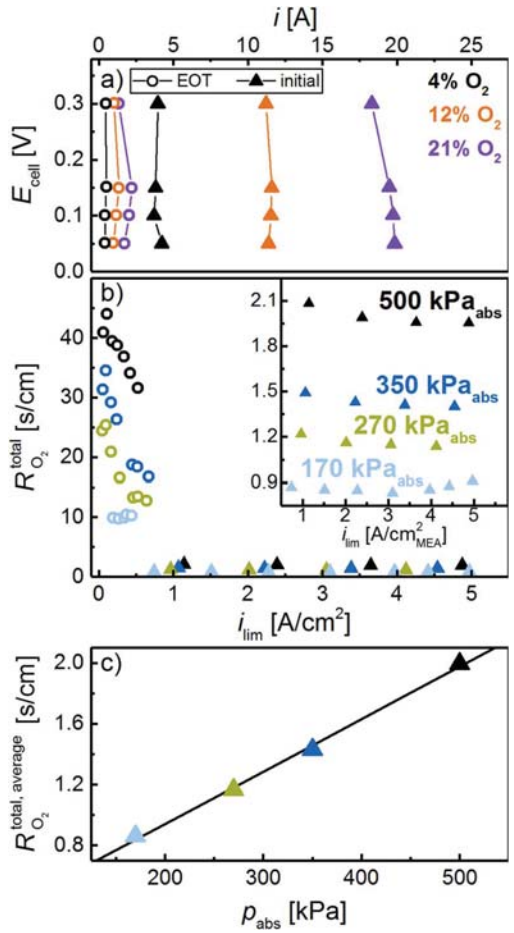

Figure 10. a) Limiting current measurement in the potential range between 0.30 and 0.05 V at O_2 concentrations of 4%, 12%, and 21%, comparing a 0.1 mg_{Pt}/cm^2 cathode at BOT (triangles) and after 30000 SW cycles (circles). Measurements were performed at 80°C, 100% *RH*, and 170 kPa_{abs} (using 2000 nccm H_2 and 5000 nccm O_2 in N_2). b) Total O_2 mass transport resistance vs limiting current density at 170, 270, 350 and 500 kPa_{abs} (O_2 concentration between 4% and 24%); the inset is a zoom into the low $R_{O_2}^{total}$ region at high limiting current densities. c) $R_{O_2}^{total}$ of the BOT cathode averaged over all O_2 concentrations at the respective pressure; the shown linear regression line is used to deconvolute $R_{O_2}^{total}$ into $R_{O_2}^{PD}$ and $R_{O_2}^{PI}$.

Nevertheless, a severe decrease of the limiting current is observed for low-loaded cathodes after extended TW or SW cycling, exemplarily shown in Figure 10a for the SW protocol (BOT ≡ triangles; EOT ≡ circles). At EOT, the limiting current density (circles in Figure 10a) is significantly lower, and the resulting $R_{O_2}^{total}$ values are more than an order of magnitude larger than at BOT and change severely with limiting current density, especially at higher pressures (circles in Figure 10b). We attribute this unsteady transport resistance at higher pressures to a local catalyst layer/GDL flooding (at an inlet *RH* of 100%) due to the low limiting current, at which no significant through-plane temperature gradient between MEA and flow field can be established, thereby hampering product water removal through the gas phase. This hypothesis is underpinned by the fact that the transport resistance is strongly decreasing with increasing current density, i.e., at a higher temperature gradient. The effect of flooding is even more pronounced at higher applied pressures, analogous to what is generally observed.[66] As the evaluation of $R_{O_2}^{total}$ at higher pressure is not reliable in cases like the one shown in Figure 10b (circles), a deconvolution of $R_{O_2}^{total}$ into $R_{O_2}^{PD}$ and $R_{O_2}^{PI}$ is not trustworthy, hence only the total transport resistance at 170 kPa_{abs} is considered in these instances. The origin of this effect is yet unclear, but as will be shown in the following, it is not related to carbon support corrosion.

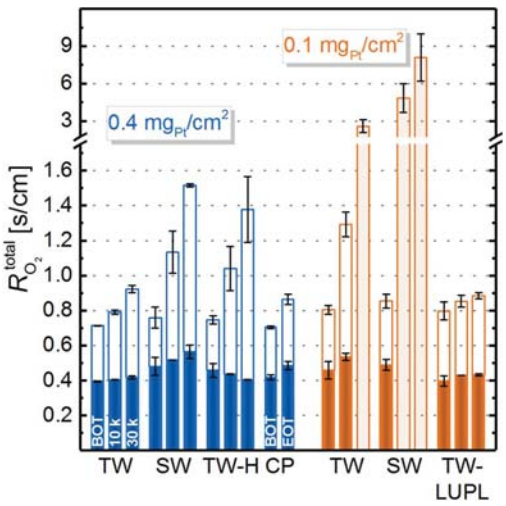

Figure 11. Total oxygen mass transport resistance ($R_{O_2}^{total}$) determined at 80°C, 100% *RH*, and 170 kPa_{abs} (differential flow of hydrogen and 4% - 21% O_2 (balance N_2) for high-loaded (blue) and low-loaded (orange) cathodes tested by different ASTs (for each, left bars are at BOT, middle bars at 10000 cycles, and right bars 30000 cycles). $R_{O_2}^{total}$ was also separated into pressure dependent ($R_{O_2}^{PD}$, solid bar) and pressure independent ($R_{O_2}^{PI}$, open bar) oxygen mass transport resistance contributions. For certain experiments, the deconvolution of $R_{O_2}^{total}$ was not reliable, thus only the total transport resistance at 170 kPa_{abs} is plotted as a dotted bar. Error bars correspond to the mean absolute deviation of two repeat experiments with different MEAs.

The total oxygen mass transport resistance at different stages of the aging protocol is shown for high-loaded (blue) and low-loaded (orange) cathodes in Figure 11, separated into pressure dependent, $R_{O_2}^{PD}$ (solid bars), and pressure independent, $R_{O_2}^{PI}$ (hollow bars) contributions, according to the above described analysis. All high-loaded (average of 0.73 ± 0.09 s/cm), as well as all low-loaded cathodes (average of 0.82 ± 0.10 s/cm) show a similar $R_{O_2}^{total}$ at BOT, demonstrating a reproducible MEA fabrication. In general, low-loaded cathodes show a slightly higher transport resistance than high-loaded electrodes at BOT, as already indicated by the observed voltage losses in H_2/air (Figure 9a) and H_2/10% O_2 polarization curves (Figure 9b). The pressure dependent transport resistance associated with the GDL is, as expected, essentially identical for high- ($R_{O_2}^{PD} = 0.44 \pm 0.05$ s/cm) and low-loaded ($R_{O_2}^{PD} = 0.45 \pm 0.05$ s/cm) cathodes at BOT. Therefore, the differences in $R_{O_2}^{total}$ originate from a higher pressure independent transport resistance, due to their lower cathode *rf* values ($R_{O_2}^{PI}$ high-loaded: 0.29 ± 0.04 s/cm; $R_{O_2}^{PI}$ low-loaded: 0.37 ± 0.05 s/cm).

Over the course of catalyst layer aging, the pressure dependent transport resistance remains reasonably constant, considering that the observed fluctuations are within the experimental accuracy. At the same time, $R_{O_2}^{PI}$ increases significantly. In general, $R_{O_2}^{PI}$ is composed of various contributions, namely Knudsen diffusion in small pores, diffusion in the ionomer and in water, as well as of the so-called Pt surface specific resistance ($R_{O_2}^{Pt}$). Since the ionomer content and the overall electrode thickness was constant in all experiments, we ascribe the higher $R_{O_2}^{PI}$ of low-loaded electrodes to a *rf* specific mass transport resistance. An increase of $R_{O_2}^{PI}$ was also observed by other researchers who conducted limiting current measurements for MEAs with different loading.[9,10,37,55] In accordance with the *ECSA* trends presented in Figure 5, $R_{O_2}^{PI}$ increases with decreasing *ECSA* values in all aging protocols. Consistently, the highest transport resistances

were obtained for procedures which showed the most severe *ECSA* losses, namely SW and TW-H for high-loaded cathodes as well as TW and SW for low-loaded cathodes. Comparing the transport resistance evolution for high-loaded catalyst layers, TW aging leads to less significant increases of $R_{O_2}^{PI}$ compared to SW and TW-H aging, which in turn show a similar transport resistance at each aging interval. Taking the similar *ECSA* decrease and the same performance in polarization curves of TW-H and SW into account, it is evident that the potential transient during aging is of minor importance, while the hold time at high potentials is the main contributor to electrode degradation. As described earlier, for degraded cathodes with ultra-low *rf* values (low-loaded cathodes subjected to 30000 TW cycles or to ≥10000 SW cycles), the deconvolution of pressure dependent and pressure independent resistance is not reliable, hence only the total transport resistance at 170 kPa_{abs} is shown in Figure 11.

To disentangle the effect of low *rf* values on the observed increase of the total transport resistance from possible transport limitations originating from carbon corrosion, cathodes were exposed to a constant potential hold (CP) of 1.2 V_{cell} for 8 h at 95°C and 100% *RH*. This procedure results in a thinning of the catalyst layer by approximately 40%, while maintaining a reasonably high *rf* value (from 222 ± 10 at BOT to 90 ± 2 cm^2_{Pt}/cm^2 at EOT). Despite the fact that the catalyst layer structure collapses in this experiment, the total transport resistance increases only moderately from 0.70 ± 0.01 to 0.86 ± 0.01 s/cm (see Figure 11). On the one hand, the slight increase of the pressure independent resistance can be attributed to the loss of *ECSA*, comparable to the other testing procedures which lead to lower *rf* values. On the other hand, since $R_{O_2}^{PD}$ is mostly associated with the transport resistances in the flow-field, the GDL, and the in the void volume within the catalyst layer, it would be reasonable to expect that it increases upon cathode thinning. Nevertheless, since the pressure dependent part of the transport resistance increases solely by 0.07 ± 0.04 s/cm (Figure 11), this hypothesis cannot be proven within the limited accuracy of this method. Considering that no thinning was observed for electrodes exposed to voltage cycling, the changes of $R_{O_2}^{total}$, and especially $R_{O_2}^{PI}$ in the course of aging are clearly not attributed to carbon corrosion. In other words, the much larger increase of $R_{O_2}^{total}$ and $R_{O_2}^{PI}$ over the course of all voltage cycling protocols (with the exception of the TW–LUPL protocol) where no cathode thinning was observed, must be related to phenomena other than carbon corrosion. Consistent with the essentially identical BOT and EOT performance of low-loaded cathodes subjected to TW-LUPL cycling, there is also essentially no increase of the total oxygen mass transport resistance.

As a comparison to the data in literature,[9] the pressure independent part of the O_2 mass transport resistance was plotted as a function of the *rf* in Figure 12. The clear trend of strongly increasing $R_{O_2}^{PI}$ with decreasing platinum surface area (i.e., *rf* < 50 cm^2_{Pt}/cm^2) presented here, was also observed by Greszler et al. and underlines the previously stated hypothesis that the high O_2 mass transport resistance is a strong function of the cathode *rf*. The fact that aged, high-loaded electrodes show a similar $R_{O_2}^{PI}$ (e.g., after 30000 TW cycles) compared to low-loaded cathodes at BOT further clarifies that the *rf* is indeed a major influencing factor on the O_2 mass transport. However, a disentanglement of $R_{O_2}^{PI}$ into a fraction caused by the AST and another contribution, originating solely from the *rf* of the cathode, cannot be drawn unambiguously with respect to the accuracy of the measurement.

Voltage loss analysis of aged cathodes.—Using the total oxygen mass transport resistance at BOT and EOT (Figure 11), the corresponding air polarization curves were corrected for all voltage loss contributions that are currently accessible by in situ measurement techniques, according to a preceding publication[11] and are shown in Figure 13. In short, corrections of the potential include the *HFR*, the effective cathode proton conduction resistance, and the total oxygen mass transport resistance, while the current density was corrected

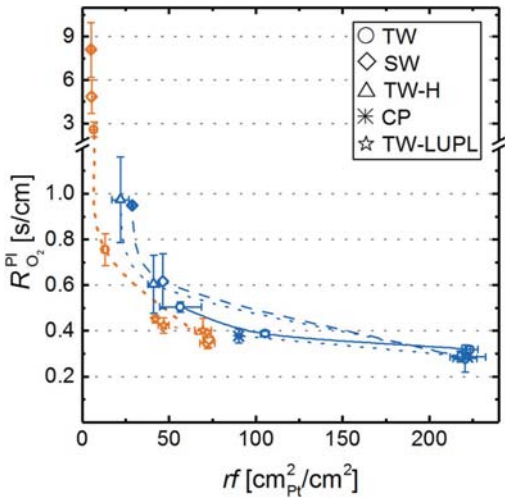

Figure 12. Pressure independent oxygen mass transport resistance, $R_{O_2}^{PI}$, as a function of the electrode's roughness factor, *rf*, for high-loaded (blue) and low-loaded (orange) MEAs at BOT and the respective aging intervals. If the EOT transport resistance could not be separated into pressure dependent and independent contributions (see open bars in Figure 11), the total transport resistance at 170 kPa_{abs} is given in this figure.

for H_2 crossover, electrical short current and was normalized to the cathode's *ECSA*.

For BOT, all H_2/air polarization curves coincide with a Tafel slope of ≈73 mV/dec for high-loaded and ≈80 mV/dec for low-loaded catalyst layers. We attribute the higher Tafel slope in air compared to pure O_2 to unaccounted mass transport limitations, which increase as the O_2 concentration decreases. Upon aging, a strong deviation from the theoretical 70 mV/dec slope is observed at high current density, similar to the limitations observed in pure O_2 (deviations from a straight $E_{corrected}$ vs log(*i*) line at EOT occur at ≈30 mA/cm^2_{Pt} for all aged cathodes, except for the low-loaded cathode subjected to SW cycling). However, the deviation from a straight $E_{corrected}$ vs log(*i*) line at EOT occurs earlier in air, viz., at ≈10 mA/cm^2_{Pt} (again, with the exception of the low-loaded cathode subjected to SW cycling, which deviates much earlier), which one would expect in case of significant oxygen transport resistances. The here observed deviation was also seen by other research groups at specific current densities ranging from 5–50 mA/cm^2_{Pt} in fully corrected air polarization curves with aged MEAs or at very low cathode *rf* values, commonly attributed to a local oxygen diffusion resistance.[9,10,12] Although a correction for the mass transport was applied to these measurements, it seems that the deviation at high Pt specific current density is not accounted for by the transport resistance determined by the limiting current method. Indeed, the conditions of the MEA during the limiting current measurement (local MEA temperature and *RH* due to a high heat production rate at <0.3 V) are not identical to the operating conditions during the polarization curve (lower heat production rate at voltages of ≈0.6–0.5 V) where the corrections are applied, which certainly introduces an error. Furthermore, due to changes in temperature or local *RH*, the utilization of the Pt surface area may change, increasing the oxygen flux to the remaining Pt surface or altering the ORR kinetics.[59,67] While we cannot prove one or the other hypothesis, we consider the limitations of the oxygen mass transport determination method to be a probable cause of at least part of the observed deviations at high current density. However, whatever the origin of these unaccounted transport resistances may be, they clearly scale with the specific current density.

After full correction of the recorded H_2/air polarization curves for all known voltage loss contributions (namely the *HFR*, the effective cathode proton conduction resistance, and the total oxygen mass

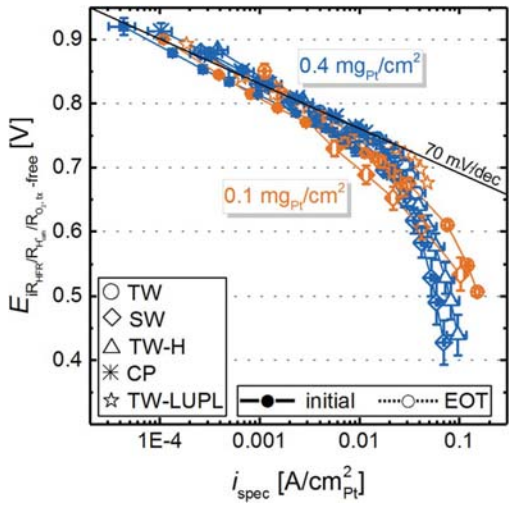

Figure 13. Transport-corrected differential flow H_2/air polarization curves at 80°C, 100% *RH*, and 170 kPa$_{abs}$ at BOT (full symbols) and EOT (open symbols) for high-loaded (blue) and low-loaded (orange) MEAs. The potential is corrected for the *HFR*, effective cathode proton conduction resistance, and the total oxygen mass transport resistance, while the current is corrected for the H_2 crossover and ohmic shorting currents, and is normalized to the cathode *ECSA*. The two slanted lines indicate the specific current density region for high-loaded (blue) and low-loaded (orange) MEAs at BOT. BOT polarization curves of all tested MEAs were averaged and error bars symbolize the standard deviation over all MEAs. Error bars for EOT curves represent the mean absolute deviation between two measurements.

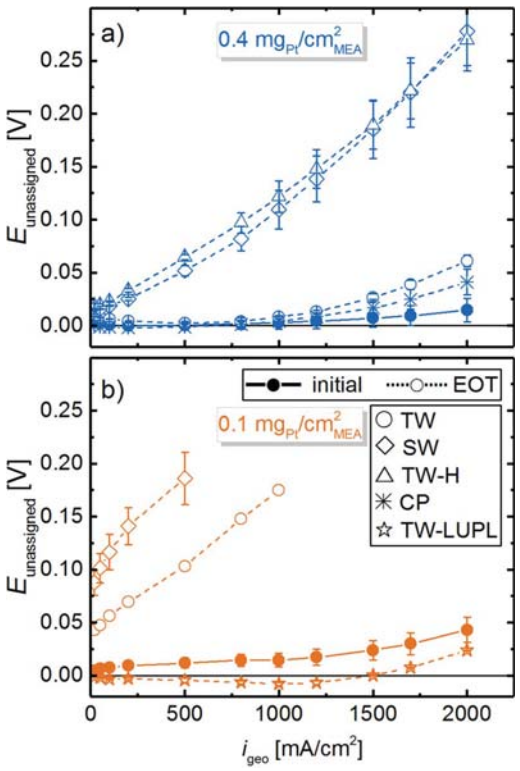

Figure 14. Unaccounted voltage losses between a theoretical, kinetically limited H_2/air polarization curve calculated from the measured ORR mass activity (assuming simple Tafel kinetics with an intrinsic Tafel slope of 70 mV/dec) and polarization curves recorded in H_2/air (differential flow, 170 kPa$_{abs}$, 80°C, and 100% *RH*), where the potential is corrected for the *HFR*, effective cathode proton conduction resistance, and the total oxygen mass transport resistance for a) high-loaded and b) low-loaded cathode catalyst layers at BOT (full symbols) and EOT (open symbols).

transport resistance), the H_2/air polarization curves can be compared to the theoretical, kinetically limited polarization curve, constructed from the experimentally determined ORR mass activities (see Figure 8a) and assuming simple Tafel kinetics with an intrinsic Tafel slope of 70 mV/decade. The remaining unaccounted voltage losses are shown in Figure 14a for high-loaded and in Figure 14b for low-loaded catalyst layers at BOT (solid lines) and EOT for all aging protocols.

An analysis of Figure 14a reveals an almost quantitative account of all voltage losses for high-loaded MEAs at BOT (blue solid line), with only minor unaccounted losses at 2 A/cm^2 (15 ± 11 mV). Upon catalyst layer aging over 30000 TW cycles (open blue circles), the unaccounted voltage losses at higher current density (>1 A/cm^2) increase, pointing to the fact that not all voltage losses can be assessed by the current in situ diagnostic measurements. This discrepancy is even more pronounced for the MEAs exposed to SW and TW-H aging, where unaccounted voltage losses on the order of 250 mV were observed at 2 A/cm^2. In accordance with the previously described evolution of the *ECSA*, the ORR mass activity, and the total oxygen mass transport resistance, both aging protocols (SW and TW-H) lead to identical unaccounted losses. In contrast, the corrosion of the carbon support (CP aging) does not lead to a significant increase of the unaccounted losses (e.g., 41 ± 12 mV at 2 A/cm^2) and therefore cannot explain the high, unaccounted voltage losses for SW and TW-H cycling.

The unaccounted voltage losses for low-loaded MEAs (Figure 14b) at BOT are slightly higher compared to high-loaded MEAs, and are in reasonably good agreement with our previous voltage-loss analysis with the same catalyst.[11] After aging by the TW or SW procedure, rather dramatic unaccounted voltage losses are already observed at low geometric current densities and become increasingly larger with current density. Considering the SW and TW-H aged, high-loaded catalyst layers, the significant unaccounted voltage losses of all these measurements suggest that the quantitative evaluation of voltage loss contributions is impaired when using cathodes with low *rf* values, i.e. at a high Pt specific current density. This hypothesis is further validated by the TW-LUPL voltage cycling test applied to the 0.1 mg$_{Pt}$/cm^2 cathodes: even after 30000 potential cycles, the unaccounted voltage losses were substantially less compared to all other aging protocols, being as little as 24 ± 1 mV at 2 A/cm^2 at EOT, where the roughness factor is 42 ± 2 cm$^2_{Pt}$/cm^2. A very intriguing observation is that this roughness factor is only ≈2–fold larger than the EOT roughness factor of the high-loaded cathodes subjected to SW cycling (29 ± 1 cm$^2_{Pt}$/cm^2), while the unaccounted voltage losses of the latter are >250 mV at 2 A/cm^2. Quite clearly, the currently available in situ diagnostics do not capture the critical voltage loss phenomena which must be related to the morphological changes with regards to Pt particle size and location within the electrode.

Conclusions

To better understand the influence of voltage cycling based ASTs on the development of mass transport resistances and on the extent to which they can be captured by currently available in situ diagnostics (ORR kinetics in H_2/O_2, cathode proton conduction resistance by impedance, oxygen transport resistance via limiting current measurements), we conducted a comprehensive voltage loss analysis on MEAs with high- and low-loaded cathodes (0.4 and 0.1 mg$_{Pt}$/cm^2) over the course of ASTs based on different voltage cycling protocols. These include triangular wave (TW) and square wave (SW) cycles between 0.6 and 1.0 V_{RHE}, TW cycles between 0.6 and a lowered upper potential limit of 0.85 V_{RHE} (TW–LUPL), as well as a combination of a triangular sweeps between 0.6 and 1.0 V_{RHE}, with potential hold periods at the upper and lower potential (TW–H), all conducted in H_2/N_2 (anode/cathode) at ambient pressure, 80°C, and 100% *RH*.

A comparison of the *ECSA* and the O_2 mass transport resistance evolution of MEAs aged by SW cycles leads to considerably faster degradation compared to TW cycles. To identify whether the fast potential transients or the potential hold phase is responsible for the faster degradation rates during SW aging, an additional procedure, consisting of a triangular potential scan followed by potential hold phase (TW-H) was tested. A comparison of the evolution of the cathode's *ECSA*, mass activity, and mass transport resistance revealed that the potential hold rather than the rate of the potential transient is the main contributor to cathode aging in voltage cycling ASTs, so that SW and TW–H cycling profiles lead to identical aging rates with respect to the number of cycles.

For all ASTs, the magnitude of assignable and unassigned O_2 mass transport resistances scaled predominantly with the cathode roughness factor, increasing with decreasing roughness factor, whereby the pressure dependent O_2 transport resistance remained essentially constant. At the same time, ex situ cathode thickness measurements indicated the absence of cathode thinning and thus of significant carbon support corrosion. These results were further compared to an aging procedure which consisted of a constant potential hold at 1.2 V_{cell} for 8 h (at 95°C and 100% *RH*), leading to significant carbon corrosion and concomitant cathode thinning, while maintaining a reasonably high cathode roughness factor. This analysis showed that the impact of carbon corrosion on the O_2 mass transport resistance is minor compared to its increase with decreasing roughness factor.

While 30000 TW or SW cycles between 0.6 and 1.0 V_{RHE} dramatically decrease the H_2/air performance of low-loaded MEAs, it shows negligible degradation over 30000 cycles when a lowered upper potential limit of 0.85 V_{RHE} is applied (TW–LUPL). This provides a guideline to limit cathode degradation under automotive conditions, namely by eliminating high potential periods (e.g., OCV).

Acknowledgment

The authors of this work would like to guide special thanks to Christoph Simon for insightful discussions about limiting current measurements and mass transport resistances. We would also like to thank Daniel Herein and Annett Reichl for fruitful discussions and valuable suggestions. Furthermore, the effort of Hany A. El-Sayed to acquire high quality TEM images is greatly appreciated.

ORCID

Gregor S. Harzer https://orcid.org/0000-0002-1830-1931
Jan N. Schwämmlein https://orcid.org/0000-0001-8902-4508

References

1. *Toyota Motor Co. (accessed* 05/18/2017), http://newsroom.toyota.co.jp/en/detail/4198334/.
2. *Hyundai Motor Co. (accessed* 05/18/2017), http://globalpr.hyundai.com/prCenter/news/newsView.do?dID=1581.
3. *Honda Motor Co., Ltd. (accessed* 10/13/2017), http://hondanews.com/honda-automobiles/channels/clarity-fuel-cell-press-releases/releases/southern-california-customers-take-delivery-of-new-2017-honda-clarity-fuel-cell-sedan.
4. M. F. Mathias, R. Makharia, H. A. Gasteiger, J. J. Conley, T. J. Fuller, C. J. Gittleman, S. S. Kocha, D. P. Miller, C. K. Mittelsteadt, T. Xie, S. G. Yan, and P. T. Yu, *Electrochem. Soc. Interface*, **14**, 24 (2005).
5. A. Veziroglu and R. Macario, *Int. J. Hydrogen Energ.*, **36**, 25 (2011).
6. H. A. Gasteiger, J. E. Panels, and S. G. Yan, *J. Power Sources*, **127**, 162 (2004).
7. H. A. Gasteiger, S. S. Kocha, B. Sompalli, and F. T. Wagner, *Appl. Catal., B.*, **56**, 9 (2005).
8. A. Kongkanand and M. F. Mathias, *J. Phys. Chem. Lett.*, **7**, 1127 (2016).
9. T. A. Greszler, D. Caulk, and P. Sinha, *J. Electrochem. Soc.*, **159**, F831 (2012).
10. J. P. Owejan, J. E. Owejan, and W. Gu, *J. Electrochem. Soc.*, **160**, F824 (2013).
11. A. Orfanidi, P. Madkikar, H. A. El-Sayed, G. S. Harzer, T. Kratky, and H. A. Gasteiger, *J. Electrochem. Soc.*, **164**, F418 (2017).
12. P. Zihrul, I. Hartung, S. Kirsch, G. Huebner, F. Hasché, and H. A. Gasteiger, *J. Electrochem. Soc.*, **163**, F492 (2016).
13. C. H. Paik, G. S. Saloka, and G. W. Graham, *Electrochem. Solid-State Lett.*, **10**, B39 (2007).
14. R. Mukundan, G. James, J. Davey, D. Langlois, D. Torraco, W. Yoon, A. Z. Weber, and R. Borup, *ECS Trans*. **41**, 613 (2011).
15. S. Jomori, N. Nonoyama, and T. Yoshida, *J. Power Sources*, **215**, 18 (2012).
16. R. K. Ahluwalia, S. Arisetty, J.-K. Peng, R. Subbaraman, X. Wang, N. Kariuki, D. J. Myers, R. Mukundan, R. Borup, and O. Polevaya, *J. Electrochem. Soc.*, **161**, F291 (2014).
17. A. P. Young, J. Stumper, and E. Gyenge, *J. Electrochem. Soc.*, **156**, B913 (2009).
18. R. L. Borup, J. R. Davey, F. H. Garzon, D. L. Wood, and M. A. Inbody, *J. Power Sources*, **163**, 76 (2006).
19. K. Yu, D. J. Groom, X. Wang, Z. Yang, M. Gummalla, S. C. Ball, D. J. Myers, and P. J. Ferreira, *Chem. Mater.*, **26**, 5540 (2014).
20. P. J. Ferreira, G. J. la O', Y. Shao-Horn, D. Morgan, R. Makharia, S. Kocha, and H. A. Gasteiger, *J. Electrochem. Soc.*, **152**, A2256 (2005).
21. S. Arisetty, X. Wang, R. K. Ahluwalia, R. Mukundan, R. Borup, J. Davey, D. Langlois, F. Gambini, O. Polevaya, and S. Blanchet, *J. Electrochem. Soc.*, **159**, B455 (2012).
22. R. G. Compton and G. H. W. Sanders, in *Electrode potentials*, Oxford University Press, Oxford, New York (1996).
23. J. P. Meyers and R. M. Darling, *J. Electrochem. Soc.*, **153**, A1432 (2006).
24. R. L. Borup, D. D. Papadias, R. Mukundan, D. Spernjak, D. A. Langlois, R. Ahluwalia, K. L. More, and S. Grot, *ECS Trans*. **69**, 1029 (2015).
25. C. A. Reiser, L. Bregoli, T. W. Patterson, J. S. Yi, J. D. Yang, M. L. Perry, and T. D. Jarvi, *Electrochem. Solid-State Lett.*, **8**, A273 (2005).
26. Y. Yu, H. Li, H. Wang, X.-Z. Yuan, G. Wang, and M. Pan, *J. Power Sources*, **205**, 10 (2012).
27. J. N. Schwämmlein, P. J. Rheinländer, Y. Chen, K. F. Freyer, and H. A. Gasteiger, *ECS Trans*. **80**, 927 (2017).
28. C. Wagner, *Z. Elektrochem. (Zeitschrift für Elektrochemie).*, **65**, 581 (1961).
29. R. M. Darling and J. P. Meyers, *J. Electrochem. Soc.*, **150**, A1523 (2003).
30. J. Zhang, B. A. Litteer, W. Gu, H. Liu, and H. A. Gasteiger, *J. Electrochem. Soc.*, **154**, B1006 (2007).
31. C. Simon, F. Hasché, D. Müller, and H. A. Gasteiger, *ECS Trans*. **69**, 1293 (2015).
32. C. Simon, F. Hasché, and H. A. Gasteiger, *J. Electrochem. Soc.*, **164**, F591 (2017).
33. R. Makharia, M. F. Mathias, and D. R. Baker, *J. Electrochem. Soc.*, **152**, A970 (2005).
34. Y. Liu, M. W. Murphy, D. R. Baker, W. Gu, C. Ji, J. Jorne, and H. A. Gasteiger, *J. Electrochem. Soc.*, **156**, B970 (2009).
35. M. Eikerling and A. A. Kornyshev, *J. Electroanal. Chem.*, **475**, 107 (1999).
36. D. R. Baker, D. A. Caulk, K. C. Neyerlin, and M. W. Murphy, *J. Electrochem. Soc.*, **156**, B991 (2009).
37. N. Nonoyama, S. Okazaki, A. Z. Weber, Y. Ikogi, and T. Yoshida, *J. Electrochem. Soc.*, **158**, B416 (2011).
38. W. Gu, D. R. Baker, Y. Liu, and H. A. Gasteiger, in *Handbook of Fuel Cells*, 1st ed., W. Vielstich, H. Yokokawa, and H. A. Gasteiger, p. 631, John Wiley & Sons Ltd, Chichester (2009).
39. J. A. Gilbert, N. N. Kariuki, X. Wang, A. J. Kropf, K. Yu, D. J. Groom, P. J. Ferreira, D. Morgan, and D. J. Myers, *Electrochimica Acta*. **173**, 223 (2015).
40. M. Uchimura and S. S. Kocha, *ECS Trans*. **11**, 1215 (2007).
41. A. Ohma, T. Mashio, K. Sato, H. Iden, Y. Ono, K. Sakai, K. Akizuki, S. Takaichi, and K. Shinohara, *Electrochim. Acta.*, **56**, 10832 (2011).
42. R. N. Carter, S. S. Kocha, F. Wagner, M. Fay, and H. A. Gasteiger, *ECS Trans*. **11**, 403 (2007).
43. T. R. Garrick, T. E. Moylan, V. Yarlagadda, and A. Kongkanand, *J. Electrochem. Soc.*, **164**, F55 (2017).
44. T. J. Schmidt, H. A. Gasteiger, G. D. Stäb, P. M. Urban, D. M. Kolb, and R. J. Behm, *J. Electrochem. Soc.*, **145**, 2354 (1998).
45. A. López-Cudero, A. Cuesta, and C. Gutiérrez, *J. Electroanal. Chem.*, **579**, 1 (2005).
46. A. Cuesta, A. Couto, A. Rincón, M. C. Pérez, A. López-Cudero, and C. Gutiérrez, *J. Electroanal. Chem.*, **586**, 184 (2006).
47. A. López-Cudero, Á. Cuesta, and C. Gutiérrez, *J. Electroanal. Chem.*, **586**, 204 (2006).
48. D. Strmcnik, D. Tripkovic, D. van der Vliet, V. Stamenkovic, and N. M. Marković, *Electrochem. Commun.*, **10**, 1602 (2008).
49. F. T. Wagner, S. G. Yan, and P. T. Yu, in *Handbook of Fuel Cells*, 1st ed., W. Vielstich, H. Yokokawa, and H. A. Gasteiger, p. 250, John Wiley & Sons Ltd, Chichester (2009).
50. F. Mailard, S. Pronkin, and E. R. Savinova, in *Handbook of Fuel Cells*, 1st ed., W. Vielstich, H. Yokokawa, and H. A. Gasteiger, p. 101, John Wiley & Sons Ltd, Chichester (2009).
51. J. A. Gilbert, N. N. Kariuki, R. Subbaraman, A. J. Kropf, M. C. Smith, E. F. Holby, D. Morgan, and D. J. Myers, *J. Am. Chem. Soc.*, **134**, 14823 (2012).
52. S. Cherevko, A. R. Zeradjanin, A. A. Topalov, N. Kulyk, I. Katsounaros, and K. J. J. Mayrhofer, *ChemCatChem*. **6**, 2219 (2014).
53. H. A. Gasteiger, W. Gu, B. Litteer, R. Makharia, B. Brady, M. Budinski, E. Thompson, F. T. Wagner, S. G. Yan, and P. T. Yu, in *Mini-Micro Fuel Cells*, 1st ed., S. Kakaç, A. Pramuanjaroenkij, and L. Vasiliev, p. 225, Springer Netherlands, Dordrecht (2008).
54. P. D. Beattie, V. I. Basura, and S. Holdcroft, *J. Electroanal. Chem.*, **468**, 180 (1999).
55. S. Shukla, D. Stanier, M. S. Saha, J. Stumper, and M. Secanell, *J. Electrochem. Soc.*, **163**, F677 (2016).
56. H. Liu, H. A. Gasteiger, A. Laconti, and J. Zhang, *ECS Trans*. **1**, 283 (2006).
57. K. Kudo, T. Suzuki, and Y. Morimoto, *ECS Trans*. **33**, 1495 (2010).
58. T. V. Reshetenko and J. St-Pierre, *J. Electrochem. Soc.*, **161**, F1089 (2014).
59. N. P. Subramanian, T. A. Greszler, J. Zhang, W. Gu, and R. Makharia, *J. Electrochem. Soc.*, **159**, B531 (2012).
60. S. S. Kocha, in *Handbook of Fuel Cells*, 1st ed., W. Vielstich, A. Lamm, and H. A. Gasteiger, p. 538, John Wiley & Sons Ltd, Chichester (2009).

61. H. A. Gasteiger, W. Gu, R. Makharia, M. F. Mathias, and B. Sompalli, in *Handbook of Fuel Cells*, 1st ed., W. Vielstich, A. Lamm, and H. A. Gasteiger, p. 593, John Wiley & Sons Ltd, Chichester (2009).
62. S. Zhang, X.-Z. Yuan, J. N. C. Hin, H. Wang, K. A. Friedrich, and M. Schulze, *J. Power Sources*, **194**, 588 (2009).
63. K. Kinoshita, *J. Electrochem. Soc.*, **137**, 845 (1990).
64. K. J. J. Mayrhofer, D. Strmcnik, B. B. Blizanac, V. Stamenkovic, M. Arenz, and N. M. Marković, *Electrochim. Acta.*, **53**, 3181 (2008).
65. C. Simon, D. Kartouzian, D. Müller, F. Wilhelm, and H. A. Gasteiger, *J. Electrochem. Soc.*, **164**, F1697 (2017).
66. D. A. Caulk and D. R. Baker, *J. Electrochem. Soc.*, **157**, B1237 (2010).
67. K. Shinozaki, H. Yamada, and Y. Morimoto, *J. Electrochem. Soc.*, **158**, B467 (2011).

4 Conclusion

The motivation of this thesis was to elucidate the influence of catalyst and catalyst layer properties on the performance of proton exchange membrane fuel cells (PEMFC), especially in the high current density region. Additionally, the degradation mechanisms of catalyst layers were investigated with a here refined accelerated stress test in order to deduce optimized operating conditions for increased lifetime.

Firstly, the influence of the ionomer distribution in the catalyst layer was investigated. We could show by electrochemical techniques that the ionomer distribution in the catalyst layer is inhomogeneous for a standard platinum catalyst on Vulcan carbon. This inhomogeneity results in significant unaccounted voltage losses after correction of transport (O_2 and H^+) and ionic/electric resistances (*HFR*). By a surface modification of the Vulcan carbon with -NH_x groups, a strong coulomb interaction between the ionomer's side chain and the positively charged -NH_x group is expected. Our analysis suggests that this facilitates a more homogeneous ionomer distribution during catalyst layer fabrication. Altering the ionomer to carbon ratio (I/C) leads to an optimized performance at I/C=0.4, where the perfect balance between sufficient proton transport and a thin ionomer layer with low O_2 transport resistance is obtained. Figure 4.1 a graphically summarized the results of this investigation.

In a subsequent study, the influence of the Pt particle distribution on a high surface area carbon support (Ketjenblack) was investigated. As this type of carbon possesses a large fraction of internal porosity, the Pt particles can either be deposited on the outside of the carbon or within the micropores of the primary carbon particles. By choosing the appropriate synthesis method (incipient wetness or polyol reduction), the Pt deposition was controlled preferentially to the inside or outside of the pores. When Pt particles are deposited on the outer surface, the fuel cell performance at high current density was found to be superior due to shorter paths for oxygen diffusion towards the catalyst, hence lower O_2 transport resistance. Pt inside the pores shows a ≈2-fold higher mass activity due to the absence of ionomer poisoning, but performs inferior at high current density as a large transport resistance is imposed by the O_2 diffusion into the pore. Similar electrochemical observations (high mass activity – low performance at high current, and vice versa) have been made by other researchers for different carbon support types. With our study we could prove that not primarily the type of carbon support but the location of platinum

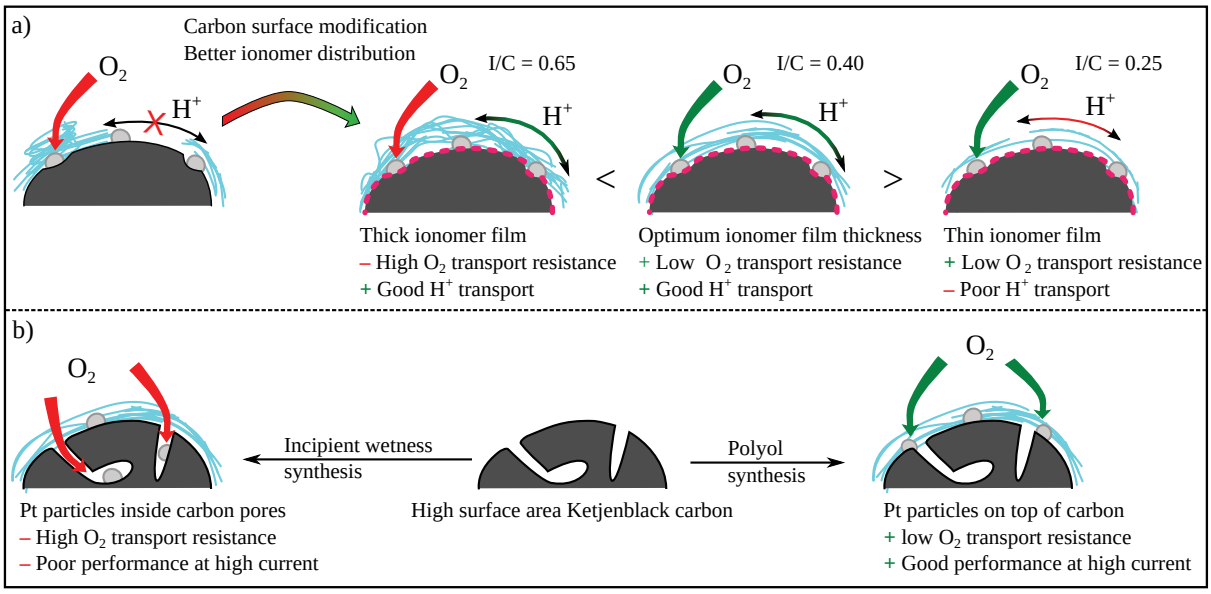

Figure 4.1: a) Graphical summary of catalyst optimization by surface modification of Vulcan carbon (black) with -NH_x groups (dotted pink line) and the influence of ionomer to carbon ratio (I/C) on MEA performance. b) Graphical representation of the influence of synthesis method on Pt particle distribution on high surface area Ketjenblack and the resulting high current density performance.

particles on its surface is the governing factor.

Finally, the degradation mechanism of catalyst layers upon accelerated stress tests with different voltage profiles was investigated. The emphasis of this study was put on mass transport related phenomena and the evaluation of voltage loss contributions. We could show that carbon corrosion and the concomitant catalyst layer thinning was absent for potential cycles with an upper potential limit of 1.0 V (or below); the increase in oxygen mass transport resistance was solely due to the decreased *ECSA*. By analyzing different voltage profiles, it became clear that the potential transient (sweep or step) has insignificant influence on MEA deterioration, while the hold time at high potentials is the main cause for voltage cycling induced degradation. Presumably, a long hold time enables dissolved Pt species to diffuse in the electrolyte phase and thereby accelerate Pt surface area loss. Additionally, we could show that lowering the upper potential limit during voltage cycling to 0.85 V, the H_2/air fuel cell performance does not degrade over the 30000 cycles of the AST. This provides a guideline to extend PEMFC lifetime under operating conditions by avoiding high potential excursions, e.g., OCV periods.

In short, our work has contributed in several ways to current problems within the fuel cell research community. The carbon support modification has shown that the same catalyst activity determined ex situ, e.g., by RDE experiments, does not necessarily translate to the same fuel cell performance. In case of a better ionomer distribution, the MEA performance is significantly increased for the same catalyst. This stresses the necessity of

early MEA studies to determine if catalyst surface properties are suitable for catalyst layer fabrication.

The study on Pt location within the carbon support has disproven a hypothesis which prevailed for a long time in the fuel cell research community, namely the influence of carbon support on MEA performance. With our study we could show that not the type of carbon support but the location of Pt particles on the support is the main factor influencing MEA performance.

With our study on MEA degradation, we identified detrimental operating conditions and proposed a mitigation strategy. Additionally, we could support the current understanding of oxygen transport resistance with respect to catalyst surface area. Overall, these results could represent ways for fuel cell manufacturers to increase MEA performance by optimizing the catalyst morphology and ionomer distribution and to extend system lifetime by carefully controlling operating conditions, thus underlining the importance of our research.

5 Bibliography

[1] "Statista-Dossier zu Antriebstechnologien für Pkw", https://de.statista.com/statistik/studie/id/52706/dokument/antriebstechnologien-fuer-pkw/, accessed on April 17th 2018.

[2] "Aral Studie – Trends beim Autokauf", https://www.aral.de/content/dam/aral/Presse%20Assets/pdfs-Broschueren/Aral-Studie-Trends-beim-Autokauf-2017.pdf, accessed on April 17th 2018.

[3] "Der Hyundai ix35 Fuel Cell", https://www.hyundai.de/Modelle/ix35-Fuel-Cell.html, accessed on April 17th 2018.

[4] "Der Toyota Mirai", https://www.toyota.de/automobile/der-toyota-mirai, accessed on April 17th 2018.

[5] "Wasserstoffmobilität beginnt jetzt", https://h2.live/, accessed on April 17th 2018.

[6] A. Kongkanand and M. F. Mathias, "The Priority and Challenge of High-Power Performance of Low- Platinum Proton-Exchange Membrane Fuel Cells", *The Journal of Physical Chemistry Letters* **7**, 1127–1137, (2016).

[7] G. Sandstede, E. J. Cairns, V. S. Bagotsky and K. Wiesener in: *Handbook of Fuel Cells*, "History of low temperature fuel cells", vol. 1, 1st ed., pp. 145 –219, W. Vielstich, A. Lamm and H. A. Gasteiger, John Wiley & Sons Ltd, Chichester, (2003).

[8] S. S. Kocha in: *Handbook of Fuel Cells*, "Principles of MEA preparation", vol. 3, 1st ed., pp. 538–565, W. Vielstich, A. Lamm and H. A. Gasteiger, John Wiley & Sons Ltd, Chichester, (2003).

[9] M. Doyle and G. Rajendran in: *Handbook of Fuel Cells*, "Perfluorinated Membranes", vol. 3, 1st ed., pp. 321–395, W. Vielstich, A. Lamm and H. A. Gasteiger, John Wiley & Sons Ltd, Chichester, (2003).

[10] C. Heitner-Wirguin, "Recent advances in perfluorinated ionomer membranes: structure, properties and applications", *Journal of Membrane Science* **120**, 1–33, (1996).

[11] M. F. Mathias, R. Makharia, H. A. Gasteiger, J. J. Conley, T. J. Fuller, C. J. Gittleman, S. S. Kocha, D. P. Miller, C. K. Mittelsteadt, T. Xie, S. G. Yan and P. T. Yu, "Two Fuel Cell Cars In Every Garage", *Electrochemical Society Interface* **14**, 24–35, (2005).

[12] "Production of polyamide fibers worldwide from 1975 to 2016 (in 1,000 metric tons)", https://www.statista.com/statistics/649908/polyamide-fiber-production-worldwide, accessed on April 23rd 2018.

[13] B. D. James, J. H. Huya-Koudio, C. Houchings and D. A. DeSantis, "Mass Production Cost Estimation of Direct H_2 PEM Fuel Cell Systems for Transportation Applications: 2017 Update", DOI 10.13140/RG.2.2.36532.55683.

[14] Battelle Memorial Institute, "Manufacturing Cost Analysis of PEM Fuel Cell Systems for 5- and 10-kW Backup Power Applications", https://www.energy.gov/eere/fuelcells/downloads/manufacturing-cost-analysis-pem-fuel-cell-systems-5-and-10-kw-backup-power.

[15] W. Y. Hsu and T. D. Gierke, "Ion transport and clustering in nafion perfluorinated membranes", *Journal of Membrane Science* **13**, 307 –326, (1983).

[16] T. Shimoaka, C. Wakai, T. Sakabe, S. Yamazaki and T. Hasegawa, "Hydration structure of strongly bound water on the sulfonic acid group in a Nafion membrane studied by infrared spectroscopy and quantum chemical calculation", *Physical Chemistry Chemical Physics* **17**, 8843–8849, (2015).

[17] K. A. Mauritz and R. B. Moore, "State of Understanding of Nafion", *Chemical Reviews* **104**, 4535–4586, (2004).

[18] A. Eisenberg, B. Hird and R. B. Moore, "A New Multiplet-Cluster Model for the Morphology of Random Ionomers", *Macromolecules* **23**, 4098–4107, (1990).

[19] C. K. Mittelsteadt and H. Liu in: *Handbook of Fuel Cells*, "Conductivity, permeability, and ohmic shorting of ionomeric membranes", vol. 5, 1st ed., W. Vielstich, H. Yokokawa and H. A. Gasteiger, John Wiley & Sons Ltd, Chichester, (2009).

[20] D. E. Curtin, R. D. Lousenberg, T. J. Henry, P. C. Tangeman and M. E. Tisack, "Advanced materials for improved PEMFC performance and life", *Journal of Power Sources* **131**, 41–48, (2004).

[21] M. Nakao and M. Yoshitake in: *Handbook of Fuel Cells*, "Composite perfluorinated Membranes", vol. 3, 1st ed., pp. 412–419, W. Vielstich, A. Lamm and H. A. Gasteiger, John Wiley & Sons Ltd, Chichester, (2003).

[22] M. Breitwieser, C. Klose, M. Klingele, A. Hartmann, J. Erben, H. Cho, J. Kerres, R. Zengerle and S. Thiele, "Simple fabrication of 12 μm thin nanocomposite fuel cell membranes by direct electrospinning and printing", *Journal of Power Sources* **337**, 137–144, (2017).

[23] F. D. Coms, H. Liu and J. E. Owejan, "Mitigation of Perfluorosulfonic Acid Membrane Chemical Degradation Using Cerium and Manganese Ions", *ECS Transactions* **16**, 1735–1747, (2008).

[24] H. Liu, H. A. Gasteiger, A. Laconti and J. Zhang, "Factors Impacting Chemical Degradation Of Perfluorinated Sulfonic Acid Ionomers", *ECS Transactions* **1**, 283–293, (2006).

[25] A. B. LaConti, M. Hamdan and R. C. McDonald in: *Handbook of Fuel Cells*, "Mechanisms of membrane degradation", vol. 3, 1st ed., pp. 647–662, W. Vielstich, A. Lamm and H. A. Gasteiger, John Wiley & Sons Ltd, Chichester, (2003).

[26] E. Endoh, "Development of Highly Durable PFSA Membrane and MEA for PEMFC Under High Temperature and Low Humidity Conditions", *ECS Transactions* **16**, 1229–1240, (2008).

[27] J. Durst, A. Siebel, C. Simon, F. Hasche, J. Herranz and H. A. Gasteiger, "New insights into the electrochemical hydrogen oxidation and evolution reaction mechanism", *Energy & Environmental Science* **7**, 2255–2260, (2014).

[28] H. A. Gasteiger, S. S. Kocha, B. Sompalli and F. T. Wagner, "Activity benchmarks and requirements for Pt, Pt-alloy, and non-Pt oxygen reduction catalysts for PEMFCs", *Applied Catalysis B: Environmental* **56**, 9–35, (2005).

[29] T. Y. Paul, W. Gu, J. Zhang, R. Makharia, F. T. Wagner and H. A. Gasteiger in: *Polymer electrolyte fuel cell durability*, "Carbon-support requirements for highly durable fuel cell operation", 1st ed., pp. 29–53, F. N. Büchi, M. Inaba and T. J. Schmidt, Springer, New York, (2009).

[30] F. Maillard, P. A. Simonov and E. R. Savinova in: *Carbon materials for catalysis*, "Carbon Materials as Supports for Fuel Cell Electrocatalysts", 1st ed., P. Serp and J. L. Figueiredo, John Wiley & Sons, Hoboken, (2009).

[31] K. Kinoshita in: *Carbon: Electrochemical and Physicochemical Properties*, 1st ed., pp. 3–7, John Wiley & Sons Ltd, New York, (1988).

[32] M. Wissler, "Graphite and carbon powders for electrochemical applications", *Journal of Power Sources* **156**, 142–150, (2006).

[33] P. Trogadas, T. F. Fuller and P. Strasser, "Carbon as catalyst and support for electrochemical energy conversion", *Carbon* **75**, 5–42, (2014).

[34] E. Antolini, "Carbon supports for low-temperature fuel cell catalysts", *Applied Catalysis B: Environmental* **88**, 1–24, (2009).

[35] Y. Liu, C. Ji, W. Gu, J. Jorne and H. A. Gasteiger, "Effects of Catalyst Carbon Support on Proton Conduction and Cathode Performance in PEM Fuel Cells", *Journal of The Electrochemical Society* **158**, B614–B621, (2011).

[36] A. Orfanidi, P. Madkikar, H. El-Sayed, G. S. Harzer, T. Kratky and H. A. Gasteiger, "The Key to High Performance Low Pt Loaded Electrodes", *Journal of The Electrochemical Society* **164**, F418–F426, (2017).

[37] E. P. Ambrosio, C. Francia, C. Gerbaldi, N. Penazzi, P. Spinelli, M. Manzoli and G. Ghiotti, "Mesoporous carbons as low temperature fuel cell platinum catalyst supports", *Journal of Applied Electrochemistry* **38**, 1019–1027, (2008).

[38] C.-Y. Ahn, J.-Y. Cheon, S.-H. Joo and J. Kim, "Effects of ionomer content on Pt catalyst/ordered mesoporous carbon support in polymer electrolyte membrane fuel cells", *Journal of Power Sources* **222**, 477–482, (2013).

[39] V. Yarlagadda, M. K. Carpenter, T. E. Moylan, R. S. Kukreja, R. Koestner, W. Gu, L. Thompson and A. Kongkanand, "Boosting Fuel Cell Performance with Accessible Carbon Mesopores", *ACS Energy Letters* **3**, 618–621, (2018).

[40] K. H. Choi, H. S. Kim and T. H. Lee, "Electrode fabrication for proton exchange membrane fuel cells by pulse electrodeposition", *Journal of Power Sources* **75**, 230–235, (1998).

[41] N. Veizaga, J. Fernandez, M. Bruno, O. Scelza and S. de Miguel, "Deposition of Pt nanoparticles on different carbonaceous materials by using different preparation methods for PEMFC electrocatalysts", *International Journal of Hydrogen Energy* **37**, 17910–17920, (2012).

[42] C. Lamy in: *Electrocatalysts for Low Temperature Fuel Cells: Fundamentals and Recent Trends*, "Electrocatalytic Reactions Involved in Low-temperature Fuel Cells", 1st ed., pp. 75–111, T. Maiyalagan and V. S. Saji, John Wiley & Sons, (2017).

[43] N. M. Markovic, H. A. Gasteiger and P. N. Ross Jr, "Oxygen Reduction on Platinum Low-Index Single-Crystal Surfaces in Sulfuric Acid Solution: Rotating Ring–Pt(hkl) Disk Studies", *The Journal of Physical Chemistry* **99**, 3411–3415, (1995).

[44] N. Markovic, H. A. Gasteiger and P. N. Ross, "Kinetics of Oxygen Reduction on Pt(hkl) Electrodes: Implications for the Crystallite Size Effect with Supported Pt Electrocatalysts", *Journal of the Electrochemical Society* **144**, 1591–1597, (1997).

[45] S. Guerin, B. E. Hayden, C. E. Lee, C. Mormiche, J. R. Owen, A. E. Russell, B. Theobald and D. Thompsett, "Combinatorial Electrochemical Screening of Fuel Cell Electrocatalysts", *Journal of Combinatorial Chemistry* **6**, 149–158, (2004).

[46] K. J. J. Mayrhofer, D. Strmcnik, B. B. Blizanac, V. Stamenkovic, M. Arenz and N. M. Markovic, "Measurement of oxygen reduction activities via the rotating disc electrode method: From Pt model surfaces to carbon-supported high surface area catalysts", *Electrochimica Acta* **53**, 3181–3188, (2008).

[47] B. E. Hayden and J.-P. Suchsland in: *Fuel Cell Catalysis: A Surface Science Approach*, "Support and particle size effects in electrocatalysis", 1st ed., pp. 567–592, Ed.: M. T.M. a. Koper, John Wiley & Sons, (2009).

[48] A. Rabis, P. Rodriguez and T. J. Schmidt, "Electrocatalysis for Polymer Electrolyte Fuel Cells: Recent Achievements and Future Challenges", *ACS Catalysis* **2**, 864–890, (2012).

[49] J. Greeley and M. Mavrikakis, "Alloy catalysts designed from first principles", *Nature Materials* **3**, 810–815, (2004).

[50] Y. Wang and P. B. Balbuena, "Design of Oxygen Reduction Bimetallic Catalysts: Ab-Initio-Derived Thermodynamic Guidelines", *The Journal of Physical Chemistry B* **109**, 18902–18906, (2005).

[51] J. Greeley, I. E. L. Stephens, A. Bondarenko, T. P. Johansson, H. A. Hansen, T. Jaramillo, J. Rossmeisl, I Chorkendorff and J. K. Nørskov, "Alloys of platinum and early transition metals as oxygen reduction electrocatalysts", *Nature Chemistry* **1**, 552, (2009).

[52] J. Greeley and J. K. Nørskov, "Combinatorial Density Functional Theory-Based Screening of Surface Alloys for the Oxygen Reduction Reaction", *The Journal of Physical Chemistry C* **113**, 4932–4939, (2009).

[53] V. Tripković, E. Skúlason, S. Siahrostami, J. K. Nørskov and J. Rossmeisl, "The oxygen reduction reaction mechanism on Pt (111) from density functional theory calculations", *Electrochimica Acta* **55**, 7975–7981, (2010).

[54] A. Kulkarni, S. Siahrostami, A. Patel and J. K. Nørskov, "Understanding Catalytic Activity Trends in the Oxygen Reduction Reaction", *Chemical Reviews* **118**, 2302–2312, (2018).

[55] C. Baldizzone, S. Mezzavilla, H. W. Carvalho, J. C. Meier, A. K. Schuppert, M. Heggen, C. Galeano, J.-D. Grunwaldt, F. Schüth and K. J. Mayrhofer, "Confined-Space Alloying of Nanoparticles for the Synthesis of Efficient PtNi Fuel-Cell Catalysts", *Angewandte Chemie International Edition* **53**, 14250–14254, (2014).

[56] S. Mezzavilla, C. Baldizzone, A.-C. Swertz, N. Hodnik, E. Pizzutilo, G. Polymeros, G. P. Keeley, J. Knossalla, M. Heggen, K. J. Mayrhofer and F. Schüth, "Structure–Activity–Stability Relationships for Space-Confined Pt_xNi_y Nanoparticles in the Oxygen Reduction Reaction", *ACS Catalysis* **6**, 8058–8068, (2016).

[57] K. Neyerlin, R. Srivastava, C. Yu and P. Strasser, "Electrochemical activity and stability of dealloyed Pt–Cu and Pt–Cu–Co electrocatalysts for the oxygen reduction reaction (ORR)", *Journal of Power Sources* **186**, 261–267, (2009).

[58] C. Cui, L. Gan, H.-H. Li, S.-H. Yu, M. Heggen and P. Strasser, "Octahedral PtNi Nanoparticle Catalysts: Exceptional Oxygen Reduction Activity by Tuning the Alloy Particle Surface Composition", *Nano Letters* **12**, 5885–5889, (2012).

[59] C. Cui, L. Gan, M. Heggen, S. Rudi and P. Strasser, "Compositional segregation in shaped Pt alloy nanoparticles and their structural behaviour during electrocatalysis.", *Nature Materials* **12**, 765–71, (2013).

[60] B. Han, C. E. Carlton, A. Kongkanand, R. S. Kukreja, B. R. Theobald, L. Gan, R. O'Malley, P. Strasser, F. T. Wagner and Y. Shao-Horn, "Record activity and stability of dealloyed bimetallic catalysts for proton exchange membrane fuel cells", *Energy & Environmental Science* **8**, 258–266, (2015).

[61] C. Baldizzone, L. Gan, N. Hodnik, G. P. Keeley, A. Kostka, M. Heggen, P. Strasser and K. J. J. Mayrhofer, "Stability of Dealloyed Porous Pt/Ni Nanoparticles", *ACS Catalysis* **5**, 5000–5007, (2015).

[62] V. R. Stamenkovic, B. Fowler, B. S. Mun, G. Wang, P. N. Ross, C. A. Lucas and N. M. Marković, "Improved Oxygen Reduction Activity on Pt_3Ni (111) via Increased Surface Site Availability", *Science* **315**, 493–497, (2007).

[63] L. Zhang, L. T. Roling, X. Wang, M. Vara, M. Chi, J. Liu, S.-I. Choi, J. Park, J. A. Herron, Z. Xie, M. Mavrikakis and Y. Xia, "Platinum-based nanocages with subnanometer-thick walls and well-defined, controllable facets", *Science* **349**, 412–416, (2015).

[64] P. Strasser, "Catalysts by Platonic design", *Science* **349**, 379–380, (2015).

[65] P. J. Ferreira, G. J. la O', Y. Shao-Horn, D. Morgan, R. Makharia, S. Kocha and H. A. Gasteiger, "Instability of Pt/C Electrocatalysts in Proton Exchange Membrane Fuel Cells", *Journal of The Electrochemical Society* **152**, A2256–A2271, (2005).

[66] R. K. Ahluwalia, S. Arisetty, J.-K. Peng, R. Subbaraman, X. Wang, N. Kariuki, D. J. Myers, R. Mukundan, R. Borup and O. Polevaya, "Dynamics of Particle Growth and Electrochemical Surface Area Loss due to Platinum Dissolution", *Journal of the Electrochemical Society* **161**, F291–F304, (2014).

[67] R. L. Borup, J. R. Davey, F. H. Garzon, D. L. Wood and M. A. Inbody, "PEM fuel cell electrocatalyst durability measurements", *Journal of Power Sources* **163**, 76–81, (2006).

[68] C. H. Paik, G. S. Saloka and G. W. Graham, "Influence of Cyclic Operation on PEM Fuel Cell Catalyst Stability", *Electrochemical and Solid-State Letters* **10**, B39–B42, (2007).

[69] R. Mukundan, G. James, J. Davey, D. Langlois, D. Torraco, W. Yoon, A. Z. Weber and R. Borup, "Accelerated Testing Validation", *ECS Transactions* **41**, 613–619, (2011).

[70] S. Arisetty, X. Wang, R. K. Ahluwalia, R. Mukundan, R. Borup, J. Davey, D. Langlois, F. Gambini, O. Polevaya and S. Blanchet, "Catalyst Durability in PEM Fuel Cells with Low Platinum Loading", *Journal of The Electrochemical Society* **159**, B455–B462, (2012).

[71] K. Yu, D. J. Groom, X. Wang, Z. Yang, M. Gummalla, S. C. Ball, D. J. Myers and P. J. Ferreira, "Degradation Mechanisms of Platinum Nanoparticle Catalysts in Proton Exchange Membrane Fuel Cells: The Role of Particle Size", *Chemistry of Materials* **26**, 5540–5548, (2014).

[72] J. A. Gilbert, N. N. Kariuki, X. Wang, A. J. Kropf, K. Yu, D. J. Groom, P. J. Ferreira, D. Morgan and D. J. Myers, "Pt Catalyst Degradation in Aqueous and Fuel Cell Environments studied via In-Operando Anomalous Small-Angle X-ray Scattering", *Electrochimica Acta* **173**, 223–234, (2015).

[73] S. Jomori, N. Nonoyama and T. Yoshida, "Analysis and modeling of PEMFC degradation: Effect on oxygen transport", *Journal of Power Sources* **215**, 18–27, (2012).

[74] P. Zihrul, I. Hartung, S. Kirsch, G. Huebner, F. Hasché and H. A. Gasteiger, "Voltage Cycling Induced Losses in Electrochemically Active Surface Area and in H_2/Air-Performance of PEM Fuel Cells", *Journal of The Electrochemical Society* **163**, F492–F498, (2016).

[75] M. Uchimura and S. S. Kocha, "The Impact of Cycle Profile on PEMFC Durability", *ECS Transactions* **11**, 1215–1226, (2007).

[76] G. S. Harzer, J. N. Schwämmlein, A. M. Damjanović, S. Ghosh and H. A. Gasteiger, "Cathode Loading Impact on Voltage Cycling Induced PEMFC Degradation: A Voltage Loss Analysis", *Journal of The Electrochemical Society* **165**, F3118–F3131, (2018).

[77] S. Maass, F. Finsterwalder, G. Frank, R. Hartmann and C. Merten, "Carbon support oxidation in PEM fuel cell cathodes", *Journal of Power Sources* **176**, 444–451, (2008).

[78] R. L. Borup, D. D. Papadias, R. Mukundan, D. Spernjak, D. A. Langlois, R. Ahluwalia, K. L. More and S. Grot, "Carbon Corrosion in PEM Fuel Cells During Drive Cycle Operation", *ECS Transactions* **69**, 1029–1038, (2015).

[79] T. Mittermeier, A. Weiß, F. Hasché, G. Hübner and H. A. Gasteiger, "PEM Fuel Cell Start-up/Shut-down Losses vs Temperature for Non-Graphitized and Graphitized Cathode Carbon Supports", *Journal of The Electrochemical Society* **164**, F127–F137, (2017).

[80] M. F. Mathias, J. Roth, J. Fleming and W. Lehnert in: *Handbook of Fuel Cells*, "Diffusion media materials and characterisation", vol. 3, 1st ed., pp. 517–537, W. Vielstich, A. Lamm and H. A. Gasteiger, John Wiley & Sons Ltd, Chichester, (2003).

[81] C. Simon, D. Kartouzian, D. Müller, F. Wilhelm and H. A. Gasteiger, "Impact of Microporous Layer Pore Properties on Liquid Water Transport in PEM Fuel Cells: Carbon Black Type and Perforation", *Journal of The Electrochemical Society* **164**, F1697–F1711, (2017).

[82] C. Simon, F. Hasché and H. A. Gasteiger, "Influence of the Gas Diffusion Layer Compression on the Oxygen Transport in PEM Fuel Cells at High Water Saturation Levels", *Journal of The Electrochemical Society* **164**, F591–F599, (2017).

[83] D. P. Wilkinson and O. Vanderleeden in: *Handbook of Fuel Cells*, "Sepentine flow field design", vol. 3, 1st ed., pp. 315–324, W. Vielstich, A. Lamm and H. A. Gasteiger, John Wiley & Sons Ltd, Chichester, (2003).

[84] G. O. Mopsted and J. M. Moore in: *Handbook of Fuel Cells*, "Performance and durability of bipolar plate materials", vol. 3, 1st ed., pp. 286–293, W. Vielstich, A. Lamm and H. A. Gasteiger, John Wiley & Sons Ltd, Chichester, (2003).

[85] J. Wind, A. LaCroix, S. Braeuninger, P. Hedrich, C. Heller and M. Schudy in: *Handbook of Fuel Cells*, "Metal bipolar plates and coatings", vol. 3, 1st ed., pp. 294–307, W. Vielstich, A. Lamm and H. A. Gasteiger, John Wiley & Sons Ltd, Chichester, (2003).

[86] M. Contestabile, G. Offer, R. Slade, F. Jaeger and M. Thoennes, "Battery electric vehicles, hydrogen fuel cells and biofuels. Which will be the winner?", *Energy & Environmental Science* **4**, 3754–3772, (2011).

[87] T. Hutchinson, S. Burgess and G. Herrmann, "Current hybrid-electric powertrain architectures: Applying empirical design data to life cycle assessment and whole-life cost analysis", *Applied Energy* **119**, 314–329, (2014).

[88] A. Le Duigou and A. Smatti, "On the comparison and the complementarity of batteries and fuel cells for electric driving", *International Journal of Hydrogen Energy* **39**, 17873–17883, (2014).

[89] W. Gu, D. R. Baker, Y. Liu and H. A. Gasteiger in: *Handbook of Fuel Cells*, "Proton exchange membrane fuel cell (PEMFC) down-the-channel performance model", vol. 6, 1st ed., pp. 631–657, W. Vielstich, H. A. Gasteiger, A. Lamm and H. Yokokawa, John Wiley & Sons Ltd, Chichester, (2009).

[90] A. Hamnett in: *Handbook of Fuel Cells*, "Thermodynamics of electrodes and cells", vol. 1, 1st ed., pp. 21–26, W. Vielstich, A. Lamm and H. A. Gasteiger, John Wiley & Sons Ltd, Chichester, (2003).

[91] P. Kurzweil in: *Brennstoffzellentechnik – Grundlagen, Materialien, Anwendungen, Gaserzeugung*, 3rd ed., pp. 20, 22, Springer Fachmedien GmbH, Wiesbaden, (2016).

[92] K. C. Neyerlin, W. Gu, J. Jorne and H. A. Gasteiger, "Study of the Exchange Current Density for the Hydrogen Oxidation and Evolution Reactions", *Journal of The Electrochemical Society* **154**, B631–B635, (2007).

[93] K. C. Neyerlin, W. Gu, J. Jorne, A. Clark and H. A. Gasteiger, "Cathode Catalyst Utilization for the ORR in a PEMFC Analytical Model and Experimental Validation", *Journal of The Electrochemical Society* **154**, B279–B287, (2007).

[94] K. C. Neyerlin, W. Gu, J. Jorne and H. A. Gasteiger, "Determination of Catalyst Unique Parameters for the Oxygen Reduction Reaction in a PEMFC", *Journal of the Electrochemical Society* **153**, A1955–A1963, (2006).

[95] Y. Liu, M. W. Murphy, D. R. Baker, W. Gu, C. Ji, J. Jorne and H. A. Gasteiger, "Proton Conduction and Oxygen Reduction Kinetics in PEM Fuel Cell Cathodes: Effects of Ionomer-to-Carbon Ratio and Relative Humidity", *Journal of The Electrochemical Society* **156**, B970–B980, (2009).

[96] R. Makharia, M. F. Mathias and D. R. Baker, "Measurement of Catalyst Layer Electrolyte Resistance in PEFCs Using Electrochemical Impedance Spectroscopy", *Journal of The Electrochemical Society* **152**, A970–A977, (2005).

[97] D. R. Baker, D. A. Caulk, K. C. Neyerlin and M. W. Murphy, "Measurement of Oxygen Transport Resistance in PEM Fuel Cells by Limiting Current Methods", *Journal of The Electrochemical Society* **156**, B991–B1003, (2009).

[98] A. Kongkanand, N. P. Subramanian, Y. Yu, Z. Liu, H. Igarashi and D. A. Muller, "Achieving High-Power PEM Fuel Cell Performance with an Ultralow- Pt-Content Core–Shell Catalyst", *ACS Catalysis* **6**, 1578–1583, (2016).

[99] T. R. Garrick, T. E. Moylan, M. K. Carpenter and A. Kongkanand, "Electrochemically Active Surface Area Measurement of Aged Pt Alloy Catalysts in PEM Fuel Cells by CO Stripping", *Journal of The Electrochemical Society* **164**, F55–F59, (2017).

[100] N. Nonoyama, S. Okazaki, A. Z. Weber, Y. Ikogi and T. Yoshida, "Analysis of Oxygen-Transport Diffusion Resistance in Proton-Exchange-Membrane Fuel Cells", *Journal of The Electrochemical Society* **158**, B416–B423, (2011).

[101] T. A. Greszler, D. Caulk and P. Sinha, "The Impact of Platinum Loading on Oxygen Transport Resistance", *Journal of The Electrochemical Society* **159**, F831–F840, (2012).

[102] J. P. Owejan, J. E. Owejan and W. Gu, "Impact of Platinum Loading and Catalyst Layer Structure on PEMFC Performance", *Journal of The Electrochemical Society* **160**, F824–F833, (2013).

[103] H. Liu, W. K. Epting and S. Litster, "Gas Transport Resistance in Polymer Electrolyte Thin Films on Oxygen Reduction Reaction Catalysts", *Langmuir* **31**, 9853–9858, (2015).

[104] R. Jinnouchi, K. Kudo, N. Kitano and Y. Morimoto, "Molecular Dynamics Simulations on O_2 Permeation through Nafion Ionomer on Platinum Surface", *Electrochimica Acta* **188**, 767–776, (2016).

[105] Y. Kurihara, T. Mabuchi and T. Tokumasu, "Molecular Analysis of Structural Effect of Ionomer on Oxygen Permeation Properties in PEFC", *Journal of The Electrochemical Society* **164**, F628–F637, (2017).

[106] T. Suzuki, H. Yamada, K. Tsusaka and Y. Morimoto, "Modeling of Oxygen Diffusion Resistance in Polymer Electrolyte Fuel Cells in the Intermediate Potential Region", *Journal of The Electrochemical Society* **165**, F166–F172, (2018).

[107] T. Muzaffar, T. Kadyk and M. Eikerling, "Tipping water balance and the Pt loading effect in polymer electrolyte fuel cells: a model-based analysis", *Sustainable Energy & Fuels* **2**, 1189–1196, (2018).

[108] Y. Ono, A. Ohma, K. Shinohara and K. Fushinobu, "Influence of Equivalent Weight of Ionomer on Local Oxygen Transport Resistance in Cathode Catalyst Layers", *Journal of The Electrochemical Society* **160**, F779–F787, (2013).

[109] K. Kodama, A. Shinohara, N. Hasegawa, K. Shinozaki, R. Jinnouchi, T. Suzuki, T. Hatanaka and Y. Morimoto, "Catalyst Poisoning Property of Sulfonimide Acid Ionomer on Pt (111) Surface", *Journal of The Electrochemical Society* **161**, F649–F652, (2014).

[110] A. Shinohara, K. Kudo, M. Kawasumi, Y. Morimoto and N. Hasegawa, "Non-Crosslinked Perfluoro-Polymer Electrolytes With Two Acid Groups and Their Properties", *ECS Transactions* **58**, 253–259, (2013).

[111] S. Kinoshita, T. Tanuma, K. Yamada, S. Hommura, A. Watakabe, S. Saito and T. Shimohira, "Development of PFSA Ionomers for the Membrane and the Electrodes", *ECS Transactions* **64**, 371–375, (2014).

[112] M. Lopez-Haro, L. Guétaz, T. Printemps, A. Morin, S. Escribano, P.-H. Jouneau, P. Bayle-Guillemaud, F. Chandezon and G. Gebel, "Three-dimensional analysis of Nafion layers in fuel cell electrodes", *Nature Communications* **5**, (2014).

[113] Y.-C. Park, H. Tokiwa, K. Kakinuma, M. Watanabe and M. Uchida, "Effects of carbon supports on Pt distribution, ionomer coverage and cathode performance for polymer electrolyte fuel cells", *Journal of Power Sources* **315**, 179–191, (2016).

[114] M. Uchida, Y. Fukuoka, Y. Sugawara, N. Eda and A. Ohta, "Effects of Microstructure of Carbon Support in the Catalyst Layer on the Performance of Polymer-Electrolyte Fuel Cells", *Journal of The Electrochemical Society* **143**, 2245–2252, (1996).

[115] K. Shinozaki, H. Yamada and Y. Morimoto, "Relative Humidity Dependence of Pt Utilization in Polymer Electrolyte Fuel Cell Electrodes: Effects of Electrode Thickness, Ionomer-to-Carbon Ratio, Ionomer Equivalent Weight, and Carbon Support", *Journal of The Electrochemical Society* **158**, B467–B475, (2011).

[116] T. R. Garrick, T. E. Moylan, V. Yarlagadda and A. Kongkanand, "Characterizing Electrolyte and Platinum Interface in PEM Fuel Cells Using CO Displacement", *Journal of The Electrochemical Society* **164**, F60–F64, (2017).

[117] E. Padgett, N. Andrejevic, Z. Liu, A. Kongkanand, W. Gu, K. Moriyama, Y. Jiang, S. Kumaraguru, T. E. Moylan, R. Kukreja and D. A. Muller, "Connecting Fuel Cell Catalyst Nanostructure and Accessibility Using Quantitative Cryo-STEM Tomography", *Journal of The Electrochemical Society* **165**, F173–F180, (2018).

[118] K. Shinozaki, Y. Morimoto, B. S. Pivovar and S. S. Kocha, "Suppression of oxygen reduction reaction activity on Pt-based electrocatalysts from ionomer incorporation", *Journal of Power Sources* **325**, 745–751, (2016).

[119] G. S. Harzer, A. Orfanidi, H. El-Sayed, P. Madkikar and H. A. Gasteiger, "Tailoring Catalyst Morphology towards High Performance for Low Pt Loaded PEMFC Cathodes", *Journal of The Electrochemical Society* **165**, F770–F779, (2018).

Publication List

Patents:

A. Garsuch, H. Gasteiger, C. Kavakli, **G. Harzer**, “Process for producing a carbon-supported nickel-cobalt-oxide catalyst and its use in rechargeable electrochemical metal-oxygen cells”, EP2916946 A2 (9. November 2012).

Peer-reviewed publications:

1. **G. Harzer**[=], J. Schwämmlein[=], A.-M. Damjanovic, S. Ghosh, H. Gasteiger, “Cathode Loading Impact on Voltage Cycling Induced PEMFC Degradation: A Voltage Loss Analysis”, Journal of The Electrochemical Society, 165 (6), F3118-F3131 (2018).
2. **G. Harzer**, A. Orfanidi, H. El-Sayed, P. Madkikar, H. Gasteiger, “Tailoring Catalyst Morphology towards High Performance for Low Pt Loaded PEMFC Cathodes”, Journal of The Electrochemical Society, 165 (10), F770-F779 (2018).
3. J. Schwämmlein[=], **G. Harzer**[=], P. Pfändner, A. Blankenship, H. El-Sayed, H. Gasteiger, “Activity and Stability of Carbon Supported Pt_xY Alloys for the ORR Determined by RDE and Single-Cell PEMFC Measurements”, in print, Journal of The Electrochemical Society, 165 (15) (2018).
4. P. Madkikar, D. Menga, **G. Harzer**, T. Mittermeier, A. Siebel, F. Wagner, M. Merz, S. Schuppler, P. Nagel, A. Muñoz-García, M. Pavone, H. Gasteiger, M. Piana, “Nanometric Fe-Substituted ZrO_2 on Carbon Black as Novel PGM-Free ORR Catalyst for PEMFCs“, under review (2018).
5. A. Orfanidi, P. Madkikar, H. El-Sayed, **G. Harzer**, T. Kratky, H. Gasteiger, “The Key to High Performance Low Pt Loaded Electrodes”, Journal of The Electrochemical Society, 164 (4), F418–F426 (2017).
6. C. Kavakli, S. Meini, **G. Harzer**, N. Tsiouvaras, M. Piana, A. Siebel, A. Garsuch, H. Gasteiger, J. Herranz, “Nanosized Carbon-Supported Manganese Oxide Phases as Lithium–Oxygen Battery Cathode Catalysts”, ChemCatChem, 5, 3358–3373 (2013).

Oral presentation at conferences:

1. **G. Harzer**, A. Orfanidi, P. Madkikar, H. El-Sayed, C. Simon, H. Gasteiger, “The Influence of Carbon Support and Catalyst Morphology on PEMFC Performance”, 232nd ECS Meeting, National Harbor, MA, USA (October 2017).
2. **G. Harzer**, A. Orfanidi, H. El-Sayed, P. Madkikar, H. Gasteiger, “Carbon Support Modification for High Performance Low Pt Loaded Cathodes”, 6th European PEFC and Electrolyser Forum, Lucerne, Switzerland (July 2017).

Poster presentation at conferences:

1. **G. Harzer**, T. Mittermeier and H. Gasteiger, “Reference Electrode Fuel Cell Setup for the Investigation of Iridium Oxide Dissolution during FC Operation”, Gordon Research Conference - Fuel Cells, Easton, MA, USA (August 2016).
2. **G. Harzer**, C. Chomyn, D. Henschel, J. Herranz, J. Durst, F. Hasché, H. Gasteiger, “Palladium-Based Alloy Nanoparticle Electrocatalysts for Hydrogen Oxidation in Alkaline Media”, Poster Session presented at: 4th Colloquium of the Munich School of Engineering, Munich, Germany (July 2014).